



The University of
Nottingham

UNITED KINGDOM • CHINA • MALAYSIA

Habib, Josef (2012) Development & optimization of diffusion tensor imaging at high field strengths in translational research. PhD thesis, University of Nottingham.

Access from the University of Nottingham repository:

http://eprints.nottingham.ac.uk/12405/1/PhDThesis_JosefHabib.pdf

Copyright and reuse:

The Nottingham ePrints service makes this work by researchers of the University of Nottingham available open access under the following conditions.

This article is made available under the University of Nottingham End User licence and may be reused according to the conditions of the licence. For more details see:

http://eprints.nottingham.ac.uk/end_user_agreement.pdf

A note on versions:

The version presented here may differ from the published version or from the version of record. If you wish to cite this item you are advised to consult the publisher's version. Please see the repository url above for details on accessing the published version and note that access may require a subscription.

For more information, please contact eprints@nottingham.ac.uk

Development & Optimization of Diffusion Tensor
Imaging at High Field Strengths in Translational
Research

Dipl. Ing. (FH) Josef Habib MSc

Thesis submitted to The University of Nottingham
for the degree of Doctor of Philosophy

September 2010

Abstract

Ever since the inception of Diffusion Tensor Imaging (DTI), unabated advancements in its capabilities and applications have been spearheaded by a vibrant research effort to devise dedicated acquisition sequences, protocols and hardware. In translational research, however, the transition of these innovations into the arenas of biomedical research, and ultimately clinical practice is frequently hampered by practical considerations. These include the availability of appropriate expertise, time and resources for their implementation, and considerations of compatibility with established techniques and results reported in literature. Such concerns provide the impetus to maximize the utility of existing protocols before attempting the development of novel dedicated techniques.

In this thesis, three investigations, each targeting a different DTI application, are presented. The strategy implemented throughout involves assessing the suitability of existing sequences for the intended task, and determining any limiting factors, evaluating whether appropriate modifications of the acquisition protocols used are capable of alleviating limitations, and developing novel, dedicated protocols wherever necessary. The value and, importantly, the wide scope of this approach in answering important research questions is exemplified through the breadth of the studies presented.

The first study presents, for the first time, a quantitative evaluation of the effects of cardiac pulsation on prevalent DTI metrics acquired with a specific acquisition protocol used routinely in clinical practice. Findings inform the on-going debate on whether the investment in cardiac gating is merited by improvements in data quality. Effects were observed during only 6 % of the cardiac cycle, and not 20 % as previously reported. The impact of cardiac pulsation on selected diffusion Tensor indices was minimal in group studies, but of potential practical relevance in

individual cases. Methods to predict which individuals may benefit from gating have also been suggested.

Secondly, the feasibility of post-mortem DTI was established through the successful acquisition, also for the first time, of DTI data on a chemically fixed whole human post-mortem brain using a clinical sequence. Previous failed attempts have been attributed to insufficient SNR. In this study scanner stability and distortion are found to be the main limiting factors, and mitigated using appropriate averaging and co-registration strategies.

The third study assessed the potential of ultra-high field strength DTI by identifying and optimizing the potential strengths of DTI at 7T. Subsequent to optimization with respect to SNR, the main sources of artefact were found to be B1 inhomogeneity and inadequate fat suppression. Both were alleviated by modification of the available acquisition protocol, resulting in higher SNR and data quality than previously reported.

Finally, in developing appropriate data quality measures, the 'Difference method', commonly used for the quantification of SNR, was found to be unsuitable for *in vivo* DTI acquisitions at 7 T, leading to the proposal, and successful implementation and validation of an alternative.

Acknowledgements

This work was funded by the European Commission FP6 Marie Curie Action Program (MEST-CT-2005-021170).

I would also like to express my gratitude for the continued support of my supervisors, colleagues, friends and family for their valuable help and support. In particular I would like to thank:

- Prof.Dorothee Auer
- Prof. Richard Bowtell
- Dr. Paul Morgan
- Dr.Bai Li and
- Dr. Christopher Tench.

Table of Contents

Acknowledgements.....	iii
List of Abbreviations.....	vii
List of Figures.....	viii
List of Tables.....	xiii
Chapter 1: Introduction	1
1.1 MRI Theory.....	2
1.1.1 Tissue magnetization - the origins of the NMR signal.....	3
1.1.2 The NMR signal - generation & relaxation.....	7
1.1.3 The anatomy of MRI acquisition sequences.....	14
1.1.4 Echo Formation:.....	16
1.1.5 Spatial encoding.....	20
1.1.6 Image reconstruction	25
1.2 Diffusion MRI theory	27
1.2.1 Diffusion sensitization in MRI.....	27
1.2.2 Characterization of Brownian motion.....	30
1.2.3 Relating diffusion and measured voxel intensity attenuation.....	31
1.2.4 Practical implications of diffusion time	34
1.2.5 The effect of fibrous tissue on 3D diffusion profiles	35
1.2.6 Diffusion Tensor Imaging (DTI).....	35
1.2.7 Evaluation of DTI data.....	37
1.3 Echo planar Imaging (EPI).....	39
1.3.1 Challenges of diffusion sensitized MRI.....	39
1.3.2 Ultra-fast image acquisition using EPI	41
1.4 General experimental details	44
Chapter 2. : Quantitative assessment of the impact of cardiac pulsation induced brain motion in clinical DTI	45
2.1 Introduction	46
2.1.1 How cardiac pulsation causes artefacts in DWI acquisitions	46

2.1.2	<i>Review of existing investigations of CPAs</i>	47
2.1.3	<i>Motivation & purpose of this study</i>	48
2.1.4	<i>Structure of this study</i>	49
2.2	Materials & Methods	51
2.2.1	<i>General experimental setup details</i>	51
2.2.2	<i>Datasets</i>	54
2.3	Results	63
2.3.1	<i>Characterization of CPAs in DWI acquisitions</i>	63
2.3.2	<i>Selection of a simulation technique</i>	70
2.3.3	<i>Quantitative evaluation of CPAs in practical DTI acquisitions</i>	71
2.4	Discussion	77
2.5	Literature:	83
Chapter 3. : DTI on the Post-mortem Brain		85
3.1	Introduction	86
3.1.1	<i>Motivation for post-mortem DTI</i>	86
3.1.2	<i>Challenges of post-mortem MRI</i>	89
3.1.3	<i>Previous experience with post-mortem DTI</i>	92
3.1.4	<i>Purpose of this study</i>	94
3.1.5	<i>Structure of this chapter</i>	96
3.2	Materials & Methods	97
3.2.1	<i>Post-mortem brains & pre-acquisition preparation steps:</i>	97
3.2.2	<i>Datasets</i>	100
3.3	Results	108
3.3.1	<i>Study design</i>	108
3.3.2	<i>Practical assessment and alleviation of potential critical limiting factors</i>	113
3.4	Discussion	139
3.4	Literature	143
Chapter 4. : Motivation, Optimization & Artefact Reduction		147
4.1	Introduction	148
4.1.1	<i>Motivation for pursuing DTI at UHF</i>	148
4.1.2	<i>Review of existing investigations of in vivo Diffusion MRI at UHF</i>	153

4.1.3	<i>Purpose of this study</i>	155
4.1.4	<i>Structure of this study</i>	156
4.2	Methods and Materials	157
4.2.1	<i>Datasets</i>	157
4.3	Results	168
4.3.1	<i>Preliminary assessment of UHF DTI on the in-house 7 T MRI system</i>	168
4.3.2	<i>Quantitative assessment of effects of field-strength on acquisition characteristics</i>	173
4.3.3	<i>Acquisition protocol optimization</i>	178
4.3.4	<i>Artefact alleviation</i>	186
4.4	Discussion	193
	<i>Future work</i>	196
	Appendix:.....	205
	Development of a technique for the quantification of SNR in	205
	<i>in vivo</i> single-shot spin echo EPI acquisitions at 7 T	205
4.5	Literature.....	218
	Chapter 5: Conclusion	222

List of Abbreviations

ADC	Apparent Diffusion Coefficient
BW	Bandwidth
CPA	Cardiac pulsation induced artefact
DSI	Diffusion spectrum imaging
DWI	Diffusion weighted image
DTI	Diffusion Tensor Imaging
DT	Diffusion tensor
ECD	Eddy current distortion
ETL	Echo train length
FA	Fractional Anisotropy
FDHM	Full duration at half maximum
FE	Frequency encode
FID	Free induction decay
FOV	Field of view
GE	Gradient Echo
IVIM	Intra-voxel incoherent motion
MD	Mean Diffusivity
MRI	Magnetic resonance imaging
NMR	Nuclear magnetic resonance
NSA	Number of signal averages
PC	Phase encoding
PE	Phase encode
PMI	Post mortem interval

pdf	Probability density function
RF	Radio frequency
ROI	Region of interest
SE	Spin echo
SENSE	Sensitivity encoding
SPAIR	Spectral adiabatic inversion recovery
SPIR	Spectral presaturation by inversion recovery
SS	Slice select
STE	Stimulated echo
TE	Echo time
TR	Repetition time
TRSE	Twice refocused spin echo
TSE	Turbo spin echo
UHF	Ultra high field
VCG	Vector cardiogram

List of Figures

- Figure 1-1 Illustration of the behaviour of spins in absence (A) and presence (B) of a strong external magnetic field B_0 .
- Figure 1-2 Geometric representation of the precession of the magnetic moment $\underline{\mu}$ about a strong external magnetic field B_0 .
- Figure 1-3 Illustration of the absorption and emission of RF-energy in the quantum mechanical model.
- Figure 1-4 The evolution of the bulk magnetization vector M following the application of a Larmor frequency RF-pulse. (A) The laboratory frame; (B) The rotating frame.
- Figure 1-5 Representative T1 and T2 relaxation rates following a 90° RF-excitation pulse plotted over the same time axis.
- Figure 1-6 Illustration of the restoration of the longitudinal magnetization through the loss of energy absorbed by spins (right) through RF-excitation, as thermal energy to the surrounding molecular lattice (left).
- Figure 1-7 Illustration of transverse magnetization decay through dephasing. At time-point t_1 , immediately after the cessation of the excitation RF-pulse, all spins are in phase. At progressive time-points ($t_2 - t_4$) the relative phase of individual spins change progressively resulting in the reduction of the magnitude of the net magnetization factor (red arrow).
- Figure 1-8 Illustration of the effect of the application of a magnetic field gradient $G_x(x)$ (top row) as the imposition of a spatially dependent frequency shift (middle row), and the corresponding phase change (bottom row) of the transverse magnetization.
- Figure 1-9 Illustration of a T1 (left), T2 (centre) and PD (right) weighted acquisition of the human brain (Source: <https://rcbi.rochester.edu>).
- Figure 1-10 Illustration of a simple gradient echo sequence.
- Figure 1-11 Illustration of a simple spin echo sequence.
- Figure 1-12 Selective excitation of an image slice by simultaneous application of a shaped

RF-pulse and field gradient.

- Figure 1-13 Illustration of the principle of frequency encoding.
- Figure 1-14 Illustration of the principle of phase encoding.
- Figure 1-15 Illustration of a spin-echo sequences sensitized to diffusion using a pair of diffusion sensitization gradients G_{diff} .
- Figure 1-16 Time course of the function $\int_0^t G(t')dt'$ which describes the area of an applied gradient and is related to the amount of signal phase gradation ϕ
- Figure 1-17 Illustration of diffusion Tensor Eigenvalue images (top row), the scalar diffusion indices of MD (bottom, left), and FA (bottom middle) as well as an FA colour map (bottom right).
- Figure 1-18 Illustration of typical motion artefacts: ghosting and large signal variations across image.
- Figure 1-19 Pulse diagram of the spin-echo EPI-sequence with insert (top right) illustrating the corresponding k-space trajectory.
- Figure 1-20 Three modes of distortion resulting from Eddy-currents commonly observed in diffusion sensitized acquisitions: contraction (top right), shift (bottom left) and shear (bottom right).
- Figure 2-1 FA colour map taken from the selected slice position (top), and inferior brainstem regions (bottom).
- Figure 2-2 ROI positioning. a: Sagittal view illustrating the typical positioning of an axially orientated slice (represented by the white line). b: Depiction of a typical in-plane ROI.
- Figure 2-3 Time-course measurements (Dataset 2-1a) for the comprehensive characterization of cardiac pulsation induced motion.
- Figure 2-4 Volunteer averaged time-course measurements in the midbrain.
- Figure 2-5 Average ADC_z within the midbrain acquired during the still phase (dark grey), and at the point of maximum cardiac pulsation induced motion (light grey) in Dataset 2-2.

- Figure 2-6 Cumulative histograms of deviations of simulated DT indices from a best estimate represented by the median of the simulated gated distribution for each subject in Dataset 2-2.
- Figure 2-7 Comparison of the measurement and simulation effect indices
- Figure 3-1 Depiction of T1 weighted anatomical scans (using an MPRAGE protocol) of the post-mortem brains used in this investigation.
- Figure 3-2 Depiction of the post-mortem brain in the holder including labelled part descriptions (pictured: Brain #1).
- Figure 3-3 GESE acquisition (Dataset 3-1a) depicting overlaid ROIs for grey matter (red), splenium of the corpus callosum (turquoise), anterior corona radiata (blue), putamen (pink).
- Figure 3-4 Illustration of the effects of scanner instability on b=0 images on a slice superior to the ventricles (Dataset 3-2a).
- Figure 3-5 FA colour maps at multiple slice positions, obtained by the starting acquisition protocol (set 2 of Dataset 3-2a). The region within the white box is enlarged for further analysis in Figure 3-6.
- Figure 3-6 FA and MD maps of the region highlighted by the white rectangle in Figure 3-5. Regions of reduced FA (white outline) correspond to regions of increased MD (red outline) (Dataset 3-2a).
- Figure 3-7 Illustration of coefficient of variation maps for b=0 measurements, and DWI acquisitions with diffusion weighting applied along three orthogonal orientations (set 2 of Dataset 3-2a).
- Figure 3-8 Illustration of coefficient of variation maps for ADC maps calculated from b=0 measurements, and DWI acquisitions with diffusion weighting applied along three orthogonal orientations (set 2 of Dataset 3-2a).
- Figure 3-9 Illustration of coefficient of variation maps for b=0 measurements, and DWI acquisitions with diffusion weighting applied along three orthogonal orientations recorded using an averaging strategy optimized to reduce scan-rescan variability (Dataset 3-2b).
- Figure 3-10 Colour FA images of modified averaging techniques (Dataset 3-2.b).
- Figure 3-11 FA colour maps obtained from acquisition protocols with modified averaging

and Eddy-current corrections using the reversed gradient method (1) (Dataset 3-2c).

Figure 3-12 FA colour maps of resolution 2x2x4 mm obtained with just one iteration (Dataset 3-2.c).

Figure 3-13 FA colour maps of resolution 2x2x2 mm obtained with just one iteration (Dataset 3-2.d).

Figure 4-1 FA colour maps measured at 7 T (Dataset 4-1a) using the protocol proposed in (26).

Figure 4-2 Inter-site comparison of observed SNR efficiency levels of DTI acquisitions at 7 T and 3 T (Datasets 4-1a and b respectively).

Figure 4-3 SNR values measured at 3 T and 7 T resolved over space and echo time (signal decay).

Figure 4-4 Parallel Imaging performance in terms of g-factor (3).

Figure 4-5 Relationship between g-factor and SENSE at 7 T in Dataset 4-3.

Figure 4-6 Comparison between various potential DTI acquisition protocols at 7 T (Datasets 4-4).

Figure 4-7 Effects of varying SENSE, and Halfscan factors on SNR and bandwidth evaluated using Dataset 4-3.

Figure 4-8 Individual acquisitions of Dataset 4-5a illustrating the signal void in lateral regions under default settings.

Figure 4-9 Flip angle optimization performed in Dataset 4-5c of the echo2 refocusing pulse with respect to SNR.

Figure 4-10 Individual acquisitions of Dataset 4-5b, illustrating the homogeneity of the in-plane signal intensity when using echo2 refocusing pulses.

Figure 4-11 Single-shot 2D EPI acquisitions of Dataset 4-6a and colour FA map without fat suppression.

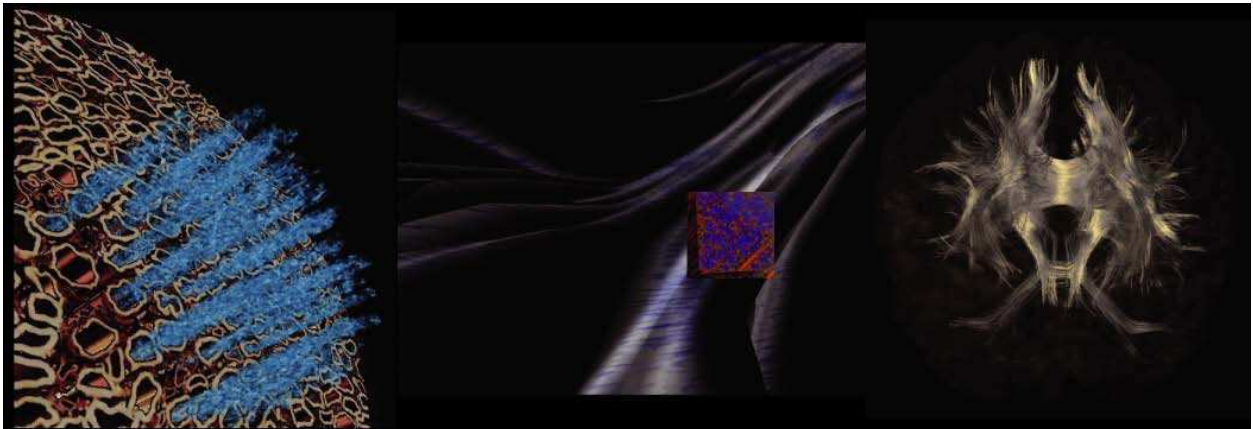
Figure 4-12 Single-shot 2D EPI acquisitions of Dataset 4-6b and colour FA map with SPIR fat suppression.

- Figure 4-13 Single-shot 2D EPI acquisitions of Dataset 4-6c and colour FA map with SPAIR fat suppression
- Figure 4-14 Single-shot 2D EPI colour acquisitions of Dataset 4-6d with and FA map of SSGR fat suppression.
- Figure 4-15 Comparison of DTI acquisitions of different voxel sizes recorded on the in-house 7 T scanner using the standard DTI protocol.
- Figure 4-16 Comparison of colour FA maps acquired under SENSE reduction factors 2 and 4.
- Figure 4-17 First attempts towards *in vivo* DTI acquisitions using zoomed EPI.
- Figure 4-18 Twelve repeated ADC measurements with diffusion sensitization applied along the through-slice orientation in two volunteers (top and bottom bar charts respectively).
- Figure 4-19 FA measurements within the ROIs illustrated in Figure 4-1 added to the results of the investigation of (2).
- Figure 4-20 Difference of two identical acquisitions (S1 and S2) recorded consecutively at 7 T: Unwanted structural noise (highlighted by white arrows) outweighed thermal noise.
- Figure 4-21 Qualitative comparison of estimated noise-only images from MA, difference and NEMA-DNS techniques (Slice 18, flip angle 15 °).
- Figure 4-22 Quantitative noise maps generated using the MA, Difference and NEMA-DNS method.
- Figure 4-23 Comparison of the various noise calculation techniques at different flip angles to the gold standard acquisition (MA technique at flip angle 15 °).
- Figure 4-24 Comparison of noise profiles at high parallel Imaging reduction factor (R = 5).

List of Tables

Table 2-1	Acquisition parameters for scan sequences comprising Dataset 2-1a
Table 3-1	Acquisition parameters listing for Datasets 3-1b - Datasets 3-1e
Table 3-2	Acquisition parameters listing for Datasets 3-2a - Datasets 3-2d
Table 3-3	Comparison of pertinent acquisition parameters of the benchmark and starting DTI acquisition protocol (Dataset 3-2a).
Table 3-4	Values of T2 and T2' of grey and white matter of the human <i>in vivo</i> brain at 1.5 T, 3 T and 7 T (4).
Table 4-1	Summary of reported artefacts and proposed techniques for their alleviation in reported ultra high field-strength DTI investigations
Table 4-2	Acquisition parameters listing for Datasets 4-1
Table 4-3	Acquisition parameters listing for Datasets 4-2
Table 4-4	Acquisition parameters listing for Datasets 4-3
Table 4-5	Set echo times for Dataset 4-3 for various SENSE and Halfscan factor settings
Table 4-6	Acquisition parameters listing for Datasets 4-5
Table 4-7	Acquisition parameters listing for Datasets 4-6

Chapter 1: Introduction



Depiction of water diffusion providing information about the structure and bio-chemical environment of neuronal tissue at a range of different scales (image taken from (5)).

Theoretical foundations

1.1 MRI Theory

Ever since its inception in 1973, Magnetic Resonance Imaging (MRI) has undergone a remarkable series of developments to quickly establish itself as one of today's most useful Imaging modalities. This development has been the result of a string of ground breaking discoveries that have taken place throughout the latter half of the last century (3):

1945-1946: Bloch et. al. and Purcell et. al. discover the phenomenon of 'Nuclear Induction' also known as 'Nuclear Magnetic Resonance' (NMR).

1950: Hahn generated the first spin echo.

1950: Dickinson, Procter and Yu discovered the chemical shift.

1971: Damadian patented his discovery that T1 relaxation times could be used as a marker of the malignancy of cancerous tissue.

1973: The birth of MRI - methods for spatially encoding the origin of the NMR signal were proposed independently by Lauterbur, Mansfield and Grannell.

One of the main reasons for the popularity of MRI in clinical and research communities is its ability to produce high quality tomographic images without relying on the use of potentially harmful ionizing radiation. Another major advantage is that image-contrast is determined via a complex interplay of signal generation and relaxation processes, which are both tissue-specific and environment-dependant. This arises from the fact that in MRI, the tissue being imaged plays an active role in signal generation rather than being limited to passively altering the passage of a measurable signal from a foreign source.

While MRI thus presents an extremely powerful and versatile tool for the probing, quantitative characterization and tomographic visualization of tissue, its relatively complex nature makes an appreciation of its underlying principles a prerequisite for its application and interpretation.

This section aims to lay the theoretical foundations upon which subsequent application chapters will be based.

1.1.1 Tissue magnetization - the origins of the NMR signal

Two models are commonly used to describe physical principles underlying the generation of the NMR-signal. These are the quantum-mechanical model, which governs the behaviour of individual molecules, and the classical model, used to describe the collective behaviour of large ensembles of molecules. While the latter cannot account for some of the more detailed processes of the NMR experiment, it offers an intuitive approach of describing the effects of pulse sequence components (c.f. Section 1.1.3) on tissue sample magnetization.

Nuclei with an uneven number of nucleons possess the property of 'spin'. Spin refers to an angular momentum \underline{J} (here, and in the rest of this thesis, the 'underline' is used to signify a vector quantity) causing nuclei to rotate about their axis. The frequency of this rotation is defined by the atom-specific gyromagnetic ratio γ . Resulting from the angular momentum experienced by these charged particles, a minute magnetic moment, $\underline{\mu}$, in the direction of its rotational axis is produced. The relationship between the \underline{J} and the resulting $\underline{\mu}$ is governed by equation 1.1

$$\underline{\mu} = \gamma \underline{J} \tag{1.1}$$

When placed within a strong external magnetic field \underline{B}_0 , these magnetic moments assume an orientation in alignment with \underline{B}_0 as illustrated in Figure 1-1. However, as illustrated in Figure 1-2, this alignment is imperfect (with θ representing the angle between $\underline{\mu}$ and \underline{B}_0) and spins experience a torque causing them to precess about \underline{B}_0 at a rate of $d\phi$. The change in angular momentum is described by equation 1.2.

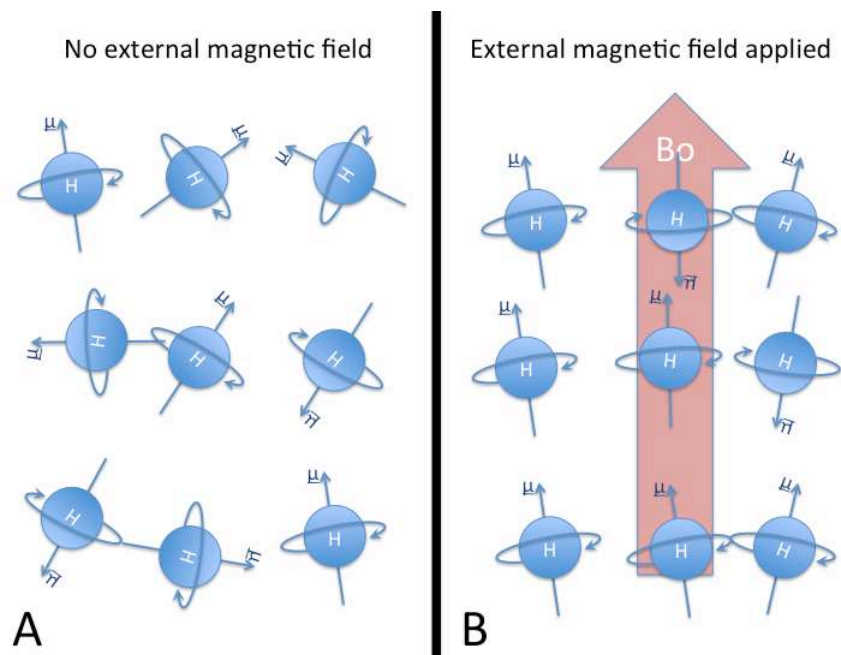


Figure 1-1: Illustration of the behaviour of spins in absence (A) and presence (B) of a strong external magnetic field, B_0 .

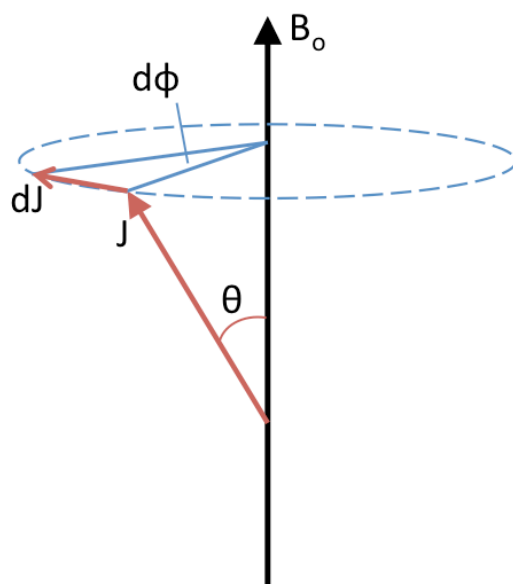


Figure 1-2: Geometric representation of the precession of the magnetic moment, μ , about a strong external magnetic field, B_0 .

$$\left| \frac{d\mathbf{J}}{dt} \right| = |\underline{\mu} \times \underline{B}_0| \quad (1.2)$$

By combining equations 1.1 and 1.2, this can be re-written as:

$$\left| \frac{d\mathbf{J}}{dt} \right| = |\gamma \mathbf{J} \times \underline{B}_0| = \gamma J B_0 \sin \theta \quad (1.3)$$

The precessional frequency, called the Larmor frequency ω_o , is given by rate of change of ϕ (c.f. Figure 1-2). The geometric relationship between the arc-length $d\mathbf{J}$ and \mathbf{J} (c.f. Figure 1-2) is given by

$$d\mathbf{J} = J \sin \theta d\phi \quad (1.4)$$

This allows ω_o to be calculated from \underline{B}_0 and the material specific constant γ .

$$\underline{\omega}_o = \frac{d\phi}{dt} = \frac{d\phi}{d\mathbf{J}} \cdot \frac{d\mathbf{J}}{dt} = \frac{1}{J \sin \theta} \cdot -\gamma J B_0 \sin \theta$$

$$\therefore \underline{\omega}_o = -\gamma \underline{B}_0 \quad (1.5)$$

The minus sign in equation 1.5 denotes a clockwise direction of rotation.

The random distribution of the relative precessional phases of individual spins results in the mutual cancellation of their in-plane components. This results in the formation of a net magnetization vector, \underline{M} , in perfect alignment with \underline{B}_0 .

As illustrated in Figure 1-1, however, in addition to the alignment of spins with \underline{B}_0 , spins may also assume an alignment state against the orientation of \underline{B}_0 . The classical model cannot account for this. In the quantum mechanical model, the orientations of precession of individual spins are described as quantum mechanical states. The alignment of spins with B_0 represents the low energy state, also referred to as the 'parallel' or 'spin-up' state, while the alignment

against B_0 represents the high energy state, also referred to as the ‘anti-parallel’ or ‘spin-down’ state.

In the quantum mechanical model, the proton’s magnetic moment is related to the quantized angular momentum as given by equation 1.6.

$$\underline{\mu} = \gamma \underline{J} = \gamma \hbar I \quad (1.6)$$

Where:

I : Spin angular momentum quantum number

\hbar : Planck’s constant divided by 2π

The number of quantized states that a spin in an external magnetic field may assume is given by $2I + 1$. In the case of protons, $I=1/2$ thus giving rise to two spin states. Protons can swap between the low-to-high and high-to-low energy states by gaining or losing photons corresponding to the energy difference between the states respectively. The energy ε and energy difference $\Delta\varepsilon$ between the spin states are given by equation 1.7 and 1.8 below.

$$\varepsilon = \underline{\mu} \cdot \underline{B} = \gamma \hbar I \cdot B_0 \quad (1.7)$$

$$\Delta\varepsilon = \left(\frac{1}{2} - \left(-\frac{1}{2} \right) \right) \gamma \hbar B_0 = \gamma \hbar B_0 \quad (1.8)$$

Following de Broglie’s wave equation a specific frequency, the Larmor frequency, is associated with the transition between energy states.

$$\Delta\varepsilon = \hbar \omega_0 \quad (1.9)$$

Combining equations 1.8 and 1.9 it follows as in the classical model (equation 1.5),

$$\omega_0 = \gamma B_0 \quad (1.10)$$

In absence of external sources of energy, all spins would occupy the lower energy state resulting in an accordingly large net magnetization vector. Thermal energy at body temperature

of *in vivo* samples, however, typically exceeds the energy difference between low and high-energy states, allowing spins to transition between them and thus effecting a reduction in the magnitude of the net magnetization vector. On a whole however, the low-energy orientations are still preferred, resulting in a net magnetization of the sample.

1.1.2 The NMR signal - generation & relaxation

The magnetization of tissue achieved by placing it inside a static external magnetic field alone, however, does not generate a detectable signal. In the classical model, the net magnetization vector is static and, according to Faraday's law of electromagnetic induction, incapable of inducing a detectable signal in an RF coil. Similarly, in the quantum mechanical model, the populations of spins in the high and low energy states exist in an equilibrium, and thus do not represent a net dissipation of measurable photons.

In order to generate a detectable signal, the equilibrium state of tissue magnetization must be perturbed through the absorption of energy from an external source. Since the Larmor frequency represents a natural frequency of the protons in the external magnetic field, energy of this frequency can be efficiently transferred into and out of the system of spins. Since the Larmor frequency is in the radiofrequency (RF) spectral region, electromagnetic pulses for the excitation of the sample are commonly referred to as RF-excitation pulses.

In the quantum mechanical model (Figure 1-3), the absorption of energy from the RF-excitation pulse corresponds to elevating spins from the low to the high-energy states. After cessation of the RF-excitation pulse, excited spins transition back to the low energy state by giving off photons of Larmor frequency to restore the equilibrium spin-state populations.

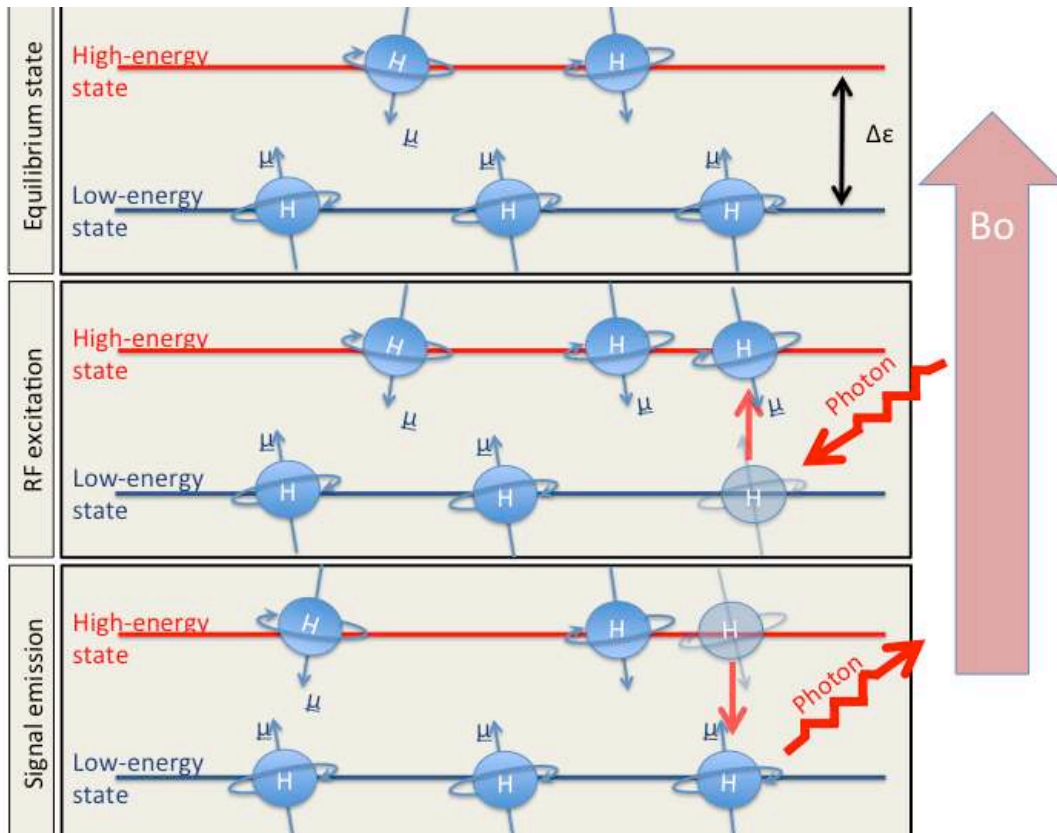


Figure 1-3: Illustration of the quantum mechanical model for the absorption and emission of RF-energy.

In the classical model, the administration of an RF-excitation pulse perpendicular to \underline{B}_0 effectively generates a magnetic field rotating at Larmor frequency about the axis of \underline{B}_0 . This has two important consequences on the net magnetization vector. First, as illustrated in Figure 1-4 A, it causes it to spiral away from the orientation of \underline{B}_0 into the transverse plane; second, it achieves phase coherence so that all spins point in the same direction on the trajectory of precession. The direction of the \underline{B}_0 field will henceforth be denoted as the z-direction, while the x and y-directions define the perpendicular transverse plane. The component of the net magnetization vector in the transverse plane represents an oscillating magnetic field that, according to Faradays law of electromagnetic induction, can induce a voltage in an electrical conductor and thus generate a measurable signal.

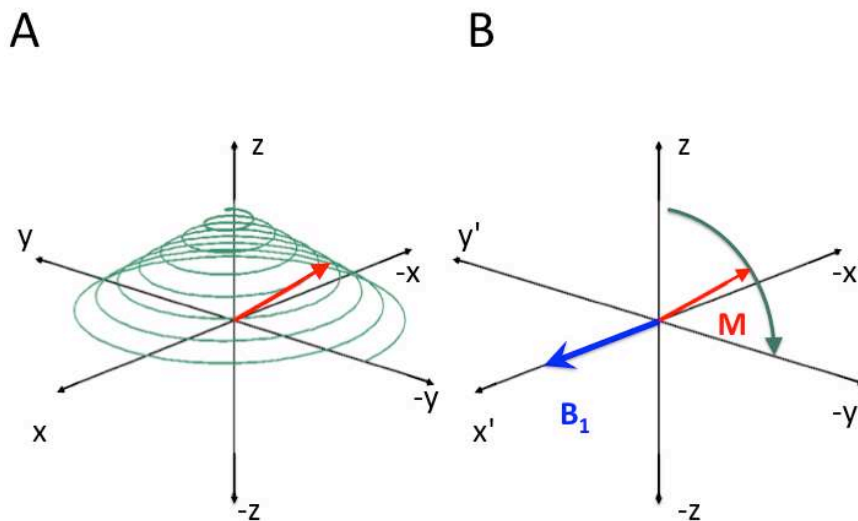


Figure 1-4: The evolution of the net magnetization vector, M , following the application of an RF-pulse of Larmor frequency. This is illustrated in both, the laboratory (A), and the rotating frame of reference (B).

The coordinate system specified by the x , y and z -axis in Figure 1-4A is usually referred to as the laboratory frame of reference as they relate to the physical space of the scanner. A commonly used simplification of the net magnetization vector trajectory is to use a reference frame rotating about z with the Larmor frequency. The transverse coordinates in the rotating frame are denoted as x' and y' respectively. As illustrated in Figure 1-4B, matching the frequency with which the M precesses about z , allows its complex spiralling motion in the laboratory frame of reference to be viewed as a simple rotation from z to y' . Similarly, the magnetic field generated by the RF-excitation pulse may now be seen as a static field B_1 aligned with x' .

The angle of rotation, between the net magnetization vector and the z -direction is a function of both the strength and duration of the applied pulse, commonly referred to as the flip angle, α , which is given by:

$$\alpha = \gamma B_1 t_p \quad (1.11)$$

Where:

t_p : Duration of the RF pulse

Immediately following the cessation of RF-excitation, the system of spins begins to return to its equilibrium state.

Signal relaxation of the longitudinal and transverse components of the net magnetization vector, is governed by two simultaneous but largely independent processes: spin-lattice and spin-spin relaxation respectively. The rates of relaxation of the longitudinal and transverse components are sensitive to tissue specific properties, and are characterized by the time constants T1 and T2 respectively.

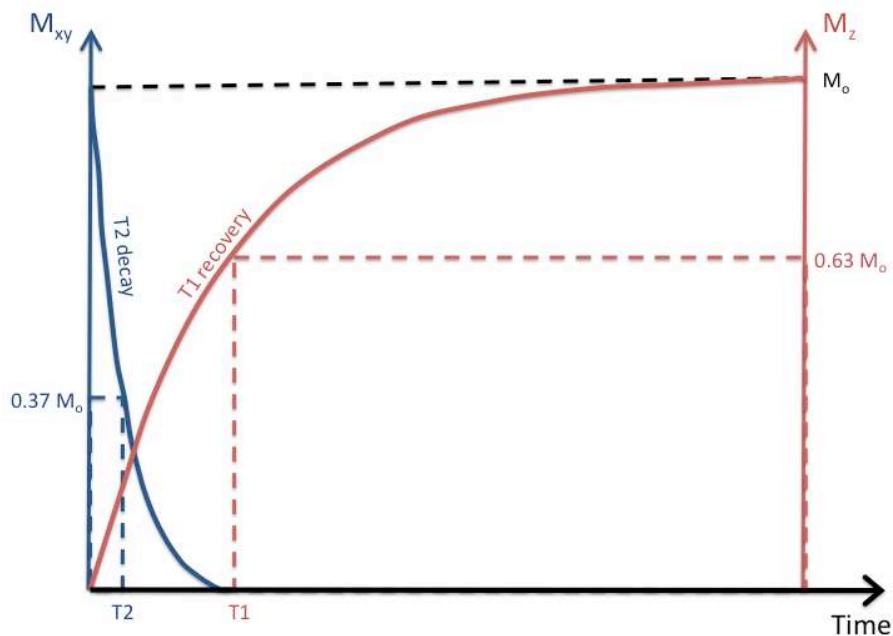


Figure 1-5: Representative illustration of T1 and T2 relaxation rates following a 90° RF-excitation pulse. For this purpose longitudinal (M_z) and transverse (M_{xy}) magnetization are plotted over the same time axis.

'Spin-Lattice', 'Longitudinal' or 'T1' relaxation

This type of relaxation describes the recovery of the longitudinal component of the net magnetization vector. Following the RF-excitation of spins, absorbed energy is dissipated into the surrounding tissue, or 'lattice' as heat (c.f. Figure 1-6). The restoration of the longitudinal magnetization is characterized by the T1-relaxation time, which is defined as the time needed for 63.2 % of the longitudinal magnetization at equilibrium to be restored (c.f. Figure 1-5).

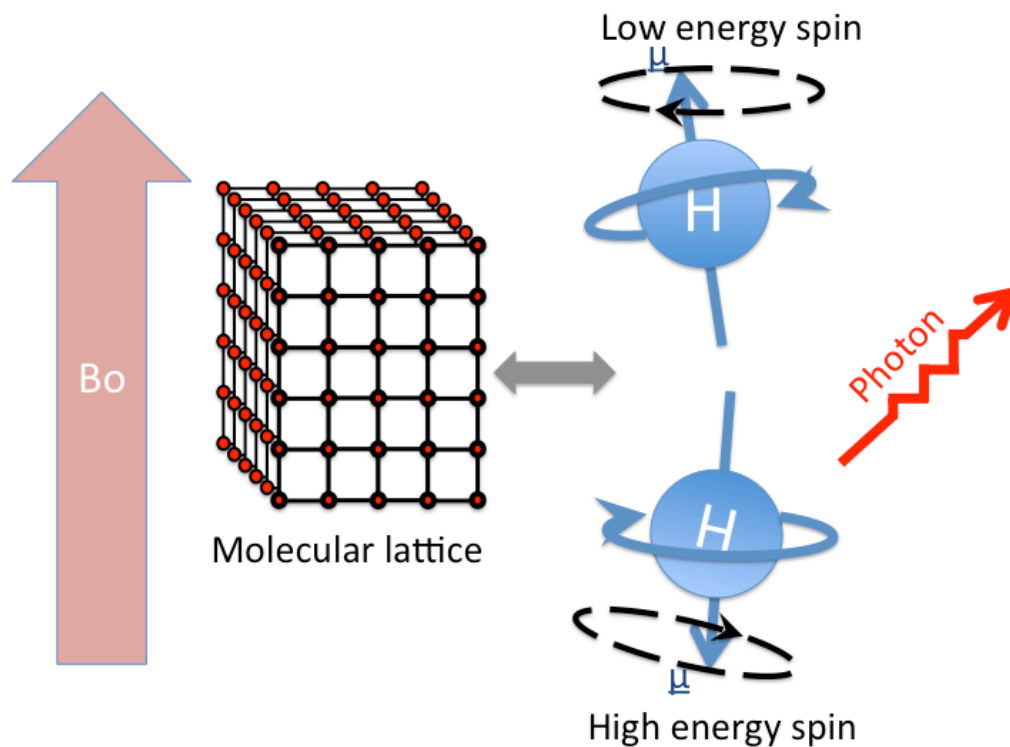


Figure 1-6: Illustration of how energy absorbed by spins from the RF-excitation pulse is dissipated as detectable photons and as thermal energy to the surrounding molecular lattice.

'Spin-spin', 'Transverse' or 'T2' and 'T2*' relaxation

This type of relaxation describes the reduction of the transverse component of the excited net magnetization vector. This process is governed by the loss of the phase coherence of spins comprising the net magnetization vector, as a result of interactions with other spins (c.f. Figure 1-7). If spins come into close proximity, their respective magnetic fields either add or subtract

from the main magnetic field causing an instantaneous change in their precessional frequency. As the spins move apart, they return to their original frequency of precession, but the resulting phase change is retained. This type of relaxation is characterized by the T2 relaxation time, defined as the time after which 63.2 % of the magnitude of the transverse component of the net magnetization vector has been lost, assuming a perfectly homogenous magnetic field.

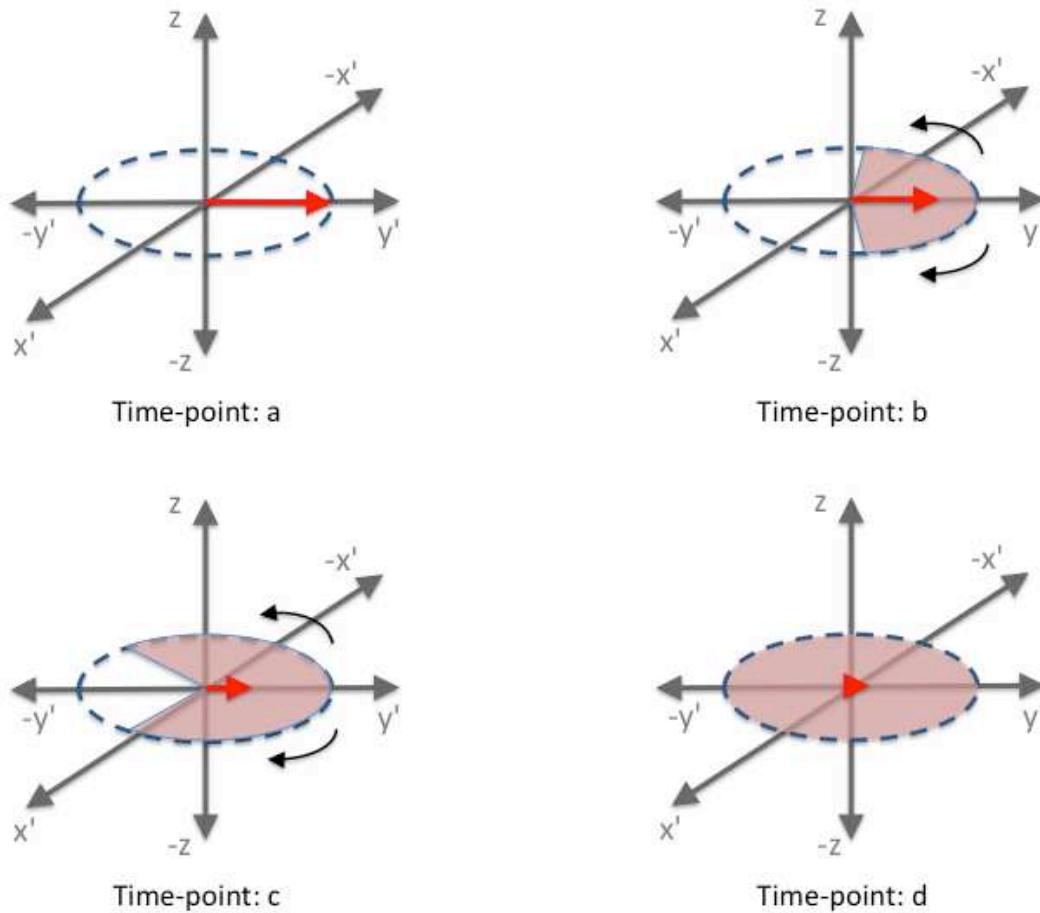


Figure 1-7: Illustration of the decay of transverse magnetization resulting from the loss of the inter-spin phase coherence, which was achieved through RF-excitation. AT time-point 'a', immediately following the application of a 90° RF excitation pulse, the magnitude of the net magnetization vector (red arrow) is highest. At progressive time-points (b - d) the relative phases of individual spins change progressively (represented by the shaded regions). This loss of phase-coherence leads to a reduction, and ultimately elimination, of the measurable net magnetization vector.

In practice, unavoidable inhomogeneities in the magnetic field compound the dephasing effect. These include imperfections in B_0 , differences in the magnetic susceptibility of different tissues,

the presence of metal etc. These lead to an increased rate of the dephasing of the transverse magnetization, which is characterized by the time constant T_2^* .

The rates of signal relaxation are described by a set of empirical differential equations known as the Bloch equations. These are based on a general expression for the total magnetic field \underline{B} , comprising both \underline{B}_0 and \underline{B}_1 (Eq. 1.12), and terms to account for signal relaxation (Eq. 1.13 – 1.15).

$$\frac{d\underline{M}}{dt} = \gamma \underline{M} \times \underline{B} \quad (1.12)$$

$$\frac{dM_x}{dt} = \gamma(M_y B_0 - M_z B_1) - \frac{M_x}{T_2} \quad (1.13)$$

$$\frac{dM_y}{dt} = \gamma(M_z B_1 \cos \omega t - M_x B_0) - \frac{M_y}{T_2} \quad (1.14)$$

$$\frac{dM_z}{dt} = \gamma(M_x B_1 \sin \omega t - M_y B_1 \cos \omega t) + \frac{M_0 - M_z}{T_1} \quad (1.15)$$

These equations can be solved for appropriate boundary conditions. For example, immediately after a 90° RF excitation pulse ($t=0$) where $B_1 = 0$, $M_x(t=0) = M_0$, and $M_z(t=0) = 0$. Ignoring terms describing rotations, these differential equations can then be solved to describe, at time τ , the recovery of longitudinal and transverse magnetization to their equilibrium state.

Longitudinal magnetization

$$\frac{dM_z}{dt} = -\frac{(M_z - M_0)}{T_1} \quad (1.16)$$

$$\int_{M_z(0)}^{M_z(\tau)} \frac{1}{(M_z - M_0)} dM_z = \int_0^\tau -\frac{1}{T_1} dt$$

$$\ln(M_z - M_0) \Big|_{M_z(0)}^{M_z(\tau)} = -\frac{t}{T_1} \Big|_0^\tau$$

$$\ln(M_z(\tau) - M_0) - \ln(M_z(0) - M_0) = -\frac{\tau}{T_1}$$

$$\frac{(M_z(\tau) - M_0)}{(M_z(0) - M_0)} = e^{-\frac{\tau}{T_1}}$$

$$M_z(\tau) = (M_z(0) - M_0)e^{-\frac{\tau}{T_1}} + M_0$$

$$M_z(\tau) = M_0 \left(1 - e^{-\frac{\tau}{T_1}}\right) \quad (1.17)$$

Transverse magnetization

$$\frac{dM_{xy}}{dt} = -\frac{M_{xy}}{T_2} \quad (1.18)$$

$$\int_{M_{xy}(0)}^{M_{xy}(\tau)} \frac{1}{M_{xy}} dM_{xy} = \int_0^\tau -\frac{1}{T_2} dt$$

$$\ln(M_{xy}(\tau)) - \ln(M_{xy}(0)) = -\frac{\tau}{T_2}$$

$$\ln(M_{xy}(\tau)) = -\frac{\tau}{T_2} + \ln(M_{xy}(0))$$

$$M_{xy}(\tau) = M_{xy}(0)e^{-\frac{\tau}{T_2}}$$

$$M_{xy}(\tau) = M_0 e^{-\frac{\tau}{T_2}} \quad (1.19)$$

1.1.3 The anatomy of MRI acquisition sequences

As alluded to in Section 1.1.1, the versatility of MRI as an imaging modality is largely the result of available freedoms for signal generation and manipulation through the design of suitable pulse sequences, and the selection of appropriate acquisition protocol parameters.

Pulse sequences comprise RF-pulses and magnetic field gradients, allowing the controlled manipulation of tissue magnetization to ascertain tissue characteristics and/or sensitize the signal to a number of physical and biochemical processes. As already illustrated in Figure 1-4B, in the rotating reference frame the application of an RF-pulse achieves a rotation of the net magnetization vector in the plane perpendicular to the orientation of the pulse. Magnetic field

gradients represent switchable controlled spatially-linear magnetic field inhomogeneities and thus, as is evident from equations 1.5 and 1.10, lead to a modulation of the Larmor frequency along the direction of the gradient (c.f. Figure 1-8). An important consequence of this is that it allows the incorporation of a spatial component in the NMR signal. This, for example, allows the reconstruction of images in 3D, and also makes possible the sensitization of acquisitions to different types of motion. These concepts will be discussed in greater depth in following sections.

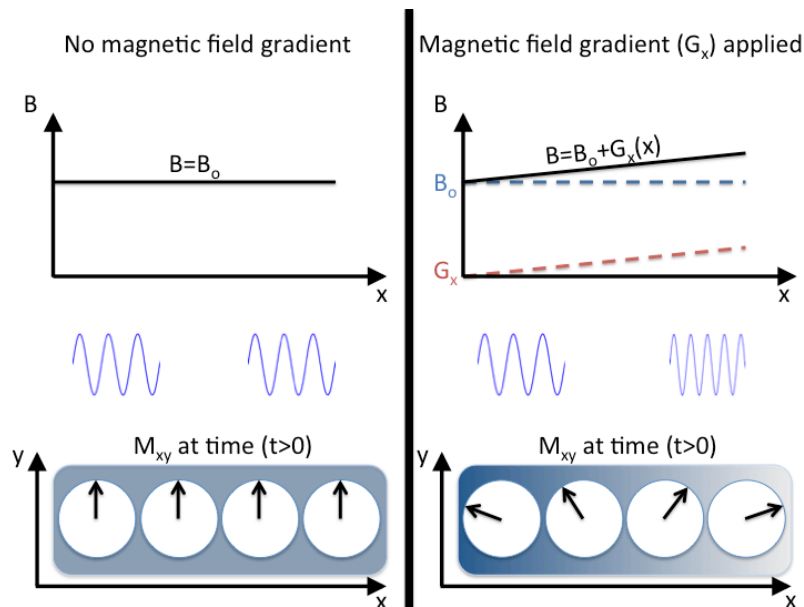


Figure 1-8 Illustration of the effect of the application of a magnetic field gradient $G_x(x)$ (top row) as the imposition of a spatially dependent frequency shift (middle row), and the corresponding phase change at a specific time-point (bottom row).

Acquisition protocol parameters define the settings at which acquisitions are recorded under a selected sequence. An example of this is illustrated in Figure 1-9, where different types of image contrast (proton density, T1 and T2 weighted) are generated using an identical acquisition sequence with different echo and repetition times.

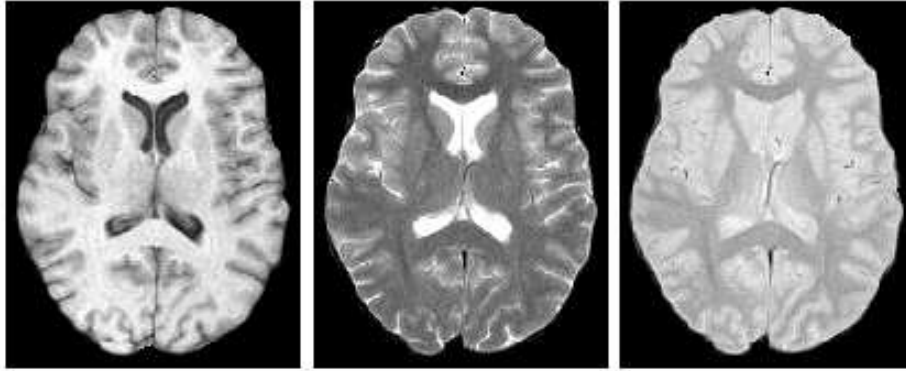


Figure 1-9 Illustration of a T1 (left), T2 (centre) and PD (right) weighted acquisition of the human brain (Source: <https://rcbi.rochester.edu>).

1.1.4 Echo Formation:

As stated in section 1.1.2, immediately following the application of an RF-excitation pulse the energy transferred into the system of spins is dissipated into the lattice as thermal energy, and an oscillating magnetic field representing the detectable signal. The amplitude of this signal, which is known as the Free Induction Decay (FID), is affected by the various relaxation processes and thus decays at a rate determined by T_2^* .

In practice, however, rather than sampling FIDs directly, echoes are generally generated and subsequently recorded. A number of different types of echoes may be generated through the application of RF-pulses and magnetic field gradients (c.f. Section 1.1.3). In this section two pertinent types of echoes, gradient echoes (GE) and spin echoes (SE), are described.

Gradient Echoes:

GEs are formed through the application of a pair of read out magnetic field gradients of opposite polarity. As illustrated in Figure 1-10, immediately following an RF-excitation pulse, a gradient lobe is applied effectively increasing or decreasing the rate of precession or slower relative to their spatial position within the gradient. Next, a gradient of opposite polarity is applied effectively causing spins that under the first gradient were precessing slower to now precess faster and vice versa. As a result, spins that were dephasing in response to the first

gradient lobe now begin to rephase, until a peak in signal intensity, the gradient echo, is reached.

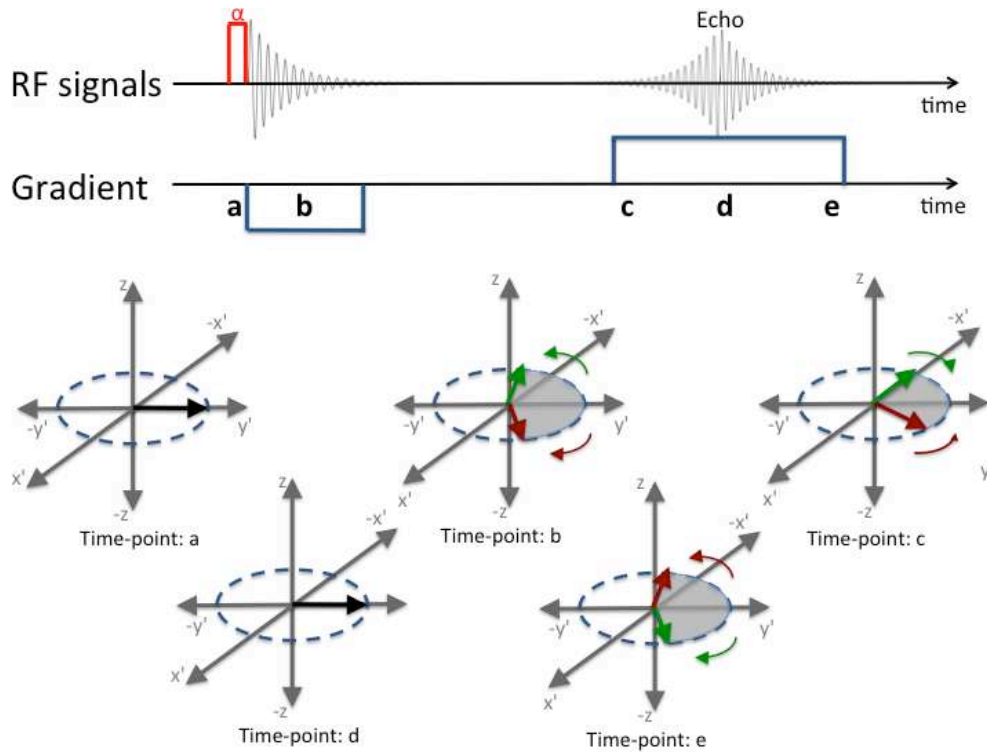


Figure 1-10 Illustration of a simple gradient echo sequence. Immediately following the application of an RF excitation pulse along the x' -axis, the net magnetization vector is flipped into the transverse x' - y' plane along the y' -axis (time-point a). Spins are rapidly de-phased through the application of a negative lobe gradients (time-point b), and subsequently begin to re-phase when a gradient of opposite polarity is applied (time-point c) to form a gradient echo (time-point d). If gradients are left on beyond this point they will actively dephase the net magnetization vector again (time-point e).

In gradient echoes, the second rephasing gradients only compensates for the effects caused by the initial dephasing gradient. It thus cannot refocus dephasing due to other sources of magnetic field inhomogeneities such as imperfections of B_0 , differences in magnetic susceptibilities between tissues, or spin-spin relaxation. As a result, the amplitude of gradient echoes decreases with $T2^*$.

The time between successive RF-excitation pulses is referred to as the repetition time (TR). TR determines the extent to which the longitudinal magnetization may recover before the subsequent excitation is performed. Similarly, the time between the centre of the RF-excitation pulse and the centre of the echo is referred to as the echo time (TE). With the amplitude of the echo decreasing with T2*, the selection of TE affects the T2* weighting of acquisitions. Following from Eq. 1.19, and assuming sufficiently long TRs to allow for full recovery of the longitudinal magnetization vector, the relationship between signal amplitude and the echo time is given in equation 1.20.

$$S_{GE} = S_0 e^{-\frac{TE}{T_2^*}} \quad (1.20)$$

Where:

S₀: Initial height of the FID

S_{GE}: Height of the echo

Spin Echoes:

For the formation of spin echoes, the re-phasing of spins is achieved through the application of an 180° RF pulse, effectively flipping spins in the transverse plane. This principle is illustrated in Figure 1-11 below.

As above, spin dephasing of the transverse component of the excited net magnetization vector may result from spin-spin interactions and local magnetic field inhomogeneities. In the rotating frame of reference (x', y', z coordinate system), dephasing is seen as the rotation of spins comprising the net magnetization vector in either a clockwise or anticlockwise direction. While the effect of spin-spin interactions is random, the effect of static magnetic field inhomogeneities is systematic leading to spins located in regions experiencing net lower/higher field strength than B₀ rotating in anticlockwise/clockwise directions.

In spin echoes, this distinction between random and systematic dephasing effects is important because the 180° pulse flips spins in the transverse plane effectively inverting the phase shift that has occurred (c.f. Figure 1-11). This means that spins that had experienced

anticlockwise/clockwise dephasing now have a negative/positive phase angle respectively. Assuming spins do not move far within the imaging volume, they will continue to experience the same magnetic field inhomogeneities, and thus continue to rotate in the same direction at the same rate. After a time equal to the delay between the 90° and 180° pulses ($TE/2$), the effect of static magnetic field inhomogeneities is reversed bringing spins back into phase and thus generating the echo.

Since this strategy affects the spins, while leaving the magnetic field in which they reside unchanged, the echo amplitude will reduce only as a result of random spin-spin interactions and diffusion, rather than magnetic field inhomogeneities. In theory, these echoes therefore reduce in amplitude with T_2 rather than T_2^* as illustrated in equation 1.21 and 1.22

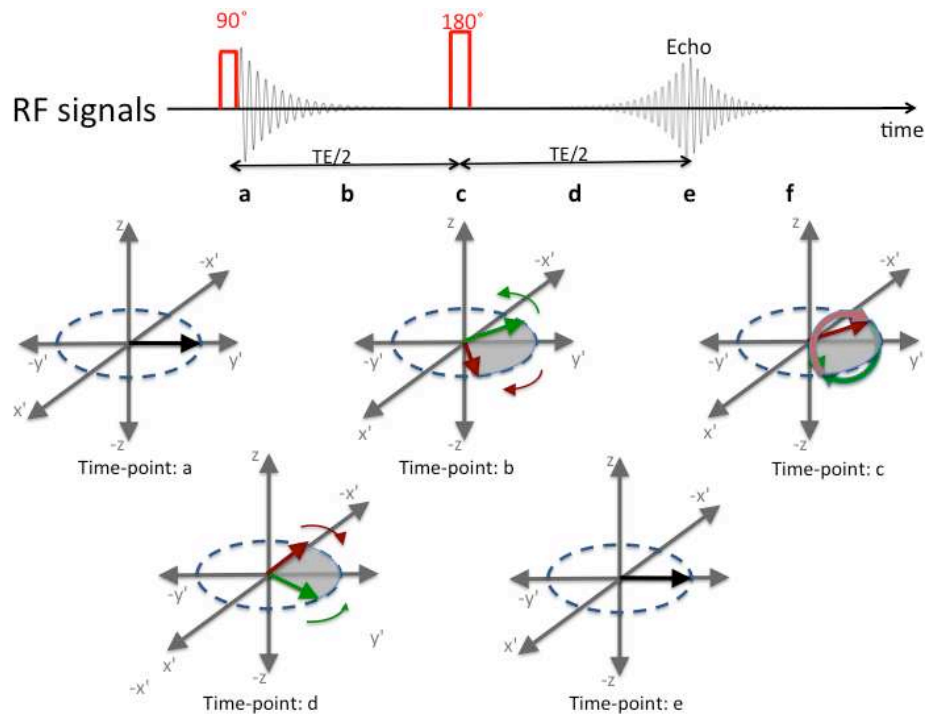


Figure 1-11 Illustration of a simple spin echo sequence. Immediately following the application of an RF-excitation pulse along the x' -axis, the net magnetization vector is flipped towards the transverse x' - y' plane along the y' -axis (time-point a). Spins dephase randomly as a result of spin-spin interactions, and systematically as a result of local magnetic field inhomogeneities (time-point b). To rephase spins they are flipped in the transverse plane by 180° effectively inverting their respective phase offsets (time-point c). Since the effects of local field inhomogeneities remains unaltered, resulting relative phase shifts decrease (time-point d) until a spin echo is produced (time-point e).

$$S_{SE} = S_0 e^{-\frac{TE}{T_2}} e^{-\frac{2}{3} \gamma^2 \Delta B^2 D \left(\frac{TE}{2}\right)^3} \quad (1.21)$$

Where:

ΔB : Magnetic field inhomogeneities

D: Apparent diffusion coefficient

If the TE is short compared to T2, the second exponential term can be neglected and equation 1.21 simplified to:

$$S_{SE} = S_0 e^{-\frac{TE}{T_2}} \quad (1.22)$$

In practical acquisitions where the effects of diffusion cannot be neglected, the displacement of diffusing protons across regions experiencing magnetic field inhomogeneities leads to irreversible dephasing and thus signal loss. One such application is the accurate quantification of T2 measured over a range of TEs. It has been shown that following a 90° excitation pulse applied along the x' axis, a series of equally spaced 180° pulses also applied along the x' axis create a train of alternating positive and negative spin echoes that compensate for diffusion (4). This is known as the Carr-Purcell T2 measurement. A practical challenge is posed by imperfections in the 180° pulses, which have a cumulative effect over the echo train. This can be addressed by applying the train of 180° pulses along the y'-axis leading to a train of positive echoes. If the 180° pulse is imperfect, odd-numbered echoes will be attenuated slightly, but even-numbered echoes will be of the correct amplitude. The acquisition of five even-numbered echoes should suffice for the precise measurement of T2. This modification is known as the Carr-Purcell-Meiboom-Gill (CPMG) sequence.

1.1.5 Spatial encoding

Previous sections have addressed concepts underlying the generation and characteristics of NMR signals, as well as their manipulation through the use of gradients and RF pulses.

Following the cessation of an RF-excitation pulse, all regions within the excited volume simultaneously contribute to the recordable RF-signal. To reconstruct images from this composite signal, the spatial origin of each component must be established. In this section, the prevalent encoding strategies for each of the three spatial dimensions are outlined. Section 1.1.6 will address how this information is subsequently decoded and images reconstructed. To allow spatial localization in 3D, three sets of switchable orthogonally arranged gradients are generally available on modern MRI systems.

Slab selective excitation:

Since the transfer of RF-energy into a system of spins is only efficient at the Larmor frequency, the thickness of slabs of tissue being excited, and thus contributing to the generated signal, can be controlled through the combined application of an appropriate magnetic field gradient, and an RF-excitation pulse of appropriate bandwidth (BW). This is illustrated in Figure 1-12, and the thickness of the excited slab is given by equation 1.23.

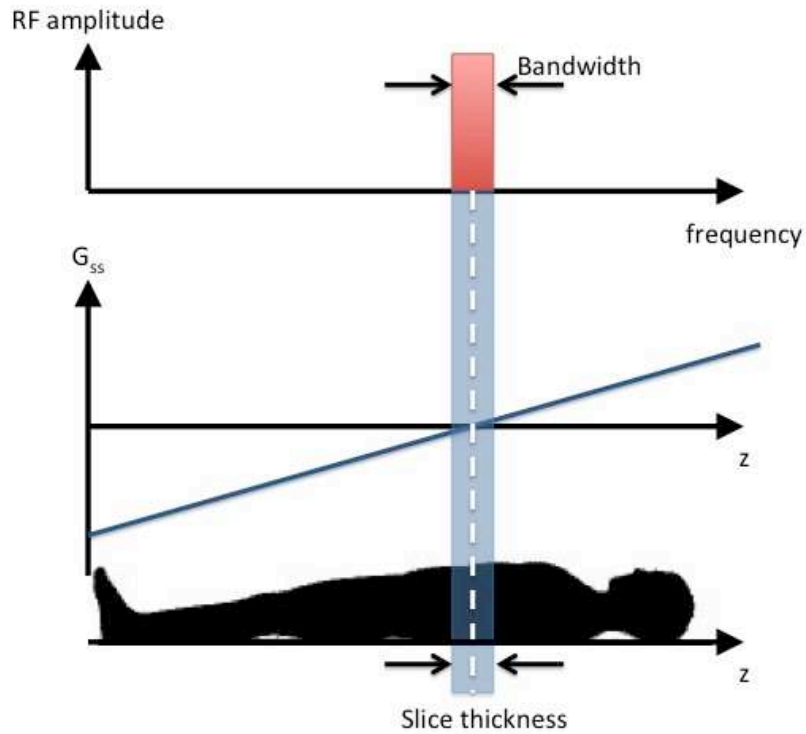


Figure 1-12: Selective excitation of a slab along the slice selective orientation through the simultaneous application of a field gradient (G_{ss}) and RF-pulse of appropriate shape and bandwidth.

$$\text{slab thickness} = \frac{2\pi BW}{\gamma G_{ss}} \quad (1.23)$$

Where:

G_{ss} : the slab selective gradient

Volumes of interest can generally be recorded as a stack of 2D slices or a single 3D dataset. In 2D MRI acquisitions, the selectively excited slab is sufficiently thin to not require any further spatial encoding, and is generally referred to as a 'slice'. In 3D MRI, a slab corresponding in thickness to multiple slices is excited and thus simultaneously contributes to the measurable

signal. To reconstruct the individual slices comprising this slab, phase encoding (see below) must also be performed along the slice select direction.

Frequency Encoding (x-direction):

Following the slab selective excitation of a system of spins, a magnetic field oscillating at the Larmor frequency is generated. The application of a read out gradient modulates the Larmor frequencies along the gradient orientation thereby encoding the spatial origin of spins along the frequency encode direction into the resulting signal. The Fourier transformation (c.f. Section 1.1.6) of this RF-signal sampled in time is an image-domain projection along the x-axis (c.f. Figure 1-13).

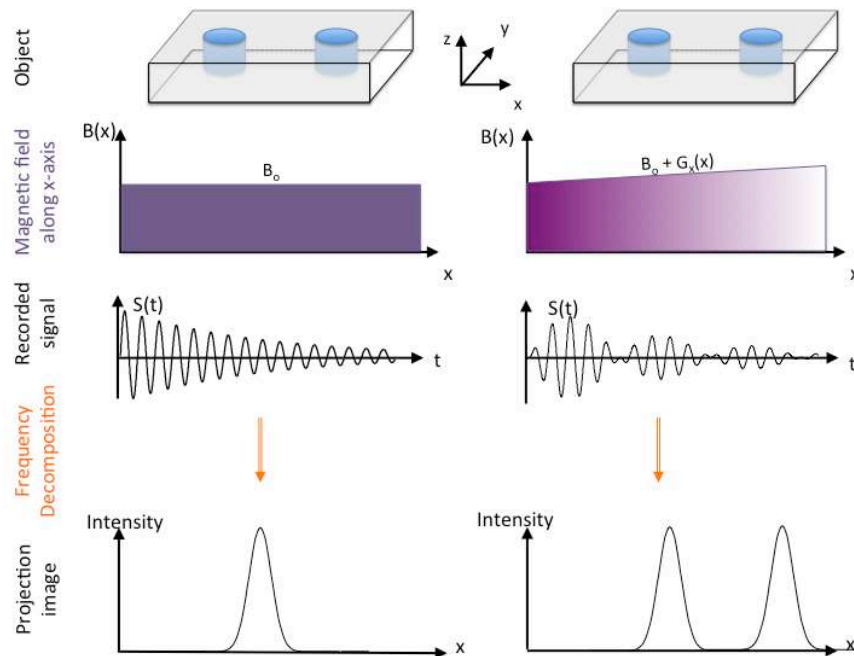


Figure 1-13: Illustration of the principle of frequency encoding. The object being imaged comprises two water filled containers displaced along the direction of the frequency encode axis. In absence of a gradient (LHS) a single FID is generated lacking information about the spatial location of the containers. In presence of a frequency encoding gradient (RHS) the Larmor frequency of each container is modulated thus encoding its spatial location.

Phase Encoding (*y*-direction):

The frequency encoding approach cannot be extended to a further spatial dimension since two spatial encoding gradients applied simultaneously would linearly add up into a single effective gradient. Instead, the strategy of phase encoding is adopted. Following slice selective excitation all spins are in phase. The application of a gradient of particular amplitude for a specific duration of time imposes a position-dependent phase offset along the orientation of the gradient (c.f. Figure 1-14). The application of this phase offset is subsequently followed by signal acquisition in presence of frequency encoding gradients, as described above. This process is repeated with different phase offsets keeping the rate of change of phase within a voxel constant between successive iterations.

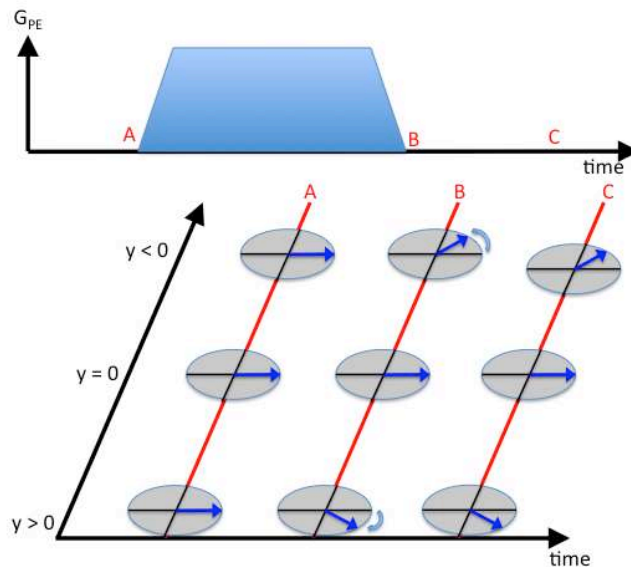


Figure 1-14: Illustration of the principle of phase encoding; A phase encoding gradient of one of a number of amplitudes but set duration temporarily modulates the Larmor frequency of spins along the phase encode direction. After its cessation, the Larmor frequency is restored, but with a net phase shift imposed.

To summarize, in MRI the signal phase changes over time and with the strength of an applied gradient. Since frequency is defined as the rate of change of phase, the main difference

between frequency and phase encoding lies in the way in which the encoding is applied. In frequency encoding the evolution of the signal over time is sampled at a constant gradient strength, while in phase encoding the gradient strength is altered and applied for a given duration of time. Both frequency and phase encoding produce a spatially dependent rate of change of phase, allowing their spatial information to be recovered using the Fourier transform. This will be discussed in the following section.

1.1.6 Image reconstruction

With spatial encoding performed as described above, the recorded signal will comprise an additive combination of signals from all voxel elements (voxels) of the excited slab. The spatial location of each signal-contributing voxel is encoded by its frequency, and the corresponding image-pixel brightness through its amplitude. The Fourier transform is commonly used to generate images from this data by splitting up components of the composite signal according to their frequencies.

The Fourier theorem, states that any complex waveform can be created from a sum of sine and cosine waves of appropriate frequencies and amplitudes. The Fourier series is defined in equation 1.24,

$$s(x) = \frac{a_0}{2} + \sum_{n=1}^{\infty} (a_n \cos nx + b_n \sin nx) = \sum_{n=-\infty}^{\infty} a_n e^{inx} \quad (1.24)$$

Where:

$s(x)$: The measured signal

x : Independent variable (coordinate) of the 1D function to undergo Fourier transformation

n : Frequency component (harmonic)

a, b : Amplitudes of cosine and sine components of each harmonic

The Fourier transform is a generalization of the Fourier series allowing the conversion between images and spectra. In MRI, the measured spectral data is represented by $s(x)$, and reconstructed images by $S(k)$ in equations 1.25a and b below. $S(k)$ and $s(x)$ are called a Fourier transform pair.

$$S(k) = \int_{-\infty}^{\infty} s(x)e^{-i2\pi kx} dx \quad (1.25a)$$

$$s(x) = \int_{-\infty}^{\infty} S(k)e^{i2\pi kx} . dk \quad (1.25b)$$

Following a slice-selective excitation and the application of frequency- and phase encode gradients for in-plane spatial encoding, a discrete signal element $\partial s(t)$ can be described as:

$$\partial s(t) = \rho(x, y) \cdot e^{\left(\frac{-t}{T_2^*}\right)} \cdot e^{(i\gamma x G_{FE} t)} \cdot e^{(i\gamma y G_{PE} \tau)} dx dy \quad (1.26)$$

Where:

$\rho(x, y)$: Proton density at location

x, y : Location of $\partial s(t)$ along the frequency and phase encode directions respectively

G_{FE} : Frequency encoding gradient

G_{PE} : Phase encoding gradient

τ : Duration of G_{PE}

The term $\rho(x, y) \cdot e^{\left(\frac{-t}{T_2^*}\right)}$ describes the signal amplitude at time t , which is determined by the spin density and T_2^* relaxation. The terms $e^{(i\gamma x G_{FE} t)}$ and $e^{(i\gamma y G_{PE} \tau)}$ describe the phase change imposed by the frequency and phase encoding gradients respectively.

The total MRI signal is the integral of equation 1.26 over the in-plane dimensions x and y . This signal is subsequently sampled M times at intervals of Δt for each of N phase encode lines. At each phase encode line n , the phase encode gradient amplitude is incremented by ΔG .

The sampled signal $S(m,n)$, where m and n represent a coordinate pair along the frequency and phase encode direction respectively, can be described as:

$$S(m,n) = \int \int \rho(x,y) \cdot e^{\left(\frac{-t}{T_2^*}\right)} \cdot e^{(i \gamma x G_{FE} \Delta t m)} \cdot e^{(i \gamma y G_{PE} n \tau)} dx dy \quad (1.28)$$

Defining $k_{FE} = \frac{\gamma}{2\pi} G_{FE} \Delta t m$ and $k_{PE} = \frac{\gamma}{2\pi} \Delta G n \tau$, and neglecting the effects of T_2^* dephasing, allows equation 1.28 to be rewritten in the form of a 2D Fourier transform.

$$S(m,n) = \int \int \rho(x,y) \cdot e^{(i 2\pi x k_{FE})} \cdot e^{(i 2\pi y k_{PE})} dx dy \quad (1.29)$$

As a result, images can be calculated from measurements performed in k-space by performing a 2D Fourier transform.

1.2 Diffusion MRI theory

Diffusion, or Brownian motion, is defined as a thermally driven mass transport process which results in molecular or particle mixing in absence of bulk motion (2). It was first reported by Robert Brown in 1828 (5), and later characterized by Fick (6) and Einstein (7). In tissue, the random motion of thermally excited water molecules leads to the physical interaction of diffusing spins and surrounding tissue. Various tissue components, such as cell membranes, fibres and macromolecules impede diffusion paths, thus imprinting information about the tissue microstructure on the statistical distribution of Brownian displacements. Quantitative characterizations of the resulting diffusion profiles thus provide information about the microstructural composition and structural organization of tissue on a macroscopic scale.

This section will outline common techniques used to sensitize MRI acquisitions to diffusion, calculate diffusion properties from measured data, and interpret results.

1.2.1 Diffusion sensitization in MRI

As already alluded to in Section 1.1.3, magnetic field gradients can be used to impose a position-dependent phase-shift on spins. The sensitization of acquisitions to motion can be achieved through the application of a set of gradients of equal magnitude but opposing effect. This has no effect on static spins since phase shifts imposed by the first gradient are reversed by the second. If mobile spins, on the other hand, are at different physical locations during the application of the first and second gradient, a net phase shift is imposed.

On a voxel level, the effects of different categories of motion will differ as well. This can be exploited to allow the selective assessment of a specific category of motion. In general, motion can be grouped into three main categories (8). Bulk motion is defined as the coherent displacement of all water molecules by more than a voxel-dimension. This sort of motion is often observed when the subject being scanned moves during the acquisition, and results in mis-registration of datasets and image artefacts such as ghosting. The second category of motion is flow, which is defined as a one-directional movement of water molecules resulting in displacements of less than the voxel-dimension. Flow results in a shift in the phase of the signal, and does not appear in reconstructed magnitude images. In practical applications, however, flow often is not uni-directional due to the convoluted capillary structure, and thus can lead to net attenuations in magnitude images. Flow effects are often neglected in the brain due to the relatively small population of blood vessels (approx. 50 % compared to parenchyma) (8)). The third category of motion is intra-voxel incoherent motion (IVIM), which includes Brownian motion. In the presence of displacement encoding gradients, the ensuing loss in phase coherence of spins within a voxel results in a loss in signal amplitude of magnitude images as illustrated in Figure 1-15.

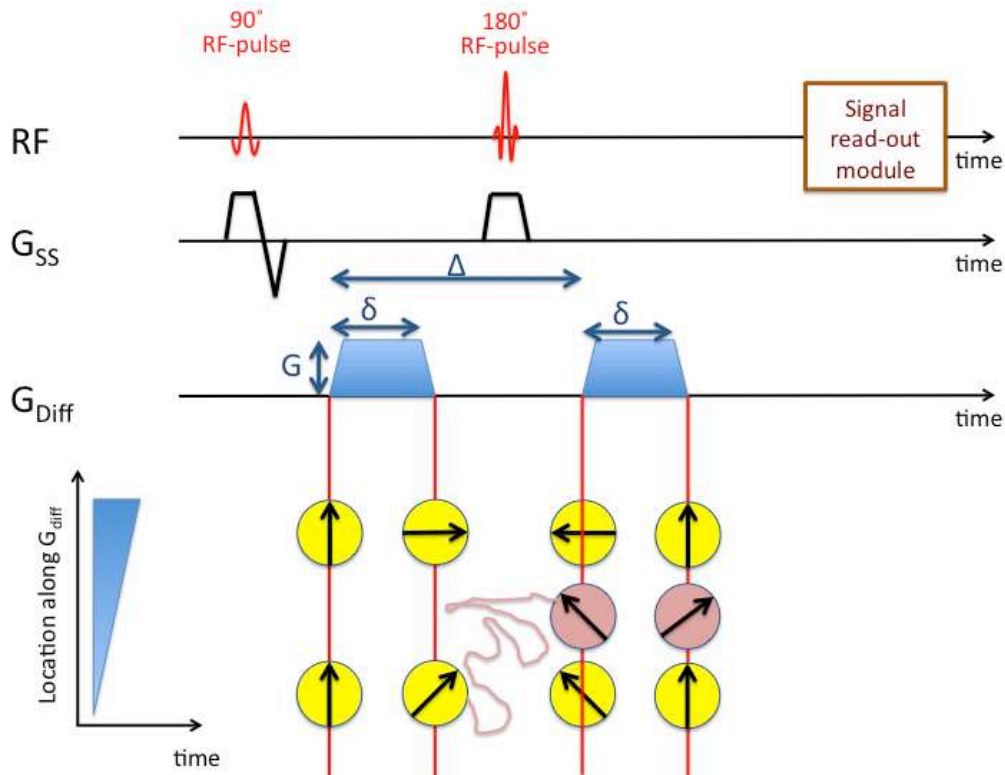


Figure 1-15: Illustration of a spin-echo sequence sensitized to diffusion using a pair of diffusion sensitization gradients G_{diff} . Static spins (yellow) are shown to be rephased by the 180° pulse and second gradient pulse. Diffusing spins (pink) are not rephased leading to intra voxel spin dephasing and thus signal attenuation. The level of diffusion sensitization is characterized by the gradient amplitude (G), the gradient duration (δ) and the gradient separation or ‘diffusion time’ (Δ).

Given a gradient pulse of strength G and duration δ , the phase difference with respect to an arbitrarily defined reference point ($x=0$) is given by equation 1.30 below.

$$\phi(x, t) = e^{i\gamma G(t)x} \quad (1.30)$$

Where:

- ϕ : Phase shift
- t : Duration of the applied gradient
- $G(t)$: Applied gradient waveform
- x : Spatial position

Due to the finite slew rate and length of the applied diffusion encoding gradients G , the imposed phase shift is not only a function of space, but also of the time over which gradients are applied.

1.2.2 Characterization of Brownian motion

Diffusion MRI aims to characterize Brownian motion of underlying spins. Due to its random nature, Brownian motion is typically characterized through its probability distribution function (pdf), describing the population of molecules at a defined location. In absence of physical barriers, Brownian displacements follow a symmetric Gaussian distribution, as defined in equation 1.31.

$$P_{\text{gauss}}(x) = \frac{1}{\sigma\sqrt{2\pi}} e^{-x^2/2\sigma^2} \quad (1.31)$$

Where:

- P_{gauss} : Gaussian probability density function
- x : location at which the population P_{gauss} is being assessed
- σ : The distribution spread

Albert Einstein described the Brownian motion of an ensemble of particles through the average diffusion distance over time using a probabilistic framework (7) through equation 1.32.

$$\sigma = \sqrt{2Dt} \quad (1.32)$$

Where:

- σ : Mean diffusion distance
- D : Diffusion constant
- t : Diffusion time

Substituting the measure of spread in equation 1.32 into equation 1.31, we can describe the displacement distribution of a population of diffusing spins depending on the diffusion constant and diffusion time (equation 1.33).

$$P(x, t) = \frac{1}{\sqrt{4\pi Dt}} e^{-x^2/4Dt} \quad (1.33)$$

1.2.3 Relating diffusion and measured voxel intensity attenuation

Having defined a relationship between the imposed phase shift and spin displacement in presence of a linear gradient in equation 1.30, and the mean displacement and the diffusion constant in equation 1.33, this can be related to the measurable signal attenuation.

It is intuitive that the magnitude of the measurable signal intensity can be calculated by integrating the product of spin population and the corresponding components of magnetization along direction x . As illustrated in equation 1.34, the relative signal change, \bar{S} , of a voxel corresponds to the ratio of the signal intensity measured after application of a diffusion sensitization gradient, S , to that without diffusion sensitization, S_0 .

$$\bar{S} = \frac{S}{S_0} = \int_x P(x, t) \phi(x, t) dx = \frac{1}{\sqrt{4\pi Dt}} \int_x e^{-\left(\frac{x^2}{4Dt}\right)} e^{i\gamma G(t)tx} dx \quad (1.34)$$

Where:

\bar{S} : Relative signal intensity change

It is noted that in the absence of a diffusion sensitization gradient (i.e. $G(t) = 0$), equation 1.34 describes a Gaussian distribution of unit area. Also, since in the presence of an applied diffusion sensitization gradient \bar{S} will be less than one, we can establish that diffusion will result in an attenuation of the signal. Since these depend also on the proton density, signal relaxation properties (T_1 , T_2) and acquisition protocol parameters (e.g. TE , TR) both need to be determined through individual measurements.

To calculate the signal intensity, we integrate equation 1.34 over both location, x , and time, t . The various time-intervals comprising a simplified diffusion sensitized acquisition sequence are illustrated in Figure 1-16.

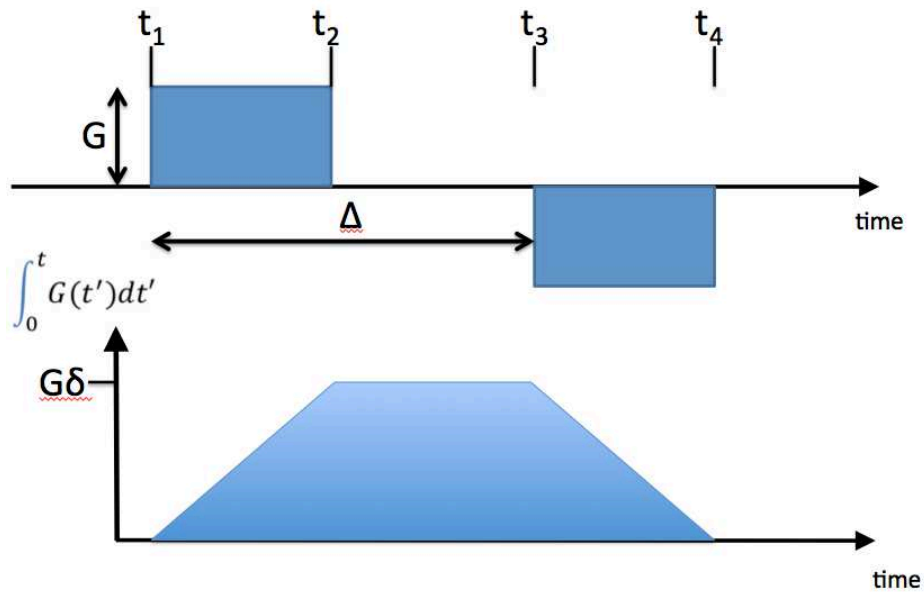


Figure 1-16: Time course of the function $\int_0^t G(t')dt'$ which describes the area of an applied gradient and is related to the amount of signal phase gradation ϕ .

A simplification of the relationship for \bar{S} can be achieved by splitting the phase term into trigonometric real and imaginary components.

$$\bar{S} = \frac{1}{\sqrt{4\pi Dt}} \left[\int_x e^{-\left(\frac{x^2}{4Dt}\right)} \cos(\gamma G(t)tx) - i \int_x e^{-\left(\frac{x^2}{4Dt}\right)} - \sin(\gamma G(t)tx) \right] \quad (1.35)$$

The imaginary term is an asymmetric function integrated over $-\infty$ to ∞ and thus reduces to zero. By integrating the real term of 1.35 over space (x), we obtain

$$\ln(\bar{S}) = \ln\left(\frac{S}{S_0}\right) = -D\gamma^2 \int_{t_1}^{t_4} \left(\int_0^t G(t') dt' \right)^2 dt \quad (1.36)$$

Where:

$\int_0^t G(t') dt'$: Describes the area of the applied gradient and is related to the amount of signal phase gradation (c.f. Figure 1-15).

To integrate 1.36 over the time t , it is divided into three time segments $t_1:t_2$, $t_2:t_3$, and $t_3:t_4$ (c.f. Figure 1.14) and written as equation 1.37.

$$\ln\left(\frac{S}{S_0}\right) = -D\gamma^2 \left(\int_{t_1}^{t_2} G^2 t^2 dt + \int_{t_2}^{t_3} G^2 \delta^2 dt + \int_{t_3}^{t_4} (G\delta - G(t - t_3))^2 dt \right) \quad (1.37)$$

To simplify this equation, we define time $t_1 = 0$, and the time intervals $t_1 : t_2 = \delta$, $t_1 : t_3 = \Delta$. Following these conventions $t_2 = \delta$ and $t_4 = \Delta + \delta$. This allows us to re-write the integrals of equation 1.37 as:

$$\int_{t_1}^{t_2} G^2 t^2 dt = \int_0^{\delta} G^2 t^2 dt = \frac{1}{3} G^2 \delta^3 \quad (1.38a)$$

$$\int_{t_2}^{t_3} G^2 \delta^2 dt = \int_{\delta}^{\Delta} G^2 \delta^2 dt = G^2 \delta^2 \Delta - G^2 \delta^3 \quad (1.38b)$$

$$\int_{t_3}^{t_4} (G\delta - G(t - t_3))^2 dt = \int_{\Delta}^{\Delta + \delta} (G\delta - G(t - \Delta))^2 dt = \frac{1}{3} G^2 \delta^3 \quad (1.38c)$$

Combining the terms 1.38a-c, Equation 1.37 can be re-written as:

$$\ln\left(\frac{S}{S_0}\right) = -\gamma^2 G^2 \delta^2 \left(\Delta - \frac{\delta}{3} \right) D \quad (1.39)$$

The parameters G , δ and Δ define the scale of diffusion sensitization being applied, and thus represent known user-selected acquisition protocol parameters. For simplicity, these are commonly summarized as a single value termed the b-value.

$$b = \gamma^2 G^2 \delta^2 \left(\Delta - \frac{\delta}{3} \right) \quad (1.40)$$

Equation 1.39 can thus be simplified to

$$\ln \left(\frac{S}{S_0} \right) = -bD \quad (1.41)$$

or

$$S = S_0 e^{-bD} \quad (1.42)$$

1.2.4 Practical implications of diffusion time

Typical diffusion times for contemporary *in vivo* DTI measurements range between 10 and 100 ms (8). The diffusion constant of water inside the brain is typically $0.8 - 0.9 \times 10^{-3} \text{ mm}^2 \text{ s}^{-1}$ (8). Accordingly, using Einstein's equation for diffusion (equation 1.32) typical molecular displacements during this time are in the order of 4 – 15 μm .

The magnitude of this displacement is thus comparable to the size of cells (9). This illustrates that measurements are sensitive to characteristics of the tissue environment on a cellular scale. This unique and powerful ability allows Diffusion MRI measurements to provide information about the micro-structural environment of cells. Combined with its quantitative nature, which allows for the detection of minute deviations from normality, this potentially makes diffusion measurements a powerful biomarker of disease.

Any environmental property that is to be assessed through its effect on diffusion must have a smaller dimension than the diffusion distance. This highlights the role of diffusion times for sampling structures of different physical sizes. In *in vivo* measurements of human neuronal tissue, these diffusion distances are in the order of magnitude of protein filaments, cell membranes, cell organelles and myelin sheaths (8).

Strictly speaking, the presence of obstacles impeding Brownian motion violates the assumption that displacements follow a Gaussian distribution (equation 1.31). As a result, calculated

diffusion constants (D in equations 1.41, 1.42s) are commonly referred to as ‘Apparent’ Diffusion Constants (ADC).

The minute scale of these displacements, however, also indicates the high sensitivity to motion needed for their reliable and accurate quantification. This, however, also makes measurements susceptible to other sources of motion, thus necessitating the use of acquisition strategies to effectively reduce sensitivity to non-Brownian motion. This will be addressed in greater detail in Section 1.3.

1.2.5 The effect of fibrous tissue on 3D diffusion profiles

As is evident from Section 1.2.1, only the component of IVIM occurring along the orientation of the applied gradients results in spin dephasing and hence signal attenuation. While knowledge of diffusion along one direction is sufficient for the characterization of isotropic free diffusion, in living systems physical boundaries often lead to inhibited and preferred axes of diffusion, resulting in anisotropic diffusion profiles. In tissue regions comprising coherent fibrous structures (e.g. axonal tracts, protein filaments in muscle), the orientation of preferred diffusion forms contiguous paths allowing the depiction of their structural connectivity.

While an intuitive approach for the characterization of 3D diffusion profiles is to directly measure signal attenuation along a large number of non-collinear measurements, this approach is time-consuming and may reduce the practical applicability of such measurements in many routine applications. A popular alternative technique is to define a geometric model of the diffusion profile shape allowing the number of required measurements to be limited to the parameters underlying that model. This is the strategy pursued in Diffusion Tensor Imaging (DTI) where 3D diffusion profiles are assumed to take the shape of a symmetric ellipsoid.

1.2.6 Diffusion Tensor Imaging (DTI)

DTI has established itself as the prevalent technique for the characterization of diffusion in living tissue by offering a favourable compromise between the achievable accuracy of diffusion models and the number of acquisitions required. To uniquely characterize a symmetric ellipsoid of unknown orientation, a minimum of six measurements performed along non-collinear orientations are required. Since, as discussed in Section 1.2.3, at least two data points are needed for the quantification of diffusion along the direction of the applied gradient, at least one acquisition with minimal or without diffusion sensitization (S_0) must also be recorded.

In DTI, the six parameters describing the 3D diffusion profile are generally represented either in the form of a symmetric 3 x 3 Tensor $\bar{\bar{D}}$, or its Eigenvalues ($\lambda_1, \lambda_2, \lambda_3$) and Eigenvectors ($\underline{v}_1, \underline{v}_2, \underline{v}_3$) following diagonalization.

$$\bar{\bar{D}} = \begin{bmatrix} D_{xx} & D_{xy} & D_{xz} \\ D_{yx} & D_{yy} & D_{yz} \\ D_{zx} & D_{zy} & D_{zz} \end{bmatrix} \xrightarrow{\text{Diagonalization}} \lambda_1, \lambda_2, \lambda_3; \underline{v}_1, \underline{v}_2, \underline{v}_3$$

Both the Tensor and the Eigenvector/value representations describe the diffusion within a voxel ellipsoid in 3D space in which they are measured. In the Tensor representation, the diagonal elements provide information about the size of the ellipsoid, while the off-diagonal elements carry information about its rotation (i.e. D_{xy}/D_{yx} specify rotation about the z-axis, D_{xz}/D_{yz} about the y-axis, and D_{yz}/D_{zy} about the x-axis). The Eigenvector/value representation, on the other hand, conveniently splits measurements into the three (rotationally invariant) radii $\lambda_1, \lambda_2, \lambda_3$ and their respective orientations $\underline{v}_1, \underline{v}_2, \underline{v}_3$ corresponding to the principal axes of the ellipsoid.

While the Eigenvector/value representation may be more intuitive to interpret, it is easier to relate measurements to Tensor elements. To incorporate information about not only the degree of diffusion sensitization used, but also the direction of gradients applied, the b-value and gradient strength of equation 1.40 must be replaced by vectors \underline{b} and \underline{G} respectively. Equation 1.43 depicts the equation relating multiple diffusion measurements to the diffusion Tensor

$$\frac{S}{S_0} = e^{-\sqrt{\bar{b}}\bar{D}\sqrt{\bar{b}}^T} \quad (1.43)$$

Where:

$$\sqrt{\bar{b}} = \gamma G \delta \sqrt{(\Delta - \delta/3)}$$

In practical applications, however, it is more common to calculate the Tensor using a least-squares fit rather than to calculate it directly. This has two main advantages (8): First the signal intensity with zero diffusion weighting (S_0) often cannot be obtained directly because imaging techniques always incur a finite amount of diffusion weighting. Secondly, it is common to acquire DTI datasets comprising more than the minimum seven measurements as it has been shown that to alleviate the effects of unavoidable measurement errors diffusion measurements along at least 20 non-collinear orientations should be performed (10,11).

To facilitate fitting, equation 1.43 is expanded as follows:

$$\sqrt{\bar{b}} = [\sqrt{\bar{b}_x}, \sqrt{\bar{b}_y}, \sqrt{\bar{b}_z}] \quad (1.44)$$

$$b_{x,y,z} = \gamma^2 G_{x,y,z}^2 \delta^2 (\Delta - \delta/3)$$

Expanding $\sqrt{\bar{b}}\bar{D}\sqrt{\bar{b}}^T$

$$\sqrt{\bar{b}}\bar{D}\sqrt{\bar{b}}^T = [\sqrt{\bar{b}_x} \quad \sqrt{\bar{b}_y} \quad \sqrt{\bar{b}_z}] \begin{bmatrix} D_{xx} & D_{xy} & D_{xz} \\ D_{yx} & D_{yy} & D_{yz} \\ D_{zx} & D_{zy} & D_{zz} \end{bmatrix} \begin{bmatrix} \sqrt{\bar{b}_x} \\ \sqrt{\bar{b}_y} \\ \sqrt{\bar{b}_z} \end{bmatrix} \quad (1.45)$$

$$= D_{xx}b_x + D_{yy}b_y + D_{zz}b_z + 2D_{xy}\sqrt{\bar{b}_x}\sqrt{\bar{b}_y} + 2D_{xz}\sqrt{\bar{b}_x}\sqrt{\bar{b}_z} + 2D_{yz}\sqrt{\bar{b}_y}\sqrt{\bar{b}_z}$$

By defining two new vectors this is simplified to:

$$= \bar{D}\bar{b}$$

This allows equation 1.43 to be re-written in a form that can be solved by least square fitting.

1.2.7 Evaluation of DTI data

To simplify the representation, and extract characteristics of interest from the multi-dimensional diffusion Tensor, various scalar indices have been defined. Prominent examples include:

(i) Mean diffusivity (MD):

The MD is defined as the mean of the 3 Eigenvalues describing the directionally averaged diffusivity of water within a voxel.

$$\ln(S) = \ln(S_0) - \bar{D}b \quad (1.46)$$

(ii) Fractional Anisotropy (FA):

The FA is a measure of the degree of directionality of diffusion within a particular voxel.

$$FA = \frac{\sqrt{(\lambda_1 - \lambda_2)^2 + (\lambda_2 - \lambda_3)^2 + (\lambda_3 - \lambda_1)^2}}{\sqrt{2}\sqrt{\lambda_1^2 + \lambda_2^2 + \lambda_3^2}} \quad (1.48)$$

A common way of enriching the information contained by the FA maps is to superimpose a colour coding corresponding to the orientation of the principal Eigenvector to represent the direction of the underlying fibre bundles. Examples of Eigenvalue images, MD, FA and colour FA maps are illustrated in Figure 1-17 below.

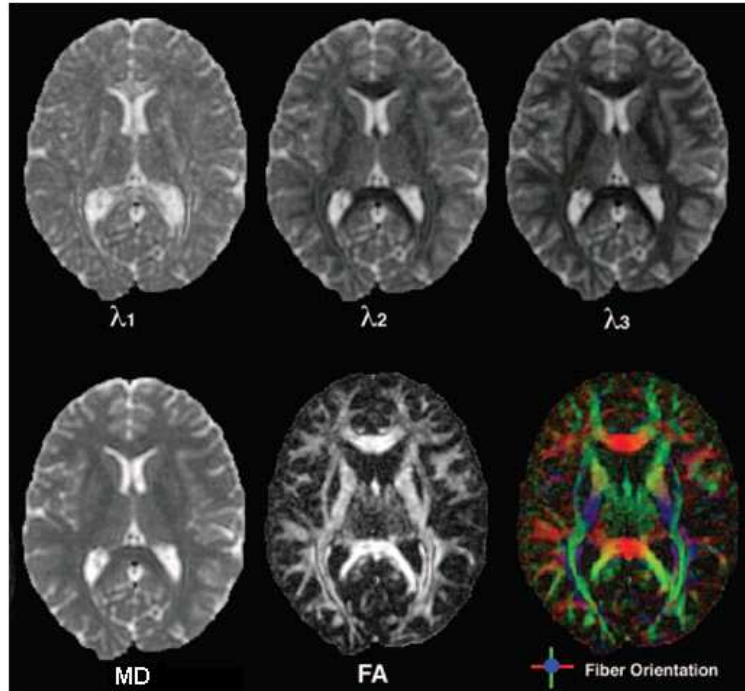


Figure 1-17 Illustration of diffusion Tensor Eigenvalue images (top row), the scalar diffusion indices of MD (bottom, left), and FA (bottom middle) as well as an FA colour map (bottom right) (Adapted from (12)).

1.3 Echo planar Imaging (EPI)

As discussed in section 1.2, an acquisition sequence may be sensitized to Brownian motion through the application of a set of magnetic field gradient pulses. This, however, also makes acquisitions susceptible to other types of motion, thus adversely affecting image quality and diffusion measurement accuracy. As a result, an important practical requirement of *in vivo* DTI is the availability of data sampling strategies displaying sufficient insensitivity to coherent motion. The most widely used, and current gold standard acquisition module (13) in contemporary DTI acquisitions is EPI (12). In fact, diffusion MRI only entered the clinical domain when manufacturers made EPI available on MRI scanners (13). This section will outline the challenges of motion to diffusion MRI measurements, introduce EPI and outline both its strengths and weaknesses.

1.3.1 Challenges of diffusion sensitized MRI

To sufficiently sensitize an acquisition sequence to Brownian motion, necessitates the inclusion of diffusion sensitization gradients, (as illustrated in Figure 1.15). This, however, also makes acquisitions more sensitive to coherent bulk motion. Over the duration of a typical MRI acquisition, phase shifts resulting from macroscopic motion are in the order of 10 to 100 times larger than those resulting from diffusion (13). Although in theory the effect of coherent motion results in global coherent phase shifts, which should not manifest in magnitude images, a problem arises when significantly different motion patterns occur between various phase encode lines. For instance, a 2D spin echo sequence of matrix 192 x 192 comprises 192 echoes, each recorded one TR (typically 5-10 s) apart. Since macroscopic motion typically will not repeat itself identically over such considerable periods of time, each phase encode line in k-space will experience a different phase shift depending on the magnitude and direction of motion that has occurred at the time of its acquisition. Such phase incoherencies across phase encode lines in k-space result in image ghosts along the phase encode direction, and the spreading of signal over the image rather than its confinement to its corresponding voxel. An illustration of such artefacts is depicted in Figure 1-18.

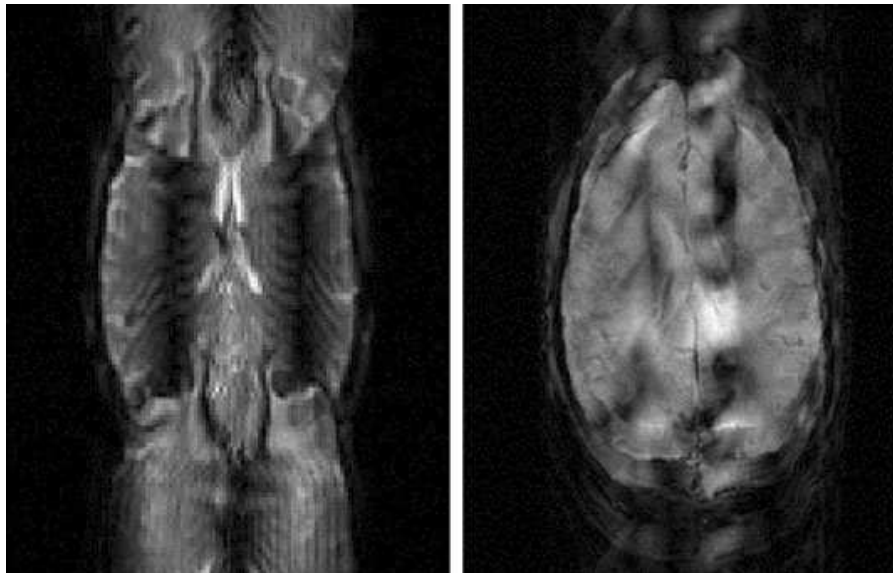


Figure 1-18: Illustration of typical motion artefacts: ghosting and large signal variations across image (taken from (13)).

Various techniques have been developed to alleviate and/or correct motion induced phase errors. These include the minimization of motion through physical restraints (14) and, primarily in animal studies, the use of anesthetization. The synchronization of the acquisition with a source of motion (e.g cardiac gating) aims at minimizing the motion acquisitions are exposed to. Finally, the use of navigator echoes (e.g. (15,16)) has been proposed to correct phase errors by recording phase changes prior to data acquisition, thus allowing their alleviation prior to image reconstruction. While these strategies provide different levels of relief from motion induced phase errors and come at different costs in terms of scan time and complexity, currently the most effective way of avoiding motion artefacts of *in vivo* diffusion sensitized MRI in humans is to use ultrafast acquisition sequences such as EPI.

1.3.2 Ultra-fast image acquisition using EPI

EPI produces a series of gradient echoes with a bipolar oscillating readout gradient. Each gradient echo in the echo train is individually phase encoded through phase encode gradient 'blips' so that multiple k-space lines can be recorded from a single RF-excitation. Single-shot EPI (Figure 1-19) is an acquisition sequence capable of recording a full image from the echoes generated by a single excitation. As a result, diffusion sensitization gradients for an entire image only need to be applied once, and the time allowed to lapse between the acquisition of successive phase encode lines of k-space is reduced effectively.

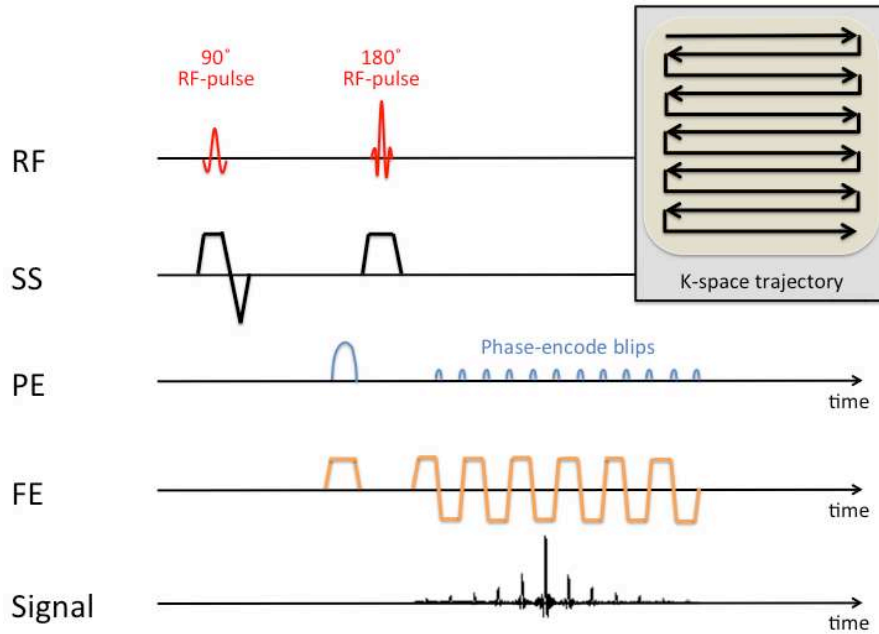


Figure 1-19: Pulse diagram of the spin-echo EPI-sequence with insert (top right) illustrating the corresponding k-space trajectory.

While the speed of acquisition achieved by EPI thus provides it with distinct advantages, the lengthy k-space trajectory (traversing all of k-space rather than just one line per excitation) and limitations in gradient performance result in long sampling times, imposing a number of limitations on this technique.

One such limitation is that the number of echoes that can be formed from a single excitation, and thus the number of lines of k-space that may be sampled, is inherently limited. For a given FOV, this imposes a hard and fast limit on the achievable in-plane resolution. Typically, in-plane resolutions of 2 x 2 mm are used in the human brain at 3 T.

Another main challenge of EPI is its relatively low receiver bandwidth along the phase encode direction. The receiver bandwidth is defined through the sampling rate in k-space. Since an entire frequency encoded line in k-space is sampled before each phase encode increment, the sampling rate along the phase encode direction is relatively low. In MRI, the pixel bandwidth refers to the difference in MRI frequencies between adjacent pixels. Any frequency error

greater than the pixel bandwidth will thus translate into a misallocation of the pixel, resulting in image distortions or even signal voids.

Phase errors may result from unwanted magnetic field inhomogeneities. These may arise from imperfections in B_0 , imperfect shimming and magnetic field gradients between regions within the FOV of different magnetic susceptibility (e.g. bone, air filled cavities). Rapidly switching of magnetic fields may induce Eddy-currents in conducting components of the MRI system. The powerful and rapidly switched gradients used for the sensitization of acquisitions to diffusion thus pose an inherent challenge for the acquisition of diffusion weighted images (DWI). Variations in the orientation of these gradients lead to different Eddy-current distortions in the various images, thereby reducing voxel-to-voxel correspondence in acquisitions comprising composite DTI datasets. Three patterns of Eddy-current induced distortion that can generally be observed in DTI images are illustrated in Figure 1-20.

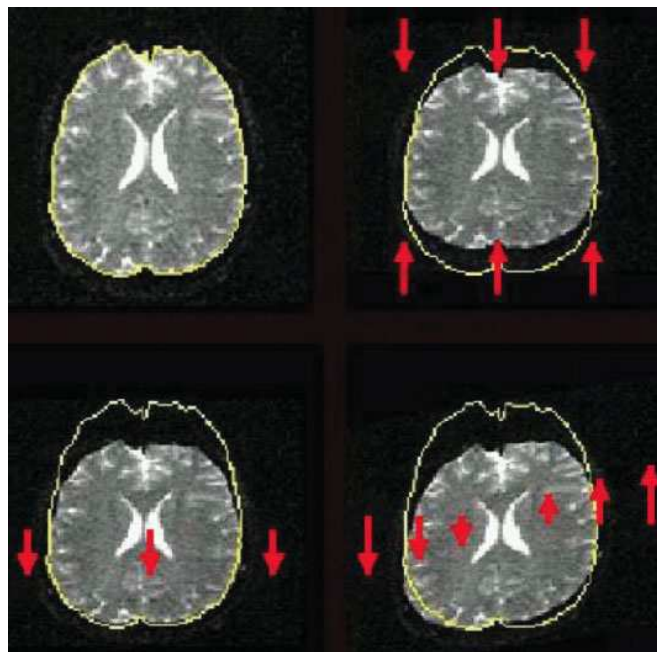


Figure 1-20: Three modes of distortion resulting from Eddy-currents commonly observed in diffusion sensitized acquisitions: contraction (top right), shift (bottom left) and shear (bottom right) (taken from (13)).

Apart from image distortions, Eddy-currents may also affect the voxel intensities as a result of image compression/dilation altering the voxel size.

Another implication of the low per-pixel receiver bandwidth along the phase encode direction is that due to their chemical shifts, the signals of water and fat may be displaced by several pixels. This effect increases at higher field strengths and necessitates the use of effective fat suppression.

Finally, image blurring (or point spread function artefact) results from $T2^*$ related signal decay occurring during the signal readout (4).

Consequently, the main limitations of EPI sequences can be addressed through the reduction of echo train length (ETL). This can be achieved through parallel Imaging (e.g. (17-21)) and/or through the use of stronger gradients.

1.4 General experimental details

The local research ethics committee approved all studies presented in this thesis, and informed written consent was obtained from all volunteers prior to scanning. All scans were acquired at the University of Nottingham on the Philips Achieva 3 T scanner at the Queens Medical Centre (QMC 3 T), and/or the Philips Achieva 3 T and 7 T scanners at the Sir Peter Mansfield Magnetic Resonance Centre (SPMMRC 3 T, 7 T).

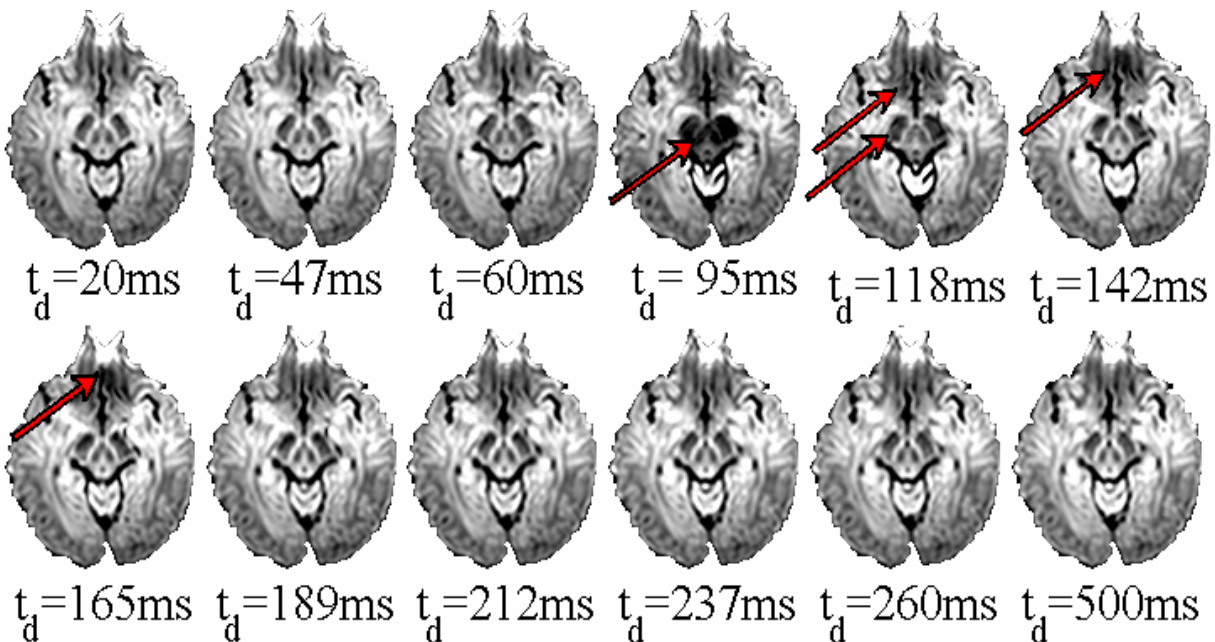
The gradient system on the 3 T scanners provided maximum strengths of 80 mT m⁻¹. Shimming was provided with 36 fixed rails and 3 first-order and 5 second-order independent channels. An 8-channel SENSE head coil with inner diameters of 23 cm x 24 cm used was. The gradient system on the 7 T scanner was comparatively weaker achieving 40 mT m⁻¹ using passive shielding and gradients achieving a maximum gradient strength of 40 mT m⁻¹. The head coil was a Nova Medical (Wilmington, MA, USA) receive SENSE head coil with 16 output channels.

Literature

1. Cox E, Gowland P. Measuring T2 and T2' in the Brain at 1.5T, 3T and 7T Using a Hybrid Gradient Echo-Spin Echo Sequence and EPI. 2008; Toronto, Ontario, Canada. p 1411.
2. Johansen-Berg H, Behrens T. Diffusion MRI. Press A, editor; 2009.
3. Morgan P. Spatial distortion in MRI with application to stereotactic neurosurgery. Nottingham: University of Nottingham; 1999.
4. McRobbie D, Moore E, Graves M, Prince M. MRI From Picture to Proton; Second edition: Cambridge University Press; 2007.
5. Brown R. A brief account of microscopical observations made in the months of June, July and August, 1827, on particles containing the pollen of plants; and on the general existence of active molecules in organic and inorganic bodies Phil Mag 1828;4:161-173.
6. Fick A. Concerns diffusion and concentration gradient. Ann Phys Lpz 1855;107.
7. Einstein A. Ueber die von der Molekularkinetischen Theorie der Waerme geforderte Bewegung von in ruhenden Fluessigkeiten suspendierten Teilchen. Ann Physik 1905;4:549-560.
8. Mori S. Introduction to Diffusion Tensor Imaging. Elsevier, editor; 2007.
9. Mukherjee P, Berman J, Chung S, Hess C, Henry R. Diffusion Tensor MR Imaging and Fiber Tractography: Theoretic Underpinnings. American Journal of Neuroradiology 2008;29(4):632-641.
10. Jones D. The effect of gradient sampling schemes on measures derived from diffusion Tensor MRI: A Monte Carlo study. Magnetic Resonance in Medicine 2004;51(4):807-815.
11. Jones D, Horsfield M, Simmons A. Optimal Strategies for Measuring Diffusion in Anisotropic Systems by Magnetic Resonance Imaging. Magnetic Resonance in Medicine 1999;42:515-525.
12. P. Mansfield RJO, R Coxon. Zonally magnified EPI in real time by NMR. J Phys E: Sci Instrum 1988;21:275-280.

13. Le Bihan D, Poupon C, Amadon A, Lethimonnier F. Artifacts and Pitfalls in Diffusion MRI. *Journal of Magnetic Resonance Imaging* 2006; 24:478-488.
14. Heim S, Hahn K, Sämann P, Fahrmeir L, Auer D. Assessing DTI data quality using bootstrap analysis. *Magnetic Resonance in Medicine* 2004;52(3):582-589.
15. Ordidge R, Helpert J, Qing Z, Knight A, Nagesh V. Correction of motional artefacts in diffusion weighted MR images using navigator echoes. *Magnetic Resonance Imaging*;1994(12):455-460.
16. Anderson A, Gore J. Analysis and correction of motion artefacts in diffusion weighted imaging. *Magnetic Resonance in Medicine* 1994;32(379- 387).
17. Bammer R, Auer M, Keeling S, Augustin M, Stables L, Prokesch R, Stollberger R, Moseley M, Fazekas F. Diffusion Tensor Imaging Using Single-Shot SENSE-EPI. *Magnetic Resonance in Medicine* 2002;51:6.
18. Jaermann T, Crelier G, Pruessmann K, Golay X, Netsch T, Van Muiswinkel A, Mori S, Van Zijl P, Valavanis A, Kollias S, Boesiger P. SENSE-DTI at 3T. *Magnetic Resonance in Medicine* 2004;51:230-236.
19. M. Blaimer FB, M. Mueller, R. M. Heidemann, M. A. Griswold, P. M. Jakob. SMASH, SENSE, PILS, GRAPPA - How to Choose the Optimal Method. *Top Magnetic Resonance Imaging* 2004;15:236223-.
20. Pruessmann K, Weiger M, Scheidegger M, Boesiger P. SENSE: sensitivity encoding for fast MRI. *Magnetic Resonance in Medicine* 1999;42:952-962.
21. Wilm B, Gamper U, Buehrer M, Pruessmann K, Luchinger R, Kollias S, Boesiger P. The Benefit of Reduced FOV Diffusion Imaging with and without SENSE. 2007; Berlin, Germany.

Chapter 2.: Quantitative assessment of the impact of cardiac pulsation induced brain motion in clinical DTI



Axial slices of single-shot spin echo 2D-EPI scans through the midbrain with diffusion weighting gradients applied along the through-slice direction. Acquisitions were recorded at times t_d after detection of an R-wave. Red arrows highlight signal-void artefacts induced by cardiac pulsation.

2.1 Introduction

The aim of this study was to quantitatively assess the effects of cardiac pulsation on DTI acquisitions recorded under a protocol used routinely in clinical and biomedical research applications. This was to address the question whether the use of techniques towards the alleviation of cardiac pulsation induced artefacts are merited, or even necessitated, by potential effects on data quality. The gating of all acquisitions comprising a DTI dataset to a specific point in the cardiac cycle during which no discernable brain motion is induced, has been shown to be effective in eliminating cardiac pulsation induced artefacts. Therefore, to assess the impact of cardiac pulsation in DTI, the precision and accuracy of prevalent scalar DTI indices measured with and without cardiac gating are compared.

2.1.1 How cardiac pulsation causes artefacts in DWI acquisitions

The intrinsically high motion sensitivity of Diffusion MRI measurements is a prerequisite for the reliable detection of Brownian motion which, during diffusion encoding times of 50 ms (typical for contemporary human DWI scans), results in displacements of approximately 10 μm (1,2). The high motion sensitivity, however, also makes Diffusion sensitized acquisitions susceptible to unwanted sources of motion.

In order to selectively sensitize acquisitions to a particular type of motion, the effects of unwanted motion must thus be minimized. This can be achieved through the use of appropriate acquisition sequences that are insensitive to the effects of the unwanted motion. For this purpose, motion can be divided into two main categories, namely voxel coherent and intra-voxel incoherent motion (IVIM).

In voxel-coherent motion, such as physical head movements, spins within voxels experience identical displacements. The resulting preservation of phase coherence leads to a net phase shift in the resulting signal, while its intensity remains unchanged. If all lines of k-space are acquired under identical motion patterns, this type of motion would therefore not manifest in magnitude images. However, since specific physical motion patterns typically do not repeat themselves identically, acquisition sequences based on multiple excitations lead to phase

inconsistencies between k-space lines. This may lead to image ghosts along the phase encode direction. The prevalent strategy to reduce the susceptibility of *in vivo* DTI acquisitions to physical motion is to use ultra-fast single-shot acquisition sequences capable of producing an entire image from the signal generated by a single RF excitation. Alternatively, phase errors can be determined, and subsequently corrected, by the use of navigator echoes.

Intra-voxel incoherent motion (IVIM) can result from spins moving in fluids with different velocities and/or directions at a sub-voxel level. Processes resulting in IVIM include Brownian motion, capillary perfusion and complex tissue motion patterns and deformations. The incoherent nature of this motion effects a dephasing of spins within voxels, and thus manifests as signal intensity losses in reconstructed magnitude images. As this effect depends on the time over which IVIM is allowed to occur and the intensity of applied motion sensitization gradients, it is not eliminated by the acquisition strategies described above. The ability to selectively measure the effect of IVIMs provides a basis for practical diffusion MRI measurements.

The multitude of processes that may lead to IVIM, however, may lead to overestimations of diffusion coefficients. Indeed, the quantification of IVIM has also been proposed for the measurement of tissue perfusion (e.g. (28)). Specifically in the presence of cardiac pulsation, blood pressure changes may lead to varying rates of capillary blood flow and thus IVIM. Alternatively, phase contrast (PC) and complementary spatial modulation of magnetization (CSPAMM) measurements of the brain have shown cardiac pulsation to induce tissue displacements ranging between 130 μm (3) and 184 μm (4) reaching velocities of up to 1.5 mm s^{-1} (3). In conjunction with the typically complex tissue deformation and flow patterns, cardiac pulsation may thus induce IVIM within extra-vascular tissue of levels sufficient to induce measurable cardiac pulsation induced artefacts (CPAs).

2.1.2 Review of existing investigations of CPAs

A number of investigations into the effect of cardiac pulsation on diffusion MRI measurements in the human brain have been reported in recent years. With the exception of one study (5), artefacts were observed unanimously in ungated single direction DWI measurements (6,7), scalar Diffusion Tensor (DT) indices (6,8,9) and tractography results (10).

Observations supporting the attribution of observed signal-void artefacts in DWI acquisitions to cardiac pulsation induced motion include that they could be detected in roughly 20 % of ungated acquisitions (6,7). This corresponds to the portion of the cardiac cycle during which the human heart experiences systolic contraction and may therefore result in heightened levels of induced motion. The spatial locations most susceptible to artefacts have been identified as the brainstem and medial inferior brain regions (11,12,14,15) which concur with the regions shown by PC (3) and CSPAMM (4) measurements to experience maximum cardiac pulsation induced brain motion. In all cases, cardiac gating was found effective in eliminating these artefacts.

2.1.3 Motivation & purpose of this study

In spite of the compelling data reviewed above, routine clinical practice has not embraced the recommended inclusion of cardiac gating into DTI acquisition protocols. This may be attributed, in part, to the increase in overall scan time incurred by limiting acquisitions to a particular time-window within the cardiac cycle. Although optimized acquisition-gating schemes that reduce scan time increases by acquiring data in unaffected regions during periods of increased motion have been developed (6), these tend to increase the complexity of scan planning and execution.

On the other hand, while the ‘costs’ of gating are thus considerable, limited quantitative information is available about the benefit it provides in terms of data quality improvements. The transient character of CPAs, combined with long acquisition times resulting from the composite nature of DTI acquisitions make their reliable quantitative characterization challenging. Previous investigations into description of CPAs typically minimized the number of directions along which diffusion was measured. This strategy achieved two effects conducive for the detection of CPAs. First, by maximizing the number of acquisition repeats that can be acquired, shortening of the acquisition time per dataset improves the likelihood of recording DWI acquisitions with CPAs in representative proportions to acquisitions free of CPAs. Second, by eliminating the averaging effect of basing Diffusion Tensor (DT) calculations on more than the minimum required number of measurements, the susceptibility of each dataset to CPAs is effectively maximized. Indeed, single diffusion weighted acquisitions were generally sensitized to motion along the z-axis which was expected to concur with the direction of maximum

motion (3) and thus artefact. However, single direction DWI measurements are rarely used in clinical practice. Similarly, clinical DT calculations are usually based on measurements along more than the minimum six directions (11,12). The true susceptibility of DTI acquisitions acquired under routinely used protocols to CPAs, and the magnitude of resulting artefacts, can thus not be inferred from the existing studies. This lack of information has led to decisions of whether or not to include gating in DTI acquisition protocols to be considered on a case-by-case basis, and at the discretion of the physician/researcher. This may result in inconsistent and possibly sub-optimal design of DTI acquisition protocols.

Furthermore, for a wide range of DTI applications (e.g. detection of regions affected by ischemic stroke (13), depiction of the gross structural connectivity of cortical regions in the brain etc.), a qualitative visual analysis of diffusion measurements is sufficient to obtain the desired information due to the obvious contrast between diseased and healthy tissue. However, a shift towards a better utilization of the quantitative nature of diffusion metrics is currently underway (14). Quantitative analysis allows the detection and tracking of deviations not necessarily visible to the human observer. The ability to detect and track subtle abnormalities is a powerful tool in the diagnosis and prognosis of disease, as well as monitoring the effectiveness of treatment (15). An example of a topical application is the use of functional Diffusion maps as sensitive and non-invasive biomarkers in cancer treatment (16,17). Together with the growing popularity of diffusion MRI in both research and clinical practice, this paradigm shift towards the inclusion of quantitative Diffusion MRI into the repertoire of diagnostic measures, further emphasizes the need for a re-evaluation of the impact of potential sources of artefact.

2.1.4 Structure of this study

This investigation was aimed at the providing a quantitative assessment of CPAs in a DTI acquisition protocol used routinely in clinical practice.

The design of this investigation built on existing knowledge: A pilot to this study (18) demonstrated two findings important for both the motivation of this investigation and its general strategy. First, it established, for the first time, that CPAs could indeed lead to a

measurable loss in precision of DTI metrics recorded under routinely used DTI protocols. Second, it demonstrated that the number of DTI acquisitions that can be recorded during a single scan session was insufficient for a quantitative characterization, or even reliable detection, of CPAs. Subjectively perceived variability in the magnitude of CPAs reported from different sites (ranging from being very pronounced (7), to moderate (6), to not detectable at all (5)) stressed the need to minimize assumptions, and to individually validate them where they cannot be avoided.

In this study, simulations are used to generate populations of both gated and ungated datasets large enough for the quantitative evaluation of the effect of CPAs on the precision and accuracy of DT indices measured under a routinely used DTI protocol. This is achieved in two stages. First *in vivo* DWI time-course measurements are recorded for the comprehensive characterization of CPA-properties. Secondly, this information is used to design appropriate simulations for the quantification of the effects of CPAs on DT indices. Finally, this characterization is used to inform whether, and if so when, cardiac gating should be considered in clinical/biomedical research applications.

2.2 Materials & Methods

2.2.1 General experimental setup details

Ethics

This study was approved by the local research ethics committee, and informed written consent was obtained from all volunteers prior to scanning.

Scanner

All scans were acquired at the Queens Medical Centre, Nottingham, UK, on a Philips Achieva 3T scanner with an 8-channel SENSE-head coil (c.f. Chapter 1).

Physiological monitoring

Physiological monitoring and cardiac triggering was performed using the product vector cardiogram (VCG) device with four electrodes. The leads of the VCG gating unit were separated from the body using a layer of thick paper towels to reduce interference with the acquired VCG traces.

Recruitment

All recruited volunteers were healthy individuals. Male volunteers were favoured as recorded VCG traces were observed to be more accurate, thus allowing precise triggering. No discrimination was made with respect to age.

Slice positioning

The characterization of CPAs, and their effects on DTs require the acquisition of large volumes of data gated to specific points in the cardiac cycle. To keep within the maximum total scan duration of 1 hour per session, as specified in the project approval from the local ethics committee, the slice coverage was limited to a single slice. The positioning of this slice was to be selected to ascertain the strongest CPA effects induced in the brain. Both cardiac pulsation induced tissue displacements (3,4), and CPAs in DWI acquisitions (6,7,9) have been reported

highest in the brainstem and medial inferior brain regions, It was thus decided to position axially orientated slices to traverse the brainstem.

The inferior regions of the brainstem contain highly coherent fibre bundles such as the Corticospinal tract (CST), which lie roughly collinear to the predominant direction of cardiac pulsation induced motion in this region. The resulting coincidence of the principal direction of anisotropic Brownian motion with cardiac pulsation induced motion suggests that CPAs are likely to result in a positive bias of FA values in this region. However, since the high coherence of these tracts results in FA values inherently approaching the maximum even in absence of cardiac pulsation induced motion, an underestimation of FA errors due to saturation effects may occur. Further reasons why highly anisotropic structures are better avoided include concerns over the low SNR, as discussed by Nunes (6). The midbrain, while also expected to experience maximum induced motion due to its position in the brain stem, is less likely to experience abovementioned saturation effects due to the perpendicular orientation of neuronal fibres (as illustrated in Figure 2-1) to cardiac pulsation induced motion.

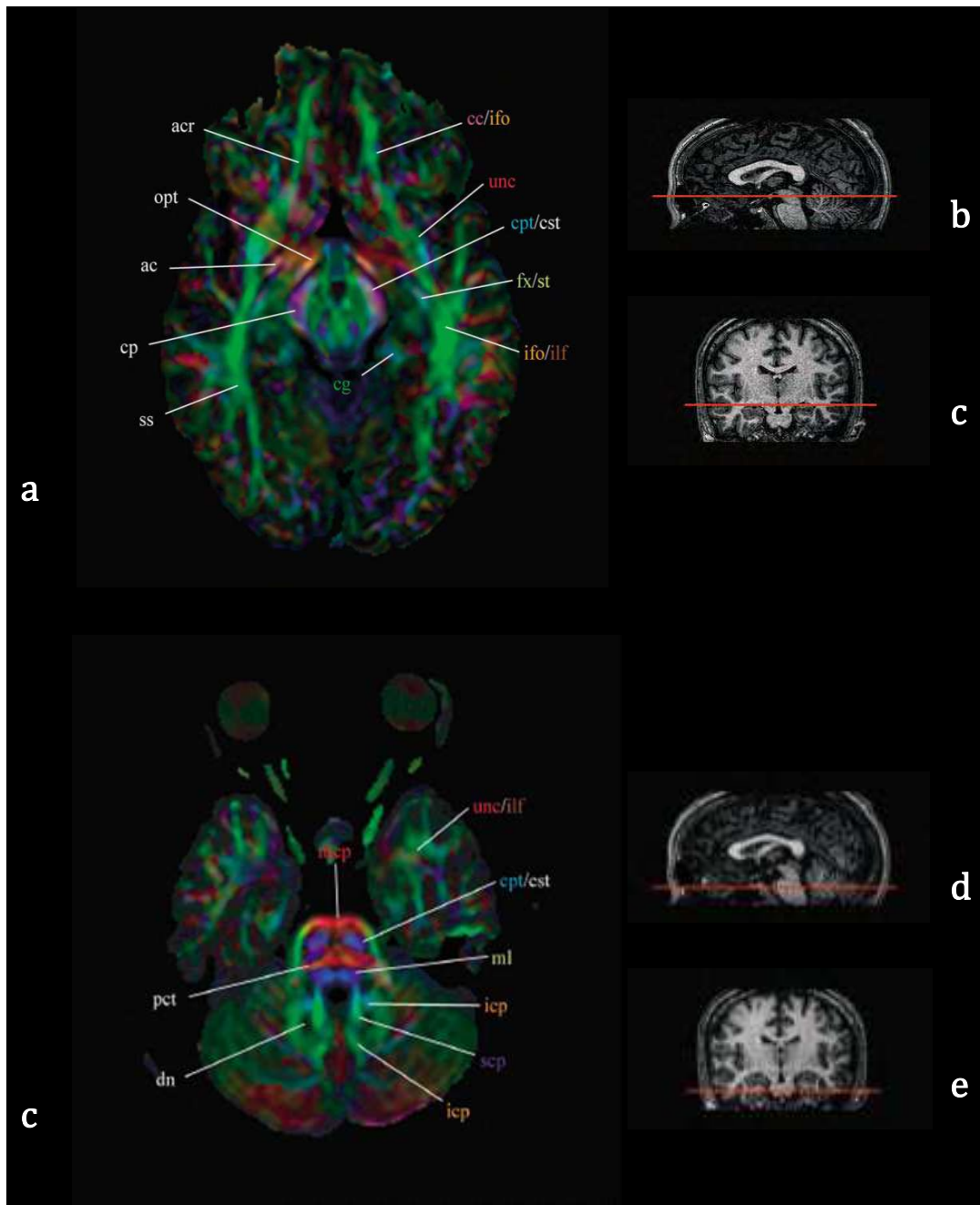


Figure 2-1 FA colour map taken from the selected slice position (top), and inferior brainstem regions (bottom) to display that in inferior regions of the brainstem, fibres are predominantly orientated along the superior-inferior direction (Images taken from (19)).

Motion reduction & co-registration

The acquisition of single slices makes in-plane motion correction by co-registration more difficult, and through slice motion correction impossible. Great care was taken to minimize motion during the scan. Volunteers were instructed to keep still, efforts were made to improve the comfort of volunteers and their heads were carefully padded in the RF coil. Correction of residual in-plane motion and Eddy-current distortions were performed using FSL (20).

2.2.2 Datasets

Artefact characterization on ADC measurements (Dataset 2-1)

Purpose:

Datasets 2-1 comprises ADC and PC time-course measurements for the characterization of effects of cardiac pulsation induced brain motion on DWI acquisitions, and tissue displacements respectively. This was to provide information for the subsequent design and implementation of simulations, as well as the interpretation of results. Dataset 2-1 comprises two data acquisition protocols, Dataset 2-1a and 2-1b. Information acquired from Dataset 2-1a was used to refine the measurement protocol in Dataset 2-1b, allowing artefact characteristics to be extracted more accurately and reliably.

Region of interest (ROI) selection:

As discussed in Section 2.2.1, the characterization of CPAs was performed in the upper brainstem region to provide an estimate of their maximum impact on diffusion MRI measurements. Figure 2-2a below illustrates the typical slice positioning (white line). The black contour in Figure 2-2b illustrates the brainstem delineation in the corresponding in-plane view. As detailed in the introduction to this chapter, CPAs are expected to result in a change in signal intensity in DWI acquisitions. The intricate anatomical structure of the brainstem results in very bright and dark image regions existing in close proximity. This, in combination with the relatively small size of the brainstem ROI effectively makes signal intensity measurements very

sensitive to motion. To minimize the susceptibility to motion artefacts, ROIs were drawn with an arbitrarily selected margin of 2.5 mm (while outline in Figure 2-2b).

All ROIs were drawn using JIM (<http://www.xinapse.com>) and subsequently converted into binary masks of the Analyze format using in-house software. These ROIs were used in all subsequent acquisitions in this investigation.

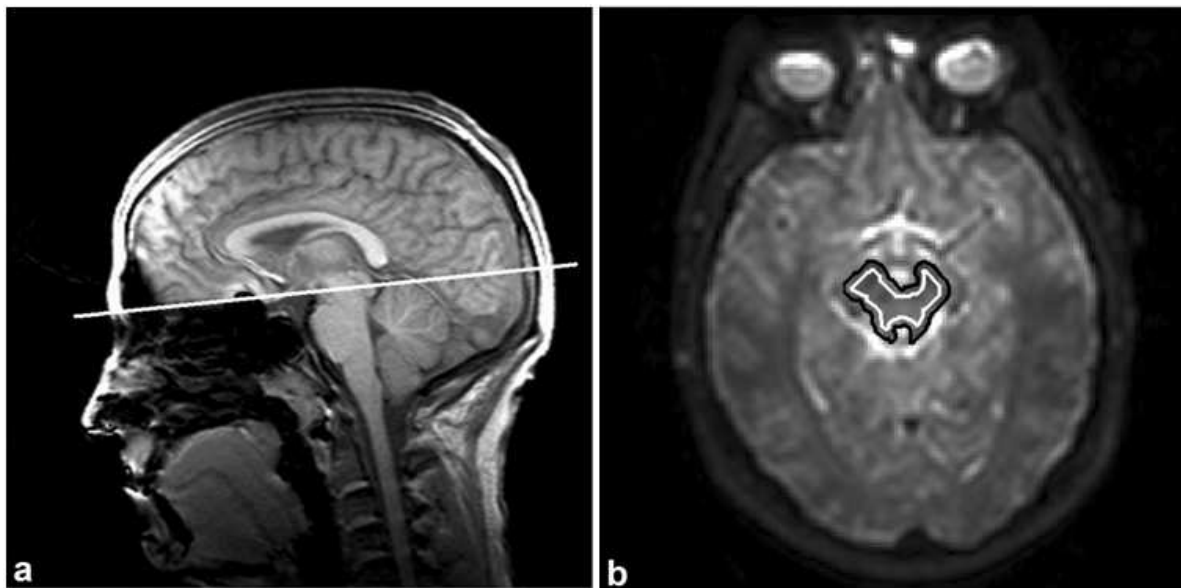


Figure 2-2 ROI positioning. a: Sagittal view illustrating the typical positioning of an axially orientated slice (represented by the white line). b: Depiction of a typical in-plane ROI. The brainstem was first delineated (black outline) and subsequently used to define the actual ROI (white outline) with a margin of 2.5 mm.

Acquisition details

Datasets 2-1a and b both comprise PC and ADC time-course measurements each performed on three volunteers.

PC time-course measurements were performed at the beginning of each scan session to measure the gross through-slice tissue motion occurring within the ROI. This provided reference information against which CPAs in DWI time-course measurements could subsequently be compared.

ADC time-course measurements were calculated from corresponding $b=0$ and DWI acquisitions. To account for orientation dependencies of CPAs, ADC time-course measurements were performed with diffusion sensitization administered along the three orthogonal (read, phase encode and slice select) orientations. These measurements will henceforth be referred to as ADC_x , ADC_y and ADC_z time courses respectively.

- *Dataset 2-1.a*

Parameter	Dataset 2-1.a	
Acquisition description	ADC time-course measurements	PC time-course measurements (1x at beginning of session)
Scanner	3 T Philips Achieva (QMC)	3 T Philips Achieva (QMC)
Number of volunteers	3 (2 male, 1 female)	3 (2 male, 1 female)
Volunteer numbers	1-3	1-3
Repetition time (in ms)	Approx. 4 800 ⁱ	21
Echo time (in ms)	54	13.38
Diffusion sensitization scheme	Philips 3 direction scheme	n/a
b-value	1000 s mm ⁻²	n/a
Velocity encoding	n/a	2 cm s ⁻¹
Number of time-points	15 (+2 ⁱⁱ)	15
Cardiac cycle coverage	100%	100 %
Field of view (in mm)	240 x 240	240 x 240
Matrix	96 x 96	192 x 192
Slice thickness (in mm)	2.5	10
Number of slices	34	1
Number of signal averages	4 ⁱⁱⁱ	2
SENSE reduction factor	2	2
Fat suppression technique	SPIR	SPIR

Table 2-1 Acquisition parameters for scan sequences comprising Dataset 2-1a.

ⁱ Each slice acquisition was triggered by the next R-wave as measured by the scanner VCG, after which triggers

ⁱⁱ To improve the temporal sampling at the times within the cardiac cycle experiencing maximum change, two further ADC measurements were performed at intermediate time-points during which the slope of the ascending and descending arm of the PC curve was observed to be steepest.

ⁱⁱⁱ The maximum total scan session duration of one hour was designed to require 50 minutes in to allow for variations in session duration due to inter-subject differences in heart rate. Under these constraints, four signal averages could be achieved.

- *Dataset 2-1.b*

Following the analysis of time-course measurements in Dataset 2-1a, a number of refinements to improve the precision and representative quality of ADC time-course measurements were implemented in Dataset 2-1b. These changes are described below. All other settings remained identical to those described in Table 2-1.

Only male volunteers were considered for Dataset 2-1b as a result of the observation that VCG traces were of higher quality in men. Prior to commencing scanning, the volunteers were given 5 minutes on the scanner bed to allow their heart rates to settle. This step was to minimize confounding effects of heart rate variations occurring during the ADC time-course acquisition on both the timing and duration of CPAs. PC time-course measurements were performed once at the onset and once at the culmination of each volunteer's scan session allowing the consistency of the heart rate over the duration of the scan session to be monitored.

To improve the precision of measured ADC, time-courses were recorded with eight signal averages. This mandated a compromise in the portion of the cardiac cycle over which ADC time-courses were recorded. Findings of Section 2.3.1 (Characterization of CPAs in DWI acquisitions) demonstrated that cardiac pulsation induced effects occur exclusively in the first half of the cardiac cycle, allowing the second half to be omitted.

Data analysis

ADC and PC time-course measurements were represented by their average voxel intensity within the ROI defined in Figure 2-2.

A number of data processing steps were implemented prior to the quantitative evaluation of ADC time-course measurements from Dataset 2-1b. These were aimed at identifying and isolating CPA properties that remain consistent across volunteers, thus facilitating their subsequent quantification. This had several advantages. First, it facilitates the accurate quantification of CPA properties, by using the optimized ADC time-course acquisitions of

Dataset 2-1b. In addition, by reducing the amount of data that needs to be acquired to characterize CPA properties in each volunteer of Dataset 2-2, the scan protocol is simplified and more scan-time can be dedicated for the acquisition of volunteer specific data. Finally, knowledge of CPA properties that need to be accounted for in the simulation of large populations of DTI acquisitions informs the selection and design of simulation techniques. The specific post-processing steps are detailed in Section 2.3.1 (Characterization of CPAs in DWI acquisitions) on the basis of Figure 2-4.

Both effect magnitudes and the delay time between the detection of an R-wave and the corresponding maximum CPA in ADC time-courses were found to vary between volunteers and thus need to be determined on a case-by-case basis. To facilitate the quantitative comparison of other CPA properties, these effects were omitted from measured ADC time-courses through the following three steps. First, cardiac pulsation-induced ADC changes (ΔADC) were isolated by subtracting ADC_x , ADC_y , and ADC_z observed during the still phase ($t_0=500$ ms) from all corresponding ADC values; ΔADCs were then normalized to the maximum value for each volunteer to omit inter-subject differences in the magnitude of the effects. Finally, the origin of the time-axis was aligned with the point of maximum ΔADC_z measured in each subject to account for inter-subject differences in delay time (t_0) between the detection of an R-wave and the observation of the maximum induced effect.

Dataset 2-2 (Artefact quantification in DTI measurements)

Purpose

The aim of this experiment was to quantitatively estimate the maximum effect of CPAs in prevalent DTI metrics based on a routinely used DTI acquisition protocol. As illustrated by a pilot study (18), scan-time limitations do not allow the acquisition of sufficient number of repeats for the direct assessment, or even reliable detection, of CPA-induced effects. For this reason, Bootstrapping was used to simulate large populations of gated and ungated DTI datasets from multiple DTI acquisitions performed during cardiac phases of high and no cardiac

pulsation induced motion (henceforth referred to as systolic and diastolic time-points respectively).

Acquisition details

Eight healthy volunteers were recruited for this experiment (volunteer numbers 7 - 14). Before commencing scanning, volunteers were allowed five minutes inside the scanner for their heart rates to settle (c.f. Section 2.3.1). Dataset 2-2 comprised two types of acquisitions in each volunteer. First, DWI time-course measurements with diffusion sensitization gradients applied along the through-slice orientation were performed to determine subject-specific time-points of maximum CPAs. This protocol was similar to the ADC time-courses described in Dataset 2-1b, with the exception that in the interest of minimizing scan-time, only DWI_z measurements were performed without signal averaging. Time-courses comprised measurements performed in 25 ms intervals between 25 ms and 200 ms after the detection of an R-wave. The brainstem delineation, and the calculation of mean pixel intensity values were performed online using the graphical user interface. The diastolic time-point was always selected to be 500 ms after the detection of a corresponding R-wave.

This information was subsequently used to gate DTI acquisitions to systolic and diastolic time-points (henceforth referred to as systolic and diastolic DTI measurements respectively). At both these time-points, eight repeats of single slice DTI acquisitions were recorded in an interleaved order.

Acquisition parameters and geometries were identical to those described in Dataset 2-1 (Table 2-1, Figure 2-2) with the only difference being that DTI measurements were acquired with the product Philips 15 direction “no overplus” scheme with one $b=0$ acquisition.

Data analysis

Omission of compromised acquisitions

Prior to the use of systolic and diastolic DTI datasets in Bootstrapping simulations, the quality of both was assessed. Volunteers were excluded from further analysis if they either displayed

obvious motion along the slice-select direction, or if it appeared that their respective time window had been missed. The former was tested by manually surveying all acquired $b=0$ scans. The latter was evaluated for each acquisition, by comparing the magnitude of the successive systolic and diastolic ADC_z scans (c.f. Figure 2-5).

Bootstrapping simulations

To simulate large populations of gated and ungated DTI datasets, DWI measurements were selected at random from appropriate systolic and diastolic subsets of each volunteer in Dataset 2-2. These were subsequently re-combined into simulated DTI datasets. To preserve the DTI direction scheme in simulated datasets, the random selection of acquisitions was performed for each prescribed direction in turn.

Both gated and ungated datasets were simulated. For the simulation of gated DTI datasets, all DWI measurements had been acquired during diastole. Both systolic and diastolic acquisitions were used in the generation of Bootstrapped ungated datasets. The probability of selecting a systolic acquisition was equated to the Full Duration at Half Maximum (FDHM) of the observed cardiac pulsation effect, normalized over the duration of a heartbeat (as determined from Dataset 2-1b).

Post-processing

To reduce the effects of subject motion, FSL's (20) 2D linear co-registration with 6 degrees of freedom (DOF) was used to register the $b=0$ scans of all DWI and DTI datasets to the first acquired $b=0$ scan of each scan session. Obtained spatial transformations were subsequently also applied to all corresponding DWI scans. Eddy Current Distortion (ECD) was reduced by individually co-registering all DWI scans to their corresponding $b=0$ scans using FSL's (20) eddy current correction routine.

In total, 1000 instances were generated for each bootstrap dataset. The number of acquired and simulated DTI datasets was informed by both scan time constraints and previously published investigations (10,21). For each simulated DTI dataset, the Diffusion Tensor and

prevalent scalar indices of FA and MD were calculated using FSL (20), and subsequently summarized by a representative value corresponding to the mean value within the brainstem ROI illustrated in Figure 2-2.

Next, the scan-rescan variability was extracted by subtracting from each dataset a baseline FA/MD value accordingly. This was intended to reduce the influences of anatomical differences between subjects, as well as unavoidable variabilities in slice positioning across sessions. The baseline was defined as the mean FA/MD value of the diastolic Bootstrap dataset, which represents the best guess for the true FA/MD value.

Finally, resulting scan-rescan variability distributions were represented in the form of cumulative histograms. This is because the likelihood of incurring an error of a specific magnitude as represented in a simple histogram has little practical relevance. Typically, one wishes to assess the likelihood of incurring an error greater than a specific value, which may then be compared to a defined threshold. Cumulative histograms were generated by integrating the frequency of occurrence of artefact levels from the points of the maximum and minimum deviation of FA and MD to zero. The number of observations in each bin was expressed as a percentage of total instances simulated. The height of such cumulative histograms at any abscissa thus represents the likelihood of incurring a deviation from the best available estimate of the true FA or MD value (assumed to correspond to the distribution median) of that or greater magnitude. The area under the cumulative histogram is a measure of both the magnitude and frequency of these deviations.

2.3 Results

The aim of this study was the quantitative evaluation of the impact of CPAs in DTI acquisitions recorded under a protocol used routinely in clinical practice. As demonstrated by a pilot to this investigation (18), the quantitative assessment of CPAs in DTI acquisition protocols cannot be achieved through direct measurements, necessitating the use of simulations. This investigation comprises two main parts. First, an initial investigation was carried out for the in-depth and quantitative characterization of CPAs in single diffusion weighted acquisitions. Next, this information was used to aid in the selection and design of appropriate simulations to quantitatively assess the impact of CPAs on DTI measurements.

2.3.1 Characterization of CPAs in DWI acquisitions

The characterization of CPAs in single-direction DWI acquisitions was also performed in two steps. First Dataset 2-1a was recorded to provide first insights into the characteristics of CPAs, and inform subsequent refinements of the measurement technique. These refinements were implemented in Dataset 2-1b, which was subsequently used for the quantitative characterization of the CPAs in single DWI measurements.

In Figure 2-3 initial observations of cardiac pulsation induced brain motion are illustrated. In this dataset (Dataset 2-1a), comprising three healthy volunteers, two types of cardiac pulsation induced motion were considered. PC measurements served the assessment of gross tissue-movement along the through-slice orientation, while ADC measurements represented cardiac pulsation induced IVIM leading to CPAs in DWI acquisitions. The measurements of gross tissue-motion provide a frame of reference against which CPAs in DWI acquisitions could be compared, thus providing insights into the physical effects underlying CPAs.

Both measurements were performed as time-courses covering the full cardiac cycle to ascertain the temporal characteristics of cardiac pulsation induced effects. The orientation-dependence of CPAs in DWI acquisitions was established by acquiring ADC time-course measurements with diffusion sensitization applied along three orthogonal directions (ADC_x , ADC_y and ADC_z). The

measurement of quantitative ADC, rather than qualitative pixel intensity values in arbitrary units, allowed the direct comparison of observed effects. To isolate CPAs in DWI acquisitions, the change in ADC (Δ ADC) from its corresponding baseline value was calculated by subtracting from each measured ADC value the median value calculated over the corresponding time-course.

In this, and subsequent experiments, plotted values represent the mean values averaged over the ROI illustrated in Figure 2-2. The PC and Δ ADC time-course measurements of all three volunteers are illustrated in Figure 2-3.

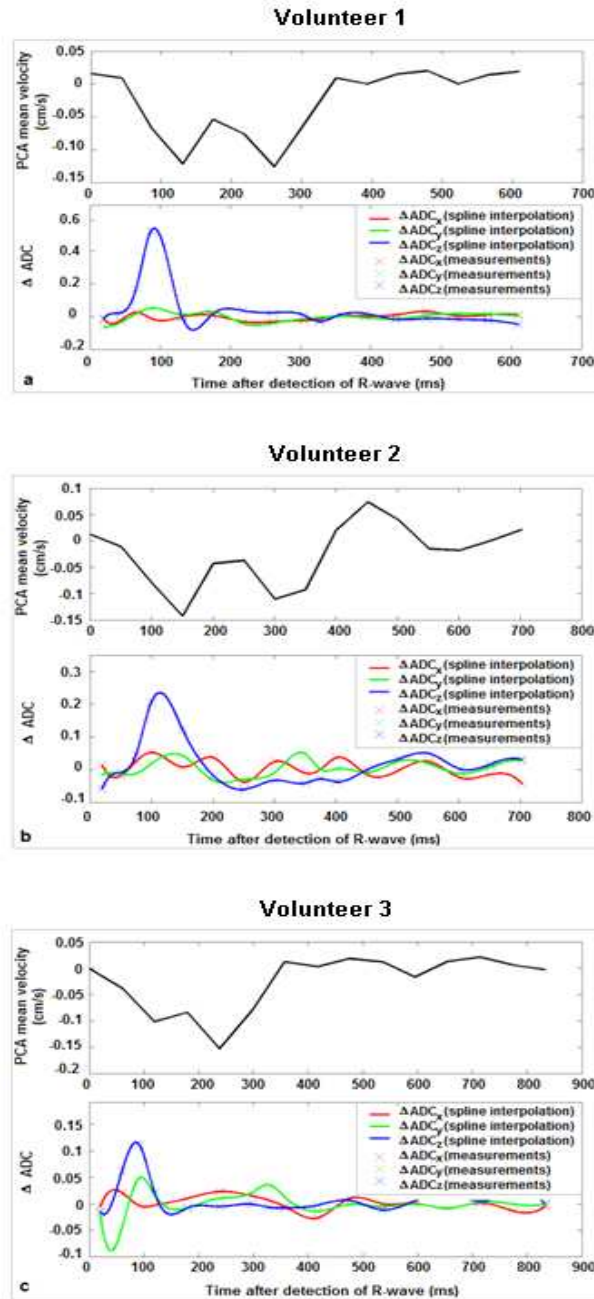


Figure 2-3 Time-course measurements (Dataset 2-1a) for the comprehensive characterization of cardiac pulsation induced motion. PC and ΔADC time-courses were recorded over the ROI depicted in Figure 2-2 in three healthy volunteers. ΔADC time-courses facilitate the assessment of the IVIM induced effects in DWI acquisitions both over time and along different orientations. PC measurements represent the bulk tissue motion occurring over the same time period.

The effects of cardiac pulsation could be observed in both PC and Δ ADC time-course measurements, confirming the presence of both bulk tissue-motion and IVIM respectively. In Δ ADC time-courses, cardiac pulsation consistently manifests as elevated levels of ADC. This is in accordance with the hypothesis that cardiac pulsation induced motion may lead to IVIM that cannot be distinguished from Brownian motion in DWI acquisitions, thus resulting in overestimations of diffusion.

The timing of CPAs in Δ ADC time-courses, with respect to the R-wave that initiates cardiac contraction, could be observed to vary across volunteers. CPAs consistently coincided with the initial acceleration phase of PC time courses. No cardiac pulsation induced effects could be observed in the latter half of the cardiac cycle.

While the duration of cardiac pulsation induced effects in PC measurements spans a full duration at half maximum (FDHM) corresponding to approximately 30% of the cardiac cycle, the duration of CPAs in Δ ADC time-course measurements is considerably shorter. The quantification of this duration is performed in Dataset 2-1b below. It can already be observed, however, that a considerably smaller portion of DWI acquisitions were affected by cardiac pulsation than in previously reported studies, where approximately 20% of ungated DWI acquisitions displayed CPAs (6,7).

The magnitude of maximum Δ ADC elevations induced by cardiac pulsation varied considerably across volunteers. This was despite the velocity of gross tissue motion in PC time-course measurements being comparatively stable. CPAs also demonstrate high levels of orientation dependence, being greatest along the direction experiencing of maximum tissue motion (i.e. in this case in Δ ADC_z where diffusion sensitization gradients are applied along the through-slice direction).

For the selection and simplification of a simulation technique in the subsequent section, those CPA characteristics that display high levels of consistency across volunteers were to be identified and accurately measured. Although similarities in the Δ ADC traces across volunteers

in Figure 2-3 are evident, the acquisition protocol was refined to assess whether residual sources of variability can be reduced prior to the quantitative characterization.

The following changes were implemented in Dataset 2-1b for three further volunteers. First, the considerable levels of seemingly random fluctuations in the ΔADC traces of Figure 2-3 suggest that measurement precision could benefit considerably from increasing the number of averages used. This was limited by the need to keep the experiment duration under an hour, as specified in the project approval granted by the local ethics committee. Since CPAs were seen to occur exclusively in the first half of the cardiac cycle (Figure 2.3), however, the second half could be omitted, thus allowing the number of recorded averages to be doubled in Dataset 2-1b.

The duration of CPAs could also be observed to vary between volunteers (Figure 2-3). While this may reflect genuine differences in the characteristics of CPAs between volunteers, changes in heart rate over time may also have contributed by blurring induced effects over time. To improve heart rate stability over the duration of the scan session, volunteers were instructed to rest for five minutes on the scanner bed outside the magnet prior to the scan.

Following the acquisition of data with these refinements, remaining differences in the characteristics of observed CPAs across volunteers were identified. These were regarded to represent true subject specific variabilities, and thus needed to be accounted for in the subsequently designed strategy to simulate large sets of gated and ungated DTI acquisitions. CPA properties that were observed to remain constant between volunteers, on the other hand, were quantitatively characterized. To do this, the effects of inter-subject variabilities were removed from recorded time-courses through normalization.

Specifically, these factors included the time-delay between the detection of an R-wave in the VCG trace, and the maximum effect induced in the ROI, as well as the amplitude of the induced effect. First, as was done in Dataset 2-1a, cardiac pulsation-induced ADC changes (ΔADC) were isolated by subtracting the corresponding baseline ADC values from ADC_x , ADC_y , and ADC_z measurements. Since CPAs could only be observed during the first half of the cardiac cycle, baseline values were measured at a time-point 500 ms after the R-wave had been detected ($t_D =$

500 ms). ΔADC s were subsequently normalized to the maximum value for each volunteer. Finally, the origin of the time-axis was aligned with the point of maximum ΔADC_z measured in each subject to account for inter-subject differences in delay time (t_D) between the detection of an R-wave and the induced effect.

Following these modifications, PC and normalized ΔADC time-course measurements were plotted as illustrated in Figure 2-4.

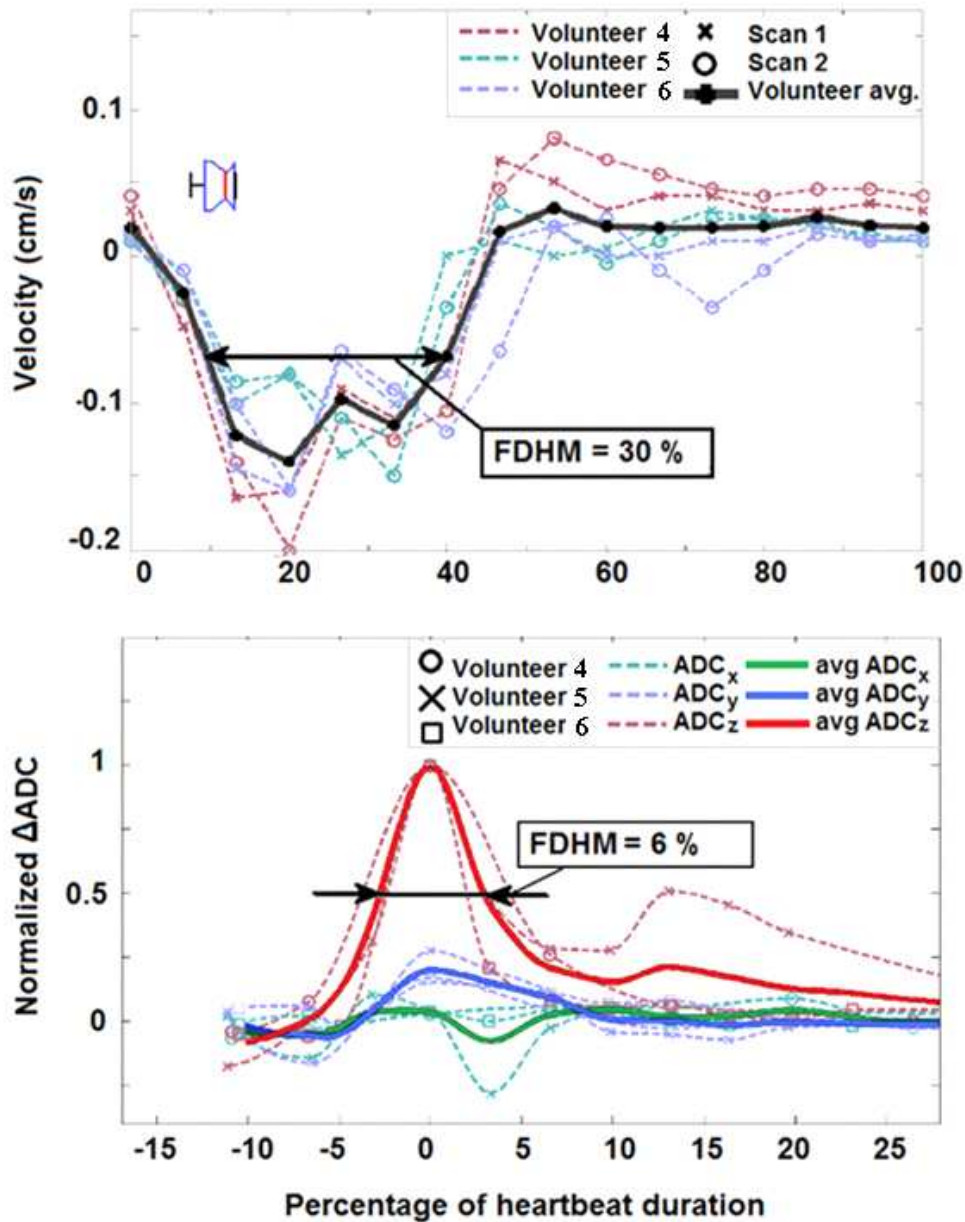


Figure 2-4 Volunteer averaged time-course measurements in the midbrain. The temporal axes are normalized to the heartbeat duration. Top: PC measurement of mean velocity along the z- (through-slice) direction within the midbrain ROI measured for each volunteer at the onset and culmination of the scan session. The origin of the time-axis represents the time point at which an R-wave was detected in the Vector CardioGram (VCG) trace. The box whisker plot represents the time delay between the detection of an R-wave in the VCG signal and detection of the maximum ΔADC_z for all volunteers of Datasets 2-1.b and 2-2. Bottom: Individual and subject averaged time courses of ΔADC_x , ΔADC_y , and ΔADC_z from volunteers 4 to 6 in Dataset 2-1.b.

As illustrated in Figure 2-4, the Full Duration at Half Maximum (FDHM) of CPAs in ΔADC time-courses could now be observed to consistently occupy only 6 % of total heart beat duration in all three volunteers. This is notably shorter than the 20 % during which significant cardiac pulsation motion has been observed in previously published DWI experiments (6,7).

The box and whisker plot in Figure 2-4 illustrates the time points after detected R-waves at which the maximum effect was induced in all ΔADC_z time courses acquired during this investigation (i.e. Datasets 2-1a, Dataset2-1b and Dataset 2-2). These ranged between 75 ms and 135 ms with an average value of 115 ms. This range is comparable to the duration of observed effects and therefore, the delay time between the R-wave and maximum CPA must be known for the reliable acquisition of systolic datasets.

As in Figure 2-3, differences in the ΔADC values along the three orthogonal axes of the image coordinate system are evident from the time-course measurements in Figure 2-4.

2.3.2 Selection of a simulation technique

The selection of a simulation technique for the estimation of the effect of CPAs on DT indices was based on findings from Section 2.3.1 above.

Vital considerations included minimizing and validating assumptions. The importance of this is highlighted by differences in reported CPA properties observed between sites and volunteers. For example, the magnitude of cardiac pulsation induced signal voids between sites can be observed to range from being very pronounced (7), to moderate (6), to not detectable at all (5). In this study the magnitude of the induced effect has also been shown to vary considerably between volunteers (Figure 2-3). Similarly, while all previous investigations detected CPAs in 20 % of ungated measurements, Figure 2-4 illustrates that on the in-house scanner only 6 % of ungated acquisitions were susceptible.

Keeping these considerations in mind, the use of a modified variant of bootstrapping simulations was proposed as a means to boost the number of achievable DTI dataset repeats

for subsequent characterization of the effect of cardiac pulsation on the accuracy and precision of measurements. Bootstrapping simulations are a model-free approach based on the random selection and replacement of individual scanned measurements from a set of repeated acquisitions.

Bootstrapping simulations have received widespread acceptance as a technique for the characterization of DTI measurement precision, and have even been used to detect effects of cardiac pulsation for tractography results (10). It has been recommended that a minimum of five acquisition repeats are used for accurate bootstrapping (21). These can be achieved, and even exceeded, if acquisitions are limited to single slices.

2.3.3 Quantitative evaluation of CPAs in practical DTI acquisitions

Quality assessment of systolic and diastolic DTI datasets

Repeated systolic and diastolic DTI acquisitions were recorded in Dataset 2-2, and subsequently used to simulate large populations of gated and ungated DTI acquisitions using Bootstrapping.

As discussed in Section 2.2.2, Bootstrapping was preceded by an assessment of the quality of recorded data. Potential concerns included through-plane head motion, which cannot be corrected for by registration on account of acquisitions comprising only single slices, and missing the relatively narrow time-window for systolic acquisitions as a result of mis-triggering or a change in heart rate. Following in-plane motion correction, datasets were first assessed for visible motion effects. Acquisitions of two volunteers (Volunteer numbers 13 and 14) displayed considerable levels of head motion resulting in their exclusion from this investigation. Next, the successful gating of acquisitions to their corresponding systolic and diastolic time-windows was assessed by directly comparing the systolic and diastolic ADC_z of repeated DTI acquisitions (Datasets 2-2). The results are plotted in Figure 2-5 below.

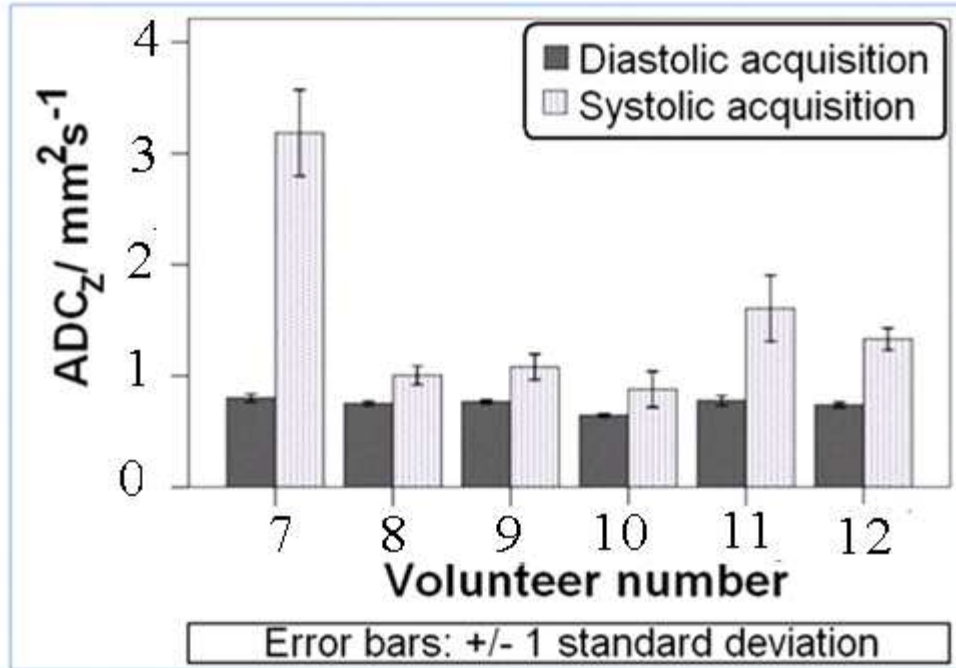


Figure 2-5 Average ADC_z within the midbrain acquired during the still phase (dark grey), and at the point of maximum cardiac pulsation induced motion (light grey) in Dataset 2-2. Error bars indicate the standard deviation over repeats.

The effectiveness of steps taken to improve the reliability of the determination of delay times at which systolic and diastolic acquisitions were recorded is demonstrated in Figure 2-5 where systolic repeat-average ADC_z values can be observed as being consistently higher than their diastolic counterparts. The relatively narrow error bars corresponding to one standard deviation of ADC_z values over repeated acquisitions also demonstrate the reliability of this approach.

Bootstrapping Simulations

The final step of this investigation was to perform the Bootstrap simulations and the subsequent evaluation of the distribution of measurements of gated and ungated acquisitions. These were assessed for both for individual subjects and averaged over the group.

As described in Section 2.2.2, following the generation of the Bootstrap DTI datasets, the baseline FA and MD values were subtracted from each simulated dataset. This had the dual effect of isolating scan-rescan variability from the simulated datasets, while making acquisitions robust against unavoidable differences in slice-placement. To determine the likelihood of

incurring an artefact equal to or greater than a particular value, the distributions of simulated gated and ungated FA and MD values were represented in a cumulative histogram. Cumulative histograms of the volunteer displaying the highest effect (volunteer number 7) and the group average are illustrated in Figure 2-6.

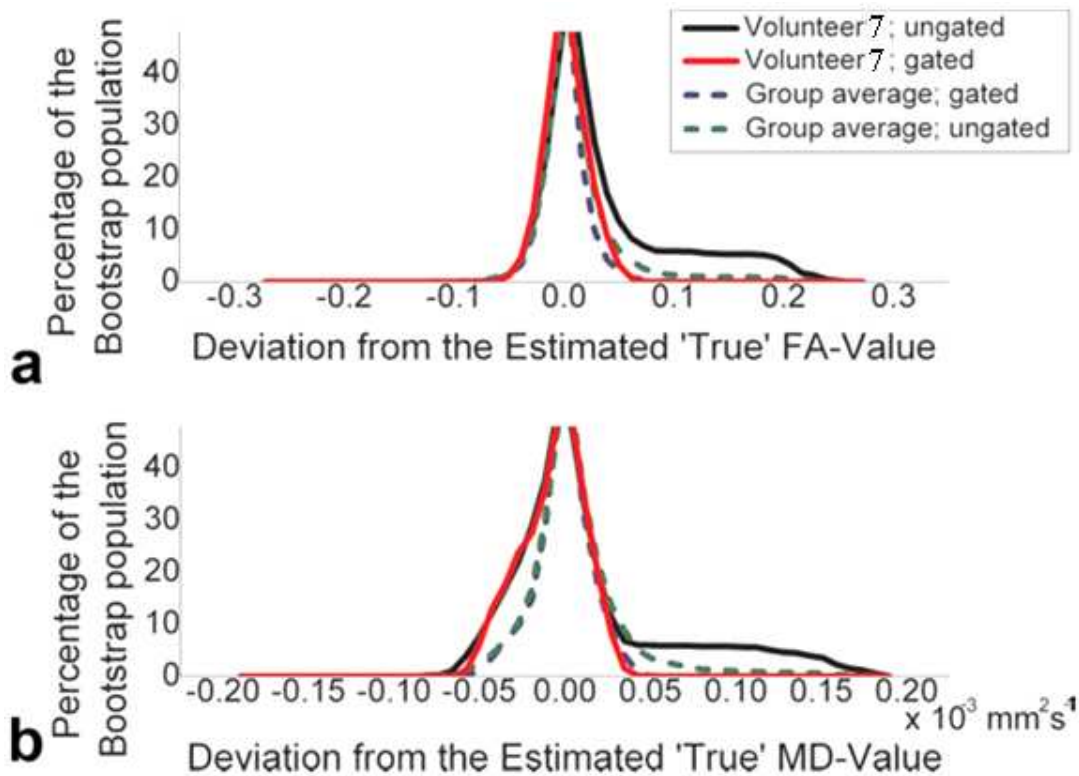


Figure 2-6 Cumulative histograms of deviations of simulated DT indices from a best estimate represented by the median of the simulated gated distribution for each subject in Dataset 2-2. The height at any abscissa represents the likelihood of incurring a deviation of that, or greater, magnitude. a: Cumulative FA histograms with and without gating of the volunteer displaying the strongest effects, and the group-average case. b: Cumulative MD histograms with and without gating of the volunteer displaying the strongest effects, and the group-average case.

While ungated Bootstrap datasets allowed the estimation of the effects of cardiac pulsation in a large population of FA and MD measurements, the distribution of results in gated Bootstrap datasets represents the scan-rescan variability resulting from factors other than CPAs. The difference thus provides a measure of the practical relevance CPAs in DTI acquisitions. The area

under the cumulative histogram can be regarded as a surrogate for the overall measurement precision. In the group averaged case, the differences between gated and ungated acquisitions are small compared to the precision of gated measurements, implying that in group studies, other sources of scan-rescan variability outweigh the effects of cardiac pulsation on the tested scanner and acquisition sequence. As a result, group studies would benefit little from being performed with cardiac gating whilst incurring a significant 'cost' in terms of scan time and/or complexity.

In individuals, however, CPA has been found to potentially result in a noticeable increase in the susceptibility to errors. In the ungated Bootstrapped dataset of volunteer 7, FA overestimations of up to 0.26 and MD overestimations of up to $0.19 \times 10^{-3} \text{ mm}^2 \text{ s}^{-1}$ were observed (Figure 2-6). 6 % of simulated FA values deviated from the best estimate by 0.1 or more, and 5.7 % of the simulated MD values deviated by $0.1 \times 10^{-3} \text{ mm}^2 \text{ s}^{-1}$ or more. The maximum observed deviation of the corresponding gated dataset was 0.072 and $0.043 \times 10^{-3} \text{ mm}^2 \text{ s}^{-1}$ for FA and MD, respectively. This level of artefact susceptibility may be of practical relevance in applications such as the diagnosis and monitoring of disease.

Since it is not practical to determine the level of cardiac pulsation induced artefact in every patient with the technique described above, factors that may be used to predict the susceptibility of individuals to CPA (e.g. blood pressure, height, age, sex) should ideally be investigated and used to screen patients in relevant applications. While this was outside the scope of this investigation, a potential interim solution is proposed below.

Two scalar indices, the measurement and simulation effect index were defined to quantify the magnitude of CPAs in measured and simulated data respectively. The measurement effect index is defined as the difference between the repeat averaged systolic and diastolic ADC_z to represent the CPA magnitude. In a practical setting, this could be determined through a simple ADC time-course measurement at the onset of the scan. The simulation effect index was defined as the percentage change in area under cumulative histograms for simulated ungated and diastolic gated datasets representing the magnitude and frequency of cardiac pulsation induced changes in FA and MD.

As illustrated in Figure 2-7, a linear relationship of good correlation (0.88 and 0.73 for FA and MD respectively) was observed between these indices across volunteers, suggesting that it may be possible to predict the severity of cardiac pulsation induced errors in DTI metrics using a simple time-course measurement.

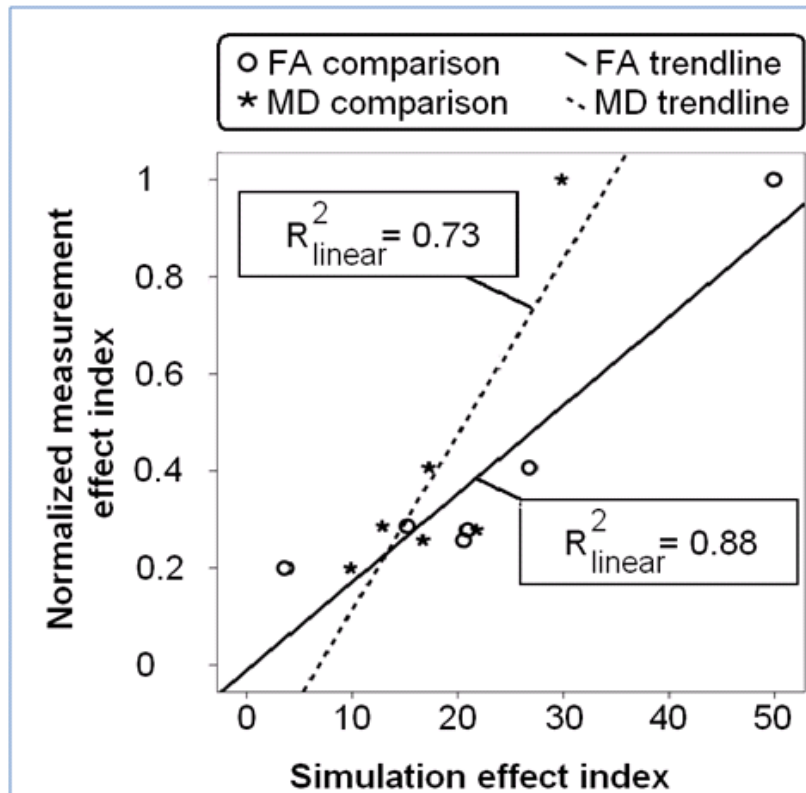


Figure 2-7 Comparison of the measurement and simulation effect indices: representing the measurable difference between systolic and diastolic ADCz values, and the simulated impact of CPAs on FA and MD distributions respectively (Dataset 2-2).

2.4 Discussion

The work presented in this chapter provides a comprehensive and quantitative characterization of CPAs in both single DWI, and composite DTI acquisitions. DTI datasets were recorded under a routinely used 15-direction DTI acquisition protocol on an in-house 3 T scanner.

Previous investigations not only established the susceptibility of *in vivo* single DWI acquisitions and DTI datasets in the human brain to cardiac pulsation induced motion (5-10), but also provided a number of strategies varying in their effectiveness and requirements towards the alleviation of artefacts. The most established technique is arguably the gating of all acquisitions to a single point in the cardiac cycle during which no discernable brain motion is induced. While effective, however, this technique also considerably increases the total acquisition time, making it impractical for a number of applications. Modifications of this technique to increase scan-time efficiency include acquiring data at locations that are not affected by cardiac pulsation at times of increased motion (6). The scan time improvement of this approach, however, is subject to the scan geometry used. Alternative strategies include post processing steps for the automatic detection and exclusion of compromised DWI acquisitions (22), or possibly the use of lower b-values to reduce the sensitivity of acquisitions to motion induced artefacts.

Despite compelling findings regarding the susceptibility of DWI acquisitions to CPAs, and considerable investment of research efforts for the development of techniques to alleviate CPAs in DTI, cardiac pulsation induced effects are often disregarded in practical applications. A main reason for this is expected to be the lack of quantitative information regarding the magnitude and frequency, and thus practical relevance, of CPA induced effects in DTI acquisitions. With the proliferation of quantitatively evaluated DTI measures in clinical and biomedical research applications, the debate of whether or not cardiac pulsation induced effects need to be alleviated, or at least accounted for, is likely to become even more important in future.

The main challenge that has thus far prevented the quantitative assessment of CPAs in DTI acquisitions has been that required scan times would be too long to be compatible with *in vivo*

acquisitions, as confirmed in a pilot study (18). To overcome this challenge, this investigation was carried out in two steps; first a comprehensive characterization of CPAs in single DWI acquisitions was undertaken, and subsequently used to inform the design of simulations allowing the quantitative characterization of CPA effects in a routinely used DTI protocol.

For the first step, ADC measurements were recorded over the duration of the cardiac cycle and along different diffusion sensitization orientations. The characterization of CPAs in DWI acquisitions was necessitated by a number of reasons. First, artefact characteristics have been observed to vary across sites (e.g. in (5), (6) and (7)) and thus needed to be independently determined for the scanner used. Second, artefact characteristics that are consistent across volunteers could be accurately quantified here. This was subsequently used to both inform the selection and simplify the design of simulations. Finally, direct comparisons of the effects of IVIM and bulk tissue displacements of constant velocity provide further insight into the mechanisms underlying the induced artefacts.

ADC_z time-course measurements were found to consistently coincide with the initial acceleration phase of PC measurements of tissue motion. The duration of cardiac pulsation-induced effects was consistently found to correspond to approximately 6 % of the heartbeat duration, in contrast to previous studies (6,7) where roughly 20 % of ungated DWI acquisitions displayed effects of cardiac pulsation. Finally although according to PC measurements, the rates of tissue displacement were relatively consistent across volunteers, the magnitude of CPAs was observed to vary considerably more. Time courses for ADC (Figure 2-3, Figure 2-4) closely resemble pulsatile brain movements experienced by the brainstem (3) in both shape and duration.

Investigations into signal attenuations instigated by non-Brownian motion (23-27) have identified a number of attenuation mechanisms that may lead to motion induced signal-void artefacts. Such movement could potentially be linked to unwanted attenuation effects via ghosting (24). In-plane intra-voxel velocity inhomogeneity has also been shown to cause signal voids if motion-induced intra-voxel phase changes exceed π (26). However, while such effects

are expected to be “all-or-none”, overestimations of ADC_x and ADC_y were found to be comparatively small, suggesting that this condition was not met. Alternatively, such findings could be attributed to averaging if attenuation effects were limited to localized regions within the ROI. However, no evidence to substantiate such a hypothesis was found. A further potential source of artefact is presented by the reconstruction technique (23). In partial k-space reconstruction, the boundaries of symmetrically sampled k-space are effectively moved toward the origin. Subsequent phase corrections implicitly assume that phase errors can be characterized within this reduced frequency range. Violations of this assumption have been shown to lead to image artefacts (23,25). Furthermore, phase-correction algorithms generally assume that motion is that of a rigid body. In more complex types of motion (such as pulsatile brain movement), the relationship between the motion experienced and phase change induced may no longer be unique (2).

The second part of this investigation was to estimate the maximum impact cardiac pulsation might have on FA and MD measurements. For this, a modification of Bootstrapping simulations was selected for a number of reasons. These include that Bootstrapping has become an established technique in the evaluation of the scan-rescan variability in DTI datasets. Practical considerations include that the minimum number of measurement repeats required could be met by the experimental setup described. Its model-free approach allows the effect of CPAs to be assessed using a minimum number of assumptions. Although most pertinent assumptions were validated in the characterization of CPAs in ADC time-course measurements of the first sections some were unavoidable, and along with known limitations of this study, are outlined below.

(i) *Motion & co-registration:*

With acquisitions being limited to single slice scans, motion along the slice select orientation could not be corrected for.

(ii) *Prolongation of the effective scan time:*

Bootstrapping combines acquisitions taken at different time points throughout the duration of the scan session. This is likely to prolong the effective acquisition duration of simulated DTI datasets. Effects such as subject motion and scanner drift may therefore exist in larger amounts in the simulated datasets than in their measured counterparts.

Measures to minimize motion effects included padding of volunteers' heads in the RF coil, performing co-registration and reducing motion-induced partial volume effects by averaging values over relatively large ROIs drawn with conservative margins. Manual screening of DTI datasets to detect motion along the slice select direction resulted in the omission of two volunteers from the study. The factors in points (i) and (ii) could not be taken into account in the simulations and therefore must be low enough to be considered negligible. The relatively large difference in magnitude of systolic and diastolic ADC_2s compared to the scan-rescan variability in Figure 2-5, however, demonstrate that cardiac pulsation effects strongly outweigh others such sources of scan rescan variability. The high correlation between simulation and measurement effect indices Figure 2-7 further attest to the quality of simulation results.

(iii) *Two state model of cardiac pulsation induced motion:*

Under the deployed model for cardiac pulsation, measurements are limited to one of two states: that of maximal, and that of minimal motion (taking up 6 % and 94 % of the cardiac cycle respectively).

(iv) *Choice of slice position:*

The positioning of the axial single-slice acquisition was intended to include the region of the brain demonstrating the strongest cardiac pulsation induced effects in FA and MD. This was done using existing knowledge of anatomy, flow effects and impact of cardiac pulsation in Diffusion measurements. While, on this basis, cardiac pulsation induced effects are likely to be representative of the highest observable in the brain, the possibility of other regions experiencing equal or greater effects cannot be excluded.

(v) *Applicability of results to other acquisition setups:*

The magnitude of CPAs presented previously can be observed to differ across sites (5-7). Here, the duration of the observed effect was found to be shorter than was reported in the previous studies. Another factor that may play a role in determining the susceptibility of DWI acquisitions to cardiac pulsation is the scanner field strength (6). Similarly, the use of higher numbers of directions along which motion is measured and/or the deployment of robust DT reconstruction schemes might reduce sensitivity to cardiac pulsation induced effects. An in-depth evaluation and comparison of scanner hardware, acquisition schemes and DT calculations, however, was beyond the scope of this study.

It was observed that cardiac pulsation induced effects may cause artefacts of practical relevance in DTI indices in individuals. In applications based on the quantitative assessment of DTI measures in individuals (e.g. the use of DTI biomarkers for the diagnosis of disease), predictive factors would be extremely valuable in screening individuals for which gating would be advisable. Such factors could include blood pressure, height, BMI, sex, age etc. In this investigation a highly correlated linear relationship was reported between scalar indices representing the magnitude of CPA effects in large populations of simulated DTI acquisitions, and time-course measurements. Such time-course measurements require between 5 and 8 minutes and could thus be performed at the beginning of a scan session for use as an ad hoc predictor of the advisability of gating.

2.5 Literature:

1. Le Bihan D, Mangin J, Poupon C, Clark C, Pappata S, Molko N, Chabriat H. Diffusion Tensor Imaging: Concepts and Applications. *Journal of Magnetic Resonance Imaging* 2001;13(4):534-546.
2. Norris D. Implications of Bulk Motion for Diffusion-Weighted Imaging Experiments: Effects, Mechanisms, and Solutions. *Journal of Magnetic Resonance Imaging* 2001;13:486-495.
3. Greitz D, Wirestam R, Franck A, Nordell B, Thomsen C, Stahlberg F. Pulsatile brain movement and associated hydrodynamics studies my magnetic resonance phase imaging. The Monro-Kellie doctrine revisited. *Neuroradiology* 1992;34:370-380.
4. Soellinger M, Salome R, Boesiger P, Kozerke S. Assessment of human brain motion using CSPAMM. *Journal of Magnetic Resonance Imaging* 2007;25(4):709-714.
5. Nagy Z, Weisskopf N, Deichmann R. Employing Bootstrapping to Examine the Need for Pulse Triggering In Diffusion-Weighted MR Imaging. ISMRM (British Chapter). Birmingham, UK; 2007.
6. Nunes R, Jezzard P, Clare S. Investigations on the efficiency of cardiac-gated methods for the acquisition of diffusion-weighted images. *Journal of magnetic Resonance* 2005;177:102-110.
7. Skare S, Andersson J. On the effects of gating in diffusion imaging of the brain using single shot EPI. *Magnetic Resonance Imaging* 2001;19:1125-1128.
8. Brockstedt S, Borg M, Geijer B, Wirestam R, Thomson C, Holtas S, Stahlberg F. Triggering in quantitative diffusion imaging with single shot EPI. *Acta Radiologica* 1999;40(3):263-269.
9. Pierpaoli C, Marenco S, Rohde G, Jones D, Barnett A. Analyzing the contribution of cardiac pulsation to the variability of quantities derived from the diffusion tensor. ISMRM. Toronto, Canada; 2003.
10. Jones D, Pierpaoli C. Contribution of Cardiac Pulsation to Variability of Tractography Results. ISMRM. Florida, U.S.A; 2005.
11. Jones D. The effect of gradient sampling schemes on measures derived from diffusion tensor MRI: A Monte Carlo study. *Magnetic Resonance in Medicine* 2004;51(4):807-815.
12. Ni H, Kavcic V, Zhu T, Ekholm S, Zhong J. Effects of Number of Diffusion Gradient Directions on Derived Diffusion Tensor Imaging Indices in Human Brain *American Journal of Neuroradiology* 2006;27(8):1776 - 1781.
13. Warach S, Gaa J, Siewert B, Wielopolski P, Edelman R. Acute human stroke studied by the whole brain echo planar diffusion weighted magnetic resonance imaging. *Ann Neurol* 1995;37(2):231-241.

14. Johansen-Berg H, Behrens T. Diffusion MRI. Press A, editor; 2009.
15. Assaf Y. Can we use diffusion MRI as a bio-marker of neurodegenerative processes? *BioEssays* 2008;30(11-12):1235-1245.
16. Moffat B, Chenevert T, Lawrence T, Meyer C, Johnson T, Dong Q, Tsien C, Mukherji S, Quint D, Gebarski S, Robertson P, Junck L, Rehemtulla A, Ross B. Functional diffusion map: a noninvasive MRI biomarker for early stratification of clinical brain tumor response. *PNAS* 2005;102(15):5524-5529.
17. Moffat B, Chenevert T, Meyer C, Mckeever P, Hall D, Hoff B, Johnson T, Rehemtulla A, Ross B. The Functional Diffusion Map: An Imaging Biomarker for the Early Prediction of Cancer Treatment Outcome. *Neoplasia* 2006;8(4):259-267.
18. Habib J, Hlinka J, Sotiropoulos S, Tench C, Auer D, Morgan P. Relevance of Cardiac-Gating in Longitudinal Diffusion Weighted MRI Studies. *ISMRM*. Toronto, Canada; 2008.
19. Mori S, Wakana S, Nagae-Poetscher L, Van Zijl P. MRI Atlas of Human White Matter. Elsevier, editor; 2005.
20. Smith S, Jenkinson M, Woolrich M, Beckmann C, Behrens T, Johansen-Berg H, Bannister P, De Luca M, Drobnjak I, Flitney D, Niazy R, Saunders J, Vickers J, Zhang Y, De Stefano N, Brady J, Matthews P. Advances in functional and structural MR image analysis and implementation as FSL. *NeuroImage* 2004;23:208-219.
21. O'Gorman R, Jones D. Just How Much Data Need To Be Collected for Reliable Bootstrap DT-MRI? *Magnetic Resonance in Medicine* 2006;56(4):884-890.
22. Chang L, Jones D, Pierpaoli C. RESTORE: Robust estimation of tensors by outlier rejection. *Magnetic Resonance in Medicine* 2005;53(5):1088–1095.
23. Robson M, Porter D. Reconstruction as a source of artifact in nongated single-shot diffusion-weighted EPI. *Magnetic Resonance Imaging* 2005;23(6).
24. Chenevert T, Pipe J. Effect of bulk tissue motion on quantitative perfusion and diffusion magnetic resonance imaging. *Magnetic Resonance in Medicine* 1991;19(4).
25. Storey P, Frigo F, Hinks R, Mock B, Collick B, Baker N, Marmurek J, Graham S. Partial k-space reconstruction in single-shot diffusion weighted echo-planar imaging. *Magnetic Resonance in Medicine* 2007;57(5).
26. Wedeen V, Weisskoff R, Poncelet B. MRI signal void due to in-plane motion is all-or-none. *Magnetic Resonance in Medicine* 1994;32(4).
27. Wirestam R, Greitz D, Thomsen C, Brockstedt S, Olsson M, Stahlberg F. Theoretical and experimental evaluation of phase-dispersion effects caused by brain motion in diffusion and perfusion MR imaging. *Journal of Magnetic Resonance Imaging* 1996;6.
28. LeBihan D. Intravoxel incoherent motion perfusion MR Imaging: A wakeup call. *Radiology* 2008;249(3):748-752.

Chapter 3. : DTI on the Post-mortem Brain



Illustration of a post-mortem brain in the purpose designed MRI compatible holder

3.1 Introduction

While diffusion MRI has established itself as a unique and indispensable tool for ascertaining the structural organization and microstructure of fibrous tissue, *in vivo* measurements are subject to a number of inherent practical limitations. Diffusion measurements on post-mortem tissue, which complement *in vivo* acquisitions in a number of ways, as detailed below, have been proposed as a way of overcoming these limitations. On the other hand, however, post-mortem tissue also presents challenges of its own for diffusion measurements. Acquisition protocols and hardware used routinely in clinical practice have thus far achieved inadequate data quality when used in conjunction with post-mortem tissue. Alternative strategies capable of achieving high quality DTI acquisitions in the post-mortem brain have been developed, but typically rely on the use of specialized hardware, acquisition sequences and/or tissue procurement procedures. As a result, their accessibility is limited to specialized research centres.

The aim of this chapter was to experimentally identify, and if possible overcome, limitations that have thus far prevented standard DTI acquisition sequences from being used to acquire DTI of chemically fixed whole human brains under a clinical setting.

3.1.1 Motivation for post-mortem DTI

In this section, the main limitations of *in vivo* DTI and anticipated opportunities of post-mortem DTI are outlined.

Limitations of single-shot DTI acquisition sequences

The presence of subject motion and total scan time constraints limit the number of suitable acquisition sequences that can be used for *in vivo* DTI. The most prevalently used is single-shot EPI due to its high acquisition speed, which allows both, the overall acquisition time and motion occurring during an acquisition, to be effectively reduced.

Single-shot acquisition sequences, however, also impose intrinsic resolution limits at a given FOV, and suffer from a high susceptibility to bandwidth related artefacts.

The use of post-mortem tissue effectively eliminates motion and relaxes total scan-time constraints, thus allowing DTI acquisitions to be based on a wider range of sequences. Resulting improvements in the achievable data quality (e.g. higher resolutions, lower distortion etc.) may thus provide novel insights into the microstructure and structural organization of brain tissue.

Practical limitations of in vivo DTI

Although the calculation of a 3D diffusion tensor requires a minimum six acquisitions of non-collinear diffusion weighting, at least 20 acquisitions (2) have been recommended to improve the precision and accuracy of diffusion estimations. Increasing the directional resolution of DTI acquisitions, however, demands longer total scan times. In practical applications, the scan time is limited by both legal regulations (e.g. <http://www.icnirp.de/documents/emfgdl.pdf>), and the ability of a subject to keep still. Although the use of single-shot acquisition sequences can reduce the susceptibility of individual acquisitions to subject motion, it cannot eliminate it. Motion occurring during the acquisition of a single image may result in image artefacts including ghosting and even signal dropout (3). Motion occurring between acquisitions comprising a composite DTI dataset may result in misalignment of corresponding voxels. The impact of subject motion on data quality, and the statistical power of results, is evidenced by observed improvements when DTI acquisitions are performed in conjunction with motion reduction techniques, such as anaesthetization and motion restraining devices (4).

Complexity of diffusion properties and tissue microstructure

The interaction between thermally excited protons and neuronal tissue is highly complex, depending not only on the intricate microstructure of the tissue, but also its biochemical properties. Consequently, inferring the structural organization, bio-physiological properties and pathological changes of tissue from DTI measurements is

an inherently ill-posed task (5). Consequently, the interpretation and biophysical implications of measurable DTI indices is topic of ongoing research (5). These efforts, however, are constrained by limitations in the quality and amount of data that can be collected in *in vivo* DTI experiments as outlined in the previous two sections. To resolve crossing fibres and/or attain insights into the micro-structural composition of tissue, higher order diffusion measurements relying on higher directional resolutions and/or higher numbers of b-values (e.g. diffusion spectrum imaging (DSI), High Angular Resolution Diffusion Imaging (HARDI) etc. (5)) have been proposed. The lengthy scan times required by these techniques, however, limit their practical applicability *in vivo*. Another important limitation in the interpretation of *in vivo* measurements of diffusion is the inability to directly correlate diffusion properties with histology. Currently, the development of DTI indices as biomarkers of disease is typically driven by comparisons of previously selected diffusion properties in a cohort of patients and healthy volunteers, and/or by correlating it with a scale of disease related impairments. The ability to accurately characterize diffusion using higher order diffusion MRI measurements, and to directly compare results with histology could provide a more sensitive means of detecting pathological changes while potentially also facilitating the development of optimized diffusion metrics. Improved insights into this relationship could thus prove pivotal in the development of novel diffusion measures and the interpretation of results.

The above considerations highlight the highly complementary role that could be played by post-mortem DTI as a tool for facilitating the development of DTI.

3.1.2 Challenges of post-mortem MRI

This section presents a summary of the main limitations of post-mortem MRI, as well as measures that have been proposed to address them.

Post-mortem tissue degradation

Tissue degradation after death presents a main challenge for post-mortem MRI. Resulting changes in NMR signal characteristics and tissue microstructure, may potentially reduce the comparability of *ex vivo* and *in vivo* tissue. This results in part from autolysis, where intracellular enzymes cause the breakdown of proteins and the self-destruction of cells, and bacterial degradation, which is brought about by bacterial proliferation in the dead tissue. Together, these processes lead to the eventual liquefaction of cells (6). Chemical fixation aims to preserve cells and tissue constituents in as close a life-like state as possible (6,7), and is used to inhibit this post-mortem tissue degradation.

In studies with animals, tissue is fixed either by submersion of the tissue in a fixative solution (immersion fixation) immediately following death, or even pre-mortem via the intra-cardiac perfusion of fixative solutions (known as perfusion fixation) (8). In the case of humans, the latter can, of course, not be used. In addition, the removal, refrigeration and eventual immersion fixation of human tissue is typically delayed by several hours to a few days for a number of practical reasons including family grieving and logistics (8,9). This time between somatic death and immersion fixation is known as the post-mortem interval (PMI).

The length of the PMI also has been found to affect the signal relaxation and diffusion properties of post-mortem tissue, although these findings have not always been consistent, as described below.

The effect of PMI on T1 and T2

Reports on changes in T1 and T2 of post-mortem tissue with increasing PMI are conflicting; while a number of investigations have observed T1 and T2 reductions in nervous tissue with increasing PMI (10-12), significant increases have also been reported (8,9,13). Shepherd et al. commented on the methodology used to measure the effects of PMI, which generally involved fixing tissues at different PMIs and

subsequently evaluating the change on T1 and T2 of samples still immersed in fixatives. It was suggested that the decrease in T2 seen by other groups was caused by bulk free fixative solution, and could be reversed by washing the brain overnight in phosphate buffered saline (PBS) (13).

The effect of PMI on the Apparent Diffusion Coefficient (ADC) and Mean Diffusivity (MD)

At death, ADC in the brain declines by 30-50 % of the *in vivo* value, and studies have shown that the ADC continues to decrease significantly with increasing PMI (6,7). It has been suggested that this decrease may, at least in part, be due to the reduction in temperature of the imaged *ex vivo* tissue when compared with tissue imaged *in vivo* (37 °C to 20 °C) (13,14). A study of water diffusion in *Xenopus* oocytes at constant temperature found only a 6 % reduction in ADC after the formaldehyde-fixed oocytes were washed (15), corroborating this hypothesis, whilst also demonstrating the presence of a temperature independent change in ADC.

Reductions in the MD of post-mortem tissue have also been extensively reported (6-9,16,17), with changes seen to occur as soon as 6 hours post-mortem (8,9). This reduction has been attributed to changes in membrane permeability and the redistribution of magnetization between compartments (8,9).

Effects of PMI on Fractional Anisotropy (FA)

There is also no consensus in the literature on the effects of increasing PMI on the FA in grey and white matter; it has been seen to both decrease (6-9) and increase (18).

Chemical fixation of post-mortem tissue

Protocols for fixation aim to achieve rapid cessation of metabolic activity and irreversible structural preservation for subsequent MRI experiments. Commonly used fixatives, such as formaldehyde, typically achieve tissue fixation by cross-linking protein amine groups via methylene bridges, thus rendering tissues structurally stable (13). The action of aldehyde fixation on the cross linking of proteins throughout the tissue alters

the local chemical environment. Diffusion properties are sensitive to such changes and may thus be affected by fixation. In addition, the cross-linking of membrane proteins to each other may impact the integrity and permeability of the cellular membranes. These biophysical changes to the tissue microstructure may alter MRI contrast mechanisms and must be considered when extrapolating results of post-mortem to *in vivo* MRI data (13).

The effect of chemical fixation on T1 and T2

Previous studies on rat and human neuronal tissue have demonstrated a reduction in T1 and T2 following the immersion fixation of tissue with 4 % formaldehyde solutions (10-12,19-23). This has been attributed to the direct effect of the formaldehyde solution itself (13,21), also to the dehydration of tissues fixed in formaldehyde (21).

The effect of chemical fixation on MD

Studies have also suggested that chemical fixation leads to a decrease of 30 % or more in the MD of water in nervous tissue (16, 24-26). As with PMI, however, this decrease may potentially be attributable to the reduced temperature at which post-mortem tissue is acquired (13-15).

The effect of chemical fixation on FA

To date, findings regarding the effects of fixation on diffusion anisotropy suggest that, despite postulated changes in cell membrane permeability (13), only slight decreases (25) or no changes (16, 19, 24, 26) in diffusion anisotropy can be expected between fixed and *in vivo* tissue.

In summary, PMI, chemical fixation and tissue preparation procedures have been reported to affect both tissue diffusion and signal relaxation characteristics. Details regarding the precise effects of fixative solutions on the tissue microstructures and MRI signal properties, however, remain sparse, and observed effects are often conflicting. Despite the widespread use of chemically fixed tissue samples for high-resolution MRI

studies, no optimal tissue procurement and preparation procedure has yet been formulated.

3.1.3 Previous experience with post-mortem DTI

In light of the potential benefits of performing DTI on post-mortem brain tissue, a number of attempts have been reported in literature. In this section the various approaches that have been used are summarised, and their advantages and disadvantages highlighted.

DTI on the chemically fixed whole human post-mortem brain using in vivo sequences

The detrimental implications on diffusion measurements, of the aforementioned effects of PMI and fixation on tissue and signal characteristics, were evidenced by the poor data quality of initial DTI maps acquired on chemically fixed whole human post-mortem brain. Acquisition protocols in early investigations (17, 27, 28) were limited to large slice thicknesses (5-6 mm), only 6 diffusion-encoding directions and b-values of 1000 s/mm², but nevertheless resulted in poor image quality. Using an acquisition protocol applicable for *in vivo* DTI, Pfefferbaum et al. reported negative results (12). The primary cause for this was hypothesized to be insufficient SNR as a consequence of increased rates of T2 signal relaxation (12), and tissue dehydration (21) by aldehyde fixative chemicals.

The failure to obtain high data quality DTI images of the chemically fixed whole human post-mortem brain using *in vivo* sequences led to the development of alternative strategies, which were implemented with greater levels of success. These are described below:

Post-mortem DTI on small bore scanners

Most experience in post-mortem DTI and tractography is on small animal brains or sections of nervous tissue. This allows the use of high field strength scanners to maximize the recordable signal, and powerful gradient coils allowing high levels of diffusion weighting to be achieved within short echo times. However, while animal

models of disease (e.g. (29, 30)) have found widespread application, these may not always be directly transferrable to human anatomy (31).

DTI of whole human un-fixed post-mortem brain

An alternative approach is to use unfixed post-mortem brain specimens (32). To alleviate the detrimental effects of PMI, acquisitions were performed within a time-window of six to ten hours post-mortem, during which signal properties are still well preserved (32). One advantage of this technique is the effectively reduced PMI when compared with immersion-fixed whole human brains. This is because the slow rate of aldehyde fixative penetration, found to be 0.5 to 1 mm/h at room temperature (31), suggests that the effects of PMI would likely be more pronounced, especially in deep tissue regions, of an immersion fixed human brain. Additional advantages include the compatibility of this technique with standard DTI sequences, and the elimination of potential confounding effects of fixation. The specific and limited time-window during which acquisitions can be performed, however, also gives rise to a number of limitations and practical challenges. These include the availability of the necessary infrastructure to extract and scan the brain within just six hours after death, the limited time available for scanning, the recruitment of highly motivated subjects and ethical justification.

DTI on the chemically fixed whole human post-mortem brain using specialised sequences

A final approach saw the development of specialized acquisition sequences to address the challenges posed by chemically fixed post-mortem whole human brain specimens (33, 34). To this end, the highly SNR-efficient multi-shot 3D EPI (34) and SSFP (33) sequences, with b-values of 3000 s mm^{-2} were proposed. This allowed high levels of data quality and spatial resolutions of 0.73^3 mm^3 (isotropic) to be achieved, even displaying apparent anisotropies in the grey matter.

As in the case of the approach using unfixed brains (32), however, the practical requirements for the use of specialised sequence may prove prohibitive for a large segment of clinical and research centres. Both acquisition protocols were based on

specialized acquisition sequences that are typically not available on a standard clinical scanner. Furthermore, data obtained with SSFP needed to undergo specific post-processing steps to calculate the diffusion tensor. The implementation and use of such sequences would thus require the availability of appropriate expertise, and investments of time and labour. The required scan time, which in the case of (34) exceeded 99 hours also requires the availability of a scanner for such a prolonged period of time. Finally, the applicability of the proposed acquisition sequences to *in vivo* acquisitions is limited by their long acquisition times and sensitivity to bulk motion. This adds an additional potential confounding factor when comparing results with *in vivo* acquisitions and literature.

3.1.4 Purpose of this study

In summary, while a number of studies have been dedicated to investigating the effects of PMI and chemical fixation on MRI signal characteristics, reported findings display considerable disparities. These may be the result of the specific experimental setup or tissue procurement procedures used. Attempts to acquire DTI in chemically fixed whole human post-mortem brain specimens using standard acquisition sequences (18, 33, 34, 13) have to date not been successful in achieving levels of data quality comparable to *in vivo* acquisitions. This was hypothesized to be result of insufficient SNR levels resulting from tissue dehydration and/or increased rate of T2 decay (12, 21). Although to the best of our knowledge, this hypothesis has never been validated experimentally, it appears to have received widespread acceptance. This is evidenced by the focus on the maximization of SNR in investigations developing DTI acquisition protocols for post-mortem brain specimens.

While a number of these strategies were indeed successful in recording DTI data of high quality, their emphasis on achieving high SNR typically make them inaccessible and incompatible with requirements of a typical clinical setting. For instance high field small-bore MRI scanners (28, 29) are often not available and are not suitable for whole human brain scans. Tissue procurement steps that require brain specimens to be scanned

within hours of death (35) require flexible scanner availabilities, appropriate logistics, ethical justification and highly motivated volunteers. Similarly, specialized acquisition protocols and post-acquisition processing steps that require appropriate expertise, acquisition sequences and scanner availabilities (36, 37) are generally not feasible in routine clinical practice. This limits the use of DTI on post-mortem brains to a small selection of centres with available expertise and resources, and thus poses a significant bottleneck in utilizing this technology to its full potential. Also, the use of acquisition sequences incompatible for use *in vivo* could pose a challenge for the translation of findings to *in vivo* measurements. Nevertheless, these investigations have effectively demonstrated the principle feasibility of DTI in post-mortem brain tissue, as well as provided insights into the conditions under which DTI data of high quality can be recorded successfully.

The aim of this investigation was to identify, characterise and, where possible, overcome factors that have prevented the acquisition of adequate quality DTI data of the chemically fixed whole human brain, using clinical sequences, scanners and time-frames. These factors will henceforth be referred to as potential 'critical limiting factors.

3.1.5 Structure of this chapter

As alluded to above, the main challenge in this investigation is posed by a combination of the anticipated long acquisition times needed to overcome hypothesized SNR limitations, and the sheer number of additional potential factors that that may contribute to observed losses in data quality. The latter results from the lack of coherent information on the detrimental effects of death and tissue fixation on signal characteristics, the optimum acquisition protocol settings, and the minimum requirements to achieve adequate DTI data quality in post-mortem brain specimens.

The strategy pursued in this study was to compare and contrast the performance of a routinely used clinical acquisition sequence, with the most closely related acquisition protocol that has been successfully used to record DTI in the chemically fixed whole human post-mortem brain. This latter sequence will henceforth be referred to as the

"benchmark protocol" in this chapter. By using identical parameter settings wherever possible, the list of potential critical limiting factors was effectively narrowed down to include only those acquisition parameters that differed significantly.

The investigation was performed in two parts. First, a framework was defined, where stipulations that must be met in order for the developed protocol to be considered compatible with a clinical environment were defined, and the potential critical limiting factors identified. In the second part, dedicated practical experiments were performed, in which each of the potential critical limiting factors was tested in turn to establish its contribution to losses in data quality in post-mortem DTI acquisitions. Wherever appropriate, strategies towards the alleviation of these factors were proposed and practically assessed.

3.2 Materials & Methods

3.2.1 Post-mortem brains & pre-acquisition preparation steps:

Post-mortem brain selection

In total, three post-mortem brains were used in this investigation. In compliance with the ethical approval this project was performed under, post-mortem brain donors suffered from neurological disorders. Case specific details (such as PMI, time since fixation, cause of death, age of patient etc.) were not available. For the comparison of brain anatomies, T1 weighted anatomical acquisitions are illustrated in Figure 3-1 below.

Post-mortem brain fixation

Fixation was performed after a post-mortem interval (PMI) of typically 4 days by submersing the brain in 4 % formalin for a time span of 6 weeks.

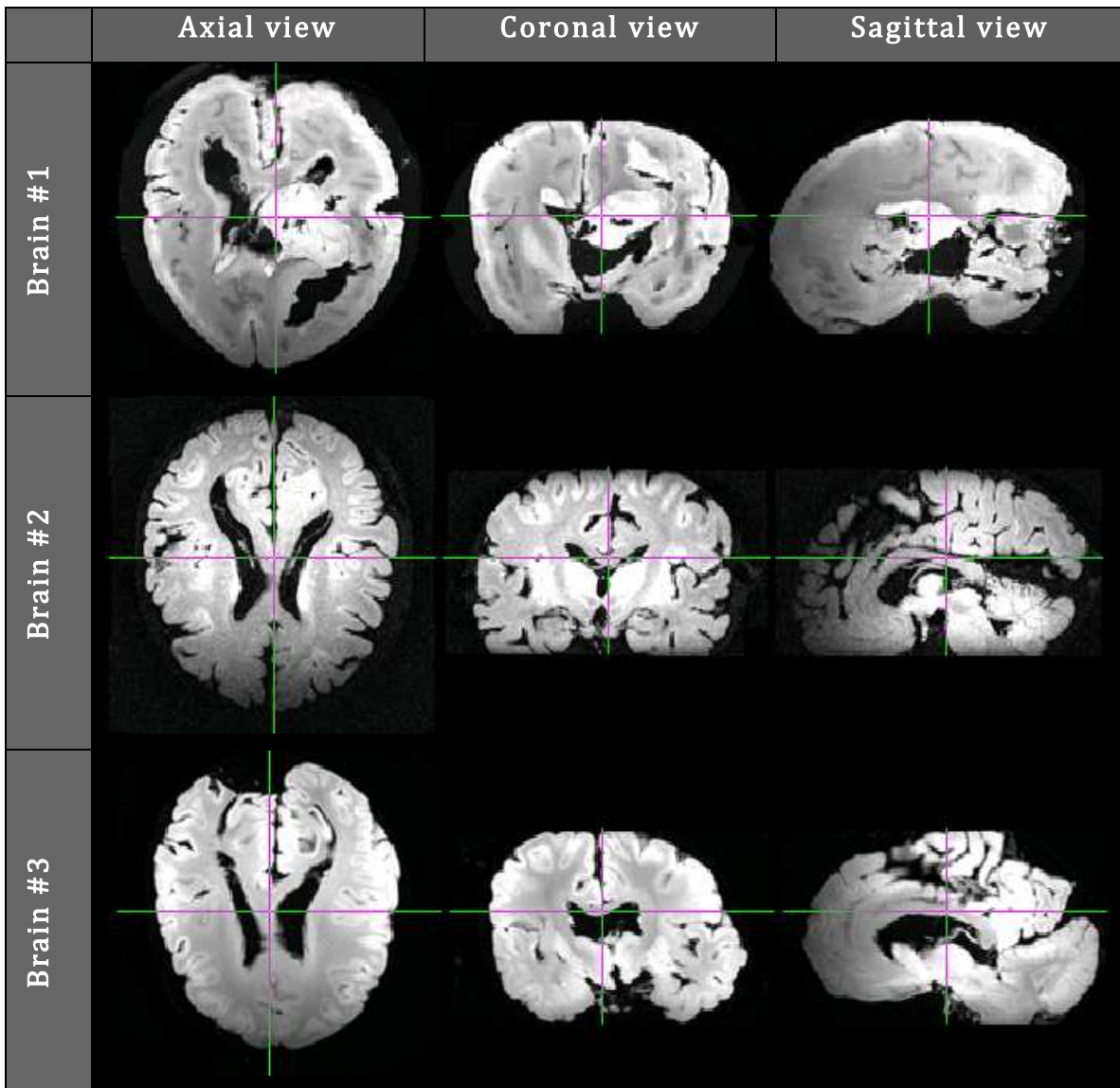


Figure 3-1 Depiction of T1 weighted anatomical scans (using an MPRAGE protocol) of the post-mortem brains used in this investigation.

Pre-scan post-mortem brain preparation:

Prior to placing the post-mortem brain in the scanner, a number of preparatory steps were taken to allow the specimen to remain in the scanner for long periods of time, and improve the quality of acquisitions. To preserve the structural integrity of the brain, extreme care was taken when handling the specimen during all steps of the preparation.

As a preliminary step to prepare formalin fixed brains for scanning, they were washed for 24 hours in tap water. This had the dual advantage of facilitating rehydration and reducing formaldehyde-induced T2 shorting. The brain was then placed into an MR compatible holder, comprising two hemispheres, as illustrated in Figure 3-2. The brain was placed top-down into the bottom hemisphere, with the occipital lobes aligned with the position of the plastic screws, (label 3.a and 3.b in Figure 3-2). This facilitated the subsequent identification of the orientation of the brain in the holder when positioning it in the scanner. Blu-tack® was placed along the rim of the hemispheres (as illustrated in Figure 3-2) to provide a watertight seal. The holder was closed by joining the rims of both hemispheres, which were then fastened using plastic screws. 10 % (w/v) saline solution, prepared using 99 % pure NaCl and distilled water, was filled through a hole in the top hemisphere (label 2 in Figure 3-2). This opening was subsequently sealed using a plastic screw. The holder was finally wrapped with cling film to provide external pressure on the Blu-tack® thus improving the seal.

Air pockets within the brain tissue were unavoidable and introduced magnetic field inhomogeneities at the tissue-air interface. The high sensitivity of EPI acquisitions to magnetic field inhomogeneities could potentially result in significant distortions and signal dropout. The holder was carefully rotated in all directions for about 20 minutes to facilitate the escape of air thus minimizing air pockets. Displaced saline solution was refilled to replace the volume of air in the holder. Finally, the brain was placed into the RF-coil of the scanner and left there for an hour before Diffusion acquisitions were performed. This was to allow for the brain tissue to settle, thus reducing any residual motion that may occur between acquisitions.

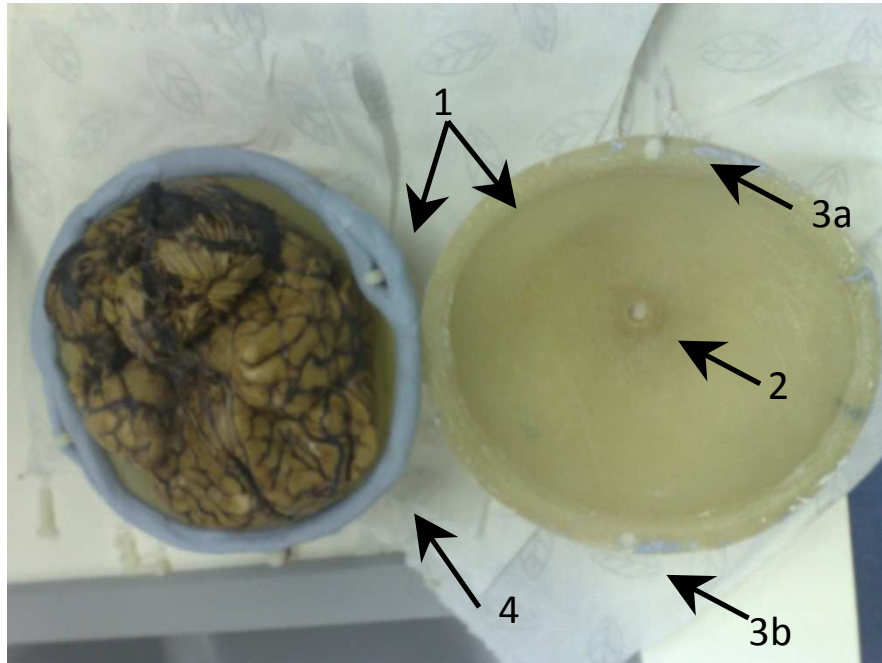


Figure 3-2 Depiction of the post-mortem brain in the holder including labelled part descriptions (pictured: Brain #1); Image labels: 1: the brain holder comprising two oval half-shells; 2: the hole through with saline solution was filled to submerge the brain; 3a,b: the two half-shells were joined together by means of two plastic screws; 4 Blu-tack formed a water proof barrier between the two half-shells (1).

3.2.2 Datasets

Identification & characterization of potentially critical limiting factors (Datasets 3-1):

Purpose:

The purpose of Datasets 3-1 was to assess if, and under what acquisition parameters, SNR sufficiency could be achieved for the purpose of post-mortem DTI of the fixed, whole human brain. To the best of our knowledge, insufficient SNR to date represents

the only hypothesized critical limiting factor for chemically fixed whole human post-mortem brain specimens acquired under a standard *in vivo* acquisition protocol.

The assessment of SNR sufficiency was based on both, the rate of transverse signal decay of the white matter of a locally procured brain specimen on the local scanner (Dataset 3-1a), and on the SNR performance of the acquisition protocol (Datasets 3-1b – 3-1e).

Acquisition details:

Dataset 3-1a: T2, and T2 quantification (Brain #1)*

Dataset 3-1a was used to measure the transverse signal relaxation rates (T2, T2*) of a locally procured tissue sample (Brain #1) using the GESE protocol (35,36). This protocol has the advantages of providing both T2 and T2* measurements, and being developed and tested on the local MRI system.

Acquisitions were recorded with a repetition time of 2000 ms and an echo time of 55 ms at time increments (ΔT) of 1.43 ms. An in-plane FOV of 256 x 256 mm was used with a 1mm in-plane resolution and a slice thickness of 3 mm.

T2 and T2* values averaged over ROIs corresponding to anatomical white matter regions (illustrated in Figure 3-3) were evaluated using in-house software.

Dataset 3-1b - Dataset 3-1e: SNR measurement (agar phantom)

In Datasets 3-1b to e the SNR of a selection of non-diffusion weighted EPI-based acquisitions was measured. This was to inform the development, and subsequent validation of an equation to predict the effects of not only different acquisition protocol parameters, but also across pertinent acquisition sequence differences (i.e. single-shot vs multi-shot, 3D EPI vs 2D EPI) on measurement SNR.

SNR quantification was performed using the multiple acquisition (MA) method (37) for accuracy. For this, 40 acquisition repeats are performed consecutively without re-calibration steps. The first ten acquisition repeats were omitted to ensure steady state. The SNR was measured within an ROI of 10 x 10 x 3 voxels in the centre of the phantom to minimize effects such as B1 inhomogeneities and EPI ghosting.

Parameter	Dataset 3-1b (single-shot 2D EPI)	Dataset 3-1c (multi-shot 3D EPI)	Dataset 3-1d (single-shot 3D EPI)	Dataset 3-1e (high resolution single-shot 2D EPI)
Scanner	SPMMRC 3 T	SPMMRC 3 T	SPMMRC 3 T	SPMMRC 3 T
Repetition time (in ms)	500	100	500	500
Echo times (in ms)	19	11	17	42
EPI factor	91	31	91	181
Field of view (in mm)	182 x 182 x 84	182 x 182 x 84	182 x 182 x 84	182 x 182 x 84
Matrix	92 x 92	92 x 62	92 x 92	181 x 182
Slice thickness (in mm)	21	21	21	42
Number of slices	4	4	4	2
Number of signal averages	1	1	1	1
SENSE reduction factor	No	No	No	No
Bandwidth (Frequency encode dir)	2953.3	1761	2953	2092
Bandwidth (Phase encode dir)	15.4	37.6	15.4	5.5
Relative signal level	100 %	100 %	100 %	100 %
12:42	05:05	01:01	07:10	12:42

Table 3-1 Acquisition parameters listing for Datasets 3-1b - Datasets 3-1e.

3.2.2.1 *(Optimization (Datasets 3-2))*

Purpose:

Dataset 3-2 was recorded for the optimization of the single-shot 2D EPI sequence for DTI measurements of the chemically fixed whole human post-mortem brain.

Acquisition details:

Dataset 3-2a: First high SNR acquisition protocol (Brain #2)

This dataset was acquired under parameters as similar as possible to that of the benchmark study (34) in order to minimize the number of potentially limiting factors.

The total acquisition duration was limited to 24 hours, in accordance with stipulations to achieve compatibility of the developed acquisition protocol with a clinical environment (defined in Section 3.3.1). To assess the suitability of the various available averaging strategies in overcoming anticipated potential scanner instabilities over such an extended period of time, three common strategies for averaging data were employed:

Online signal averaging:

This type of averaging is arguably the most prevalent in routine clinical practice. The user sets a scan parameter (NSA) and is provided with a single already averaged dataset. No calibration or post-processing steps are performed prior to averaging corresponding acquisitions. The omission of recalibration steps makes this type of averaging time-efficient and ensures that individual acquisitions are recorded under identical calibration settings. *The potential disadvantage of this technique is that the lack of access to individual acquisitions prior to averaging prevents transient scanner instability-induced effects from being reduced through post-processing or dataset omission.*

Set averaging:

This technique refers to the acquisition of individual (NSA=1) datasets that may subsequently be averaged offline. Advantages of this approach include that each

dataset is preceded by calibration steps ensuring optimal acquisition quality, and that produced images can be post-processed prior to averaging. The anticipated disadvantages include that scanner recalibration and image-processing steps may effect unwanted changes in voxel intensity levels between subsequent acquisitions. Expected low diffusivity levels in post-mortem tissue at room temperature may exacerbate the susceptibility of measurements to such minute changes. A practical limitation is posed by the significant increase in scan time due to calibration steps, consequently reducing the number of signal averages that may be achieved over a given scan time. A further practical limitation on the in-house MRI system was the limited number of sets that could be placed in a study acquisition queue, which represents a list of scans that can be acquired automatically. Once a full scan queue had been acquired, subsequent scans would have to be recorded as part of a new study, which requires the presence of a scanner operator and the repositioning of the sample.

Dynamic scan averaging:

This type of averaging combines the attributes of both previously described techniques. Dynamic scans refer to the acquisition and output of individual scans, but without recalibration steps between them.

Dataset 3-2.b: Evaluating alternative signal averaging strategies (Brain #2)

In Dataset 3-2.b an alternative acquisition ordering scheme⁴ was tested to reduce the impact of scanner instabilities on DTI data recorded over extended periods of time. Instead of acquiring data as multiple sets of individual 4D DTI datasets for subsequent averaging, here, stacks of slices with identical diffusion sensitization directions were acquired and averaged first, before moving on to stacks of images with different diffusion weighting gradients. This ensured that the least possible time passed between recordings of identical acquisitions, thus improving the scan-rescan precision of

⁴ On the in-house Philips Achieva system, the appropriate acquisition parameter option was termed ‘average high b-values’ which allowed the user to specify up to 10 signal averages.

measurements. No re-calibration steps are performed in this type of averaging and up to 10 signal averages may be recorded under this regime.

Dataset 3-2.c: Optimization of Eddy-current distortion correction (Brain #3)

To alleviate the effects of Eddy-currents imposing diffusion sensitization gradient specific distortion patterns in images comprising the DTI dataset, the (38) reversed gradient method was implemented. To this end, consecutive datasets were acquired with reversed phase encode orientations.

Dataset 3-2.d: Fast, high resolution DTI acquisition protocol (Brain #3)

Following the optimization of the DTI acquisition protocol (Dataset 3-2c), Dataset 3-2d was recorded to assess the data quality achievable under identical acquisition parameters apart from using double the through plane resolution, and only a single acquisition set (total scan duration 21 min 15s).

Acquisition parameters for Dataset 3-2 a - d are listed below in Table 3-2.

Parameter	Dataset 3-2a	Dataset 3-2b	Dataset 3-2c	Dataset 3-2d
Scanner used	SPMMRC 3 T	SPMMRC 3 T	SPMMRC 3 T	SPMMRC 3 T
Brain specimen #	3	4	4	4
Repetition time (in ms)	10 000	3000	3000	3000
Gradient mode	'enhanced' gradient mode (80 mT m ⁻¹)	'maximum' gradient mode (40 mT m ⁻¹)	'enhanced' gradient mode (80 mT m ⁻¹)	'enhanced' gradient mode (80 mT m ⁻¹)
Echo times (in ms)	62	90.76	64	64.24
Field of view (in mm)	172 x 172	224 x 224	224 x 224	224 x 224
Matrix	86 x 86	112 x 112	112 x 112	112 x 112
Slice thickness (in mm)	2	4	4	2
Number of slices	19	19	19	19
Diffusion scheme	Philips 15 direction scheme	CAMINO 61 direction scheme	CAMINO 61 direction scheme	CAMINO 61 direction scheme
b-values (in s mm ⁻²)	3000	3000	3000	3000
Number of signal averages	10	1	1	1
Number of dynamics	6	1	1	1
Number of dataset repeats	3	25	62	1
Number of individual b-value averages	1	10	10	10
SENSE reduction factor	2	2	2	2
Water-fat shift (in pixels)	31.56	14.11	18.27	18.27
Acquisition duration (minutes) per set	07:40:30	0:20:22	0:20:59	0:21:15
Total acquisition duration	23:01:30	8:29:21	21:41:19	0:21:15

Table 3-2 Acquisition parameters listing for Datasets 3-2a - Datasets 3-2d.

3.3 Results

The purpose of this investigation was to both identify and, if possible, overcome the potential critical limiting factors that have thus far prevented the achievement of adequate data quality in DTI acquisitions of chemically fixed whole human brain specimens in a clinical setting. This investigation is structured into two sections. In Section, 3.3.1, the framework for subsequent practical measurements is established. This includes designing a starting protocol that meets defined requirements to achieve compatibility with a typical clinical setting, and the identification of potential critical limiting factors. In the second part of this investigation, Section 3.3.2, dedicated acquisitions are performed to assess the significance of each potential critical limiting factor on data quality losses and, wherever appropriate, to evaluate efficacy of techniques proposed for their alleviation.

3.3.1 Study design

Stipulations for post-mortem DTI in a clinical setting

To meet the requirements of a clinical setting, three stipulations were defined for the acquisition protocol being optimized in this study. First, 2D single shot EPI sequences, prevalently used for *in vivo* acquisitions, were to be employed. Second, the total scan time was to be limited to 24 hours. This would allow DTI acquisitions to potentially be performed in the downtime during weekends so as to not interfere with clinical scans. Ideally, however, total scan times were to not exceed 8 hours, which would allow a whole brain specimen to be scanned overnight. Finally, the minimum acceptable resolution was defined as $2 \times 2 \times 4 \text{ mm}^3$.

No major changes to the standard post-mortem brain procurement procedure were to be undertaken. It must be mentioned at this point, that these procedures at the local hospital allowed for PMIs of typically four days. This may result in relatively high levels of tissue decomposition, thus potentially making the optimization task challenging.

Selection of a 'benchmark' acquisition protocol

Due to the considerable number of acquisition parameter settings that may either directly or indirectly affect DTI data quality, and the anticipated long acquisition times required to achieve sufficient SNR, the identification of potential critical limiting factors needed to be streamlined. To this end, a benchmark acquisition protocol using a specialized acquisition sequence that has been shown to produce high quality DTI data in chemically fixed whole human brains was selected from literature. By adopting, wherever possible, the acquisition parameter settings of this benchmark protocol, and neglecting potential differences in scanner performance, potentially critical limiting factors could effectively be limited to those acquisition parameters that could not be replicated.

Two DTI acquisition protocols, using multi-shot 3D EPI (33, 34) and SSFP (36) sequences respectively, have thus far been used successfully to acquire DTI maps of chemically fixed whole human brain specimens. The 3D EPI multi-shot based acquisition protocol by McNab et. al. (34) was selected as the benchmark protocol due to its close relation to the 2D single shot spin echo EPI DTI sequence that was to be optimized in this study.

Specification of a starting protocol

A 'starting' acquisition protocol meeting all stipulations for compatibility with a clinical setting was designed, with acquisition protocol parameters set as similarly as possible to those of the benchmark protocol. A list of pertinent acquisition parameter settings of the proposed starting protocol, and corresponding settings for the benchmark protocol are tabulated below in Table 3-3.

Parameters	Proposed starting protocol	Benchmark protocol (34)
Scanner setup:		
Sequence	Single-shot 2D EPI	Multi-shot 3D EPI
Geometry:		
EPI factor	≈ 85	32
Voxel volume	2 x 2 x 2 mm ³	0.73 x 0.73 x 0.73 mm ³
Slab thickness (per excitation)	2 mm	140.2 mm
In-plane phase-encode steps	86	254
Through-plane phase-encode steps	1	192
Bandwidth	≈ 868 Hz/pixel	820 Hz/pixel
Diffusion parameters		
Number of non-collinear diffusion directions	15	64
Acceleration		
Parallel Imaging	2	1
Timings & averaging:		
TE	≈ 62 ms	114 ms
TR	10000 ms	670 ms
Total number of 3D images acquired (NSA ^{**})	≈ 8280	347
Acquisition time	24 (or preferably 8) hours	99 hours, 11 minutes

Table 3-3 Comparison of pertinent acquisition parameters of the benchmark and starting DTI acquisition protocol (Dataset 3-2a).

^{**} Due to the composite nature of diffusion acquisitions averaging can be performed either by acquiring diffusion sensitized data along more non-collinear directions or by acquiring and directly averaging identical acquisitions. No differentiation between these techniques was made here, however, and the number of averages was calculated as the total number of acquisitions recorded.

Identification of potential critical limiting factors

As mentioned above, acquisition protocol settings of the benchmark protocol (34) that could not be replicated in the starting protocol (Dataset 3-2a), were considered potential limiting factors and were thus investigated further using dedicated experiments. Accordingly, the following three acquisition characteristics were identified:

(i) The SNR

The benchmark acquisition protocol by McNab et. al. (34) employed a 3D EPI sequence to record, and subsequently average data over a duration of more than 99 hours.

By exciting thicker slabs of tissue, the SNR efficiency of 3D acquisition sequences can be increased over their 2D counterparts. This is because the total signal intensity produced by each excitation increases with the volume of the excited slab, while the noise contribution depends on the FOV of the RF-receiver coil, and thus remains constant. The long acquisition times and thus high numbers of averages used in (34), could also not be replicated due to practical considerations of scanner availability.

On the other hand, by reducing the spatial resolution ($0.73 \times 0.73 \times 0.73 \text{ mm}^3$ for the benchmark vs. $2 \times 2 \times 2 \text{ mm}^3$ for the single-shot 2D EPI sequence being optimized) SNR may be regained. In addition, effects of longitudinal signal relaxation must be considered when using a 3D spin echo acquisition sequence as proposed by (34). The use of a 90° excitation pulse requires adequately long repetition times in order to avoid acquisition SNR reductions due to signal saturation. In 2D multi-slice acquisition protocols, alternate slices can be recorded during the time between consecutive acquisitions, effectively achieving at least partial compensation of the difference in SNR efficiency between 2D and 3D acquisitions.

(ii) Susceptibility to image distortion

As a result of the typically low receiver bandwidths along the phase encode direction, EPI acquisitions generally display a high sensitivity to magnetic field inhomogeneities. These can lead to distortions and even signal voids. By allowing reductions in echo train

length, multi-shot sequences can achieve higher receiver bandwidths, affording lower susceptibilities to bandwidth related artefacts.

(iii) Temporal stability

Acquisition times in excess of 99 hours as used in (34) could not be replicated locally for practical reasons. Apart from implications of such long acquisition times on the achievable SNR, it may also influence the required temporal stability of acquisitions. While the temporal stability of the MRI system over the relatively short acquisition times used for *in vivo* DTI (typically 5 to 20 minutes) has been found adequate, anticipated SNR limitations suggest that longer scan times may be necessary in post-mortem applications. The impact of temporal instabilities, in turn, may be alleviated through averaging sufficiently large numbers. The adequacy of scanner stability for DTI acquisitions lasting between the stipulated 8 and 24 hours may have to be independently established.

In the following sections, experiments pertaining to the evaluation of each of these acquisition characteristics are outlined in turn.

3.3.2 Practical assessment and alleviation of potential critical limiting factors

Assessment of SNR sufficiency of the 2D single-shot SE EPI sequence

Of the three potential critical limiting factors identified in Section 3.3.1, SNR was investigated first. This allowed the widely accepted hypothesis that SNR posed the main obstacle preventing the use of standard *in vivo* DTI acquisition sequences for use on chemically fixed post-mortem brains to be tested at the onset. In addition, it also allowed the maximum acquisition resolution and required number of averages in all subsequent acquisitions to be specified.

As outlined in the introduction, the levels of diffusivity in post-mortem tissue are reduced by changes in tissue micro-structure and lower tissue temperature. This implies that signal attenuations imposed through the application of diffusion sensitization of a

particular b-value are likely to be lower in post-mortem than *in vivo* acquisitions. Accurate quantifications of diffusion are thus subject to the achievement of correspondingly higher levels of SNR. PMI and chemical fixation, however, have also been reported to increase the rate of T2 signal relaxation. In combination with the typically long echo times required for the application of diffusion weighting gradients, this reduces signal intensity and thus measurement SNR. In other words, while the minimum SNR required for the accurate characterization of diffusion in post-mortem DTI acquisitions is expected to be higher than *in vivo*, the effects of tissue decay and chemical fixation are likely to result in SNR reductions.

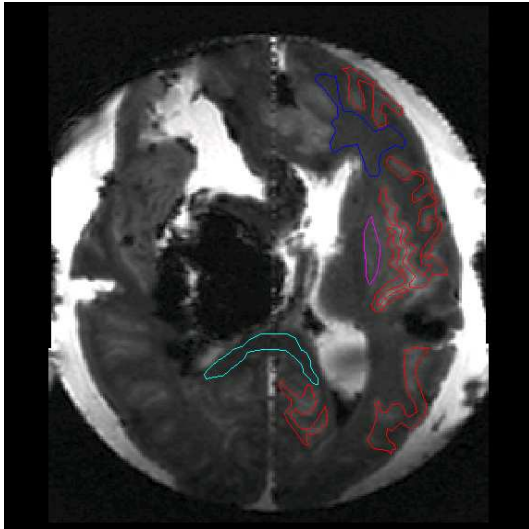
To the best of our knowledge, quantitative information about the minimum SNR necessary for post-mortem DTI has yet to be established. The assessment of the SNR sufficiency could therefore not be based simply on the quantification of SNR of measured acquisitions and well-known relationships between acquisition protocol parameters and SNR. Instead, two separate experiments were performed to quantitatively assess the rate of T2 relaxation in the available tissue samples, and the SNR performance of the acquisition protocol.

Assessment of signal characteristics:

As outlined in the introduction to this chapter, reported effects of PMI and chemical fixation on T2 varied considerably across sites. This may be a result of differences in tissue procurement, fixation and preparation procedures.

To determine whether the rate of transverse signal relaxation in available post-mortem brain specimens was prohibitive for achieving sufficient SNR, T2 and T2* measurements were performed. To this end, Dataset 3-1a was acquired using the GESE sequence (39) and rates of transverse magnetization decay assessed in a number of white and grey matter regions of Brain #1 (c.f. Figure 3-1 and Figure 3-3 below). Due to a large tumour in the left hemisphere of this post-mortem brain specimen, ROIs were drawn exclusively on the right hemisphere where the structural integrity was largely preserved (c.f. Figure 3-3). The determined T2 and T2* values for each ROI are tabulated in Figure 3-3. These

were compared to the *in vivo* measurements in Table 3-4, performed on-site at three different field strengths using an identical acquisition sequence and protocol settings (35).



ROI	T2 (in ms)	T2* (in ms)
cortex (red)	48.6	48.2
putamen (pink)	44.9	44.9
anterior corona radiata (blue)	45.7	44.7
corticopontine tract (not pictured)	47.3	45.0
splenium of the corpus callosum (turquoise)	42.0	38.8

Figure 3-3 GESE acquisition (Dataset 3-1a) depicting overlaid ROIs for grey matter (red), splenium of the corpus callosum (turquoise), anterior corona radiata (blue), putamen (pink).

Table 1	1.5T		3T		7T	
	GESE	EPI	GESE	EPI	GESE	EPI
GM front	87 ± 4	96 ± 6	76 ± 2	72 ± 2	47 ± 11	48 ± 4
GM back	80 ± 2	84 ± 6	68 ± 6	63 ± 2	46 ± 8	39 ± 2
WM	80 ± 1	94 ± 5	71 ± 2	77 ± 4	47 ± 2	50 ± 3

Table 1: Measured GM and WM T₂ (in ms) using GESE and EPI (mean ± inter-subject std. dev.). **Table 2:** Measured GM and WM T₂' (in ms) using GESE (mean ± inter-subject std. dev.)

Table 2	1.5T	3T	7T
GM front	1578 ± 243	685 ± 241	283 ± 272
GM back	1198 ± 252	492 ± 102	129 ± 73
WM	2051 ± 625	648 ± 215	236 ± 59

Table 3-4 Values of T2 and T2' of grey and white matter of the human *in vivo* brain at 1.5 T, 3 T and 7 T (35).

As illustrated by this comparison, T2 and T2* measured in the post-mortem brain at 3 T corresponds well to the values of their *in vivo* counterparts measured at 7 T. *In vivo* single-shot spin echo 2D EPI DTI acquisitions at 7 T have been widely reported (40-46). Q-Ball imaging at 7 T using b-values of up to 6000 s mm⁻² has also been shown to be feasible (47). These findings thus suggest that T2 and T2* of available post-mortem brain specimens at 3 T do not pose a critical limiting factor.

Assessment of acquisition sequence SNR performance:

Neither the minimum SNR value required for successful DTI acquisitions of post-mortem brains, nor the acquisition SNR of datasets generated by the benchmark protocol were available for a direct assessment of the sufficiency of the SNR performance of the proposed starting protocol (Dataset 3-2a). However, the information provided about the benchmark protocol acquisition parameters sufficed for a reasonable approximation of its SNR performance. In this section, an equation was derived to approximate the ratio between the SNR performance of the benchmark (34) and the proposed starting acquisition protocol. Potential differences in scanner performance and post-mortem brain specimen specific T1 and T2 relaxation times were neglected. For the development of this equation, and subsequent verification of its accuracy, dedicated test datasets (Dataset 3-1b - Dataset 3-1e) were recorded on a homogenous agar phantom, and SNR values calculated.

The following section describes the selection and specification of factors considered in the SNR comparison equation. These factors, denoted by the letter ‘f’ followed by a subscript specific to the acquisition property being considered, describe the effect of pertinent acquisition parameters on the SNR-ratio between a ‘target’ and a ‘basis’ sequence. The basis sequence was represented by the acquisition from which the measured SNR values were used to predict the SNR of the target sequence.

Three categories of parameters were considered. First, the well established effects of individual acquisition parameters on SNR of a specific acquisition sequence, then parameters allowing the comparison of 2D and 3D acquisition sequences, and finally, acquisition parameters to account for the differences between single-shot and multi-shot acquisition sequences.

Inclusion of standard SNR parameters

The factors affecting the SNR through the modification of acquisition parameters within a specific acquisition protocol are well known from literature (e.g. (48)).

Signal intensity (SI): The signal intensity factor f_{SI} , describes the effects of the echo and repetition times on a spin echo acquisition sequence. T2 was set to be 45 ms to represent T2 measured in the white matter, as illustrated in Table 3-3. T1 was set to 426 ms as reported in (12).

$$f_{SI} = \frac{\left(1 - e^{\left(\frac{-TR_{target}}{T1}\right)}\right) \cdot e^{\left(\frac{-TE_{target}}{T2}\right)}}{\left(1 - e^{\left(\frac{-TR_{basis}}{T1}\right)}\right) \cdot e^{\left(\frac{-TE_{basis}}{T2}\right)}}$$

Where TE is the echo time, TR is the repetition time and $TE \ll TR$. Factors such as flip angle and inversion time were not pertinent to this application and therefore ignored.

Voxel volume (vv): The voxel volume factor f_{vv} , is calculated from the product of the voxel dimensions ($\Delta x, \Delta y$ and Δz respectively) and is proportional to the image SNR.

$$f_{vv} = \frac{\Delta x_{target} \cdot \Delta y_{target} \cdot \Delta z_{target}}{\Delta x_{basis} \cdot \Delta y_{basis} \cdot \Delta z_{basis}}$$

Number of averages (NSA): The noise levels decrease with the square root of the number of signal averages acquired, while the signal remains constant.

$$f_{NSA} = \frac{\sqrt{NSA_{target}}}{\sqrt{NSA_{basis}}}$$

Bandwidth (BW): The receiver bandwidth affects the SNR through the noise power recorded in an acquisition. In an MRI acquisition of given resolution, the signal bandwidth is determined by the gradient strength used for the spatial encoding of the signal. Noise on the other hand, has a flat power spectrum. This means that increasing the receiver bandwidth beyond the frequency range of the spatially encoded signal increases the noise contribution and thus leads to a drop in image SNR.

In EPI, the bandwidths along the frequency encode direction generally greatly outweigh the bandwidths along the phase encode directions. Accordingly, the bandwidth factor ($1/f_{BW,FE}$) accounts for differences in the receiver bandwidth along the frequency encode direction (BW_{FE}).

$$\frac{1}{f_{BW,FE}} = \frac{\sqrt{BW_{FE,basis}}}{\sqrt{BW_{FE,target}}}$$

Parallel Imaging (PI): In parallel imaging, the density of k-space encoding lines sampled can be reduced through the simultaneous recording of signal by more than one receiver coil. The effects on SNR are described by the equation:

$$\frac{g_{basis} \sqrt{R_{PI,basis}}}{g_{target} \sqrt{R_{PI,target}}} = \frac{SNR_{target}}{SNR_{basis}}$$

Where g is the g -factor, and R_{PI} the parallel Imaging reduction factor. In acquisitions performed at 3T with the available 8-channel head coil, and SENSE factor not exceeding 2, coil g -factor elevations can generally be neglected. As a result, the SNR factor pertaining to parallel Imaging ($1/f_{PI}$) could be approximated as:

$$\frac{1}{f_{PI}} \approx \frac{\sqrt{R_{PI,basis}}}{\sqrt{R_{PI,target}}}$$

Number of in-plane phase encoding steps (PE1): In conventional 2D spin echo sequences, the acquisition of each line of k-space is preceded by an RF excitation pulse, and followed by a time delay (ideally five times T_1 to allow full longitudinal relaxation) to allow the full relaxation of the longitudinal magnetization. As a result, recorded images are based on as many signals produced by the excitation of an entire slice as there are phase-encode steps. The effect this has on SNR is similar to that of signal averaging.

$$f_{PE1} = \frac{\sqrt{N_{PE1,target}}}{\sqrt{N_{PE1,basis}}}$$

In EPI, images are based on the echoes formed from a single excitation, and thus are subject to T2 decay. A correction factor for this is proposed below (f_{sp}).

Accounting for the depth of the excited slabs (2D EPI vs 3D EPI)

In 3D acquisitions, a slab corresponding in thickness to multiple 2D acquisition slices is excited and thus simultaneously contributes to the measurable signal. Signal encoding along the through-plane direction is achieved by the inclusion of a second phase encode orientation (PE2). To account for the effect of 3D acquisition sequences on SNR, this second phase encode direction must be taken into account (in 2D acquisitions, PE2 equals 1) (49).

$$f_{3D} = \frac{\sqrt{N_{PE2,target}}}{\sqrt{N_{PE2,basis}}}$$

Accounting for differences in single-shot and multi-shot acquisitions

As already alluded to in the definition of f_{PE1} , the decline in amplitude of the echoes comprising the EPI echo train with T2 has so far been neglected. Along with reductions in the receiver bandwidth along the phase encode direction, this reduction in echo amplitude limits the number k-space lines that can be recorded, and thus the achievable image resolution at a given FOV.

In contrast, multi-shot EPI acquires k-space data in a number of segments, each following a separate excitation pulse allowing the magnetization of the sample to be replenished between shots. The precise effect of this on image SNR will depend on the repetition time and k-space trajectory used, as well as on image properties.

Here, a correction factor f_{sp} is proposed accounting for differences of the total power of the recorded signal. The number of shots (n_{sh}) used to sample k-space was calculated as the total number of phase encode steps divided by the EPI factor. The time over which data is recorded (t_{rec}) following a single excitation represents the time over which T2 decay of echo amplitudes occurs. Saturation of the longitudinal magnetization was neglected, tacitly assuming the use of sufficiently long repetition times. Influences of the selected k-space trajectory and image properties were also ignored.

The image SNR was assumed proportional to the total recorded signal power p_{total}

$$p_{total} = n_{sh} \int_0^{t_{rec}} e^{-t/T_2} \cdot dt$$

Accordingly, the ‘signal power’ factor f_{sp} is defined as:

$$f_{sp} = \frac{p_{total,target}}{p_{total,basis}}$$

Evaluation of the proposed SNR conversion equation:

After combining all these factors in equation 3.1 below, its ability to predict SNR of a target acquisition sequence from a basis sequence was assessed using Datasets 3-1b – e (results not illustrated).

$$SNR_{target} = SNR_{Basis} \frac{f_{SI} \cdot f_{VV} \cdot f_{NSA} \cdot f_{PE1} \cdot f_{3D} \cdot f_{SP}}{f_{BW,FE} \cdot f_{PI}} \quad (3.1)$$

Equation 3.1 allowed SNR between different single-shot and multi-shot, 2D and 3D EPI acquisition protocols to be determined with a mean error of 13 %.

Assessment of the SNR performance of the proposed starting and benchmark protocols:

Finally, equation 3.1 was used to predict the ratio of image SNR achievable with the proposed starting protocol (Dataset 3-2a) under the stipulations defined in Section

3.3.1, to the benchmark protocol described in (34). This was found to be 1.9 and 3.3, for the overnight (scan duration: 7 hour 40 minutes) and the whole day scan (23 hours) respectively. These values should, of course, only be seen as a rough estimate, as this approximation does not account for factors such as differences between scanners and the post-mortem specimens used.

In conclusion, these findings suggest that DTI acquisitions of the available post-mortem brain specimens, and the proposed acquisition protocol, is likely to match or exceed the minimum SNR requirement.

Practical assessment of the DTI acquisition protocol performance following the elimination of SNR as potential critical limiting factor

Having eliminated SNR constraints as a potential limiting factor in the proposed starting protocol, preliminary DTI acquisitions (Dataset 3-2a) were performed for the practical assessment of the achievable data quality.

Although in the previous section it was estimated that in an 8 hour scan, roughly double the SNR of the benchmark protocol was achievable with the proposed starting protocol it was decided to acquire this first dataset over 24 hours. This was considered prudent given that SNR estimations could not account for differences in scanner hardware, sequence implementation and tissue sample properties.

As already alluded to, scanner stability concerns were anticipated when acquiring data over such extended periods of time. For this reasons, three common averaging strategies were employed, allowing for the direct comparison of their suitability for the starting protocol for post-mortem DTI acquisitions. As detailed in Section 3.2.2 these included online averaging (individual datasets are acquired under identical scanner calibration settings, and averaged online prior to output) dynamic acquisition averaging (acquisitions are acquired under identical scanner calibration settings but output individually for offline averaging) and the averaging of individual sets (scanner calibration precede each acquisition, datasets are output individually for offline

averaging). Acquisitions comprising Dataset 3-2a were organized into three 'sets', each composed of six dynamic scans each with an NSA of 10. The acquisition time of each set was 7 hours and 40 minutes.

Figure 3-4 illustrates recorded $b=0$ acquisitions of each dynamic scan making up the three recorded sets. Both significant scanner drift and artefacts can be observed in higher dynamics of acquisition sets 1 and 3. No visible artefacts or pseudo-motion could be detected in the first dynamic acquisitions of each of the three sets, presumably as a result of centre frequency adjustments performed in preceding calibration steps. Although visible pseudo-motion can also be observed between dynamic acquisitions of the second set, these were lower and did not lead to visible artefacts.

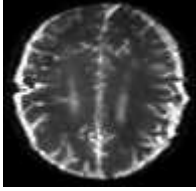
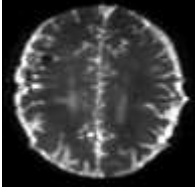
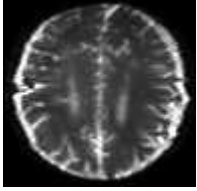
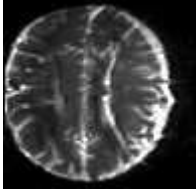
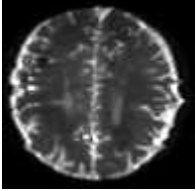
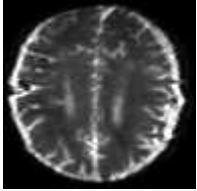

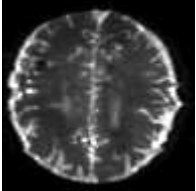
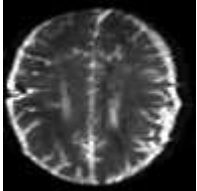
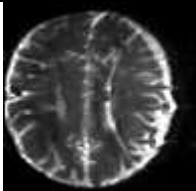
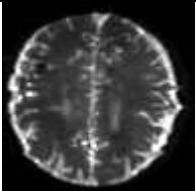
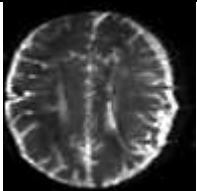
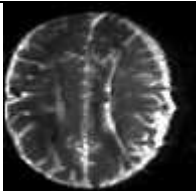
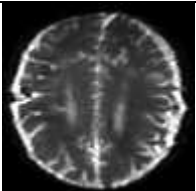
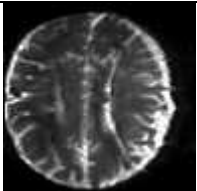
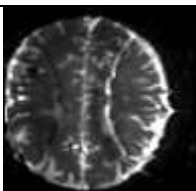
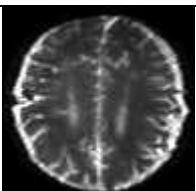

	Acquisition Set 1	Acquisition Set 2	Acquisition set 3
Dynamic 1			
Dynamic 2			
Dynamic 3			
Dynamic 4			
Dynamic 5			
Dynamic 6			

Figure 3-4 Illustration of the effects of scanner instability on $b=0$ images on a slice superior to the ventricles (Dataset 3-2a).

Practical assessment of DTI data quality

As a consequence of considerable pseudo-motion and artefacts observed in set 1 and 3 (Figure 3-4), subsequent diffusion tensor calculations were performed only on set 2. Generated colour FA maps are illustrated in Figure 3-5 below.

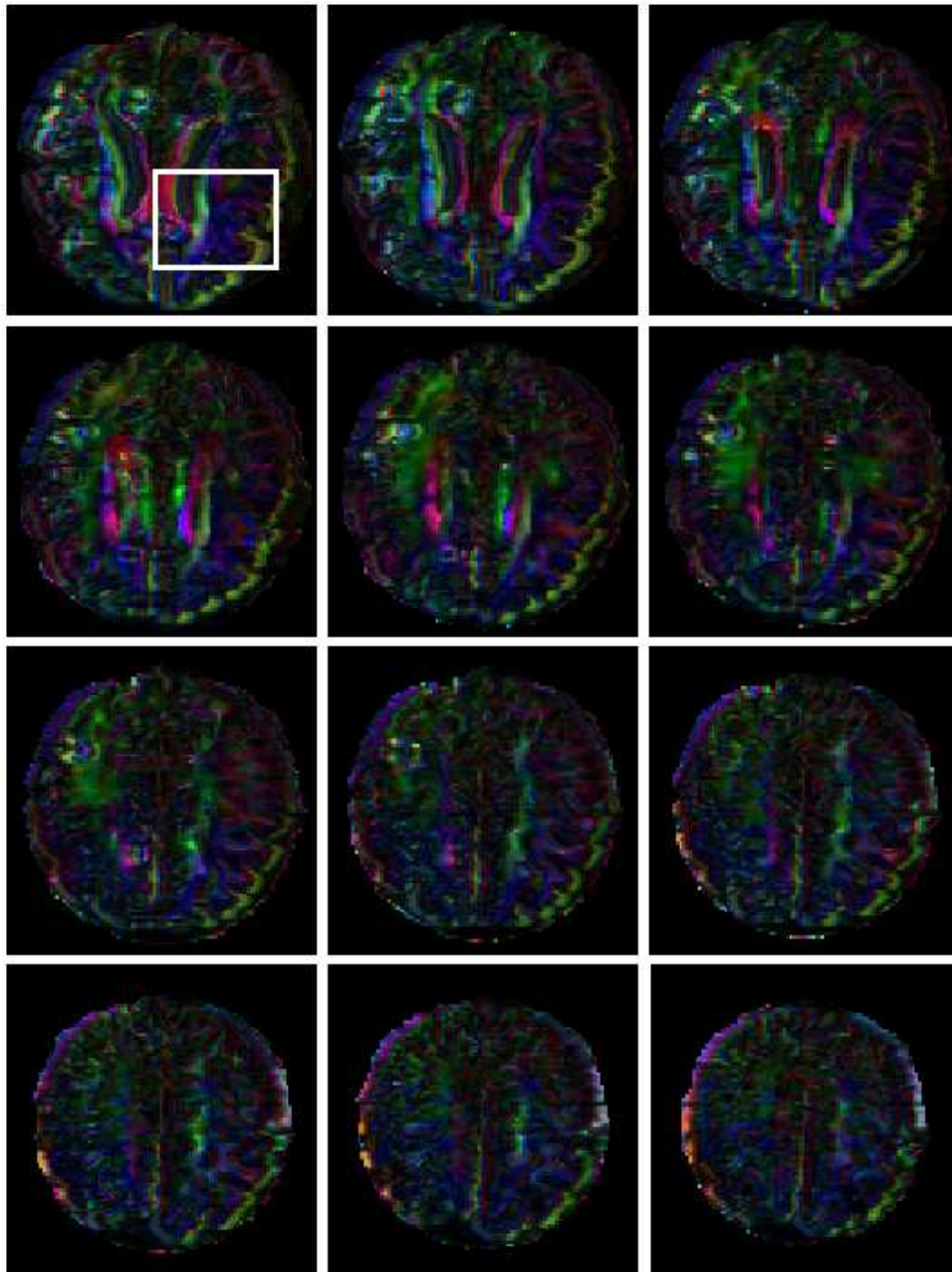


Figure 3-5 FA colour maps at multiple slice positions, obtained by the starting acquisition protocol (set 2 of Dataset 3-2a). The region within the white box is enlarged for further analysis in Figure 3-6.

A qualitative assessment of the overall quality of DTI acquisitions in Figure 3-5 showed it to still be inadequate. In following sections, the acquisition quality is assessed in depth, and the impact of the remaining potential limiting factors pertaining to the acquisition protocol (i.e. bandwidth and temporal instability) on the loss of data quality is undertaken. Possible contributions of losses in the structural integrity of the tissue scanned are also assessed.

The FA colour maps of Figure 3-5 provided first insights into the structural integrity of fibrous tissue. Indications of the preservation of the structural integrity of the post-mortem tissue specimen include that the FA value of thick coherent fibre tracts exceeded that of grey matter regions and fluid filled spaces. Furthermore, the orientation of large, highly coherent fibre bundles, such as the corpus callosum, was determined correctly. On the other hand, however, some white matter regions of low FA and high MD were also observed. One such a region is highlighted by the white square in Figure 3-5. Magnified sections of the corresponding colour FA and MD maps are illustrated in Figure 3-6 below (white matter regions of low FA and high MD are highlighted by the white/red ROI on the colour FA/MD maps). This may be the result of advanced stages of structural degradation and liquefaction of tissue due to the relatively long PMIs of 4 days.

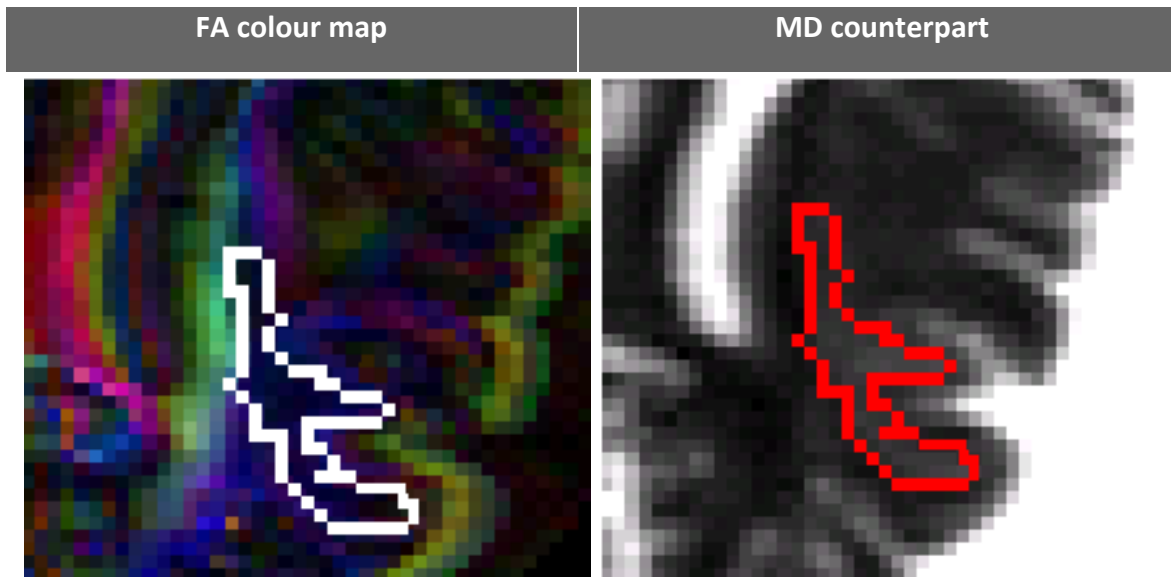


Figure 3-6 FA and MD maps of the region highlighted by the white rectangle in Figure 3-5. Regions of reduced FA (white outline) correspond to regions of increased MD (red outline) (Dataset 3-2a).

In Figure 3.5, a rim of high FA can be observed at the periphery of the brain specimen and near tissue-ventricle interfaces. This is indicative of poor co-registration between individual images comprising the composite DTI dataset, and could result from bulk sample motion (e.g. due to scanner vibration), scanner drift induced pseudo-motion (as illustrated in Figure 3-4) and Eddy-current distortions. The thickness of this rim was observed to be greater along the right-left orientation which corresponded to the phase encode direction of the EPI acquisition, implicating the latter two effects as the dominant source of co-registration imperfections. Post-acquisition image co-registration failed to provide any effective reduction of this effect despite attempts made at optimization (data not illustrated).

Visible signs of scanner instabilities including pseudo-motion and image artefacts in sets 1 and 3 of Dataset 3-2a have already been discussed (Figure 3-4). To quantitatively assess the temporal stability of set 2 of Dataset 3-2a, coefficient of variation (CoV) maps

were calculated over the six dynamic acquisitions. CoV maps for the $b=0$ acquisition, as well as three orthogonal diffusion sensitization orientations are illustrated in Figure 3-7.

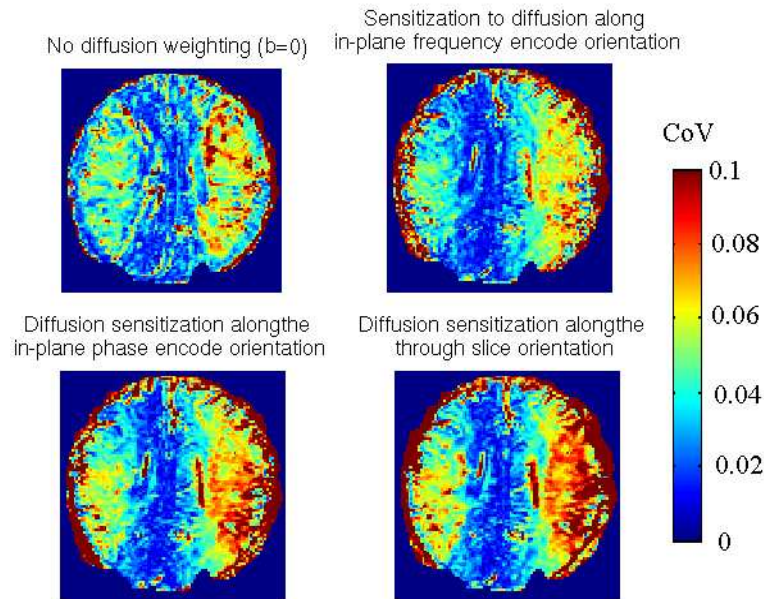


Figure 3-7 Illustration of coefficient of variation maps for $b=0$ measurements, and DWI acquisitions with diffusion weighting applied along three orthogonal orientations (set 2 of Dataset 3-2a).

CoV maps in Figure 3-7 display contiguous regions of increased scan-rescan variability over the duration of the acquisition. The regions of reduced precision can be described as corresponding to the shape of the specimen, but displaced by half a FOV along the phase encode direction. Strikingly, the level of CoV exceeded 10 % in some regions and thus could represent a significant source of error in diffusion tensor calculations.

Strategies to address this loss in scan-rescan precision would depend on whether the observed variability was random or transient in nature. While random fluctuations would require the acquisition of high numbers of averages, transient voxel intensity drifts could be reduced by the modification of the averaging strategy. To assess this, maps of CoV were calculated from ADC maps generated from each diffusion weighted acquisition and its corresponding $b=0$ acquisition (Figure 3-8).

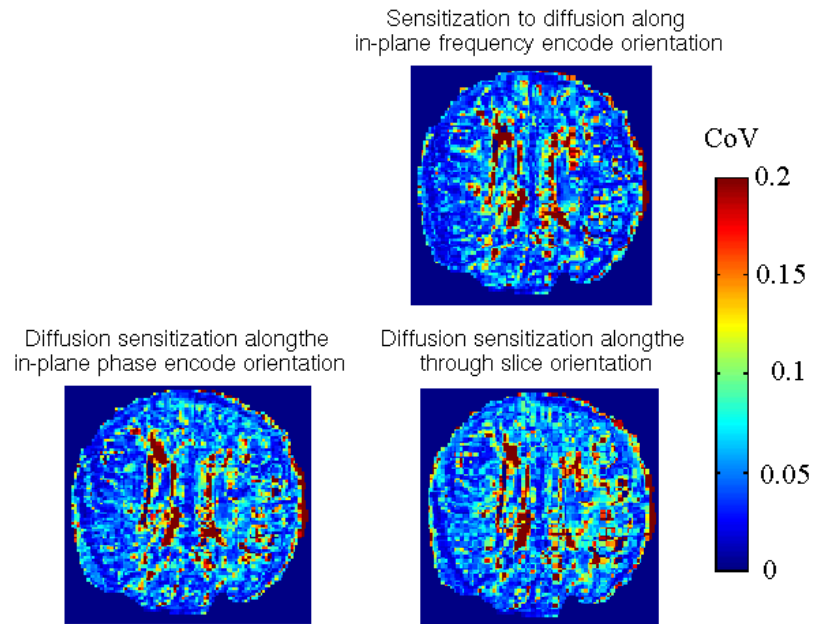


Figure 3-8 Illustration of coefficient of variation maps for ADC maps calculated from $b=0$ measurements, and DWI acquisitions with diffusion weighting applied along three orthogonal orientations (set 2 of Dataset 3-2a).

The observed absence of structured regions experiencing elevated levels of variability in the ADC maps (Figure 3-8) confirmed that transient scanner instabilities (rather than random variability) were responsible for elevated CoV levels in $b=0$ and DWI acquisitions in Figure 3-7. Furthermore, it demonstrates adequate scanner stability over the duration of a single acquisition. It was postulated that this loss in precision may be the result of the manifestation of the Nyquist ghost changing as a result of scanner drift.

In summary, in this section a DTI acquisition protocol was proposed that not only met all the requirements for compatibility with a clinical environment but also exceeded the SNR performance of the benchmark protocol. Despite effectively eliminating acquisition sensitivity as a potential critical limiting factor, however, DTI data quality was still unacceptably poor. On closer analysis, acquisitions displayed signs of distortion, and transient changes in position (pseudo motion) and voxel intensity, which may be the result of the remaining two critical limiting factors defined in Section 3.3.1 (susceptibility

to image distortion and temporal stability). Product dynamic stabilization applied during acquisitions, and standard post-acquisition co-registration, proved ineffective in alleviating mis-registration of individual acquisitions due to scanner drift and distortion. Finally, indications of advanced degradation of the structural integrity in the available post-mortem tissue specimens were observed. However, since the modification of the tissue procurement procedure was not possible for this study, and due to their observed localized nature, these effects were not investigated further.

The next step in the optimization of the post-mortem DTI acquisition protocol focused on reducing the effects of scanner instabilities. This was selected first, as improvements in acquisition precision may not only improve overall data quality, but were hypothesized to possibly also facilitate improved performance of co-registration techniques to alleviate image distortion.

Optimization of the averaging technique

This section describes acquisition protocol optimization steps taken to reduce susceptibility of DTI acquisitions to transient scanner instabilities.

The analysis of Dataset 3-2a in the previous section demonstrated the presence of both transient changes in object location and voxel intensity. In this section, acquisition protocol modifications to reduce the magnitude of transient changes and/or the susceptibility of diffusion tensor calculations to are proposed and implemented in Dataset 3-2b.

As was illustrated in Figure 3-4, pseudo motion could only be observed over dynamic acquisition repeats, and were absent in the first dynamic scan of each set. Consequently, dynamic averaging was not used in Dataset 3-2b, and the FOV was increased to reduce the susceptibility to wrap-around artefacts.

It has been demonstrated that by recording DWI acquisitions along higher numbers of non-collinear directions, rather than recording fewer directions with higher numbers of averages, the precision of the calculated diffusion tensor can be improved (1). Based on

this, it was hypothesized that by recording increased numbers of non-collinear diffusion sensitized directions (at the expense of the number of signal averages) could be effective in reducing the susceptibility of calculated diffusion tensors the transient signal variations illustrated in Figure 3-7.

On the other hand, averaging of identical acquisitions were not avoided altogether, since individual scans were considered too noisy for to allow for effective post-acquisition co-registration to reduce the effects of scanner-drift and Eddy-current distortions. On the available MRI system, online signal averaging underlies an acquisition protocol in which all $b=0$ and diffusion weighed images comprising a DTI dataset are acquired first, before being repeated and subsequently averaged. In other words, the delays between the acquisitions of scan-repeats thus correspond to the duration of a full DTI dataset effectively increasing the susceptibility to the transient artefacts illustrated in Figure 3-8.

To reduce the variability between corresponding image repeats, an acquisition parameter setting under which corresponding acquisitions were recorded consecutively (details provided in the description of Dataset 3-2b, Section 3.2.2) was used. To test the efficacy of this approach in reducing scan-rescan variability, CoV maps corresponding to those of the illustration in Figure 3-7 were calculated from Dataset 3-2b. The low and evenly distributed CoV in Figure 3-9 testify to the high level of precision achieved using of this averaging approach.

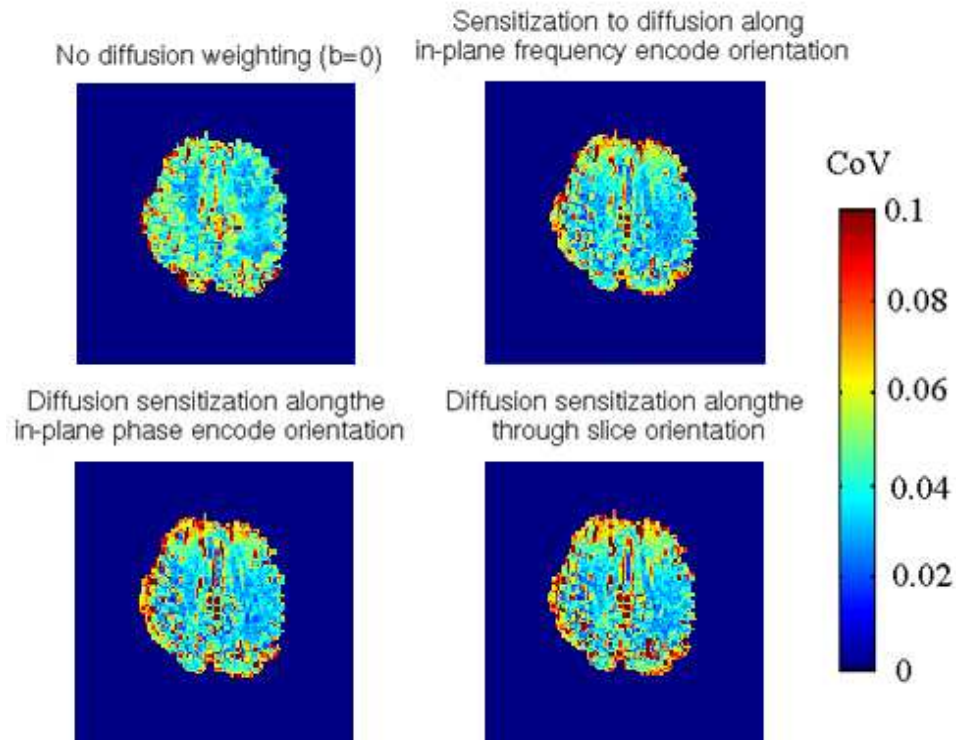


Figure 3-9 Illustration of coefficient of variation maps for $b=0$ measurements, and DWI acquisitions with diffusion weighting applied along three orthogonal orientations recorded using an averaging strategy optimized to reduce scan-rescan variability (Dataset 3-2b).

Figure 3-10 illustrates the FA colour maps of subsequent Diffusion tensor calculations performed on Dataset 3-2b, as well as representative examples of the impact of co-registration on data quality.

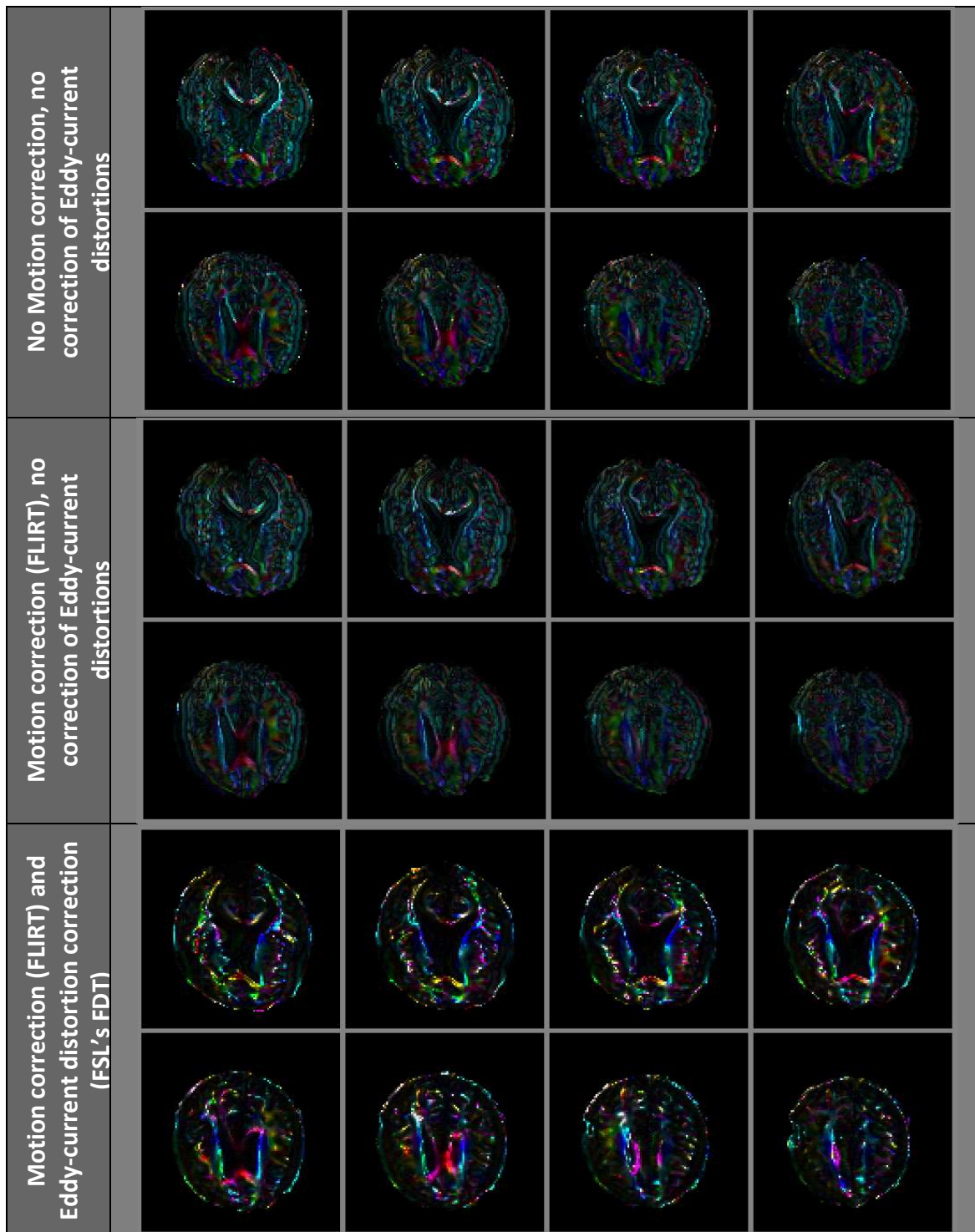


Figure 3-10 Colour FA images of modified averaging techniques (Dataset 3-2.b). FA maps calculated without the use of post-acquisition co-registration (montage of the first row) underwent averaging over acquisition repeats prior to tensor calculations. Rigid body motion correction (montages of the second and third row) was performed prior to averaging and subsequent tensor calculations. Eddy-current distortion correction (montages of the third row) was applied after averaging had been performed.

A qualitative assessment of colour coded FA maps demonstrates significant improvements over results obtained previously from Dataset 3-2a (Figure 3-5). A further indication of improved data quality is the improvement of the performance of co-registration techniques. While attempts to perform motion- and Eddy-current distortion correction in Dataset 3-2a often led to nonsensical results and therefore needed to be heavily constrained in their degrees of freedom (data not pictured) so such steps were necessary for the results of Dataset 3-2b.

A visual inspection of corresponding raw data acquisitions (data not illustrated) revealed the absence of any discernable pseudo-motion over time. This, together with the marginal effect that rigid body motion correction had on data quality (c.f. montages in the first and second rows of Figure 3-10) attested to the effectiveness of avoiding dynamic averaging to minimize the effects of scanner drift.

FA colour maps without Eddy-current distortion corrections (montages in rows 1 and 2 of Figure 3-10) displayed rims of high FA at tissue boundaries along the phase encode direction. Eddy-current distortion correction (montage row 3 of Figure 3-10) appear effective in the reduction of Eddy-current induced distortions, and allowed to improved reconstruction of major nerve fibre tracts. Nevertheless, performance of tested Eddy-current distortion correction techniques was still insufficient to allow for the accurate reconstruction of smaller fibre tracts.

In summary, described modifications to the averaging strategy used was demonstrated to be effective in reducing unwanted transient changes in the position and intensity of recorded acquisitions. Presumably as a consequence of these improvements in data quality, the performance of co-registration techniques to alleviate image distortions was found to also have improved considerably. Nevertheless, post acquisition Eddy-current distortion correction was still observed to be suboptimal and overall image quality inadequate.

Optimization of co-registration technique

In the previous sections, two of the three identified potential critical limiting factors have been assessed, and acquisition protocol modification towards their alleviation tested. In this section, the third potential critical limiting factor ‘susceptibility to image distortions’ is addressed.

The brightness at the periphery of the brain specimen in colour FA maps in Figure 3-10 is indicative of considerable Eddy-current distortions. Although a range of image co-registration techniques used routinely *in vivo* was tested (data not shown), these proved ineffective.

Previously reported DTI acquisitions using sequences specialized for applications in chemically fixed post-mortem brains (33, 34), used multi-shot EPI. This allowed receiver bandwidths along the phase encode direction to be increased, and thus the susceptibility to distortion to be reduced.

Single-shot EPI based DTI acquisition sequences are commonly used *in vivo*, and post-processing tools to alleviate Eddy-current distortion are readily available. However, post-mortem acquisitions require the use of high b-values ($b = 3000 \text{ s mm}^{-2}$) and short echo times to achieve sufficient diffusion sensitization and acquisition SNR, exacerbating the induction of Eddy-currents. Furthermore, tools to alleviate Eddy-current distortions through post-acquisition co-registration have been found to perform inadequately for post-mortem specimens (e.g. montage in of the third row in Figure 3-10). A possible explanation for this may lie in the fundamental differences in the co-registration task presented by *in vivo* and post-mortem brain acquisitions. Prevalent co-registration techniques used *in vivo* are typically based on the minimization of a cost function evaluated over a 2D or 3D set of images to calculate a single transformation matrix. Due to unavoidable motion *in vivo*, transformations must typically account for object translations, rotations, shear etc. in the evaluation of the cost function. Furthermore, the co-registration of images of different contrasts, as is the case for the acquisitions comprising a composite DTI datasets, necessitates the use of elaborate cost functions

(e.g. mutual information co-registration (50)). A number of acquisition characteristics of chemically fixed post-mortem brain tissue could present challenges for such co-registration techniques. The presence of unavoidable air-pockets in the post-mortem brain specimens often result in severe distortions in their immediate vicinity, potentially making the formulation of a global co-registration matrix impossible. The reduction in image contrast between grey and white matter regions of post mortem brain tissue (12) hinder the detection of landmark points within acquired images. Also, while regions containing saline solution are visible in $b=0$ images, they are effectively suppressed in acquisitions following the application of diffusion sensitization, thus changing the outline of the objects being co-registered. Finally, to achieve efficient co-registration, the complexity of the algorithm and cost functions used should be minimized, and the degrees of freedom (DOF) limited. The absence of motion, and successful alleviation of pseudo-motion in post-mortem acquisitions suggest that co-registration could be limited to displacements along the phase encode direction. To improve robustness of the co-registration technique towards localized severe image distortion, co-registration should be performed locally. The lack of white matter-grey matter contrast and the presence of differences between the visible image components in $b=0$ and diffusion sensitized images can be addressed by co-registering only those images that have been subjected to identical diffusion sensitization, and thus have identical contrast.

The reversed gradient Eddy-current induced distortion correction method (38) was proposed as a more suitable alternative for reducing Eddy-current induced distortions in DTI acquisitions of the post-mortem brain. In this technique, Eddy-current distortions are characterized through the acquisition of paired datasets with opposite phase encode directions. This leads to distortions occurring along opposite directions in the phase encode orientation. Corresponding voxels are identified by their line integrals along the direction of distortion. The true location of a voxel may subsequently be calculated as the intermediate position between corresponding points.

Dataset 3-2c was recorded to test the suitability of this algorithm. Acquisition parameters were kept similar to those of Dataset 3-2b, except that phase encode orientations were alternated between subsequent datasets. Averaging was performed on each of these two groups of acquisitions prior to undergoing Eddy-current distortion correction using the technique described in (38).

As illustrated in Figure 3-11, resulting DTI acquisitions of high quality could be recorded in this way. As a next step, the number of averages was reduced in order to ascertain the minimum acquisition time needed. Figure 3-12 illustrates the result of a single pair of DTI acquisitions with opposite phase encode orientations (total acquisition time \approx 21 minutes). Similarly, Figure 3-13 demonstrates the image quality that can be achieved from a single-average DTI acquisition using a 2 mm isotropic voxels (Dataset 3-2d).

The presented acquisition and post-processing protocol thus allows good quality DTI acquisitions of chemically fixed whole human brain specimens to be recorded within roughly 21 minutes using only standard acquisition sequences and hardware.

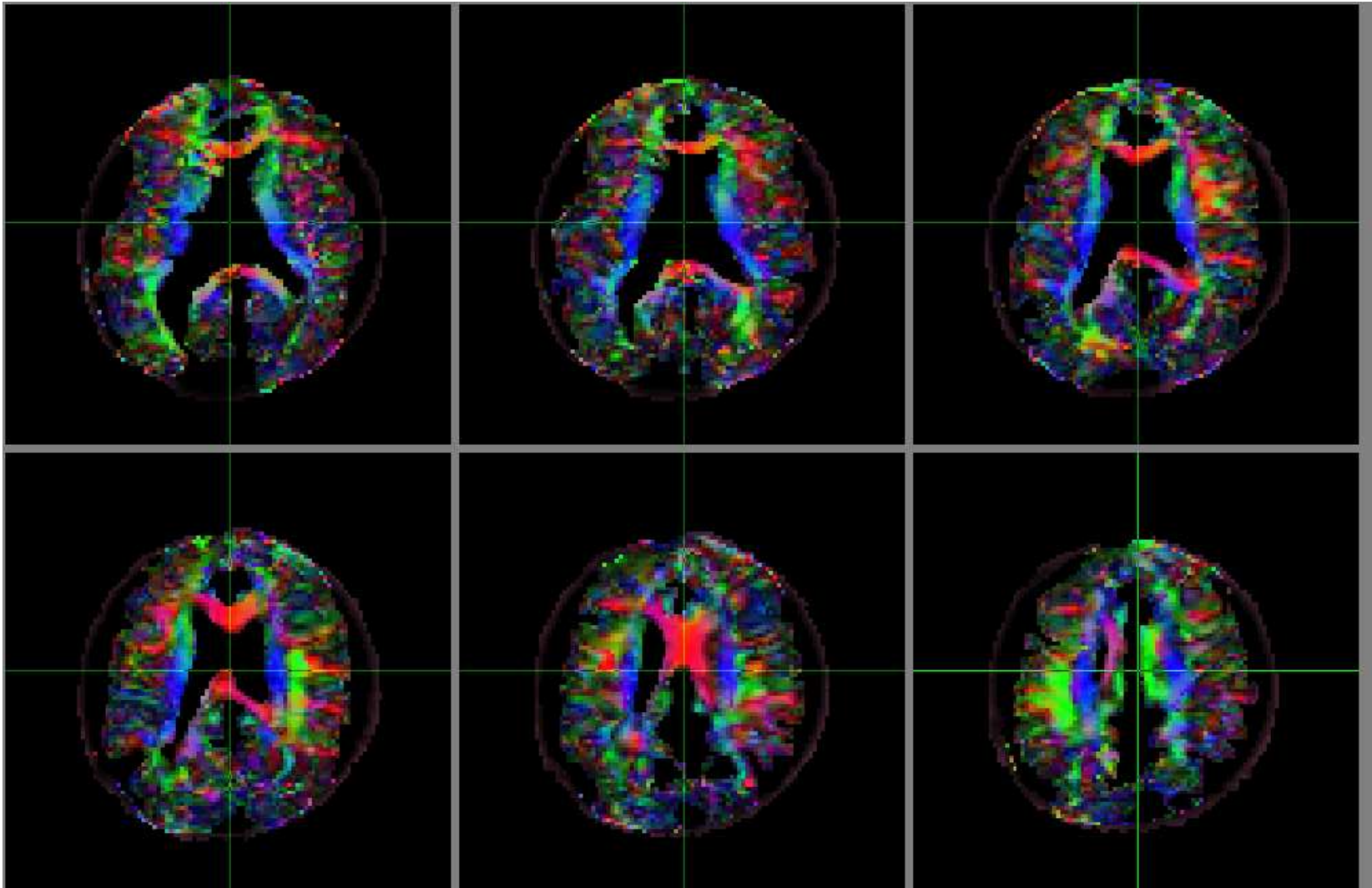


Figure 3-11 FA colour maps obtained from acquisition protocols with modified averaging and Eddy-current corrections using the reversed gradient method (51).

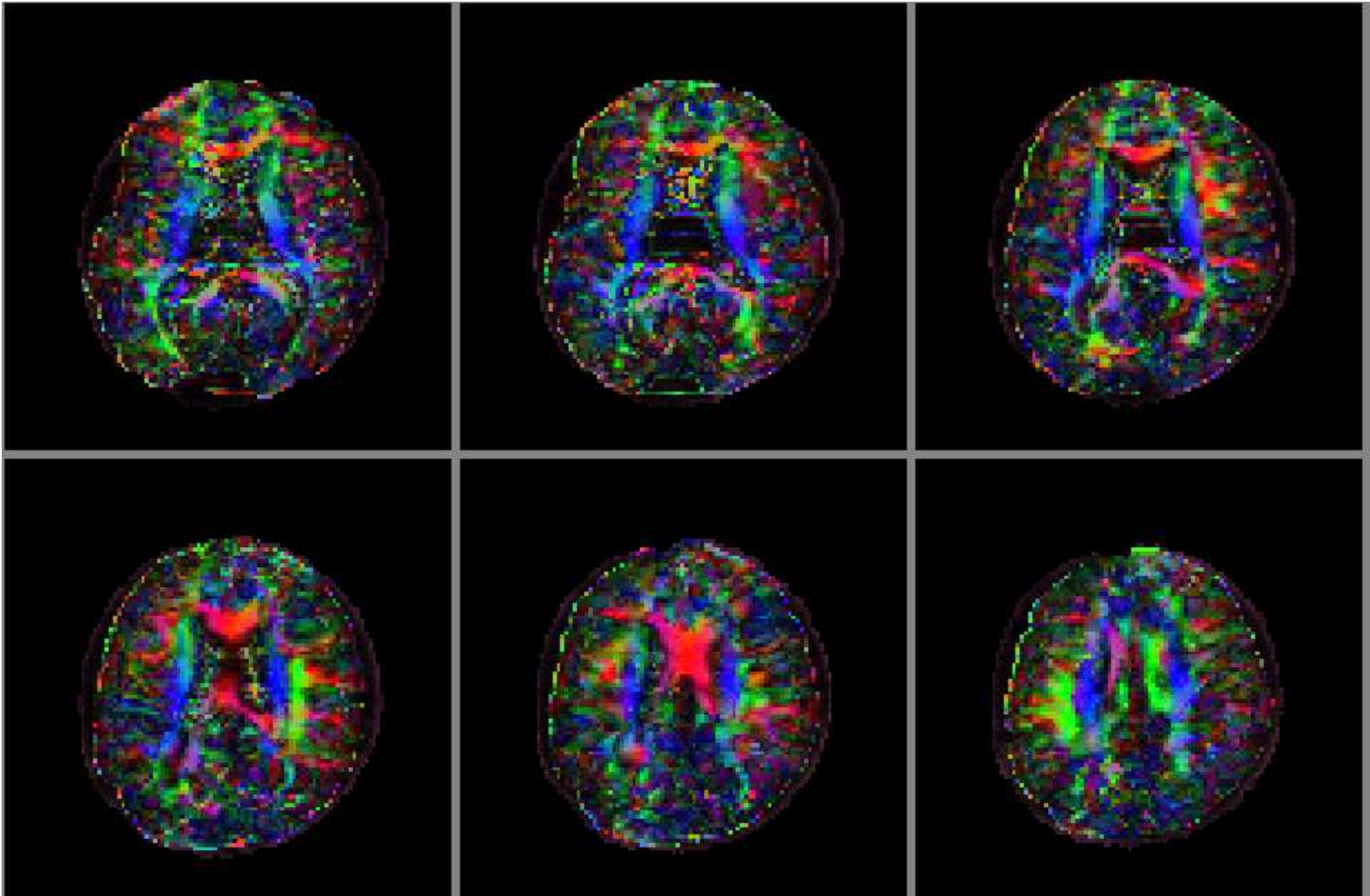


Figure 3- 12 FA colour maps of resolution 2x2x4 mm obtained with just one iteration (Dataset 3-2.c).

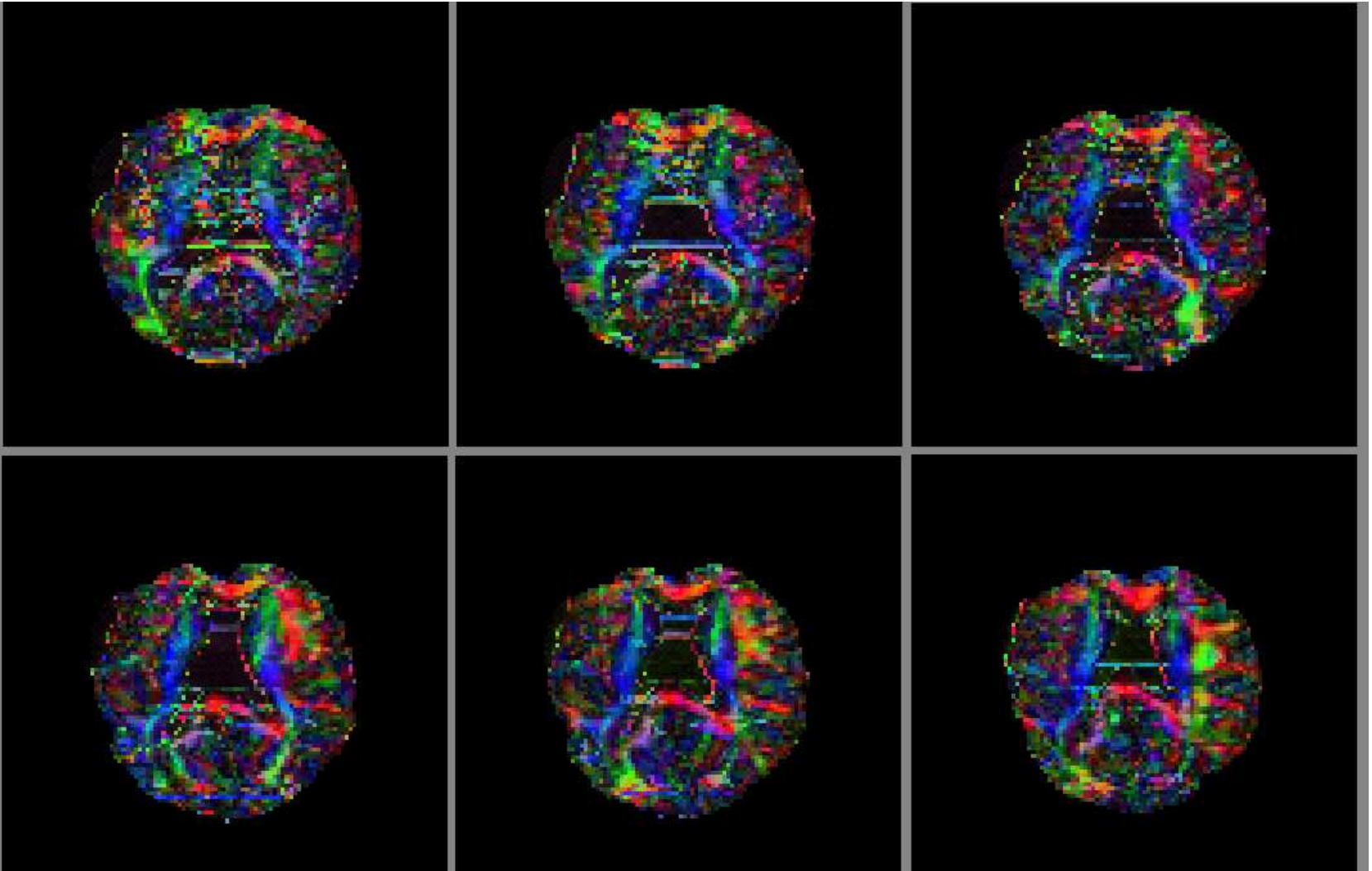


Figure 3- 13 FA colour maps of resolution 2x2x2 mm obtained with just one iteration (Dataset 3-2.d).

3.4 Discussion

The purpose of this investigation was to assess the principle feasibility of performing DTI of the chemically fixed whole human brain under a clinical setting. While a number of previous attempts using clinical scanners and standard acquisition sequences have been reported in literature (12, 17, 27, 28), the quality of data achieved in these studies was widely considered inadequate. This investigation, for the first time, identified potential critical limiting factors that have likely been responsible for this loss in data quality. Furthermore, through the development and practical assessment of strategies towards the alleviation of these factors, an acquisition protocol under which high quality DTI acquisitions of chemically fixed whole human brain specimens could be acquired within 21 minutes was developed successfully.

Due to its highly complementary nature to *in vivo* acquisitions, DTI of chemically fixed post-mortem brains can potentially offer a platform for a number of exciting research applications. These range from technical applications, such as the validation of existing, or the development of novel DTI metrics or tractography algorithms; to clinical applications, for instance allowing changes in DTI metrics as a result of disease to be compared directly to histology; to biomedical research applications, such as allowing acquisitions of high b-value and directional or spatial resolutions to be performed, thus giving hitherto unseen insights into the structural organization and microstructure of the human brain.

However, as mentioned above, previous attempts (12, 17, 27, 28) to acquire DTI maps from chemically fixed whole human brain specimens using clinical scanners and standard acquisition sequences have thus far failed to achieve acceptable levels of data quality. In one hypothesis this failure was attributed to the insufficiency of SNR (12) as a result of tissue dehydration and increased rates of T2 signal relaxation resulting from the use of aldehyde fixative agents (12, 21). Although no independent verification of this hypothesis was found in literature, it appears to have received widespread acceptance

as demonstrated by the focus of subsequent investigations on strategies that allow the alleviation of SNR limitations (18, 33, 34, 13).

Practical challenges for achieving the stated aims of this investigation of identifying, and if possible overcoming, critical limiting factors in DTI acquisition sequences applicable under a clinical setting included the sheer number of potential factors, and anticipated long scan times. To overcome this, a systematic approach, based on both, the utilization of knowledge in existing literature, and the design and execution of dedicated experiments.

The main finding of this study was the identification of Eddy-current distortions as a main critical limiting factor. The minimization of scanner drift-induced effects over the course of long acquisitions and the careful selection of an appropriate averaging strategy was also shown to be necessary. Conversely, practical assessment of SNR demonstrated that SNR sufficiency in fact did not pose a critical limiting factor, contradicting a widely accepted hypothesis. The successful development of appropriate averaging and Eddy-current correction strategies allowed high quality DTI datasets to be recorded on chemically fixed whole human brain specimens within only 21 minutes. This is despite the relatively long PMIs of four days used in local tissue procurement procedures.

In addition to establishing the feasibility of DTI acquisitions of the chemically fixed whole human brains under a clinical setting, this investigation opens new opportunities for a range of future investigations. Some potential research directions are outlined below.

Acquisition parameter optimization

The aim of acquisition protocol optimization steps was to identify and overcome critical limiting factors that have resulted in poor data quality in previous investigations and in early attempts to record DTI of the post-mortem human brain (e.g. Figure 3-5). While this was successful in establishing the feasibility of DTI under a clinical setting, further

work is needed to establish and validate optimal acquisition parameters for DTI of the post-mortem brain. This is because wherever possible acquisition parameters were adopted from the benchmark protocol. In light of the relatively short scan times needed to record good quality DTI datasets, however, other acquisition parameters such as optimal b-value, spatial resolution, directional resolution acquisition sequence etc. would be beneficial.

Acquisition sequence development:

The finding that SNR does not appear to be critical opens avenues for the exploration of DTI using acquisition sequences that may not be suitable *in vivo*. For example, if the use of longer diffusion times is found to be beneficial to overcome reduced levels of diffusivity in the post-mortem brain, acquisition sequences based on stimulated echoes may be preferable over spin echoes. Similarly, alternative read out modules may offer advantages over EPI. For instance, the relatively high scanner stability that can be achieved if appropriate averaging strategies are used could allow the utilization of the absence of motion in post-mortem brains to record data using a spin echo sequence. This may allow the acquisition of DTI data at higher spatial resolution and lower distortion than achievable *in vivo*.

Acquisition setup optimization

The high sensitivity of acquisitions to Eddy-current distortion correction algorithms may be the result of low diffusion induced contrasts, which could potentially be alleviated by warming the tissue specimen before or even during acquisitions (e.g. using an MRI compatible heater used to keep the body temperature constant in small-bore scanners).

Tissue procurement optimization and standardization

The volume of literature available on the effects of post-mortem tissue changes and chemical fixation on tissue properties is indicative of the central importance of the tissue procurement step. Despite this, considerable disagreement can be found in the reported results indicating the need to optimize and standardize tissue procurement

steps. Whole brain specimens are likely to require special attention due to the slow rates by which fixative agents diffuse into brain tissue. The relatively short acquisition times of the DTI protocol presented in this chapter may make it an ideal tool to investigate the impact of different tissue procurement steps on the whole human post-mortem brain.

Medical/biomedical research applications

The adequate performance of the proposed acquisition protocol may allow it to be used for biomedical research application. In fact, it is currently being utilized in an investigation correlating different DTI measures to the iron content of specific brain structures.

3.4 Literature

1. McRobbie D, Moore E, Graves M, Prince M. MRI From Picture to Proton; Second edition: Cambridge University Press; 2007.
2. Jones D. The effect of gradient sampling schemes on measures derived from diffusion tensor MRI: A Monte Carlo study. *Magnetic Resonance in Medicine* 2004;51(4):807-815.
3. Norris D. Implications of Bulk Motion for Diffusion-Weighted Imaging Experiments: Effects, Mechanisms, and Solutions. *Journal of Magnetic Resonance Imaging* 2001;13:486-495.
4. Heim S, Hahn K, Sämann P, Fahrmeir L, Auer D. Assessing DTI data quality using bootstrap analysis. *Magnetic Resonance in Medicine* 2004;52(3):582-589.
5. Johansen-Berg H, Behrens T. Diffusion MRI. Press A, editor; 2009.
6. D'Arceuil H, de Crespigny A. The effects of brain tissue decomposition on diffusion tensor imaging and tractography. *NeuroImage* 2007;36:64-68.
7. D'Arceuil H, Crespigny A. The effects of brain tissue decomposition on diffusion tensor imaging and tractography. *NeuroImage* 2007;36:64-68.
8. Shepherd T, Flint J, Thelwall P, Stanis G, Mareci T, Yachnis A, Blackband S. Postmortem interval alters the water relaxation and diffusion properties of rat nervous tissue - Implications for MRI studies of human autopsy samples. *NeuroImage* 2009;44:820-826.
9. Shepherd T, Flint J, Thelwall P, Stanis G, Mareci T, Yachnis A, Blackband S. Postmortem interval alters the water relaxation and diffusion properties of rat nervous tissue - Implications for MRI studies for human autopsy samples. *NeuroImage* 2009;44:820-826.
10. Blamire A, Rowe J, Styles P, McDonald B. Optimising imaging parameters for post mortem MR imaging of the human brain. *Acta Radiology* 1999;40:593-597.
11. Nagara H, Inoue T, Koga T, Kitaguchi T, Tateishi J, Goto I. Formalin fixed brains are useful for magnetic resonance imaging (MRI) study. *Journal of Neuroscience* 1987;81:67-77.
12. Pfefferbaum A, Sullivan E, Adalsteinsson E, Garrick T, Harper C. Postmortem MR imaging of formalin-fixed human brain. *NeuroImage* 2004;21:1585-1595.
13. Shepherd T, Thelwall P, Stanis G, Blackband S. Aldehyde Fixative Solutions Alter the Water Relaxation and Diffusion Properties of Nervous Tissue. *Magnetic Resonance in Medicine* 2009;62:26-34.
14. Thelwall P, Shepherd T, Stanis G, Blackband S. Effects of temperature and aldehyde fixation on tissue water diffusion properties, studied in an erythrocyte ghost tissue model. *Magnetic Resonance in Medicine* 2006;56:282-289.
15. Porea A, Webb A. Reversible and irreversible effects of chemical fixation on the NMR properties of single cells. *Magnetic Resonance in Medicine* 2006;56:927-931.
16. Pattany P, Puckett W, Klose K, Quencer R, Bunge R, Kasuboski L, Weaver R. High-resolution diffusion-weighted MR of fresh and fixed cat spinal cords: evaluation

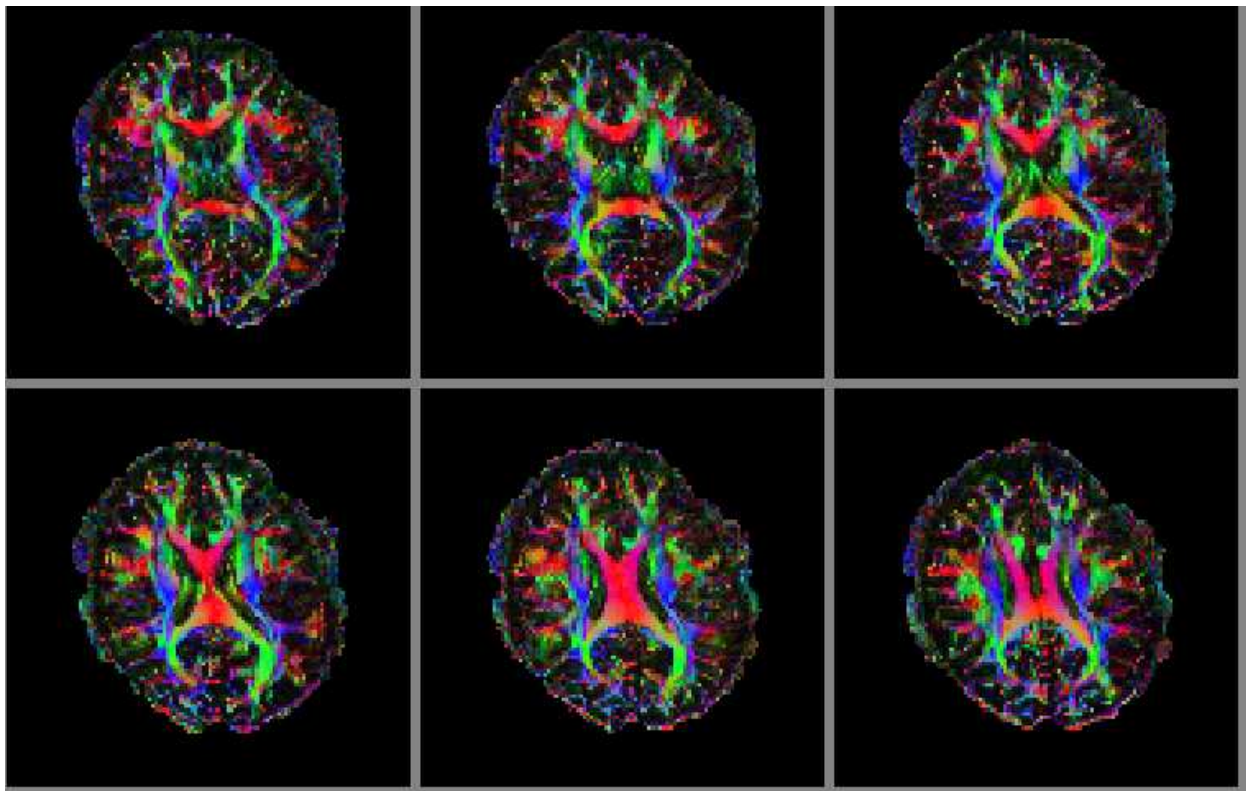
- of diffusion coefficients and anisotropy. *American Journal of Neuroradiology* 1997;18:1049-1056.
17. Schmierer K, Wheeler-Kingshott C, Tozer D, Boulby P, Parkes H, Yousry T, Scaravilli F, Barker G, Tofts P, Miller D. Quantitative magnetic resonance of postmortem multiple sclerosis brain before and after fixation. *Magnetic Resonance in Medicine* 2008;59:268-277.
 18. Widjaja E, Wei X, Vidarsson L, Moineddin R, Macgowan C, Nilsson D. Alteration of diffusion tensor parameters in the post mortem brain. *Magnetic Resonance Imaging* 2008;27:865-870.
 19. Guilfoyle D, Helpert J, Lim K. Diffusion tensor imaging in fixed brain tissue at 7T. *NMR in Biomedicine* 2003;16:77-81.
 20. Kamman R, Go K, Stomp G, Hulstaert C, Berendsen H. Changes of relaxation times T_1 and T_2 in rat tissues after biopsy and fixation. *Magnetic Resonance Imaging* 1985;3:245-250.
 21. Thickman D, Kundel H, Wolf G. Nuclear magnetic resonance characteristics of fresh and fixed tissue: The effect of elapsed time. *Radiology* 1983;148:183-185.
 22. Tovi M, Ericsson A. Measurements in T_1 and T_2 over time in formalin-fixed human whole-brain specimens. *Acta Radiology* 1992;33:400-404.
 23. Yong-Hing C, Obenaus A, Stryker R, Tong K, Sarty G. Magnetic resonance imaging and mathematical modeling of progressive formalin fixation of the brain. *Magnetic Resonance Imaging* 2005;54:324-332.
 24. D'Arceuil H, Westmoreland S, De Crespingy A. An approach to high resolution diffusion tensor imaging in fixed primate brain. *NeuroImage* 2007;35:553-565.
 25. Madi S, Hassan K, Narayana P. Diffusion tensor imaging of in vivo and excised rat spinal cord at 7 T with an icosahedral encoding scheme. *Magnetic Resonance in Medicine* 2005;53:118-125.
 26. Sun S, Neil J, Song S. Relative indices of water diffusion anisotropy are equivalent in live and formalin-fixed mouse brains. *Magnetic Resonance in Medicine* 2003;50:743-748.
 27. Englund E, Sjobeck M, Brockstedt S, Latt J, Larsson E. Diffusion Tensor MRI post mortem demonstrated cerebral white matter pathology. *Journal of Neurology* 2004;251:350-352.
 28. Larsson E, Englund E, Sjobeck M, Latt J, Brockstedt S. MRI with diffusion tensor imaging post-mortem at 3.0T in a patient with frontotemporal dementia. *Dementia and Geriatric Cognitive Disorders* 2004;17:316-319.
 29. Song S, Yoshino J, Le T, Lin S, Sun S, Cross A, et al. Demyelination increases radial diffusivity in corpus callosum of mouse brain. *NeuroImage* 2005;26:132-140.
 30. Zhang J, Miller M, Plachez C, Richards L, Yarowsky P, van Zijl P, et al. Mapping postnatal mouse brain development with diffusion tensor microimaging. *NeuroImage* 2005;26:1042-1051.
 31. McNab J, Miller K. Sensitivity of Diffusion Weighted Steady State Free Precession to Anisotropic Diffusion. *Magnetic Resonance in Medicine* 2008;60:405-413.

32. Landman B, Huang H, Prince J, Ying S. A Window for High-Resolution Post-Mortem DTI: Mapping Contrast Changes in Neural Degeneration. 2007; Berlin, Germany.
33. McNab J, Jbadi S, Deoni S, Dounaud G, Behrens T, Miller K. High resolution diffusion-weighted imaging in fixed human brain using diffusion-weighted steady state free precession. *NeuroImage* 2009;46:775-785.
34. McNab J, Voets N, Dounaud G, Jenkinson N, Aziz T, Miller K. A comparison of In Vivo and Ex Vivo Diffusion Tensor Imaging in the Same Patient. 2008; Toronto, Ontario, Canada.
35. Cox E, Gowland P. Measuring T2 and T2' in the Brain at 1.5T, 3T and 7T Using a Hybrid Gradient Echo-Spin Echo Sequence and EPI. 2008; Toronto, Ontario, Canada. p 1411.
36. Cox E, Gowland P. Simultaneous Quantification of T2 and T'2 Using a Combined Gradient Echo-Spin Echo Sequence at Ultrahigh Field. *magnetic Resonance in Medicine* 2010.
37. Schoenberg S, Dietrich O, Reiser M. *Parallel Imaging in Clinical MR Applications*. 2007.
38. Morgan P, Bowtell R, McIntyre D, Worthington B. Correction of spatial distortion in EPI due to inhomogeneous static magnetic fields using the reversed gradient method. *Journal of Magnetic Resonance Imaging* 2004;19(4):499-507.
39. Cox E, Gowland P. Measuring T2 and T2' in the brain at 1.5T, 3T and 7T using a hybrid gradient echo-spin echo sequence and EPI. 2008; Toronto, Ontario, Canada.
40. Wiggins C, Benner T, Wiggins G, Triantafyllou C, Wald L. In-vivo Human Diffusion Tensor Imaging at 7T: First Results. 2007.
41. Speck O, Zhong K. Diffusion Tensor Imaging at 7T: Expectations vs. reality check. 2009; Hawaii.
42. Sammet S, Koch R, Irfanoglu O, Schmalbrock P, Machiraju R, Knopp M. SENSE factor optimization for Diffusion Tensor Imaging of the Human Brain at 7T. 2007; Berlin.
43. Reischauer C, Jaermann T, Staempfli P, Pruessmann K, Thompson M, Boesinger P. 16-Channel DTI at 7T: initial experiments. 2007; Berlin.
44. Polders D, Hoogduin H, Donahue M, Hendrikse J, Luijten P. Comparison of SNR and Diffusion Parameters on 1.5T, 3.0T and 7.0T. 2009.
45. Morgan P, Coxon R, Habib J, Gowland P, Bowtell R. Comparison of Sequences for Improved Diffusion Weighted Imaging at 7 T. *ISMRM*; 2008.
46. Luetzkendorf R, Moench T, Hollmann M, Baecke S, Tempelmann C, Stadler J, Bernarding J. In Vivo Human Brain Diffusion Tensor Imaging (DTI) at 3T and 7 T. 2008; Toronto.
47. Mukherjee P, Hess C, Xu D, Han E, Kelley D, Vigneron D. Development and initial evaluation of 7-T q-ball imaging of the human brain. *Magnetic Resonance Imaging* 2008;26:171-180.
48. McRobbie D, Moore E, Graves M. *MRI from picture to proton*. Press CU, editor; 2007.

49. Bernstein M, King K, Zhou X. Handbook of MRI Pulse sequences. Press EA, editor; 2004.
50. Wells W, Viola P, Atsumi H, Nakajima S, Kikinis R. Multi-modal volume registration by maximization of mutual information. *Medical Image Analysis* 1996;1(1):35-51.
51. Morgan P, Bowtell R, McIntyre D, Worthington B. Correction of Spatial Distortion in EPI Due to Inhomogeneous Static Magnetic Fields Using the Reversed Gradient Method. *Journal of Magnetic Resonance Imaging* 2004;19:499-507.

Chapter 4. : Motivation, Optimization & Artefact Reduction

Reduction



DTI colour maps of a healthy volunteer acquired at 7 T with optimized settings

4.1 Introduction

This chapter explores the opportunities and challenges of performing DTI of the *in vivo* human brain at the ultra high field (UHF) strength of 7 T. Through direct comparisons of acquisitions at 7 T and 3 T DTI, potential practical advantages motivating the use of 7 T are, for the first time, assessed both comprehensively and quantitatively. The main artefacts incurred in 7 T DTI acquisitions are identified, and appropriate measures for their alleviation are explored. This information is then used to formulate a set of parameter-selection guidelines for the design of DTI acquisition protocols at 7 T, through which the benefits of UHF DTI can be optimally utilized, and artefacts minimized. Finally, novel effects observed at UHF and potential directions for future research are highlighted.

4.1.1 Motivation for pursuing DTI at UHF

Ever since the inception of MRI, an unabated trend towards the deployment of increasingly higher field-strengths can be observed (2). This section will introduce and outline potential opportunities of UHF MRI pertinent to *in vivo* DTI applications.

Measurement sensitivity

The relatively low measurement sensitivity of MRI is widely regarded as its main limitation (2). Predicted improvements in sensitivity with field-strength (2, 3) have consequently become the primary motivation driving the development of higher field-strength MRI.

In *in vivo* DTI acquisitions, several factors further exacerbate the impact of MRI's limited sensitivity. To reduce sensitivity to motion artefacts, ultra-fast single-shot acquisition sequences are prevalently used. This means that the signal generated from a single RF excitation must suffice for the formation of an entire image. To sample a corresponding region of k-space, multiple echoes of this signal are generated. Diffusion and T2 relaxation, however, result in a decline in the amplitude of successive echoes, and thus impose a hard and fast limit on the number of k-space lines that can be sampled. At a given FOV, this corresponds to an inherent image resolution limit. Typical in-plane resolutions of *in vivo* DTI datasets of the human brain at 3 T are $2 \times 2 \text{ mm}^2$. This is low compared to the intricate structure of white matter tissue, and

thus significantly limits the ability to resolve small-scale structures. The application of diffusion sensitization gradients imposes further constraints on the achievable measurement sensitivity. By amplifying the dephasing effect resulting from IVIM (intra-voxel coherent motion), the level of diffusion is encoded as an attenuation of the measurable signal. The application of these gradients also imposes relatively long echo times, during which signal amplitudes are reduced through T2 decay. Another practical limitation is the typically long scan duration of DTI datasets, which comprise at least seven acquisitions. This limits the number of averages that may be recorded for the suppression of noise components of measured signals. Finally, the effect of low SNR has been demonstrated to not only reduce the scan-rescan precision of individual DWI measurements, but also to have a knock-on effect on the accuracy of calculated scalar DTI indices; for instance, FA values have been reported to be positively biased at low SNR (4, 5).

Due to its central importance, a number of approaches have been developed to improve the SNR of MRI acquisitions. These include post-acquisition image processing to isolate, and subsequently suppress, noise components of the measured signal (e.g. (7-9)); the design and development of RF coils to more efficiently record the generated signal (e.g. (6,10-14)); and the selection of appropriate acquisition sequences and parameters. Because these approaches generally improve image SNR by maximizing the efficiency by which emitted RF-signals are utilized, however, they are ultimately still limited by the intensity of the underlying signal produced.

Increasing the field-strength at which MRI experiments are performed has the unique advantage of increasing the magnitude of generated RF-signals at the source, thus achieving a true increase in measurement sensitivity. This occurs as a result of two separate physical mechanisms. As discussed in Chapter 1, spins within a strong magnetic field may assume one of a finite number of discrete energy states, aligned either with or against the orientation of the main magnetic field. The relatively lower energy of spins aligned with the magnetic field, results in such states being inherently favoured, and thus in an intrinsic increase in their relative population. This results in the formation of a net magnetization vector aligned with the main

magnetic field. Following excitation, this net magnetization vector is flipped into the transverse plane and precesses about the direction of the main magnetic field with the Larmor frequency. This changing flux ultimately induces electric currents in tuned RF-receiver coils and thus represents the measurable signal. The magnitude of the measurable signal is therefore dependent on the magnitude of the net magnetization vector and the Larmor frequency. Both, in turn, are governed by the magnetic field-strength at which MRI experiments are performed. The magnitude of the net magnetization vector is determined by the excess of spins aligned with, over those aligned against, the main magnetic field. For large numbers of protons, the size of the population of each state is given by the Boltzmann distribution:

$$\frac{N_{LoE}}{N_{HiE}} = \exp\left(\frac{\Delta\varepsilon}{k_B T}\right) = \exp\left(\frac{\gamma\hbar B_o}{k_B T}\right) \quad (4.1)$$

Where:

N_{LoE} : Number of protons aligned with B_o

N_{HiE} : Number of protons aligned against B_o

$\Delta\varepsilon$: Energy difference between the low and high energy alignment states

k_B : Boltzmann constant

T : Temperature in K

\hbar : Plank's constant divided by 2π

Compared to the thermal energy at body temperature, the energy difference between the low and high energy-alignment states is small under magnetic field-strengths used in clinical MRI. This allows spins to readily transition between energy alignment states, effectively limiting the magnitude of the net magnetization vector. The separation of energy states increases with field-strength, resulting in the formation of larger net magnetization vectors. However, even with this increase in separation, at field-strengths of 7 T (2) the gap between energy states is still typically small compared to the levels of thermal energy, allowing Eq. 4.1 to be simplified to:

$$\frac{N_{LoE}}{N_{HiE}} = 1 + \frac{\gamma\hbar B_o}{k_B T} \quad (4.2)$$

From this, the net magnetization vector amplitude governed by the excess of protons in alignment with B_0 can be shown to thus increase linearly with field-strength:

$$N_{\text{Excess}} = N_{\text{LoE}} - N_{\text{HiE}} = \frac{N_{\text{LoE}} + N_{\text{HiE}}}{2} + \frac{\gamma \hbar B_0}{k_B T} \quad (4.3)$$

Typically, for every 2×10^6 water molecules, only 9 contribute to the MRI signal at 1.5 T, 18 at 3 T and 42 at 7 T (15). The Larmor frequency at which the net magnetization vector precesses about the main magnetic field is also linearly proportional to the magnetic field-strength (c.f. Equation 1.12 in Section 1.2.2 of Chapter 1). In combination, this linear increase in the net magnetization and the Larmor frequency achieves a quadratic increase in signal intensity with field-strength.

In addition to the abovementioned implications on signal intensity, noise levels within the measurable signal also increase with field strength. This is the result of Eddy currents induced in the body by RF-excitation. To distinguish these from Eddy currents induced gradient switching in the electrically conducting components of the scanner, they are referred to as RF-Eddy currents. RF-Eddy currents increase linearly with the Larmor frequency, and thus field-strength, resulting in a linear increase of noise in the recorded signal (10). These theoretical considerations thus predict a net linear increase of measurement sensitivity with field-strength.

Receiver bandwidth

After sensitivity, the second main challenge of *in vivo* DTI is the susceptibility of prevalently employed single-shot sequences to phase errors. Indeed, this has been referred to as the “Achilles heel of 2D single-shot EPI” (16).

Sources of phase errors include bulk motion of the subject being scanned, and magnetic field inhomogeneities. The latter may result from imperfections of the main magnetic field itself, or from external influences. These include differences in magnetic susceptibility within the object being scanned, and magnetic fields generated by Eddy-currents induced in electrically conducting components of the MRI system by powerful fast-switching gradients.

While the application of diffusion sensitization gradients amplifies motion-induced phase errors, these can effectively be reduced by the use of ultra-fast single-shot sequences. However, single-shot EPI acquisitions are more sensitive to phase errors along their phase encode direction. This is because the receiver bandwidth of an MRI acquisition is equal to the data sampling rate (17). In single-shot acquisitions, since an entire (frequency encoded) line of k-space must be acquired between each phase encode increment, the sampling rate along the phase encode direction is relatively long. Also, since the signal corresponding to an entire image is sampled using a single k-space trajectory, incurred phase errors will propagate throughout the acquired k-space.

In MRI, spatial encoding is based on the signal phase at the time of acquisition. If phase errors exceed the bandwidth separating adjacent voxels, then components of the measured signal will be allocated to incorrect spatial locations, manifesting as distortions or even signal voids in images. Eddy-current induced distortion patterns change over the course of a sequence, and according to the orientation of the applied diffusion sensitizing gradients. This adversely affects the voxel-to-voxel correspondence of the images comprising DTI datasets.

To increase the receiver bandwidth in single shot acquisition sequences, the data sampling rate must be reduced. This could be achieved through the development of more powerful gradients and/or by data acquisition strategies that reduce the number of phase encode steps needed for the formation of an image. The development of improved gradient systems is beyond the scope of this investigation. A main strategy to reduce the number of phase encode steps is parallel Imaging, where signals are recorded using multiple receiver coils, each recording a different set of interleaved lines of k-space independently. This is the equivalent of dividing the FOV into smaller sections, each being captured independently by a different coil element. The positive effect of parallel Imaging in reducing susceptibility to bandwidth related artefacts has been well documented in several investigations e.g. 18-20).

Particularly relevant to this chapter, the maximum parallel Imaging reduction factor has been shown to increase at higher field-strengths, as demonstrated in 2004 by Wiesinger et al. through simulations using electrodynamic scaling (20, 21).

4.1.2 Review of existing investigations of *in vivo* Diffusion MRI at UHF

In recent years, these potential advantages, in combination with the necessary advancements in the technical development of UHF MRI scanners, have led to a surge in interest to explore *in vivo* Diffusion MRI at UHF. This section provides an up-to-date summary of the relevant literature, describing the current state of UHF DTI, and highlighting the outstanding limitations and open questions that will subsequently be tackled in this chapter

Previously reported investigations on diffusion measurements at UHF may be divided into three main categories: feasibility studies; artefact description and alleviation strategies; and direct comparisons between measurement sensitivity and artefact susceptibility at 7 T and lower field-strengths.

Under the first category, the principle feasibility of DTI at 7 T was first independently demonstrated in 2007 by Reischauer et al. (22), Sammet et al. (23) and Wiggins et al. (24) who used standard acquisition protocols to record DTI datasets. Initial qualitative assessments suggested that the level of technical maturity reached by contemporary UHF MRI scanners was adequate for the further exploration of *in vivo* DTI at 7 T. First steps towards parameter optimisation tested the efficacy of parallel Imaging to reduce bandwidth related artefacts, with the evaluation based on visual analysis of individual acquisitions (22, 23). Sub-millimetre in-plane resolutions of $0.8 \times 0.8 \text{ mm}^2$ (22) were reported and attributed to apparent SNR gains, although this conclusion was later disputed (25, 26). Similarly, the principle feasibility of 7 T for higher order diffusion measurements such as Q-ball Imaging (27, 28) and HARDI (29) was also demonstrated. While the b-value used by most acquisition protocols had generally been limited to a range from 700 s mm^{-2} to 900 s mm^{-2} , presumably to minimize echo time and/or Eddy-current distortions, b-values of up to 6000 s mm^{-2} were used successfully for Q-ball imaging (28). By successfully resolving crossing fibres in the anterior and posterior supratentorial brain regions, the ability to achieve adequate data quality for high-order Diffusion analysis was demonstrated.

The second category of investigations, summarized in Table 4-1, built an essential knowledge base of the dominant sources of artefact displayed by UHF DTI and a repertoire of techniques proposed for their alleviation.

Artefact type	Underlying cause	Field-strength dependence	Suggested solutions
Static distortions	(i) Technical challenges to generate strong Bo fields of high homogeneity	✓	(i) Parallel Imaging to increase receiver bandwidth (22, 23, 27, 31)
	(ii) Magnetic susceptibility changes in tissue warping Bo fields	✓	(ii) Shim calibration (24)
	(iii) B1 inhomogeneities		(iii) Higher order shimming (23, 27)
	(iv) Sub-optimal system tuning	✓	(iv) Field-map correction (29)
Eddy current distortions	(i) Strong, fast-switching diffusion sensitization gradients	Subject to optimal calibration	(v) Reversed gradient method (32, 33)
			(ii) Pulse-sequence (TRSE) (33)
			(iii) Parallel Imaging (24)
Signal void	(i) Signal voids due to RF wavelength becoming comparable to object dimensions at high fields.	✓	(i) Multiple channel excitation (22)
	(ii) Image distortion	✓	(ii) Manual adjustment of EF excitation power (24)
Fat artefact	(i) Linear dependence of difference between fat and water Larmor frequencies with field-strength.	✓	(i) Improved lipid suppression RF-pulses (27) (no specific pulse shape, setting suggested).
			(ii) Parallel Imaging (24)

Table 4-1 Summary of reported artefacts and proposed techniques for their alleviation in reported ultra high field-strength DTI investigations

As at 3 T (16), the majority of artefacts in DTI at 7 T were shown to be closely related to bandwidth. The severity of these artefacts was found exacerbated at higher fields leading to considerable attention being paid to the maximization of receiver bandwidth through parallel Imaging (18, 19, 30). Based on the qualitative visual analysis of distortion, optimal parallel Imaging reduction factors ranging between three (23) and four (22) were proposed. The second main category of artefacts resulted from B1 inhomogeneity leading to signal voids and poor fat suppression. This was found exacerbated in sequences using double echo diffusion preparation (24).

The third category of investigations provided first insights into benefits and drawbacks of UHF DTI. This was achieved by direct quantitative comparisons of DTI acquisitions performed at 7 T and lower field-strengths. Quantitative inter-field-strength SNR comparisons for *in vivo* DTI protocols were performed independently by Speck et al. (25) and Polders et al. (26). Reported results, however, varied considerably: While theoretical calculations by Speck et al. predicted a 4 % increase in SNR at 7 T compared to 3 T (113), measured values ranged from a 15 % decrease (25) to a 110 % increase (26). The use of identical field-strengths, and the similar experimental aim and design suggest that these alterations in SNR efficiency are likely to be the result of differences in the hardware, as well as the acquisition sequence and/or parameters used.

4.1.3 Purpose of this study

In summary, the knowledge accumulated by previous studies have illustrated that the technical maturity displayed by the current generation of UHF scanners has reached a level adequate for the exploration of *in vivo* DTI applications. A consensus exists that at UHF the susceptibility to image artefacts, particularly those related to phase errors and B1 inhomogeneities, increases. Their alleviation is the subject of ongoing research efforts that, to date have led to the proposition of a number of strategies. The main anticipated advantages of performing *in vivo* DTI at UHF are potential improvements in measurement sensitivity and the compatibility of acquisitions with higher parallel Imaging reduction factors.

However, despite their pivotal role in motivating the continued exploration of DTI at UHF, comparatively little is known about if, how and by how much these potential advantages can be exploited in practical acquisitions. The two investigations that to date have attempted to quantitatively compare the practically realizable measurement sensitivity differences in DTI protocols at 7 T and 3 T (25, 26), used both measurements and theoretical predictions but failed to reach a consensus. The disparity between measured results indicates that if sub-optimal acquisition parameters are selected, acquisitions may in fact experience a loss in SNR at 7 T. Thus far, no guidelines exist on which parameters are pertinent for the efficient utilization of potential SNR gains in DTI acquisitions at UHF, or on how these should be selected. Similarly, while the increase in receiver bandwidth via parallel Imaging could effectively reduce the susceptibility of images to bandwidth related artefacts, the optimization of reduction factors has been limited to simulations (21) and qualitative visual assessments of image distortion (22,23,27,31). While this led to the recommendation of specific parallel Imaging reduction factors, the effect of the intrinsic penalty of parallel Imaging on measurement sensitivity, which had motivated the use of 7 T systems in the first place, had not been considered. The g-factors resulting from the use of higher parallel Imaging factors were also not quantified.

The purpose of this investigation was to address these outstanding issues, thereby facilitating the introduction of 7 T MRI scanners to DTI application in clinical and biomedical research studies.

4.1.4 Structure of this study

This study is divided into the following sections:

First, to lay the foundations for subsequent acquisition characterization, and protocol optimization steps, the optimization criteria are explicitly defined. The acquisition protocol that currently best meets these criteria is identified from literature, and acquisitions replicated on the available 7 T MRI scanner. Subsequent comparisons of measured and published results allow the reproducibility of results across sites to be established, and the suitability of the in-house scanner setup to be assessed.

Next, practical advantages of UHF for DTI applications are quantitatively assessed through measurements. Experiments were designed to minimize confounding influences pertaining to the suitability and performance of the selected acquisition sequence, protocol parameters and scanner hardware used. This was to facilitate the isolation and subsequent assessment the effects of field-strength, making results applicable to any 7 T scanner. This informs whether potential practical advantages merit the continued exploration of DTI at UHF, and indicates which technical developments are needed to improve the efficiency with which they can be utilized.

Thirdly, practical guidelines on the design of DTI acquisition protocols to optimally meet the defined optimization criteria while minimizing susceptibility to artefacts on the in-house 7 T system were formulated.

In the discussion section, observations of particular interest from a number of pilot investigations are listed to provide further insights into the practical performance of the in-house 7 T system, and to suggest avenues for future exploration. Finally, in the appendix, the incompatibility of the widely used difference method (54) for quantifying SNR *in vivo* at 7 T is demonstrated, and the implementation and validation of a suitable alternative is outlined.

4.2 Methods and Materials

4.2.1 Datasets

4.2.1.1 Selecting the starting protocol (Dataset 4-1):

Purpose

Dataset 4-1 was acquired as a replication of the investigation by Polders et al. (26) in which an acquisition protocol was presented that, to date, best met our primary optimization goal of maximizing SNR. If successful, this protocol is to be adopted as the starting protocol of this investigation to form the basis for subsequent optimization and quantitative characterization steps. The reproducibility of results will also, in turn, serve as a measure for the inter-site compatibility of results presented in this study, and allow the assessment of the in-house MRI system setup performance.

Acquisition Details

Parameter	Dataset 4-1a (<i>in vivo</i> , 7 T)	Dataset 4-1b (<i>in vivo</i> , 3 T)
Scanner used	SPMMRC 7 T	SPMMRC 3 T
Sequence	Single shot spin echo EPI	Single shot spin echo EPI
Noise-only acquisition	yes	yes
Repetition time (in ms)	10 000	10 000
Echo time	67 ms	51 ms
Diffusion sensitization scheme	Philips 15 direction scheme	Philips 15 direction scheme
b-value	800 s mm ⁻²	800 s mm ⁻²
Field of view (in mm)	220 x 220	220 x 220
Matrix	112 x 112	112 x 112
Slice thickness (in mm)	2	2
Number of slices	34	34
Number of signal averages	2	2
SENSE reduction factor	2	2
Fat suppression technique	SPIR	SPIR
Water-fat shift (in pixels)	46.3481	19.8423

Table 4-2 Acquisition parameters listing for Datasets 4-1.

Experimental Setup

Acquisitions were performed as similarly as possible to those described by Polders et al. (26). Necessary modifications of parameters included that b-values of 800 s mm⁻² were used instead of the 1000 s mm⁻² in (26). This was necessitated by the severe Eddy current distortions observed when using b-values of 1000 s mm⁻² at 7 T. SENSE factors were set to 2, which was the prevalent setting at 3 T. Finally, in the interest of the total scan time, the 15 direction Philips

diffusion sensitization scheme was used rather than the 32 direction scheme in (26). This did not affect the SNR quantification, which is performed on $b=0$ images. Conversely, the use of fewer diffusion sensitization directions facilitates the detection of artefacts, and is more representative of acquisition protocols typically used in clinical/biomedical research applications. The same volunteer was scanned at both field-strengths in order to eliminate inter-subject differences that would otherwise require the scanning of a larger cohort of volunteers.

FSL (36) was used for the Eddy-current distortion correction and calculation of diffusion tensors from the acquired datasets, and the display of FA colour maps. On these, ROIs were drawn as described in (26) delineating the corpus callosum, cerebrospinal tract and the optic radiation.

The quantification SNR was performed within these ROIs using the NEMA-DNS method described in the appendix of this chapter. To this end four dynamic $b=0$ acquisitions were recorded, with the last dynamic representing a noise-only image.

4.2.1.2 SNR characterization (Dataset 4-2):

Purpose

Dataset 4-2 was acquired for the in-depth characterization of the practical effect of field-strength on SNR performance in DTI acquisitions.

Acquisition Details

Parameter	Dataset 4-2a (<i>in vivo</i> , 7 T)	Dataset 4-2b (<i>in vivo</i> , 3 T)	Dataset 4-2c (<i>in vitro</i> , 7 T)	Dataset 4-2d (<i>in vitro</i> , 3 T)
Scanner used	SPMMRC 7 T	SPMMRC 3 T	SPMMRC 7 T	SPMMRC 3 T
Sequence	Single-shot spin echo EPI	Single-shot spin echo EPI	Single-shot spin echo EPI	Single-shot spin echo EPI
Acquisition description	4 dynamic b=0 scans; 4 th dynamic is noise-only	4 dynamic b=0 scans; 4 th dynamic is noise-only	4 dynamic b=0 scans; 4 th dynamic is noise-only	4 dynamic b=0 scans; 4 th dynamic is noise-only
Repetition time (in ms)	10 000	10 000	10 000	10 000
Range of echo times (in ms)	30ms to 130ms in 10ms increments	30ms to 130ms in 10ms increments	30ms to 100 ms in 5 ms intervals 100ms to 170 ms in 10 ms intervals	30ms to 100 ms in 5 ms intervals 100ms to 170 ms in 10 ms intervals
Field of view (in mm)	220 x 220	220 x 220	192 x 192	192 x 192
Matrix	112 x 112	112 x 112	96 x 96	96 x 96
Slice thickness (in mm)	2	2	2	2
Number of slices	34	34	34	34
Number of signal averages	2	2	1	1
SENSE reduction factor	2	2	2	2
Fat suppression technique	SPIR	SPIR	SPIR	SPIR
Water-fat shift (in pixels)	46.3481	19.8423	41.0213	17.5891

Table 4-3 Acquisition parameters listing for Datasets 4-2.

Experimental Setup

For the assessment of the field-strength dependency of SNR performance in practical DTI protocols, both *in vivo* and *in vitro* measurements were performed.

To isolate field-strength specific effects, steps were taken to minimize potential confounding factors. This included the use of identical acquisition sequences and parameters; the use of the same volunteer/phantom; and the use of MRI systems of the same manufacturer and series at both field-strengths. Unavoidable differences in the acquisition setup included the gradients and RF-receiver coil available for each system (c.f. Chapter 1).

To account for potential field-strength specific effects over space (e.g. differences in the frequencies of RF signals may result B1 inhomogeneities, differences in RF penetration etc.) and time (e.g. T2 signal relaxation rates), SNR was measured both at different spatial locations, and over a range of echo times.

SNR measurements were recorded in accordance with the NEMA-DNS (37) method detailed in the Appendix to this chapter. Both *in vivo* and *in vitro* acquisitions were recorded. The former allowed the assessment of SNR performance in white matter tissue and were recorded during the same scan session as Datasets 4-1. To assess the spatial distribution of SNR levels at both field-strengths, the ROIs depicted in Figure 4-1 were used. *In vitro* measurements used the homogenous agar phantom described in Chapter 1. This allowed SNR maps to be calculated using a sliding window approach with a 3 x 3 x 3 voxel neighbourhood.

4.2.1.3 Parallel Imaging and partial Fourier optimization (Dataset 4-3).

Purpose

The aim of Dataset 4-3 was to investigate the effects of both parallel Imaging (SENSE) and partial Fourier (Halfscan) acquisitions on single-shot 2D EPI acquisitions at 7T.

This dataset is used both in the acquisition characterization (Section 4.3.3), and acquisition protocol optimization (Section 4.3.4) sections of this investigation. For the former, the range of

SENSE factors used allows the maximum SENSE factor at which the highest g-factor did not exceed the defined maximum limit of 1.2, to be measured. For the latter, the quantification of SNR and receiver bandwidths of each of the SENSE and Halfscan factor combinations allowed the identification of optimal settings.

Acquisition Details

Parameter	Dataset 4-3 (<i>in vitro</i> , 7 T)
Scanner	SPMMRC 7 T
Sequence	Single-shot spin echo EPI
Acquisition description	4 dynamic b=0 scans; 4 th dynamic is noise-only
Repetition time (in ms)	10 000
Flip angle	15°
Field of view (in mm)	192 x 192
Matrix	96 x 96
Slice thickness (in mm)	2
Number of slices	35
Number of signal averages	1

Table 4-4 Acquisition parameters listing for Datasets 4-3.

Acquisitions were performed under all combinations of nine different SENSE factor (0, 2, 2.5, 3, 3.5, 4, 4.5, 5 and 6) and three Halfscan factor settings (1, 0.7, 0.6). To account for the effect of different SENSE and Halfscan factors on echo time, the minimum echo time required to apply b-values of 800 s mm⁻² was determined and set for each acquisition accordingly. These values are as listed in Table 4-5 below.

		SENSE reduction factor								
		off	2	2.5	3	3.5	4	4.5	5	6
Halfscan	off	114.4	85.41	79.14	74.4	72.04	69.69	68.56	67.36	65.31
	0.7	76.36	67.36	65.31	63.25	61.89	61.01	61.01	61.01	59.85
	0.6	66.29	61.89	61.01	59.85	58.98	58.98	58.98	58.98	58.98

Table 4-5 Set echo times for Dataset 4-3 for various SENSE and Halfscan factor settings.

Experimental Setup

All acquisitions were performed on the phantom (c.f. Chapter 1) in accordance with the NEMA-DNS method (c.f. Appendix to this chapter). Noise maps were generated from the noise only acquisitions with a sliding window approach using a 3 x 3 x 3 voxel neighbourhood.

4.2.1.4 Acquisition sequence selection (Dataset 4-4):

Purpose

Dataset 4-4 directly compares the quality of pertinent acquisition characteristics (SNR and susceptibility to distortion) of all DTI sequences available on the in-house system. The identification of the best-suited acquisition sequence for the subsequent refinement of parameters forms the first step of the general acquisition protocol optimization.

Acquisition Details

Acquisitions comprised 24 axial slices with 2 mm slice thickness and a FOV of 192 x 192 mm recorded under a 96 x 96 matrix. The Partial Fourier reduction factor used was 0.72, and no parallel Imaging was implemented. The repetition time was set to 10 000 ms and the minimum

echo time was used. The Philips 15 direction scheme was selected, with b-values set to 800 s mm⁻². Under these settings, the following pulse sequences were investigated:

(i) Dataset 4-4.a: Spin echo (SE) diffusion weighting with EPI readout

This acquisition sequence has established itself as the prevalent technique for routine DTI acquisitions, and was used in the gold standard protocol defined in (26).

(ii) Dataset 4-4.b: Twice refocused spin echo (TRSE) diffusion weighting (with asymmetry factor 0.2) and gradient echo EPI readout.

(iii) Dataset 4-4.c: TRSE (with asymmetry factor 0.5) and gradient echo EPI readout

(iv) Dataset 4-4.d: TRSE (with asymmetry factor 0.8) and gradient echo EPI readout

The TRSE diffusion weighting allows the alleviation of Eddy-current distortions through the mutual cancellation of opposite Eddy-currents (38). The amount of cancellation of Eddy-current distortion in TRSE sequence is influenced by the relationship between the rate of decay of the Eddy-current distortion and the two echo times used. The ratio of the two echo times is represented by an asymmetry factor.

(v) Dataset 4-4.e: Stimulated echo (STE) diffusion weighting followed by spin echo EPI readout

(vi) Dataset 4-4.f: STE diffusion weighting followed by gradient echo EPI readout

STE sequences facilitate the temporal separation of Eddy-current inducing diffusion weighting gradients from the signal recording section of the acquisition protocol by storing the magnetization in the longitudinal orientation which only experiences the comparatively slow T1 decay. The so-called mixing time was set to 50 ms.

Experimental setup

The selection of the optimum acquisition sequence was based on comparisons of SNR performance and image distortion. The use of distortion as a measure of the susceptibility to bandwidth related artefacts was partially motivated by the fact that at the time of the experiment, Eddy-current induced distortions were considered the primary limiting factor of

DTI at 7 T. These were later alleviated through improved gradient calibration by the MRI system vendor.

SNR measurements were performed over the volume of $b=0$ acquisitions of a homogenous agar phantom. Measurements were performed before the development and validation of the NEMA-DNS technique (Appendix). Acquisitions were thus performed without the use of SENSE, and noise was measured as the standard deviation of background signal outside the object (39, 40).

Spatial distortion was measured *in vivo* based on two DTI acquisitions using phase encode gradients of opposite polarity. This resulted in opposite distortion pattern allowing the mean distortions to be calculated according to the reversed gradient correction scheme (32). A scalar index of overall distortion is defined as the mean pixel shift over all measured diffusion sensitization directions.

4.2.1.5 B1-inhomogeneity artefact (Dataset 4-5):

Purpose

The final part of the acquisition protocol optimization addressed the alleviation of the most prominent artefacts. One of the main artefacts, both in literature and observed in this investigation, were signal voids as a result of B1 inhomogeneities. Dataset 4-5 forms part of a study assessing whether the use of a refocusing RF-pulse of alternative shape could provide better B1 homogeneity than the standard sinc pulses.

Acquisition Details

Parameter	Dataset 4-5a (<i>in vivo</i> ; sinc refocusing)	Dataset 4-5b (<i>in vivo</i> ; echo2 refocusing)	Dataset 4-5c (<i>in vitro</i> echo 2 flip angle optimization)
Scanner used	SPMMRC 7 T	SPMMRC 7 T	SPMMRC 7 T
Sequence	Single-shot spin echo EPI	Single-shot spin echo EPI	Single-shot spin echo EPI
Acquisition description	ADC acquisition scheme	ADC acquisition scheme	ADC acquisition scheme
Repetition time (in ms)	10 000	10 000	10 000
Echo time (in ms)	64	64	67
Diffusion sensitization scheme	Philips 3 direction scheme	Philips 3 direction scheme	Philips 3 direction scheme
b-value	800 s mm ⁻²	800 s mm ⁻²	800 s mm ⁻²
Field of view (in mm)	224 x 224	224 x 224	224 x 224
Matrix	112 x 112	112 x 112	112 x 112
Slice thickness (in mm)	2	2	2
Number of slices	34	34	34
Number of signal averages	2	2	2
SENSE reduction factor	2	2	2
Fat suppression technique	SPIR	SPIR	SPIR
RF excitation pulse shape	Sinc	Sinc	Sinc
RF excitation pulse flip angle	90	90	90
RF refocusing pulse shape	Sinc	Echo2	Echo2
RF refocusing pulse flip angle	180	220	150 to 290 in 10 intervals

Table 4-6 Acquisition parameters listing for Datasets 4-5.

Experimental setup

Datasets 4-5a and b comprised *in vivo* b=0 acquisitions, and diffusion weighted acquisitions with diffusion sensitization applied along the frequency encode, phase encode and slice select

orientations respectively. Acquisitions were performed using sinc (the standard pulse shape) and echo2 (the proposed pulse shape) shaped refocusing pulses respectively. This allowed the direct visual comparison of the effect of pulse shape on B1 homogeneity. On the in-house system under research mode, the refocusing pulse shape could be set to echo2 in the sequence development editor (the parameter 'rf_shape' was selected within the 'RF object' 'Echo' and set to echo2).

Dataset 4-5c was recorded to test whether perceived signal intensity reductions (not illustrated) when using an echo2 refocusing pulse could be overcome by changing the prescribed flip angle. *In vitro* acquisitions on a homogenous agar phantom (Chapter 1) were performed at flip angles of 150 ° to 290 ° in 10 ° intervals. SNR was measured within the central 10 x 10 x 10 voxel region, where the prescribed flip angle was expected to be most accurate. SNR measurements of dataset 4-5c were performed according to the NEMA-DNS method (c.f. Appendix) using four dynamic acquisitions with the last dynamic being a noise-only measurement.

4.2.1.6 Fat suppression artefact (Dataset 4-6):

Purpose

The second main category of observed artefact in DTI acquisitions at 7 T is poor fat suppression. Dataset 4-6 was acquired to characterize, and to assess the efficacy of both the fat suppression techniques provided by the vendor (SPIR (41) and SPAIR (41, 42), and the slice-selection reversed gradient (SSRG) technique proposed by Nagy et al. (43).

Acquisition Details

Parameter	Dataset 4-6a (no fat suppression)	Dataset 4-6b (SPIR fat suppression)	Dataset 4-6c (SPAIR fat suppression)	Dataset 4-6d (SSRG fat suppression)
Scanner used	SPMMRC 7 T	SPMMRC 7 T	SPMMRC 7 T	SPMMRC 7 T
Repetition time (in ms)	10 000	10 000	10 000	10 000
Echo time (in ms)	71	71	71	71
Field of view (in mm)	220 x 220	220 x 220	220 x 220	220 x 220
Matrix	112 x 112	112 x 112	112 x 112	112 x 112
Slice thickness (in mm)	2	2	2	2
Number of slices	34	34	34	34
Diffusion scheme	Philips 6 directions	Philips 6 directions	Philips 6 directions	Philips 6 directions
b-values (in s mm ⁻²)	800	800	800	800
SENSE factor	2	2	2	2
Fat suppression	none	SPIR	SPAIR	SSRG
Water-fat shift (in pixels)	49.348	49.348	46.348	49.348

Table 4-7 Acquisition parameters listing for Datasets 4-6.

Experimental Details

Dataset 4-6a illustrates the effect of fat on acquired images allowing the visual assessment of the efficacy of various fat suppression techniques. Datasets 4-6b and c allowed the assessment of vendor provided fat suppression techniques, while Dataset 4-6d used the SSRG technique. The SSRG technique required the polarity of the excitation and refocusing pulse to be inverted. On the in-house system, this could be done under the research mode by setting the control parameter 'GRs_echo scale' to -1, and 'Min rel slice gap_SE to zero.

4.3 Results

The aim of this investigation was to provide the information required to allow practical *in vivo* DTI applications to be conducted at 7 T. This is achieved by building on the foundations laid by previous investigations that had focused on advancing the technical development, and ultimately established the feasibility of UHF *in vivo* DTI. Inconsistent and insufficient information, however, is available on if, how, and by how much 7 T can benefit practical DTI applications. This knowledge is essential for establishing the motivation, and aiding in the design of optimal DTI acquisition protocols at 7 T.

This investigation takes a comprehensive and quantitative approach to address these outstanding issues. First, in Section 4.3.1, specifying the optimization goals, defining a suitable starting protocol and assessing the reproducibility of results between sites, lay the foundation for subsequent characterization and optimization steps. Next, in Section 4.3.2, the questions of ‘if, and by how much’ *in vivo* DTI applications may benefit from being performed at 7 T are addressed. For this, field-strength specific acquisition properties of interest are compared between 7 T and 3 T in a manner that minimizes confounding influences pertaining to the scanner hardware and acquisition protocols used. Finally, in Section 4.3.3, the question of ‘how’ these potential benefits may be optimally exploited, and potential drawbacks minimized, is addressed. For this, a set of guidelines on the design of *in vivo* DTI acquisition protocols on the in-house 7 T system is formulated.

4.3.1 Preliminary assessment of UHF DTI on the in-house 7 T MRI system

As already outlined in the Introduction to this chapter (Section 4.1.2), studies on *in vivo* DTI at UHF in literature have pursued a large variety of aims. However, even studies with identical goals, such as the characterization of SNR differences at 3 T and 7 T, using similar experimental designs (25, 26), differed in their results and subsequent conclusions drawn. This highlights the importance of clear specification of the optimization aims, and to establish the reproducibility of findings across sites.

In this section of the chapter, the foundation for subsequent acquisition characterization and optimization steps is laid in two parts. First, the optimization aims and their order of priority are

stated clearly. Next, the acquisition protocol that best meets these criteria is identified from current literature, and replicated on the in-house 7 T MRI scanner.

Details of each of these preliminary steps follow below:

4.3.1.1 Optimization goals

This study aims to inform and facilitate the adoption of 7 T scanners in clinical/biological research applications. The optimization aims were thus defined according to the anticipated benefits specific to the use of UHF.

The main optimization aim was defined as the maximization of SNR anticipated at 7 T. The secondary optimization aim was the alleviation of artefact. This is because the levels of artefact have been reported to increase with field-strength and reductions thereof are thus unlikely to present the immediate motivation for performing studies at 7 T in preference to lower field-strengths. In summary, in this investigation, settings that reduce susceptibility to artefact would only be favoured if they have no, or minimal, detrimental effects on the measurement SNR.

4.3.1.2 Selection and replication of the current best 7 T DTI acquisition protocol

The acquisition protocol that to date has been reported to achieve the highest SNR efficiency was to be adopted as the starting point for this investigation. This was to ensure the use and continued refinement of the protocol best suited to the defined primary optimization goal. Replicating acquisitions under this protocol on the in-house 7 T system also allows the reproducibility across sites to be assessed, the suitability of the available MRI setup for DTI to be validated, and the preliminary data quality to be evaluated.

While a number of investigations have recorded and directly compared DTI results acquired at different field-strengths (25, 26, 31, 34, 35), only two studies (25, 26) have thus far quantitatively evaluated SNR levels at 3 T and 7 T. Of these, only one protocol was reported to have achieved an increase in SNR (26). Subject to successful replication, this acquisition protocol was thus selected as the starting point of this investigation.

DTI acquisitions were recorded as described in (26) at both 7 T (Dataset 5-1a) and 3 T (Dataset 5-1b) for direct comparison. Unavoidable differences are outlined in the Methods and Materials

sections of this chapter. The calculation of SNR was performed on the $b=0$ images within ROIs drawn on the FA colour maps (Figure 4-1) as described in (26).

The NEMA-DNS^{††} method (37) (c.f. Appendix of this chapter for details) was used for the quantification of SNR. The NEMA method of quantifying SNR is based on the acquisition of an image following RF excitation, to allow the quantification of signal, and an identical acquisition but without the application of RF excitation, for the quantification of noise. This technique was first proposed by the National Electrical Manufacturer's Association (NEMA) (37), and is thus commonly referred to the NEMA method in literature. Practical limitations have thus far prevented the successful implementation and validation of the NEMA method on contemporary MRI systems (40). The motivation for using the NEMA method over more prevalently used in vivo SNR quantification techniques at 7 T, as well as the implementation, validation and quantitative assessment of accuracy is provided the Appendix to this chapter.

Finally, values were compared to those reported in (26) (Figure 4-2).

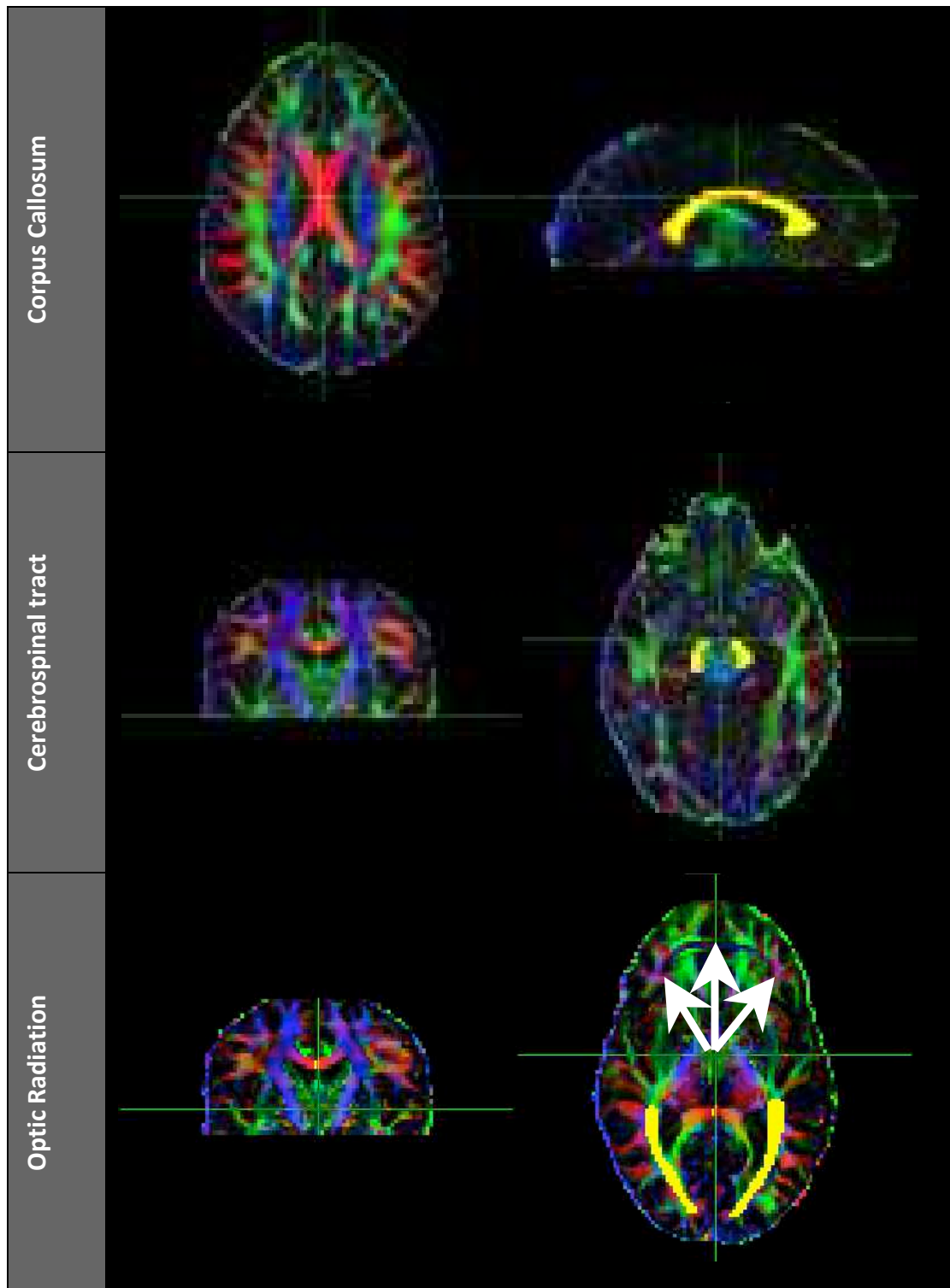


Figure 4-1: FA colour maps measured at 7 T (Dataset 4-1a) using the protocol proposed in (26). ROIs (yellow) were drawn over anatomical white matter regions for the subsequent quantification of SNR (c.f. Figure 4-2). White arrows highlight image artefacts.

Overall, the acquisition quality of DTI datasets recorded using the protocol proposed in (26) was reasonable, although a pronounced artefact (white arrows in Figure 4-1) was observed in a number of slices. Potential causes for this artefact could include Nyquist ghosting resulting from the Eddy-current induced misalignment of alternate phase encode lines in k-space, or insufficient fat suppression. This will be addressed in greater detail in section 4.3.5.

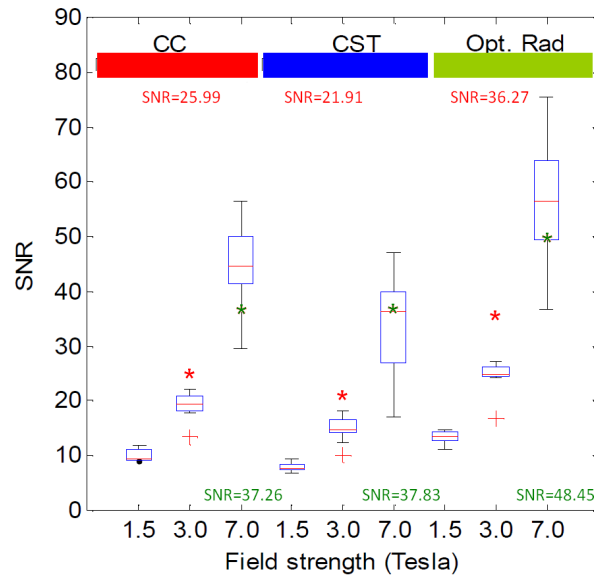


Figure 4-2: Inter-site comparison of observed SNR efficiency levels of DTI acquisitions at 7 T and 3 T (Datasets 4-1a and b respectively). The box-whisker plots are reproduced from (26), and depict the measured SNR values reported in that study. The red and green stars represent SNR values, at 3 T and 7 T respectively, as calculated in the current investigation for the same ROIs as (26).

The SNR values measured in the three defined ROIs are illustrated alongside the values reported in (26) as stars and box whisker plots respectively. As illustrated in Figure 4-2, the reported SNR values at 7 T were highly reproducible on the in-house system. SNR levels acquired at 3 T appeared to be higher than the reported levels. This may have resulted from the use of b-values of 800 s mm^{-2} in Datasets 4-1b, rather than 1000 s mm^{-2} in (26).

In summary, the data quality of results obtained under the acquisition protocol proposed by Polders et al. (26) was considered adequate for its use as a starting protocol. The high level of reproducibility of results also indicated the suitability of the in-house scanner setup for DTI applications.

4.3.2 Quantitative assessment of effects of field-strength on acquisition characteristics

The purpose of this section was to quantitatively assess potential practical advantages in *in vivo* DTI acquisitions pertaining to the use of UHF. As stated in the introduction, anticipated favourable acquisition characteristics included increased measurement SNR, and allowing high parallel Imaging reduction factors. Quantitative information about practical benefits addresses the open question of if, and by how much, *in vivo* DTI acquisitions could benefit from being performed at 7 T rather than 3 T.

It was opted to base this assessment on practical measurements in preference to theoretical calculations. The main challenge facing theoretical calculations is the complex relationship between the field-strength at which MRI experiments are performed, and a multitude of signal characteristics. These relationships are yet to be fully understood, as illustrated by the fact that theoretical predictions in the 1990's even cast doubt on the practical feasibility of human MRI scanners operating at fields of more than 3 T, effectively stalling their development by almost a decade (2). More recently, theoretical predictions of the measurement SNR of DTI acquisitions at 7 T were found to not correspond to practical measurements (25).

4.3.2.1 Comparison of measurement sensitivity of single-shot EPI at 3 T and 7 T

Previous investigations into the effect of field-strength on SNR in DTI acquisitions have typically relied on the qualitative and/or quantitative comparison of individual acquisitions performed at each field-strength (25, 26, 31, 34, 35). This approach, however, is limited by a number of shortcomings, and in some cases has led to conflicting conclusions being reported by UHF DTI studies with similar experimental aims, but using different acquisition protocols (e.g. (25, 26)).

First, although the use single acquisition protocols with parameters optimized to their respective field-strengths would allow the direct comparison of SNR efficiency of specific scanners, to the best of our knowledge, no acquisition parameter optimization has yet been performed for DTI at 7 T. Another major limitation of this approach is that, as a result of the aforementioned complex relationship between SNR and field-strength, it does not allow the generalization of findings. Although the measurement sensitivity has been predicted to increase linearly with field-strength (c.f. Section 4.1.1), additional physical (e.g. RF-penetration, dielectric

resonance phenomena etc.) and practical considerations (e.g. field-strength dependence in the rate of T2 decay coupled with typically long echo times) must also be taken into account. Furthermore, the inability to distinguish field-strength-specific effects from technical limitations (e.g. minimum TE at a given b-value) means that although the technical specifications (e.g. gradient strengths, gradient switching times etc.) of UHF scanners are likely to improve as a result of ongoing research and development efforts, the benefits this may yield for DTI acquisitions cannot be explored due to technical constraints of the current generation of scanners.

Conclusions drawn from such studies are thus valid only for that particular set of acquisition parameters performed on that particular scanner and thus fall short of a full characterization of the effect of field-strength on SNR.

We propose that a comprehensive comparison of SNR performance between different field-strengths requires a series of measurements at each field-strength allowing not only differences in the magnitude of SNR, but also potential dependencies over acquisition timelines (i.e. echo times) and space to be taken into account. To make results generally applicable for different scanner setups and acquisition protocols, confounding factors not directly relating to the effect of field-strength were minimized (as detailed in the description of Dataset 4-2 in Section 4.2).

Figure 4-3 illustrates the differences in measured SNR performance at 3 T and 7 T. *In vivo* measurements within the ROIs delineated in Figure 4-1 were supplemented by the ratio of SNR maps acquired at 7 and 3 T in a homogenous phantom (described in Chapter 1).

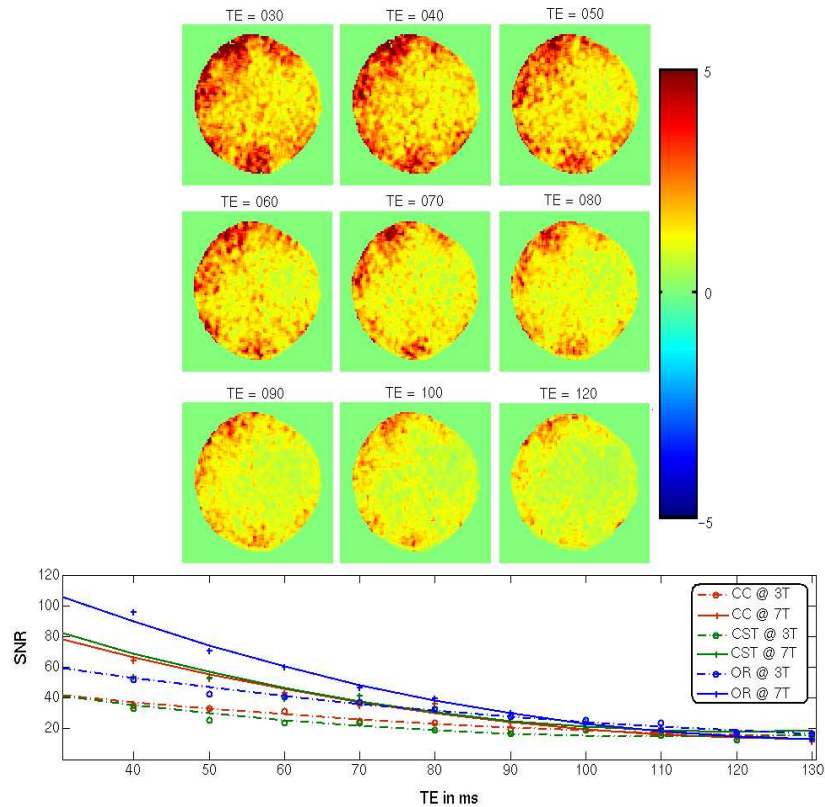


Figure 4-3: SNR values measured at 3 T and 7 T resolved over space and echo time (signal decay). Top diagram: The ratios of SNR at 7 T to 3 T were measured at different echo times on a uniform phantom to produce SNR gain maps with voxel-resolution. SNR increases are highest at the periphery. Bottom diagram: *In vivo* SNR over echo time at the ROIs delineated in Figure 4-1 on the same volunteer (Dataset 4-2).

As shown in Figure 4-3, SNR differences can be observed to reduce rapidly with increasing echo time. This highlights the need for powerful fast switching gradients, particularly at UHF.

SNR gains with field-strength are highest in peripheral regions. In the phantom, at short echo times, an up to 5-fold SNR increase could be observed. This spatial variability of SNR gain may be the result of differences in RF penetration with field-strength and/or the use of a 16-channel head coil at 7 T compared to an 8-channel coil at 3 T.

4.3.2.2 Parallel Imaging reduction (*SENSE*) factor limits

The majority of artefacts in single-shot EPI sequences result from the relatively low receiver bandwidth along the phase encode direction of acquisitions, making them highly susceptible to

phase errors (16). Also, a main practical limitation of single-shot acquisitions is that at a given FOV, the image resolution is subject to the number of echoes that can be formed from a single RF-excitation.

SENSE allows the reduction of the echo train length needed for the formation of an image at a given FOV and spatial resolution. In doing so, it effectively provides a tool for alleviating the spatial resolution limitation and/or and the susceptibility to bandwidth related artefacts. The ability of SENSE to provide significant improvements to DTI data quality has been extensively explored in literature (18-21).

The limits of parallel Imaging reduction are reached when localized noise amplifications are observed, as represented by the g-factor (6). A number of investigations based on theoretical calculations (44- 46) as well as model and simulation-based predictions (21) to determine the maximum reduction factor and its relationship with field-strength have been reported. The key findings can be summarized in Figure 4-4 below, in which parallel Imaging performance is quantified in terms of g-factor increases. An arbitrarily defined g-factor limit of 1.2 was used to separate two operating regimes. At low parallel Imaging reduction factors g-factors are typically close to the optimum value of one, representing the favourable operating regime. At higher reduction factors, the g-factor increases exponentially representing the unfavourable operating regime. The maximum parallel Imaging reduction factor at which the g-factor limit of 1.2 is exceeded increases with field-strength suggesting that acquisitions at 7 T may be compatible with the use of higher parallel Imaging reduction factors than at lower field-strengths.

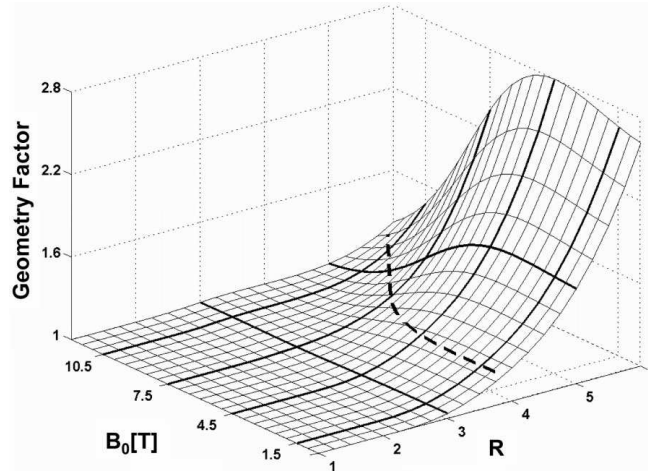


Figure 4-4: Parallel Imaging performance in terms of g-factor (21). R denotes the parallel Imaging reduction factor and B_0 denotes the strength of the main magnetic field. The dashed line represents an arbitrarily defined g-factor limit of 1.2 separating two distinct operating regimes. The favourable regime is characterized by the low g-factor, and the unfavourable regime in which the g-factor increases exponentially.

Limitations of these theoretical and simulation based predictions include the need to validate findings through direct measurements, and their inability to account for practical considerations pertaining to the RF receiver coil used. The number and optimal geometrical arrangement of coil elements comprising the RF receiver coil have been shown to strongly affect parallel Imaging performance, and counteract SNR losses (21). Thus far, the only investigations to ascertain the effect of varying SENSE factors on the quality of DTI acquisitions at 7 T through practical measurements have been based on the subjective analysis of image quality. Accordingly, the maximum SENSE reduction factor was regarded to have been reached when total signal breakdown was observed (23, 24). In this investigation, the maximum SENSE factor was quantitatively evaluated through the noise amplification, or g-factor. As in (21), the maximum SENSE factor was considered to have been reached when g-factors of 1.2 or above could be observed anywhere in the scanned object. Datasets 4-3 were acquired without SENSE, and with variable SENSE factors. At each setting, four dynamic $b=0$ acquisitions were recorded with the last dynamic comprising a noise-only acquisitions. Noise maps were subsequently calculated from these noise-only images through a sliding window approach using a $3 \times 3 \times 3$

voxel neighbourhood and, in turn, were used to generate g-factor maps. The maximum g-factor in the centre of the FOV (black square in Figure 4-5) is plotted in the graph below. The results in Figure 4-5 show that the g-factor limit of 1.2 was not reached until SENSE factors between 4.5 and 5 were used.

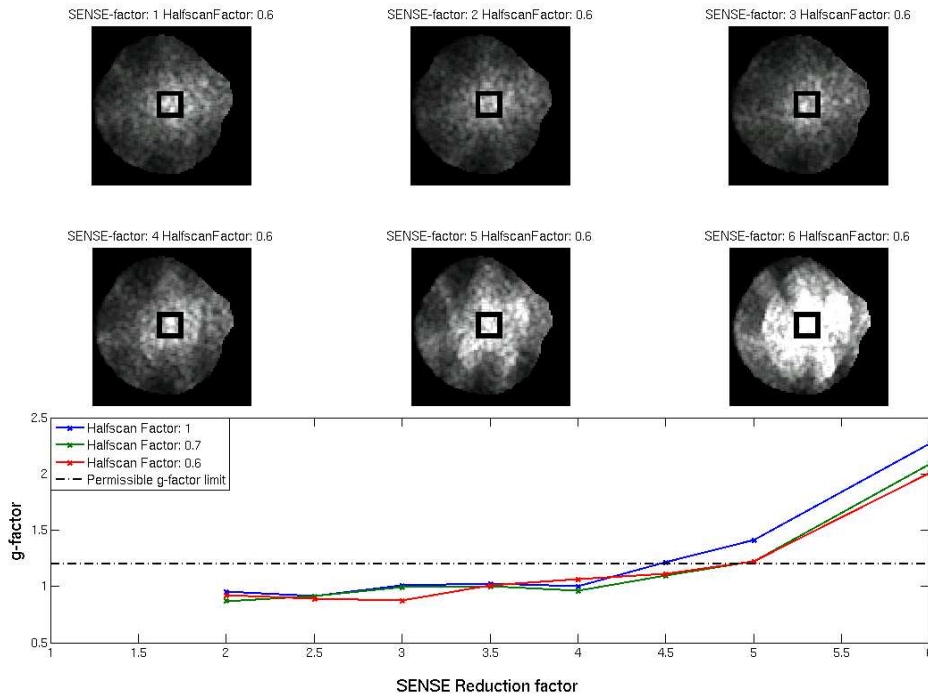


Figure 4-5: Relationship between g-factor and SENSE at 7 T in Dataset 4-3. Top: Noise maps at various SENSE factors ranging from 1 up to 6 using a Halfscan factor of 0.6. Bottom: Measured relationship of SENSE and g-factors to illustrate at which SENSE reduction the g-factor of 1.2 was exceeded. The plotted g-factor was calculated as the mean g-factor value in the marked region in the centre of the FOV for Halfscan factors of 1, 0.7 and 0.6.

4.3.3 Acquisition protocol optimization

The aim of this section is to formulate guidelines for the design of acquisition protocols for the efficient utilization of SNR benefits (Figure 4-3) while minimizing the susceptibility to bandwidth related artefacts in *in vivo* DTI acquisitions at 7 T.

Disparities in published findings comparing the SNR efficiency at 7 T to that at lower field-strengths (25, 26), are likely to have been the result of increased field-strength promoting signal characteristics that are not only favourable (e.g. higher measurement sensitivity, higher parallel

Imaging reduction factors), but also unfavourable (e.g. faster T2 decay of signal) for *in vivo* DTI applications, with the latter potentially outweighing the former.

In this respect, DTI differs from other more established UHF MRI applications that generally allow the direct utilization of a single field-strength dependent signal property of interest. Prominent examples include Magnetic Resonance Spectroscopy (MRS) which benefits from the increased chemical shift allowing for spectra to be better resolved, Blood Oxygen Level Dependence (BOLD) fMRI, which benefits from increased T2* contrast, and high resolution anatomical acquisitions that due to their comparatively short echo times can directly benefit from the increased measurement sensitivity. Therefore it must be emphasised that while acquisition protocol optimization is thus likely to benefit any application, in DTI the careful selection of appropriate acquisition parameters is an essential prerequisite without which subsequent acquisitions may actually suffer a decline in data quality.

The absence of clear recommendations for the design of acquisition protocols may thus have contributed to *in vivo* UHF DTI still being in its infancy stages in spite of tangible practical benefits. In this section, an acquisition protocol optimization was performed in three stages: First the optimal sequence was selected from the range of sequences available on the in-house 7 T scanner according to its suitability to the optimization goals defined in Section 4.3.1; next acquisition parameters that allowed the adaptation of acquisition protocol to the UHF conditions were optimized; and finally, acquisition protocol settings for the alleviation of remaining artefacts were explored.

4.3.3.1 Selection of optimal sequence

At field-strengths up to 3 T, single shot spin echo EPI has become the prevalent sequence used for *in vivo* DTI applications by offering a favourable compromise between acquisition time, sensitivity and robustness towards artefacts. However, at UHF, changes in signal characteristics and artefact susceptibility may alter this balance in favour of alternative acquisition sequences. For this reason, before addressing the optimization of protocol parameters, the suitability of the acquisition sequence was revisited.

The use of Turbo Spin Echo (TSE) readout schemes for *in vivo* DTI applications at UHF has been proposed as an alternative to EPI due to its lower sensitivity to magnetic susceptibility artefacts (10, 31, 34, 35). At 3 T both EPI and TSE was reported to produce similar results, while at 7 T the EPI readout displayed higher levels of distortions at the skull base and anterior regions of the brain, as well as a poorer visualization of peripheral cortical fibres. TSE allowed higher resolutions in targeted acquisitions of complex anatomies. This, however, came at the cost of elevated levels of T2 blurring and higher specific absorption rate (SAR) levels. Strategies towards their alleviation typically require longer acquisition times and thus effectively limit the number of signal averages that can be performed under a practical setting. This conflicts with the stated optimization aim prioritization according to which strategies to reduce the susceptibility of acquisitions to artefact were only to be considered if they came at little or no cost to SNR efficiency. As a consequence, EPI readout was considered to be better suited for the defined optimization aims than TSE which thus was not considered further.

This investigation^{§§} (33) focused on the assessment of different diffusion sensitization strategies available on the in-house 7 T scanner. The tested acquisition sequences in Dataset 4-4.a-f included single-shot 2D spin echo EPI (SE), Twice Refocused Spin Echo (TRSE) and Stimulated Echo (STE). Datasets were evaluated with respect to SNR and distortion, and results are illustrated in Figure 4-6.

§§ The lead investigator of this investigation was Dr. Paul Morgan with my responsibilities having included overcoming issues with the implemented TRSE acquisition protocol (not featured in this thesis), assisting in the acquisition and analysis of data.

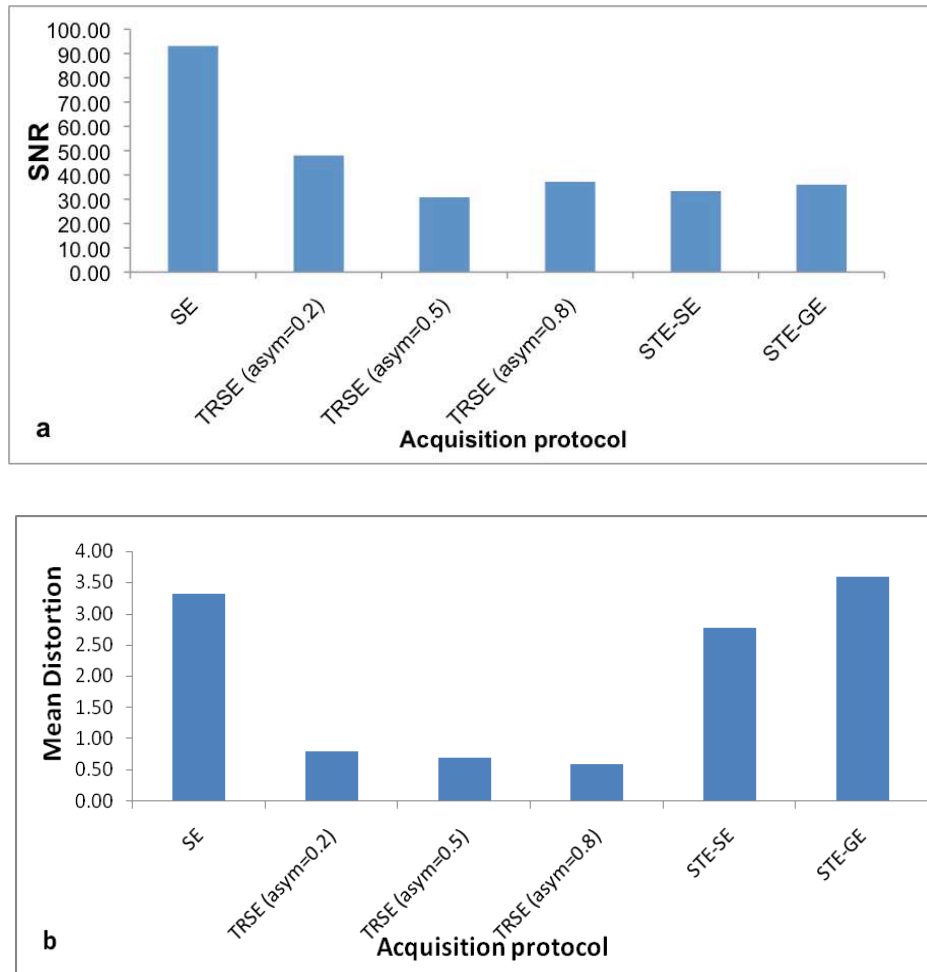


Figure 4-6: Comparison between various potential DTI acquisition protocols at 7 T (Datasets 4-4). TRSE datasets were recorded under asymmetry factors of 0.2, 0.5 and 0.8. Suitability was evaluated in terms of measured SNR (a) and mean distortion (b) as quantified by the reversed gradient technique (32). SNR measurements were performed over the volume of $b=0$ acquisitions of a homogenous agar phantom without the use of SENSE, and noise was measured as the standard deviation of background signal outside the object (39, 40).

Figure 4-6a illustrates that in DTI acquisitions using moderate b -values ($b= 800 \text{ s mm}^{-2}$), the standard SE protocol clearly outperformed both the TRSE and STE sequences in terms of SNR. This observation confirmed that this acquisition sequence is the most suitable for the optimization aims defined, and will therefore undergo acquisition parameter optimization in the following sections.

STE acquisition protocols may retain higher levels of SNR when longer echo times are needed, for example if higher b-values are required. However, for standard settings for *in vivo* acquisitions, STE displays low measurement sensitivity and high susceptibility to distortion.

TRSE acquisitions demonstrate low susceptibility to distortion. Early DTI acquisitions on the in-house 7 T scanner suffered heavily from distortions that became prohibitively large at b-values exceeding 800 s mm^{-2} . Susceptibility to Eddy current induced distortion has since been reduced though the improved gradient calibration by the MRI system manufacturer. TRSE sequences may provide a valuable tool for applications in which alleviation of Eddy-current distortions is critical (e.g. where more powerful, faster switching gradients and/or very high b-values are used). For standard *in vivo* DTI acquisitions, however, the effect of Eddy-current distortion on single-shot EPI based acquisitions is tolerable, and its alleviation thus did not warrant the reduction of SNR resulting from the use of TRSE.

4.3.3.2 Parameter selection and optimization

Having specified the acquisition sequence of choice, this section addresses the optimization of acquisition parameters. This optimization is not specific to any one application, but is aimed at providing a general set of guidelines for the efficient utilization of SNR benefits of UHF DTI. To this end, pertinent acquisition parameters were first identified, and subsequently optimized.

Maximizing potential field-strength dependent SNR-gains is limited by the field-strength dependent increased rate of T2 decay. The maximization of SNR is thus subject to the minimization of the echo time at which DTI datasets are recorded. The echo time is determined by the duration of the RF excitation and refocusing pulses, the diffusion encoding gradients, and the echo train readout.

While the time over which the diffusion sensitization gradients are applied is typically the greatest contributor to the overall echo time, its reduction would necessitate the development of stronger gradients and/or gradient inserts. This, however, was beyond the scope of this study. The echo train length can be reduced by both the use of SENSE and Halfscan reductions.

However, both SENSE and Halfscan incur an inherent SNR penalty of their own. This is because the signal contribution of measured data is limited to the number of k-space lines being sampled, while the noise contribution arises from the entire volume over which the coil is sensitive. While the former is reduced by the use of both SENSE and Halfscan, the latter remains unchanged.

The secondary optimization aim was to minimize the level of artefact. On account of the low receiver bandwidth typical in single-shot EPI based DTI acquisitions, phase errors represent the dominant source of artefact (16). The bandwidth was thus regarded as a surrogate of artefact susceptibility. The receiver bandwidth can be increased by shortening the readout time. As with the reduction of the echo time, this may be achieved through the use of stronger gradients and/or by the shortening of the echo train length through the use of SENSE and Halfscan.

In summary, SENSE and Halfscan have been identified as the parameters pertinent for the optimization of acquisition sequences according to the defined optimization goals. Halfscan is more efficient in its reduction of the echo time, but is limited to reducing the echo train length by 40 % while increasing the susceptibility to motion artefacts. In Figure 4-5, SENSE reduction factors of 4.5 to 5 were observed to be compatible with single-shot EPI acquisition protocols on the in-house 7 T scanner setup.

The relationships between the settings of selected parameters (SENSE and Halfscan) and their impact pertinent on acquisition characteristics, was measured in Dataset 4-3 and are depicted in Figure 4-7 below.

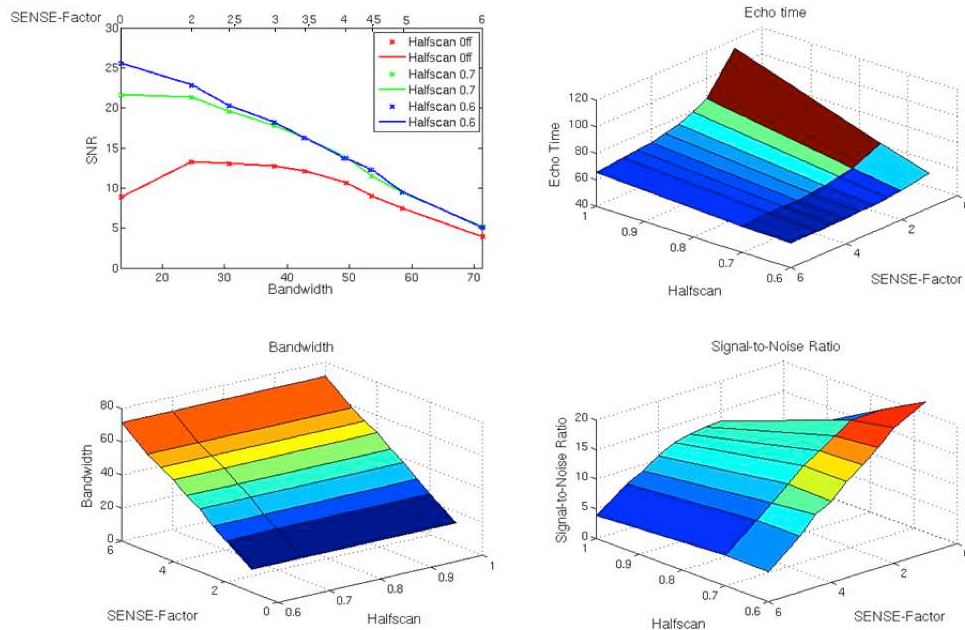


Figure 4-7: Effects of varying SENSE, and Halfscan factors on SNR and bandwidth evaluated using Dataset 4-3. Top left: Relationship between SNR and bandwidth; Top right: the minimum echo time needed on the in-house 7 T scanner to achieve b-values of 800 s mm^{-2} ; Bottom left: effect of various SENSE and Halfscan factor settings on the maximum bandwidth; Bottom right: effect on of various SENSE and Halfscan factor settings on the measurable SNR. SNR was measured in a $10 \times 10 \times 10$ voxel ROI in the centre of the phantom using the NEMA-DNS method described (c.f. appendix to this chapter for details).

Figure 4-7 comprises four graphs providing information of the effect of various SENSE and Halfscan factor settings on pertinent acquisition properties. Acquisitions comprised four dynamic $b=0$ scans, with the last dynamic representing a noise-only acquisition allowing the calculation of SNR using the NEMA-DNS method (described in the appendix to this chapter). The echo time of all acquisitions was manually set to the minimum echo time needed to apply a b-value of 800 s mm^{-2} on the in-house system. These are recorded in Table 5-4 in the Methods and Materials section, and are graphically depicted in the top right plot of Figure 4-7. The bandwidth in all acquisitions was set to maximum, effectively minimizing the duration of the data readout. This setting minimized both the echo time and artefact susceptibility, and allowed the readout duration and hence SNR to be controlled through SENSE and Halfscan settings. The SNR-performance of each of these settings was determined by measuring SNR

values in an ROI comprising 10 x 10 x 10 voxels in the centre of the FOV using the NEMA-DNS technique described in the appendix of this chapter. To establish the relationship between measurement sensitivity and artefact susceptibility for each of these settings, the measured SNR and acquisition bandwidth was plotted in the top left plot of Figure 4-7. This allowed the optimum parameter combinations to be determined directly from the graph.

For most applications, a Halfscan factor of 0.7 is recommended, as it offers a good compromise between robustness against motion artefact on the one hand, and improvements in bandwidth and reductions of the echo time on the other. With a SENSE factor of 2, the ensuing reduction in echo time was observed to compensate for its intrinsic SNR penalty. Higher SENSE factors, however, result in a significant loss of SNR. Standard *in vivo* DTI applications at 7 T are thus recommended to use Halfscan factors of 0.7 and SENSE factors of 2.

In applications where subject motion is expected to be minimal, Halfscan factors of 0.6 may be used. Since under this setting the centre of k-space is acquired very early in the echo train, SENSE reduction has next to no effect on the minimum echo time and thus incurs almost the full SNR penalty. As a result, in acquisitions using SENSE, the difference in SNR between Halfscan 0.6 and 0.7 is minimal. The only setting under which Halfscan of 0.6 can potentially be advantageous is where the SNR maximization is critical and increased susceptibility to motion artefacts can be tolerated. In this case, SENSE should not be used.

In applications where no Halfscan is to be used, the echo time reduction afforded by the application of SENSE was observed to actually overcompensate for its intrinsic SNR penalty at SENSE factor 2. The measurement sensitivity subsequently changed little until SENSE reduction factors of 3.5 to 4 was reached. According to Figure 4-5, SENSE factors of up to 4.5 can be used on the in-house 7 T scanner without exceeding g-factors of 1.2. The overall SNR level of these acquisitions, however, is low compared to acquisitions using Halfscan reduction. This combination of settings would thus only be considered for applications that primarily require a minimization of bandwidth- and motion related artefacts.

4.3.4 Artefact alleviation

After selecting the acquisition sequence and parameter settings in accordance with the defined optimization aims. In this section, residual sources of artefact were to be identified and, if possible, alleviated.

4.3.4.1 Signal voids in acquired images

The presence of signal voids, as illustrated in Figure 4-8, is widely reported in UHF acquisitions (22, 24). This is because, to match the Larmor frequency, the frequency of the RF excitation pulse must increase with field-strength. This results in a decrease in the signal wavelength, which, in acquisitions of the human head at 7 T, can lead to significant inhomogeneities in the profile of the RF excitation pulse within the FOV. The power calibration of the RF excitation is typically calculated to administer the prescribed flip angles at the centre of the FOV (24). As a consequence of RF excitation pulse inhomogeneities, however, these power calculations may not hold for peripheral regions, resulting in the observed signal voids.

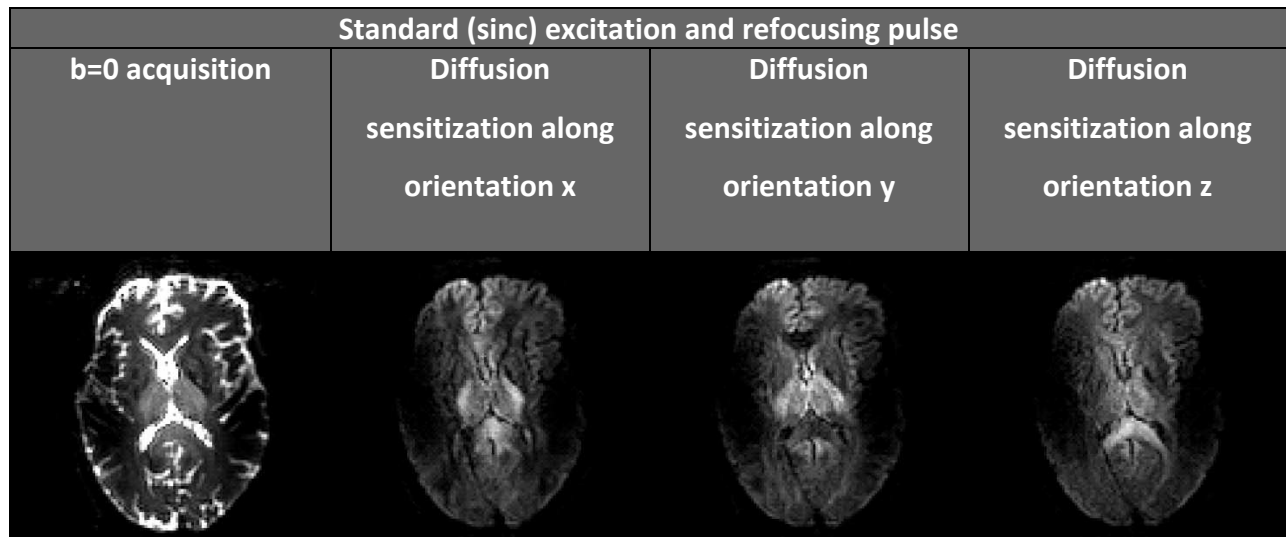


Figure 4-8: Individual acquisitions of Dataset 4-5a illustrating the signal void in lateral regions under default settings.

One proposed solution to provide better homogeneity across the FOV was to manually adjust the RF transmit power (24). Setting the RF power to 25 % higher than determined by the system software effectively increasing the prescribed flip angle, and thus signal intensity, successfully reducing signal voids in lateral regions of the human brain in DTI acquisitions at 7 T (24). However, this increase in RF power also resulted in flip angles of more than 90 ° in central brain regions leading to an overall loss in SNR. Other drawbacks resulting from the manual adjustment of RF power include the loss in scan time needed to determine suitable settings prior to each acquisition, and variability in the SNR-efficiencies between scans. This approach nevertheless demonstrated that the signal void was indeed the result of B1 inhomogeneities, and could potentially be alleviated through the modification of the RF pulse.

An alternative method was suggested by (22), where the use of multiple excitation coils was proposed to generate more homogenous B1 fields. While this is an exciting field of research, the technology was not yet available at the time of this investigation.

The approach taken in this investigation was to test alternative excitation and refocusing RF pulse shapes for the alleviation of B1 inhomogeneities. By retaining the default sinc pulse for excitation, and replacing the default sinc pulse with an echo2 pulse for refocusing, B1 inhomogeneities in both b=0 and DWI single-shot EPI acquisitions of the human head were effectively alleviated. However, this also led to a loss in signal intensity (data not shown).

To assess if this observed loss in signal intensity was the result of differences between the prescribed and administered flip angles, b=0 scans were acquired under a range of flip angles ranging from 150 ° to 290 ° in 10 ° intervals (c.f. Dataset 4-5c). For each setting, the signal amplitude in a 10 x 10 x 10 voxel region in the centre of the FOV was compared. These results are plotted in Figure 4-9. The maximum amplitude was obtained when the refocusing flip angle was set to 220 °, highlighting a discrepancy between the prescribed and administered flip angles.

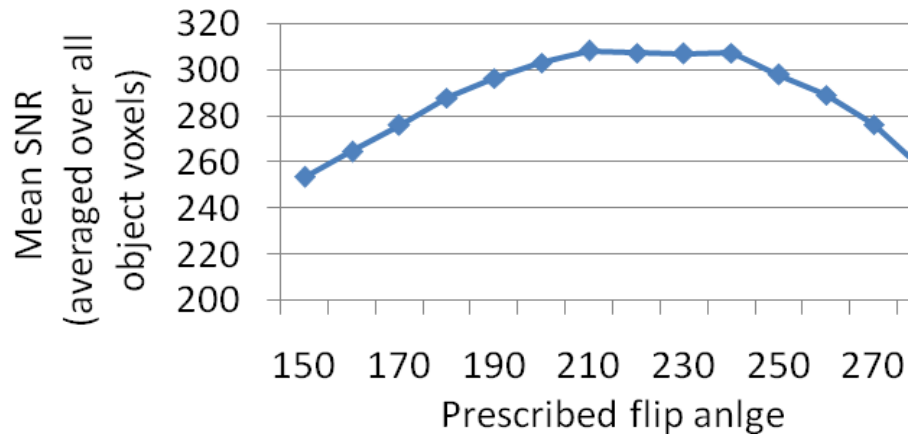


Figure 4-9: Flip angle optimization performed in Dataset 4-5c of the echo2 refocusing pulse with respect to SNR.

The effective alleviation of signal voids, and preservation of signal intensity by replacing the 180° sinc-shaped refocusing pulse (in Dataset 4-5a) with a 220° echo2 refocusing pulse (Dataset 4-5b) is illustrated in Figure 4-10 below.

Sinc excitation and echo2 refocussing pulse			
b=0 acquisition	Diffusion sensitization along orientation x	Diffusion sensitization along orientation y	Diffusion sensitization along orientation z

Figure 4-10: Individual acquisitions of Dataset 4-5b, illustrating the homogeneity of the in-plane signal intensity when using echo2 refocusing pulses.. Red arrows highlight residual artefacts.

4.3.4.2 Fat-suppression artefact

Finally, *in vivo* DTI acquisitions consistently displayed prominent artefacts resembling the contour of the brain displaced along the phase encode orientation, as highlighted by the red arrows in Figure 4-10 and earlier by the white arrows in Figure 4-1. This section describes steps taken to alleviate these artefacts through optimized fat suppression.

First, single-shot EPI acquisitions were recorded without fat suppression (Dataset 4-6a, Figure 4-11) allowing the efficacy of various techniques to be assessed.

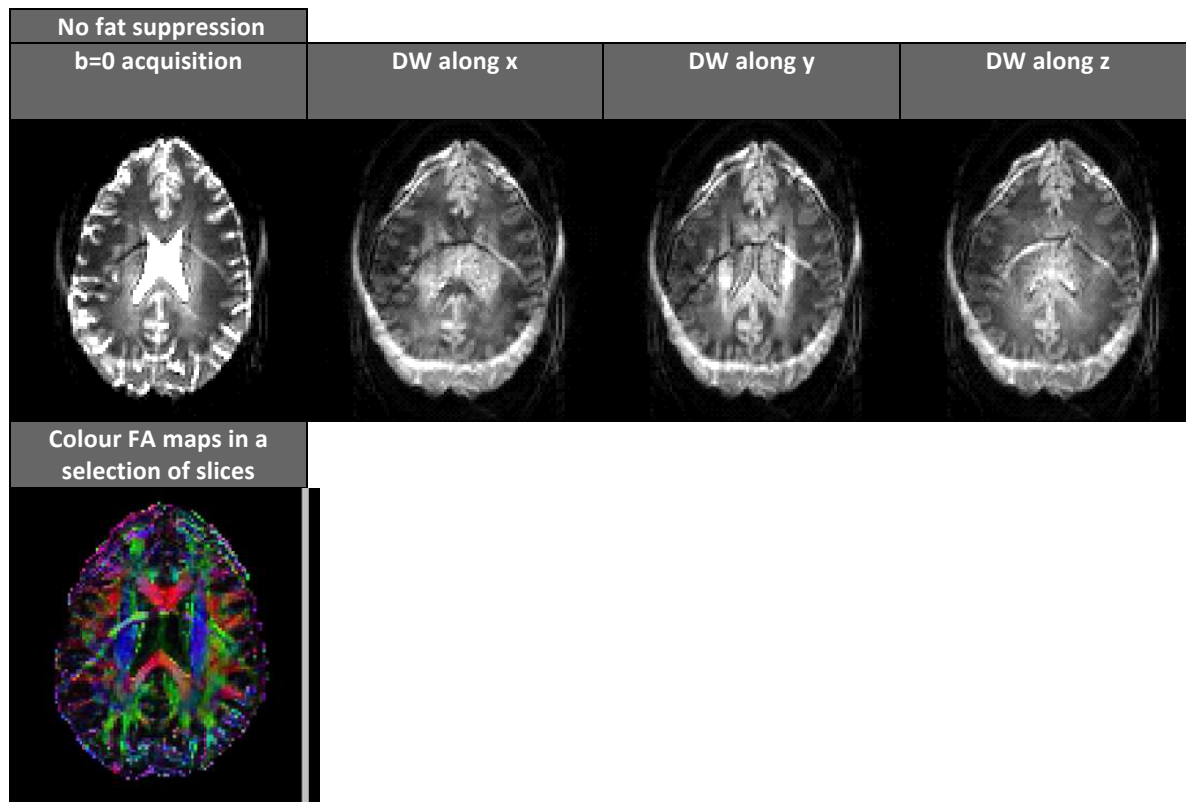


Figure 4-11: single-shot 2D EPI acquisitions of Dataset 4-6a and colour FA map without fat suppression.

Next, the manufacturer-supplied fat suppression techniques, Spectral Presaturation by Inversion Recovery (SPIR) (41) and Spectrally Adiabatic Inversion Recovery (SPAIR) (41, 42), were applied (Datasets 4-6b, Figure 4-12; and Datasets 4-6c, Figure 4-13 respectively).

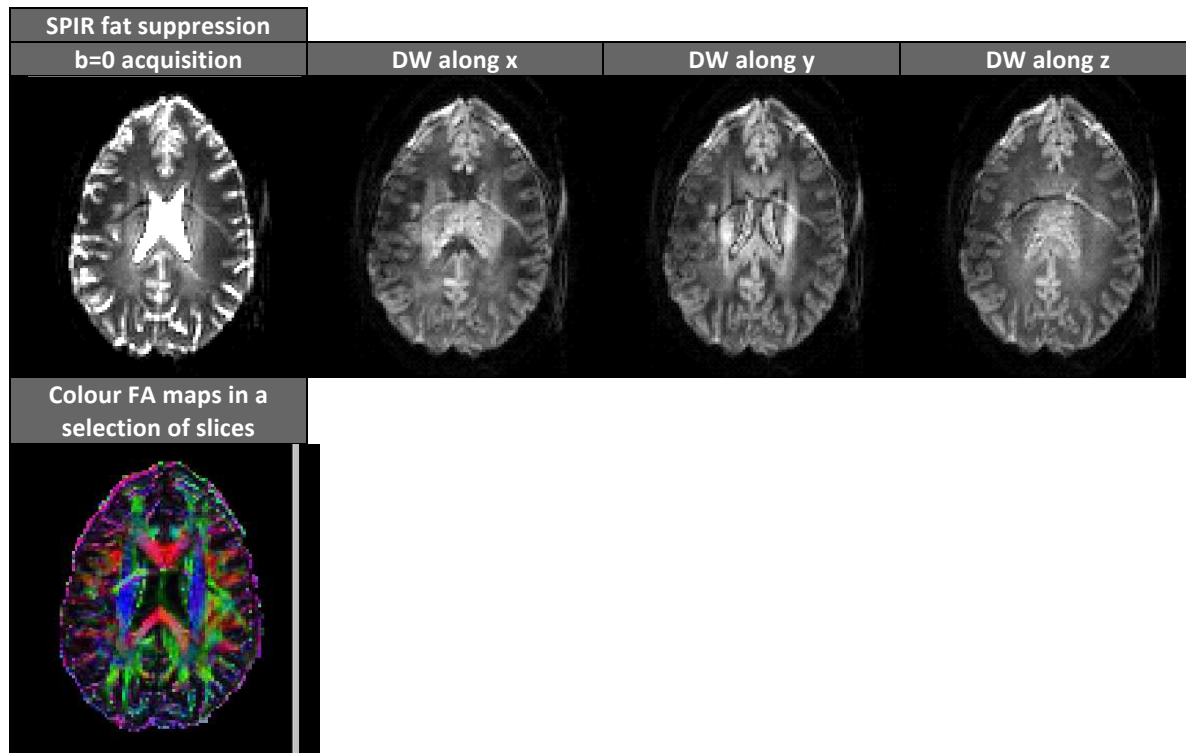


Figure 4-12: single-shot 2D EPI acquisitions of Dataset 4-6b and colour FA map with SPIR fat suppression.

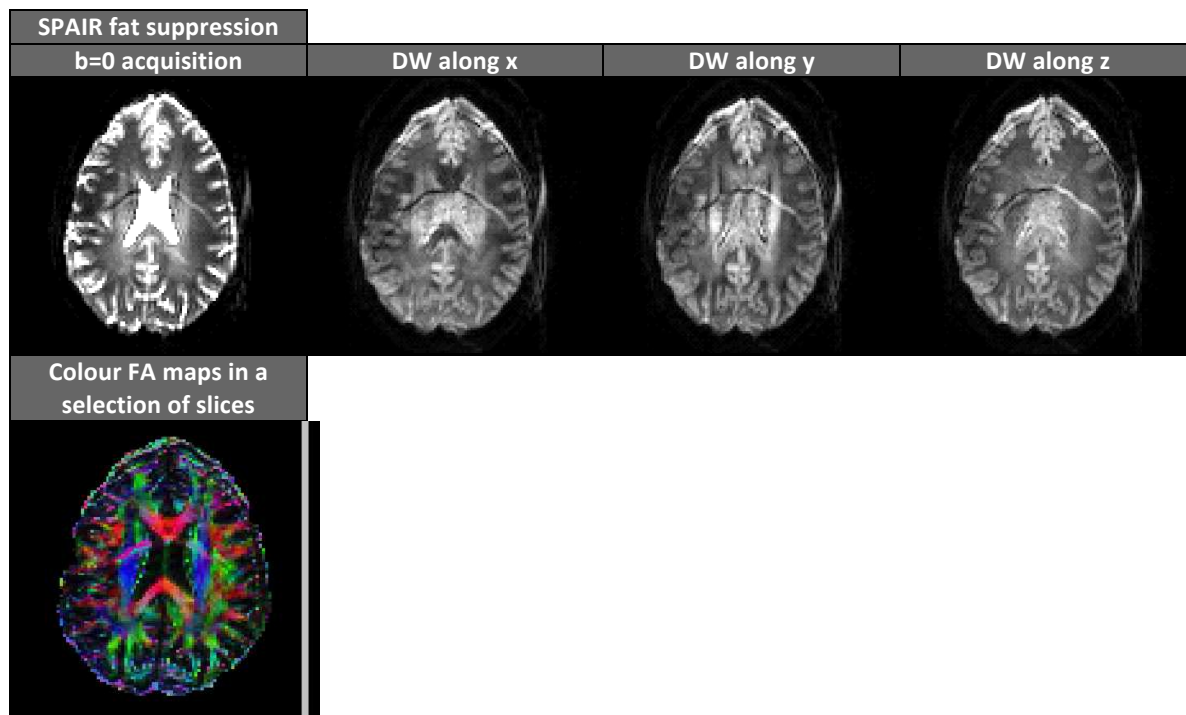


Figure 4-13: single-shot 2D EPI acquisitions of Dataset 4-6c and colour FA map with SPAIR fat suppression.

Although both techniques reduced the magnitude of the artefact considerably, they were unable to eliminate it.

As a result, the Slice Selective Gradient Reversal technique (SSGR) (43, 47) was considered. Rather than suppressing fat via inversion or saturation pulses, this technique eliminates the contribution of the fat signal by using two slice select pulses of opposite polarity, thus displacing the signal of fat in opposite directions along the slice select orientation. As a result, only the on-resonance water signal is refocused and hence contributes to the measurable signal. This technique is thus expected to be particularly suitable at UHF due to the increased chemical shift between water and fat. Furthermore, by not relying on additional RF pulses, this technique has the added benefit of reducing the acquisition SAR. The effectiveness by which SSGR eliminated the fat artefact is evidenced in Figure 4-14.

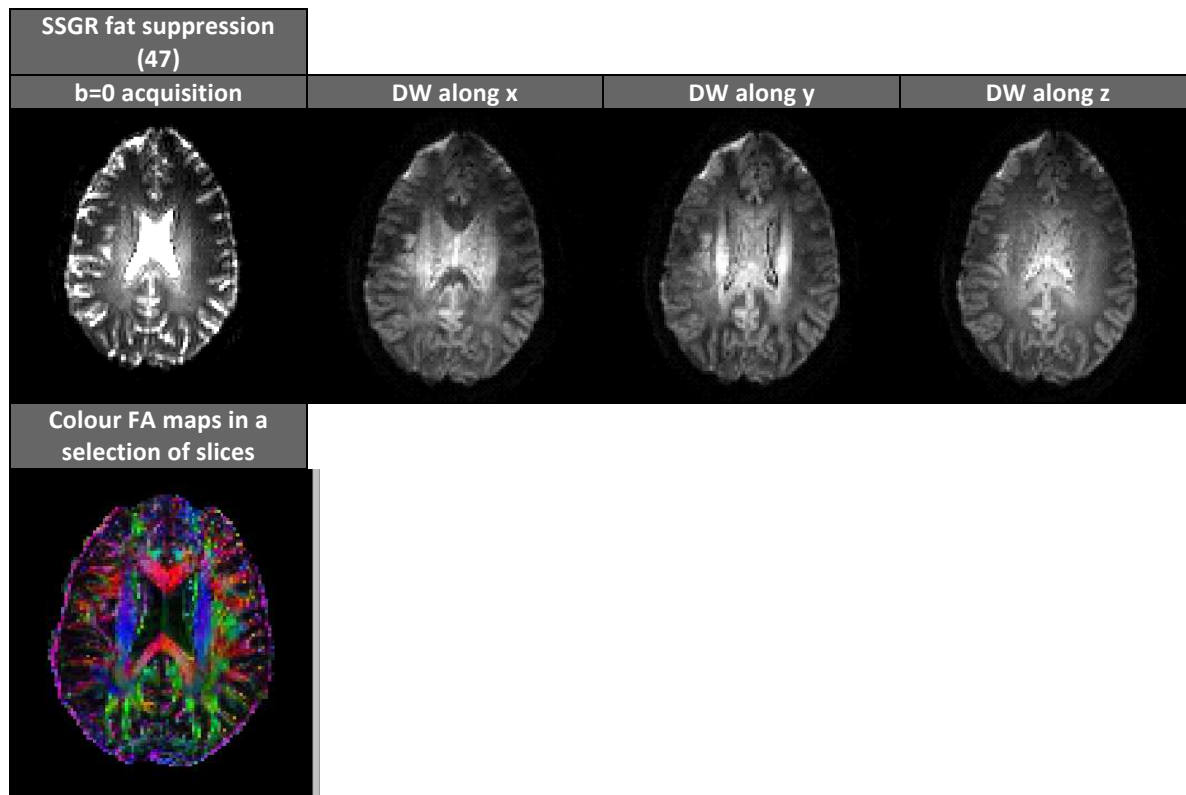


Figure 4-14: single-shot 2D EPI colour acquisitions of Dataset 4-6d with and FA map of SSGR fat suppression.

4.4 Discussion

The data presented in this chapter successfully answer currently outstanding questions pertaining to the benefits and practicality of UHF MRI for clinical/biomedical research DTI applications: What, quantitatively, are the advantages of using 7 T over lower field-strengths for *in vivo* DTI applications, and how must acquisition protocols be designed to efficiently utilize these benefits.

Two of the main limiting factors in DTI are the acquisition SNR and high susceptibility to receiver bandwidth related phase errors resulting from the use of single shot EPI acquisition sequences. UHF DTI could potentially alleviate both these limitations. The measurement sensitivity has been predicted to increase with field-strength and the susceptibility to bandwidth related artefacts can be reduced by the compatibility of UHF with higher SENSE reduction factors.

However, despite these suggested tangible benefits, DTI at UHF is still in its infancy with, to the best of our knowledge, no clinical and/or biological research studies having been performed to date. This is likely to be the result of the UHF MRI presenting not only potentially favourable, but also unfavourable signal characteristics. For instance, the rate of T2 decay also increases with field-strength. This suggests that SNR gains will be reduced at longer echo times, as are typical in DTI acquisition protocols. Similarly, while the use of higher SENSE factors may reduce the susceptibility to bandwidth related artefacts the magnitude of these errors is expected to increase at higher fields. The complexity of the relationship between beneficial and detrimental effects of UHF in DTI acquisitions distinguishes DTI from other applications that have become more established at UHF (e.g. MRS, BOLD fMRI, susceptibility imaging etc.) in that the very acquisition characteristics we wish to improve with UHF could actually be reduced if acquisition protocol parameters are not selected carefully. This was demonstrated by the conflicting results of the only two investigations that to date have attempted to quantitatively compare the SNR of DTI acquisitions at 3 T and 7 T (25, 26).

This investigation addressed these outstanding questions in the following steps:

First, the optimization aims were specified and prioritized. The specification was based on the predicted advantages of improved intrinsic measurement sensitivity, and reduced susceptibility to artefact through the use of higher parallel Imaging reduction factors. The primary optimization aim was to maximize SNR, in preference to the secondary optimization aim of reducing artefact. The prioritization of these aims was useful in reaching a resolution when there was a conflict in their requirements. For example, compared to spin echo EPI, TRSE acquisition sequences were observed to be less susceptible to Eddy-current distortions, but also displayed a lower SNR efficiency. Similarly, increased parallel Imaging reduction factors reduce not only the susceptibility to bandwidth related artefacts, but also impose an intrinsic SNR penalty of their own.

The next step was the definition of a starting protocol subject to the successful replication of the acquisition protocol in literature with the highest SNR gain. The results of (26), the only protocol to have reported a quantified SNR gain at 7 T, was successfully replicated on the in-house system. This experiment also gives confidence that the setup of the in-house system was suitable for *in vivo* DTI, and suggests that subsequent results should be applicable to other systems as well.

After successful completion of these two preliminary steps, the SNR difference between 3 T and 7 T, and maximum parallel Imaging factor at 7T was measured. To make results applicable to other scanner setups including future developments, steps were taken to isolate and fully characterize the effects of field-strength on signal characteristics. These included scanning the same object/volunteer at both field-strengths using identical acquisition sequences and parameters, and using scanners of the same vendor and series. For the comprehensive assessment of the effect of field-strength on SNR, comparisons were resolved over both space (through the use of SNR maps *in vitro* and the selection of distributed ROIs *in vivo*) and acquisition timelines (SNR measured over a pertinent range of echo times). The main findings of the first study were that SNR gains could indeed be observed at 7 T compared to 3 T with the former offering roughly double the SNR. The SNR gain increased at low echo times, which can be attributed to the faster level of T2 decay (48, 49) with field-strength. In peripheral regions

SNR levels at 7 T were up to 5 times higher than at 3 T at low echo times. This may be a result of differences in RF penetration and/or differences in the sensitivity profile of the RF receiver coils (identical coils were not available for both field-strengths). SENSE factors of up to 4.5 to 5 were successfully used without exceeding the defined g-factor limit of 1.2.

Following the general quantitative characterization of field-strength-specific differences in acquisition properties, guidelines on how DTI acquisition protocols should be designed to efficiently utilize the potential advantages of UHF DTI were formulated for a specific 7 T MRI scanner. Spin echo single shot EPI sequences were recommended as the acquisition sequence of choice, as they were found to offer the highest SNR efficiency, and acceptable levels of susceptibility to artefacts. The optimization of acquisition protocol parameters was limited to those parameters, which directly influenced SNR and phase errors. Based on these criteria, the two parameters selected for optimization were SENSE and Halfscan, with respect to SNR and bandwidth. The bandwidth was used as a surrogate for artefact susceptibility as the majority of artefacts in DTI are bandwidth related (16). In terms of SNR, SENSE and Halfscan have both positive and negative effects. While they incur an inherent SNR penalty, they also shorten the minimum echo time achievable and thus can help minimize losses in SNR as a result of the faster T2 signal decay at higher field-strengths. Receiver bandwidth can be reduced via SENSE affording a reduction in artefact susceptibility.

In keeping with the prioritization of the optimization aims three sets of SENSE/Halfscan combinations were proposed to achieve the optimal compromise between SNR and robustness towards bandwidth related artefacts. In general applications, a SENSE factor of 2 and a Halfscan factor of 0.7 are recommended. If levels of motion and phase errors permit, the highest SNR may be achieved by using a Halfscan factor of 0.6 and no SENSE. Finally, in applications where high levels of motion are expected, no Halfscan, and SENSE factors of 4 are recommended. The other main observed artefacts were found to be the result of B1 inhomogeneities and poor fat suppression. The use of an echo2 pulse in preference to the default sinc pulse for the 180 ° refocusing was found to be effective in alleviating the B1 inhomogeneities. Differences in the prescribed and administered flip angle were observed, and alleviated by prescribing a flip angle

of 220 °. Improved B1 homogeneity also improved the fat suppression, although a prominent artefact could still be observed in most acquisitions. Eliminating the fat signal contribution through selective refocusing according to the SSGR technique (43) was found to be more effective at 7 T than fat signal suppression through saturation or inversion recovery pulses, while simultaneously reducing SAR. This was achieved on the in-house system under the 'research mode', by setting the control parameter 'GRs_echo scale' to -1, and 'Min rel slice gap_SE to zero.

The work presented in this investigation thus successfully demonstrated that DTI applications can indeed benefit considerably from being performed at 7 T. As illustrated by the discrepancies of results in previous investigations, however, the appropriate selection of protocol parameters affecting SNR performance and receiver bandwidth is essential. These parameters have been identified, and appropriate combinations specified. Finally the most prominent artefacts have also been reported and techniques towards their effective alleviation described. The developed protocols may thus be directly applied to clinical and/or biomedical research studies.

Future work

The findings presented in this work form the basis for a variety of application-orientated, technical, and fundamental research investigations. Some particularly interesting avenues are outlined in this section.

4.4.1.1 Application orientated investigations

Three categories DTI applications that could benefit from being performed at UHF are proposed here.

Clinical/Biomedical research applications

The results presented in this chapter have been used in the design of acquisition protocols that are currently being used in studies on Multiple Sclerosis, Alzheimer's disease and Schizophrenia at the University of Nottingham.

Functional Diffusion Imaging

An interesting avenue for UHF DTI is the mapping of functional activation in the brain using Diffusion imaging in grey matter. In a study that may present a breakthrough in the field of brain function imaging, Le Bihan et al. proposed the measurement of neuronal activation induced changes in the ADC as a direct measurement of brain function, as opposed to the indirect nature of BOLD fMRI which relies on the haemodynamic response. The hypothesis that ADC changes are indeed a direct measurement of functional activation was in part substantiated by the observation that the induced effects precede the BOLD response by several seconds. Subsequent investigations, however, failed to reproduce these findings, preventing its independent validation (50). The improved SNR at 7 T, particularly in peripheral regions of the FOV (c.f. Figure 4-3) may provide a more sensitive measurement for subtle ADC changes. Alternatively, additional SNR may be used to allow better temporal resolution to be achieved by reducing the number of signal averages needed to detect a change of specific magnitude.

High resolution imaging

The reliance of *in vivo* DTI acquisitions on ultra-fast acquisition protocols, such as EPI, imposes an inherent resolution limit. DTI acquisitions of the whole human head at 3 T typically allow in-plane spatial resolutions of $2 \times 2 \text{ mm}^2$ to be achieved. This is low compared to the intricate structure of white matter fibres and as a result limits the accuracy of DTI measurements. Considerable interest in achieving higher resolution is frequently expressed.

Attempts have been made to use the increased measurement sensitivity of 7 T to generate larger numbers of echoes to sample wider regions of k-space, which in turn, corresponds to higher resolution images. In this way, in-plane resolutions of $0.8 \times 0.8 \text{ mm}^2$ have been reported (22).

The effectiveness of this approach, however, is put into question by two practical concerns. First, although the initial signal intensity at 7 T exceeds that at 3 T, increased rates of T2 decay with field-strength (48, 49) suggest that the formation of higher numbers of echoes is questionable. If the amplitude of echoes used to sample the outer regions of k-space is too low, apparent resolution improvements may be the result of interpolation. Second, longer echo

train lengths also reduce the receiver bandwidth making acquisitions more susceptible to bandwidth related artefacts.

Preliminary scans in Figure 4-15 tested the resolution limits that may be achieved in a single average scan through the direct increase in echo train length.

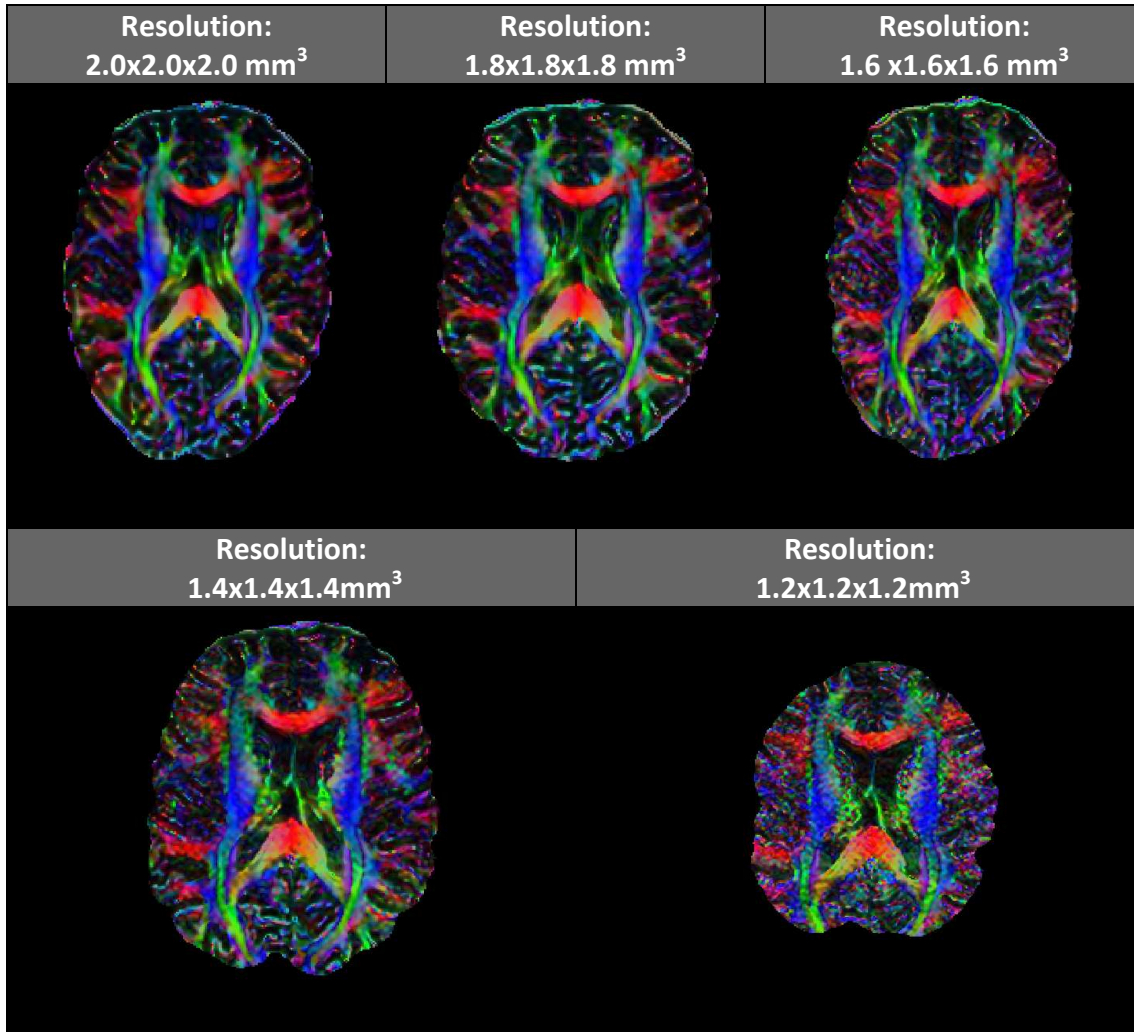


Figure 4-15: Comparison of DTI acquisitions of different voxel sizes recorded on the in-house 7 T scanner using the standard DTI protocol.

FA colour maps illustrated in Figure 4-15 demonstrate that reasonable levels of SNR could be achieved at voxel sizes upwards of 1.6 mm isotropic. However, while the level of discernable

detail was not observed to improve notably at higher resolutions, the levels of distortion increased significantly. The development of more powerful or insert gradients would be expected to alleviate these concerns and thus directly allow higher resolutions.

Here we did a preliminary assessment of an alternative strategy to utilize acquisition properties at UHF to achieve higher resolution DTI acquisitions. Rather than increasing the echo train length to extend the boundaries of the k-space region being sampled, the distance between k-space lines may be increased by using higher SENSE reduction factors. Limiting the length of the echo train also allows the optimal utilization of the increased measurement sensitivity at UHF. This strategy may be further supplemented by suppressing the signal of a section of the object being scanned along the phase encode direction, and setting a reduced FOV as proposed by Zonally Magnified (zoomed) EPI (51). Pilot scans to test this included DTI acquisitions with SENSE factor of 4 (Figure 4-16) and zoomed EPI scans with half of the FOV omitted (Figure 4-17).

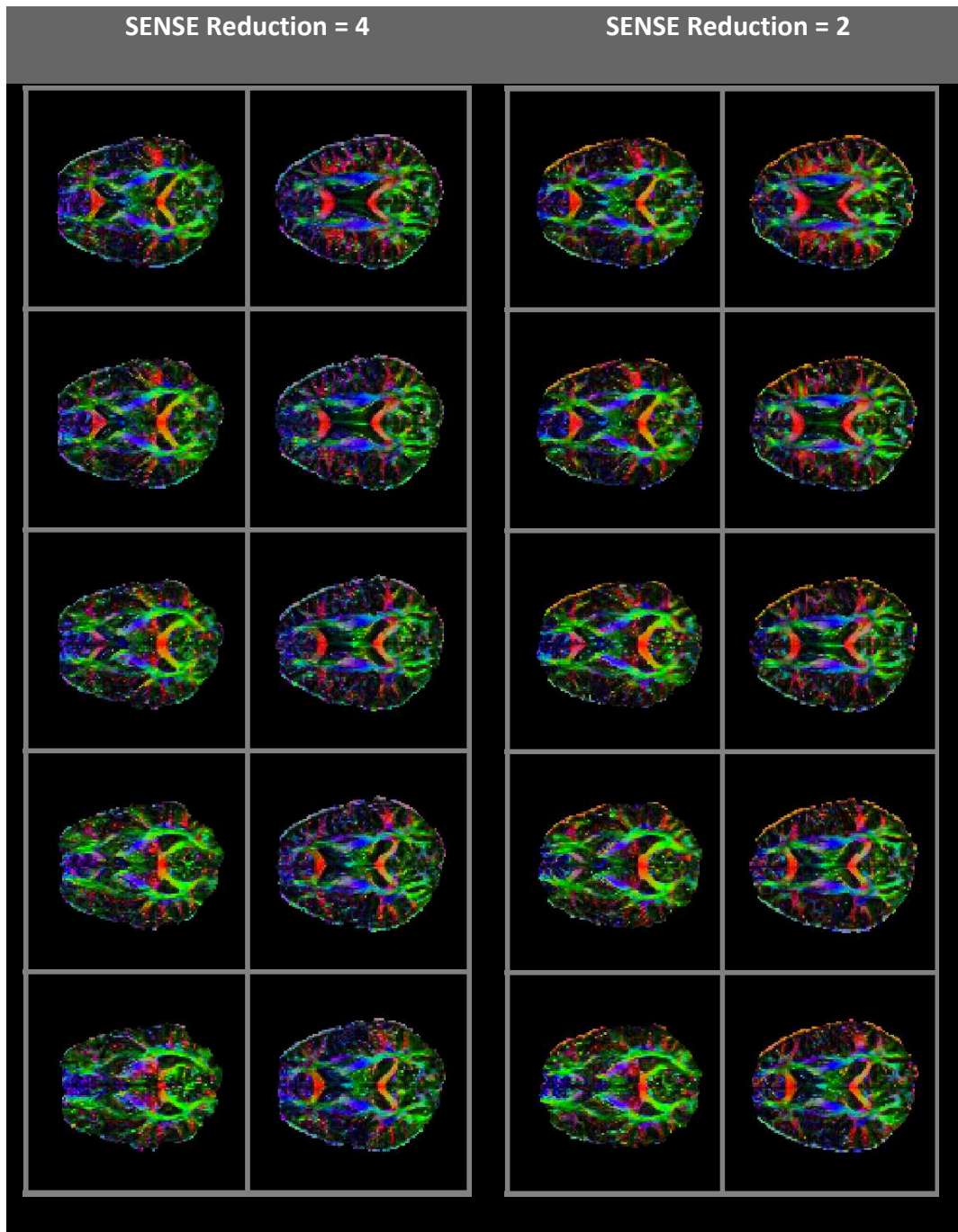


Figure 4-16: Comparison of colour FA maps acquired under SENSE reduction factors 2 and 4.

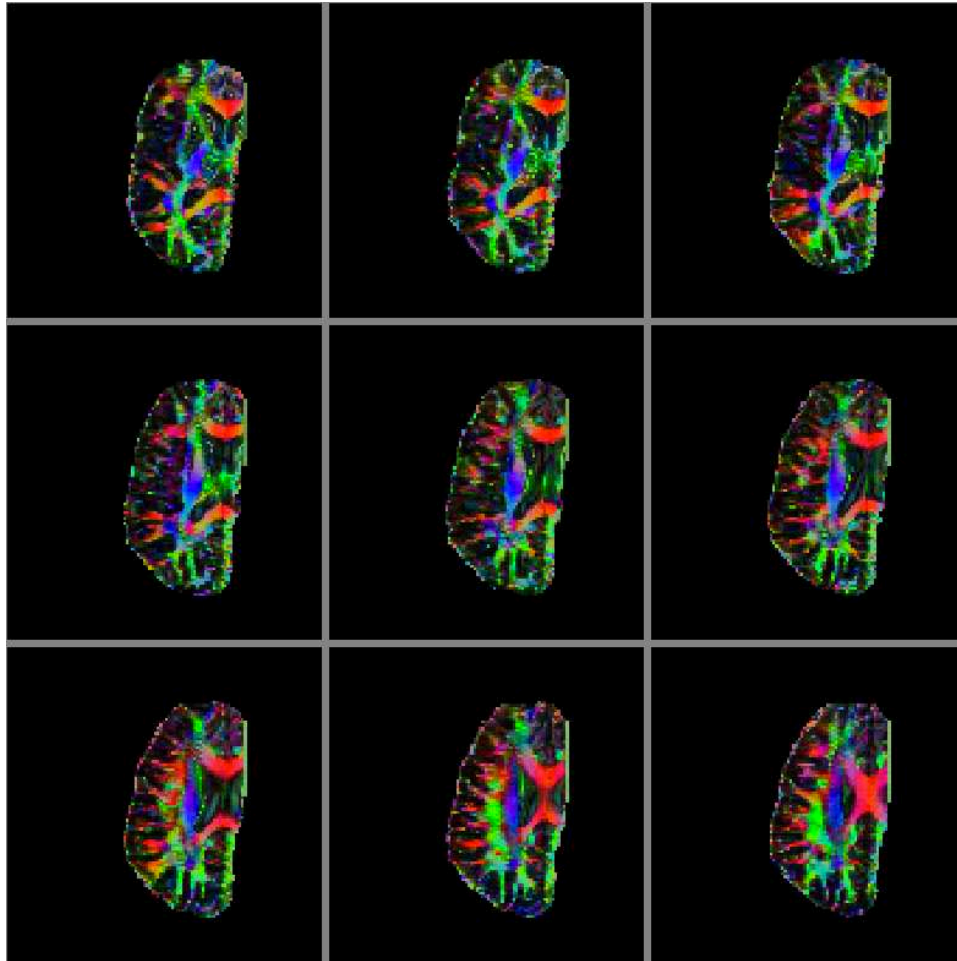


Figure 4-17: First attempts towards *in vivo* DTI acquisitions using zoomed EPI.

4.4.1.2 Technical developments

The two most imperative technical developments for UHF DTI are proposed to be the development of faster more powerful gradients and/or insert gradients to allow shorter echo times and higher acquisition bandwidths, and to investigate and reduce observed temporal instabilities.

Temporal stability

The utilization of SNR for measurements of superior precision, presupposes adequate temporal stability of the scanner. In a pilot investigation to assess the temporal stability of the in-house 7 T system, repeated ADC measurements with diffusion sensitization applied along the z-

direction were performed at systole and diastole as described in Chapter 2. The results are illustrated in Figure 4-18.

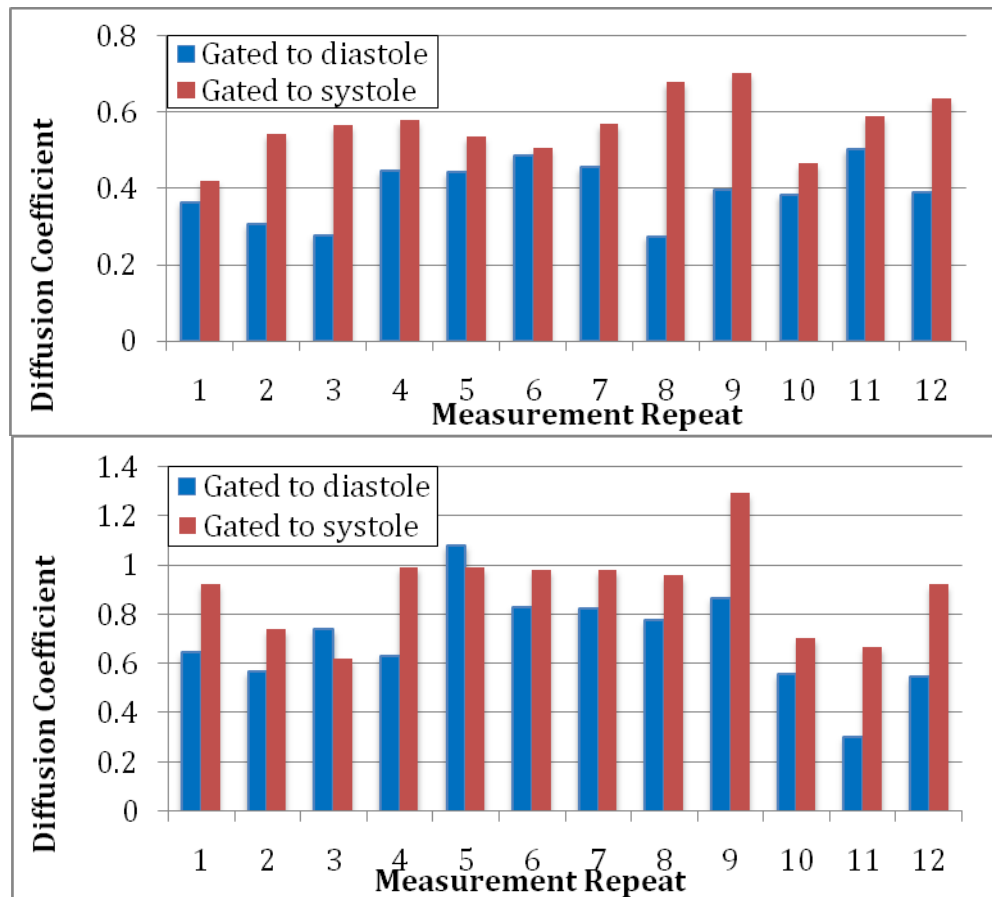


Figure 4-18: Twelve repeated ADC measurements with diffusion sensitization applied along the through-slice orientation in two volunteers (top and bottom bar charts respectively). Experimental details and ROI placement were identical to that described in Chapter 2.

Figure 4-18 demonstrates a low frequency modulation of measured ADC values. Measurements were performed during both systole and diastole to allow the assessment of whether these changes originate from cardiac pulsation, and whether their magnitude could be of practical relevance. Since ADC values acquired during systole generally exceed their counterparts acquired during diastole, this suggests that cardiac gating was successful in separating the two

cardiac phases. Since no motion is expected during diastolic scans these fluctuations do not arise as a result of cardiac pulsation induced brain motion.

Potential causes could include other sources of physiological motion (e.g. effects of respiratory motion), scanner instabilities (e.g. sub-optimally calibrated gradient cooling) or external environmental factors (e.g. air conditioning). The underlying effect could not be explored further in this study. However steps towards its alleviation would be crucial for the utilization of potential measurement precision improvements resulting from high SNR.

4.4.1.3 Fundamental research

So far this chapter has focused only on potential benefits of UHF DTI that has already been predicted as a result of previous observations and existing knowledge (i.e. increased SNR, parallel Imaging reduction). Ultra high field-strength brings with it fundamental changes in the underlying physics under which even seemingly negative effects may be discovered to contain valuable information. Good examples of such effects include magnetic susceptibility weighted imaging, and the increased chemical shift between fat and water that has been successfully utilized at UHF to eliminate the need for fat suppression/saturation RF pulses (43). The full potential of UHF will only be understood if hitherto unobserved effects are detected and explored.

A specific example is the observation reported in (26) that the despite reported SNR at 7 T being higher than that at 3 T, calculated FA maps were observed to be biased towards higher values, an effect usually attributed to low SNR. These finding were replicated in this study, as illustrated in Figure 4-19.

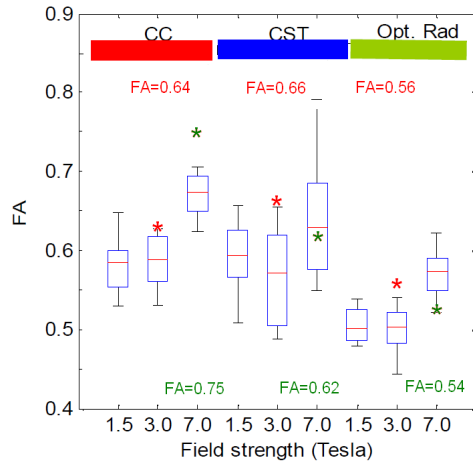


Figure 4-19: FA measurements within the ROIs illustrated in Figure 4-1 added to the results of the investigation of (2). Measured FA values are represented by the red (3 T) and green (7 T) asterisks and the numerical values are added at the top and bottom of the diagrams.

The successful replication of these findings on the in-house scanner, raises interesting questions about how the underlying physics of DTI measurements at UHF differs, and if/how this may be used to an advantage in practical measurements. A possible cause for this effect may be field strength dependent changes in T2 that have been shown to negatively correlate with FA (58).

Appendix:

Development of a technique for the quantification of SNR in *in vivo* single-shot spin echo EPI acquisitions at 7 T

This appendix outlines steps taken towards the assessment of the suitability of current *in vivo* SNR measurement techniques and, wherever necessary, provides the development and validation of alternatives. For each SNR acquisition technique assessed, its underlying assumptions are stated, and their validity tested in *in vivo* single-shot EPI measurements at 7 T.

The definition of SNR

SNR is a fundamental quality measure. In the field of Imaging, it is essential for the assessment of scanner performance and image quality, and thus also for the optimization of acquisition protocols. In MRI the importance of the availability of techniques for the accurate, precise and reliable quantification of SNR is emphasized by the modality's inherently low measurement sensitivity.

The level of white noise superimposed on the acquired signal is generally defined as its root mean square (rms) amplitude (52). In MRI, noise has been shown to follow a Gaussian distribution with zero mean (53) allowing the rms to be calculated as the standard deviation of the noise distribution. SNR of the measured signal may therefore be calculated as:

$$\text{SNR} = \frac{\mu}{\sigma} \quad (4.4)$$

Where:

μ : signal mean

σ : signal standard deviation

Since the Fourier transform of a Gaussian distribution is still Gaussian, this equation is applicable to measure the SNR of complex MRI images.

A direct pixel-per-pixel measurement of SNR is provided by the multiple acquisition (MA) technique. Here, multiple identical images (typically 30 - 300 (52)) are recorded, and the signal and noise at each voxel location may be calculated as the ratio of mean to standard deviation of measured pixel intensities over acquisition repeats, as described in Eq. 4.5.

$$\text{SNR}(x, y, z) = \frac{\mu_t(x,y,z)}{\sigma_t(x,y,z)} \quad (4.5)$$

Where:

t: acquisition repeats

μ_t : mean over repeats

σ_t : standard deviation over repeats

x, y & z: image pixel coordinates

The uncertainty of this measurement is determined by the number of image repeats acquired, which can be expressed using standard propagation of error methods (52):

$$\sigma_{\text{SNR,MA}} = \text{SNR} \sqrt{\frac{2}{N}} \quad (4.6)$$

Where:

N: number of image repeats

SNR: approximate SNR

$\sigma_{\text{SNR,MA}}$: the expected +/- deviation between actual and measured SNR using the MA method

Due to its ability to directly assess both signal and noise components on a per-pixel basis, the MA technique is frequently used as a gold standard for SNR measurements (52). However, this technique is less practical for routine SNR measurements, particularly in *in vivo*, due to the long scan times required and its susceptibility to transient signal changes (including motion).

In vivo measurement techniques of SNR

To reduce the number of acquisitions required for the quantification of SNR, a commonly used alternative is to quantify pertinent image characteristics over space (i.e. within ROIs) rather than acquisition repeats. When used in conjunction with parallel Imaging, the characteristically inhomogenous noise distribution over the FOV (6) necessitates signal and noise to be measured at the same spatial location.

The difference method (54) is based on the acquisition of two identical scans from which the repeat-average and difference images are calculated to provide estimates for signal and noise components within the measured images respectively.

The difference method (54) has received widespread acceptance with a non-exhaustive review of existing literature showing its use in over 60 studies with over a dozen conducted at field-strengths of 3 T. However, the separation of the signal and noise components of the acquired images based on two identical acquisitions is subject to the underlying assumption that the only difference between subsequent acquisitions can be attributed to random noise. The inability of the difference method to distinguish between random noise and transient signal changes makes it susceptible to effects such as scanner instabilities, physiological noise and motion artefacts.

In this study, the suitability of this technique for *in vivo* single-shot EPI acquisitions at 7 T is evaluated by testing its adherence to its underlying assumption, that thermal noise represents the dominant source of signal variation between two consecutive image acquisitions.

Groups of three identical successive acquisition repeats without recalibration steps ('dynamic' acquisitions) were performed under varying SENSE and Halfscan factors, illustrated in Table 4-8. The first acquisition was discarded as a dummy scan to achieve a steady state.

SNR measurements were performed under a range of SENSE (1, 2, 2.5, 3, 3.5, 4 and 5) and Halfscan factors (off, 0.7 and 0.6). Acquisitions were performed with a repetition time (TR) of 10000 ms, and the shortest achievable echo times. SPIR fat suppression was used in all acquisitions. All acquisitions were recorded under 2 mm isotropic resolution with 38 slices of in-

plane FOVs 192 x 192 mm. FSL FLIRT (36) motion correction was used to reduce the effects of scanner drift.

The difference image (Figure 4-20) was generated by subtracting the second and third dynamic scan of each of these datasets in order to assess if the residual voxel intensities corresponded to random noise patterns.

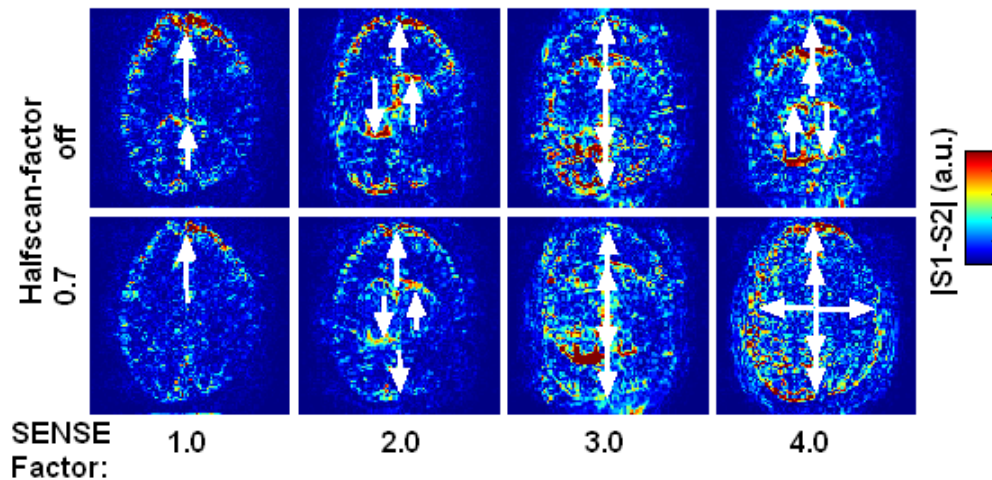


Figure 4-20: Difference of two identical acquisitions (S1 and S2) recorded consecutively at 7 T: Unwanted structural noise (highlighted by white arrows) outweighed thermal noise.

What was observed, however, was that structured noise was not only observed but, especially at higher SENSE factors, was largely found to dominate the thermal noise levels (Figure 4-20). The absence of structured noise in subsequent phantom scans (not pictured) suggested that the effects of head-, cardiac- and respiratory motion, which survive the subtraction process due to their transient nature, were the underlying cause. From these findings it was concluded that alternative techniques that are insensitive to transient signal artefacts for *in vivo* SNR quantifications at ultra high fields are needed for *in vivo* DTI acquisitions at 7 T (55).

The NEMA-DNS alternative

A number of alternatives have been proposed in literature that could potentially overcome this susceptibility of noise estimations to transient signal changes.

The SNR units method (56) is based on the fact that the g-factor profile may be calculated directly from knowledge of complex coil sensitivities and the correlation of signals acquired by different coil elements in parallel Imaging. The advantages of this approach include that SNR estimations can be performed on individual acquisitions, effectively eliminating assumptions on the temporal consistency of the acquired images. Additionally, SNR is calculated on a pixel-by-pixel basis rather than for ROIs, thus providing spatially resolved maps rather than ROI based quantification. The disadvantage of this approach is that the required information, which is collected during the reference scan at the beginning of an acquisition using parallel Imaging, is not generally made available to the user. Despite growing popularity, this technique was not made available by the vendor of the 7 T system at the time of this study, and the in-house implementation was considered too complex for this investigation.

A further potential alternative technique is the NEMA^{***} method (57) which is based on separate acquisition of signal and noise-only images. The latter may be achieved through the omission of excitation pulses prior to data recording. The NEMA method measures noise in a single acquisition rather than extracting it through the subtraction of two sequential signal acquisitions. In so doing, this technique achieves insensitivity to transient signal changes.

Although the use of this technique has been proposed in literature, technical challenges have prevented it from being successfully implemented (40). Furthermore, a validation of the compatibility of this technique with inhomogeneous noise profiles, as found in parallel imaging remains outstanding, as does an assessment of its precision and accuracy. In this investigation, all of these outstanding concerns are addressed. First the practical implementation of noise-only measurements on the in-house 7 T was performed. Secondly, underlying assumptions were identified and the validity of the technique assessed through dedicated experiments. Finally the accuracy of the technique was determined by direct comparison with the MA and difference techniques.

^{***} NEMA: National Electrical Manufacturers Associations

Implementation of the NEMA-DNS technique on the in-house scanner

Despite the absence of a standard, validated protocol for the acquisition of noise-only images provided by MRI scanner vendor, ways of omitting RF excitation were found to be available via research mode menu options. In this section the acquisition of noise-only images through dynamic noise acquisitions (NEMA-DNS) is presented in detail.

The quantification of noise levels within an ROI based on acquired noise-only images was formulated by Eq. 4.6 below. Since DTI typically uses magnitude images, this equation was based on magnitude-value data and assumes that noise profiles prior to magnitude formation follow a normal distribution with zero mean.

$$\sigma_{\text{Noise Image}} = \sqrt{\frac{\sum_{i,j,l} x^2(i, j, l)}{N}} \quad (4.7)$$

Where: i, j, l : are the voxel coordinates
 x : is the noise image
 N : number of neighbourhood voxels

Assumptions underlying the NEMA-DNS method

The quantification of SNR using the NEMA-DNS method also is subject to the fulfilment of a number of assumptions.

(i) *The elimination of signal components in noise-only images:*

Both the accurate quantification of noise, and immunity to transient signal changes are subject to acquired noise images being free of any form of signal contamination.

(ii) *Compatibility and precision of signal and noise acquisitions:*

In order to provide a suitable basis for SNR measurements, signal and noise acquisitions needed to be both compatible and represented with adequate precision. Fundamental differences in intensity and entropy of signal and noise acquisitions, combined with limited insights into the

details of the scanner calibration and post acquisition image processing steps, raised practical questions regarding the suitability of acquired data.

(iii) *Compatibility with contemporary image reconstruction techniques*

Contemporary signal acquisition strategies, such as parallel imaging, independently record signals in multiple uncoupled receiver coils. Subsequent image reconstruction procedures include signal recombination strategies based on the inherent high correlation of the signal recorded in each coil. This may be used to afford advantages in reconstructed images, such as noise identification and subsequent suppression (quadrature detection), and a reduction in the number of phase encode k-space lines needed to reconstruct images (parallel Imaging). The integral role of signal correlation on the reconstruction of images, however, poses the question whether inherently uncorrelated noise-only acquisitions can be used to represent the noise-distribution in reconstructed signal images.

Validation of the NEMA-DNS method

The suitability of the NEMA-DNS method for *in vivo* DTI acquisitions at UHF is subject to the fulfilment of the above assumptions and achievement of sufficient levels of precision and accuracy. In this section, experiments designed to validate these assumptions are described, and the precision and accuracy of the technique contrasted quantitatively against a gold standard and benchmark measurements. The MA technique was designated the gold standard since it offers a direct pixel-by-pixel quantification of SNR. The difference method was taken as the benchmark since its level of precision and accuracy achieved is widely considered adequate for most practical applications.

To assess the validity of the first assumption that noise-only images free of signal contamination could successfully be acquired, and of the second assumption that dynamically acquired noise-only images were compatible with their signal counterpart and sufficiently accurate, the following dataset was acquired: Forty $b=0$ single-shot EPI acquisitions of the agar phantom described in Chapter 1 were recorded with the final dynamic representing a noise-

only acquisition. The first 9 dynamics were discarded as dummy acquisitions to bring the acquired signal into a steady state, and alleviate the effects of transient signal changes resulting from gradient heating and scanner drift. Data was recorded both as real- and absolute-value images. The repetition time was set to 10 000 ms to ensure full signal recovery. To provide conditions typical for *in vivo* DTI, echo times were fixed to 80 ms, Halfscan reduction factors of 0.6, SENSE reduction factors of 2 and SPIR fat suppression were used. Acquisitions comprised 35 slices of Isotropic image resolution of 2 mm and in-plane FOV 192 x 192 mm. To evaluate a range of SNR values in the structurally homogenous phantom, datasets were recorded under a range of flip angles between 15 ° and 90 ° in 15 ° intervals.

The MA technique was used to generate noise maps from dynamics 10 to 39 of the absolute-value images of this dataset by calculating, for each pixel, the standard deviation over dynamics. From these noise maps, instances of noise-only images were simulated allowing direct comparisons with noise images recorded via the difference and NEMA-DNS method. To this end, a random number generator with standard deviation set to the noise-map value of each image pixel was used. The difference method noise-only image was generated through the subtraction of the 38th and 39th dynamic absolute-value acquisitions. Finally, for the NEMA-DNS method, directly acquired noise-only images were sourced from the real valued dataset. Quantitative noise maps were generated from difference method and NEMA-DNS method noise-only images via a sliding window approach using a 3 x 3 voxel neighbourhood.

Noise-only images and the distribution of their intensity values are illustrated in Figure 4-21.

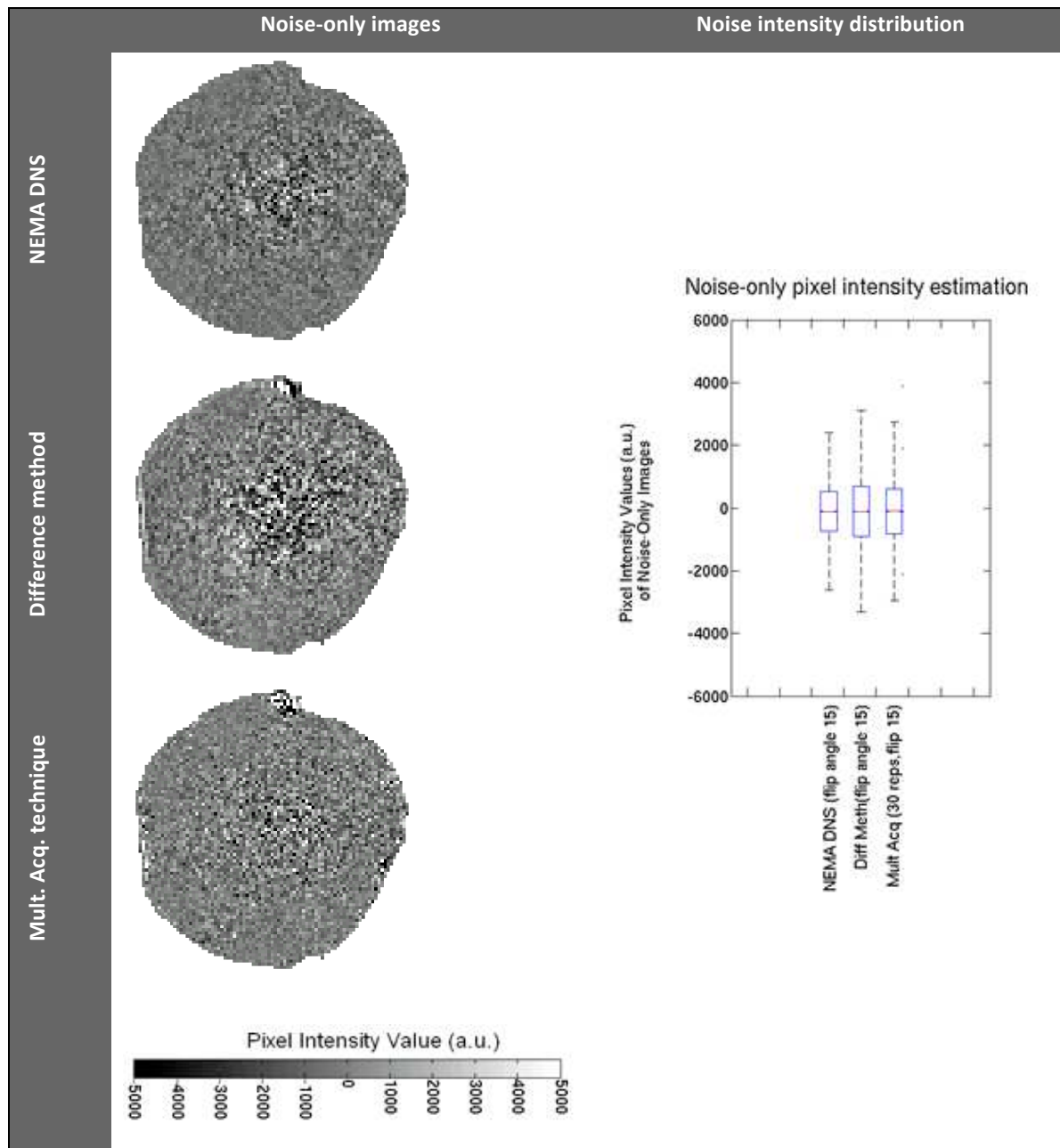


Figure 4-21: Qualitative comparison of estimated noise-only images from MA, difference and NEMA-DNS techniques (Slice 18, flip angle 15 °). Box-whisker plots (r.h.s) illustrate the distribution of pixel intensity values of noise-only images. The red bars in the centre of the box-whisker plots represent the median of the distribution after elimination of the digitization offset; Horizontal box edges represent the inter-quartile range and the whiskers 1.5, the inter-quartile range above which measurements are considered outliers (outliers were not displayed).

Noise-only images acquired with all three techniques were highly comparable, in both appearance and in the distribution and value of pixel intensities. The effectiveness of noise-only images acquired with the NEMA-DNS method to eliminate signal contamination was also demonstrated. This conclusion was drawn from the observation that noise-only images were recorded as real-valued data in which the signal appears typically as a sinusoidal modulation pattern. No such pattern was observed, however, in noise-only images, confirming the absence of signal contamination. Furthermore, the distribution of the pixel intensity values in noise-only images did not appear biased in any way, providing further evidence of the absence of a signal contribution.

The spatial distribution of noise maps was shown to not be homogenous, as illustrated in Figure 4-22. In order to quantitatively compare the accuracy of each technique, both noise intensity and the spatial distribution of noise maps were compared.

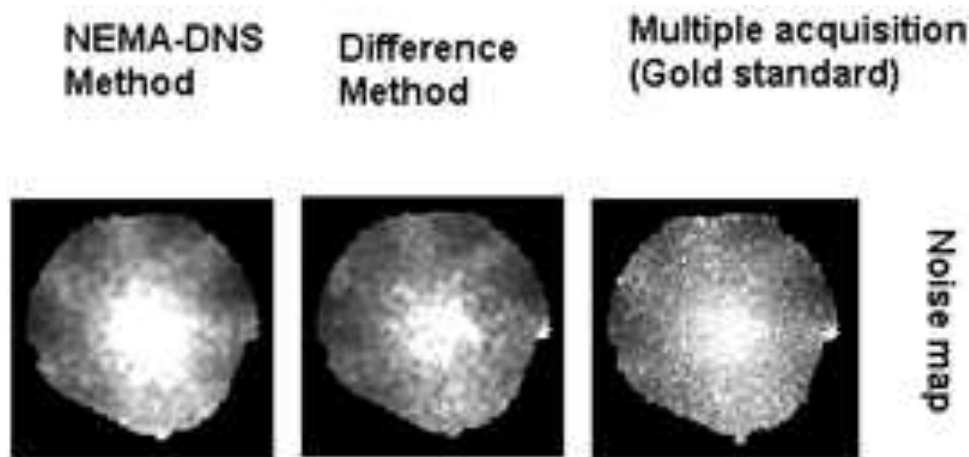


Figure 4-22: Quantitative noise maps generated using the MA, Difference and NEMA-DNS method.

To this end, noise intensity values of each voxel of the MA noise map were allocated to 1000 equidistant bins. The coordinates of all the voxels comprising a bin were recorded, and compared to the distribution of the noise intensity levels in corresponding pixels in the noise maps generated using the difference and NEMA-DNS methods. The median values of each of

these bins were subsequently plotted in all noise maps. Bins with less than 25 members were considered outliers and were omitted. This allowed a direct comparison of the reliability of noise maps generated by all three techniques.

To explore any dependencies of the accuracy of noise quantification with the intensity of corresponding signal measurements, a range of flip angles (from 15° to 90° in 15° intervals) as used. The results are illustrated in Figure 4-23.

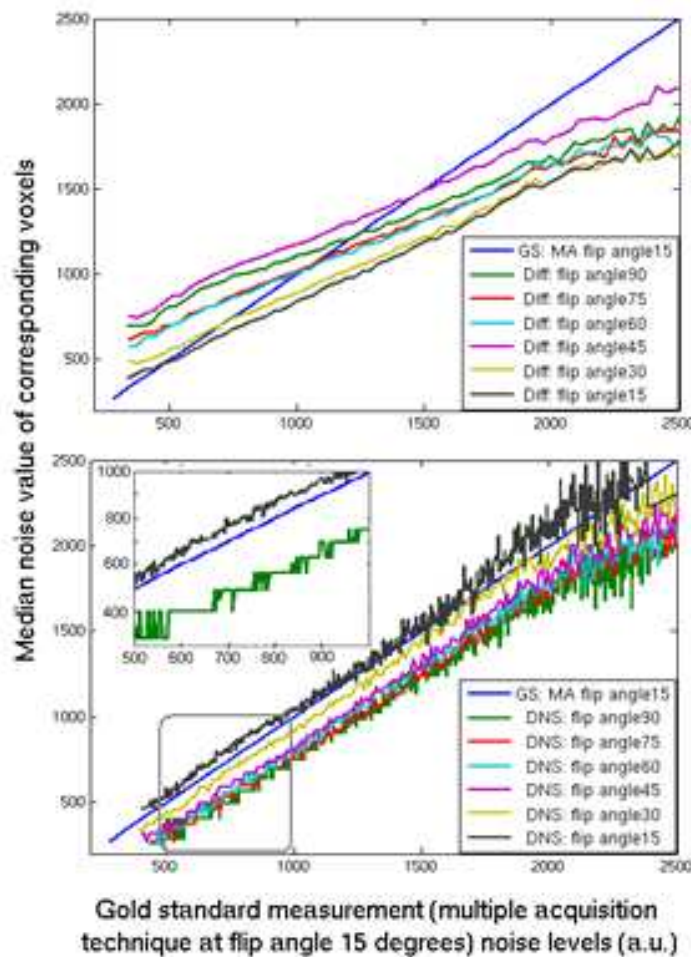


Figure 4-23: Comparison of the various noise calculation techniques at different flip angles to the gold standard acquisition (MA technique at flip angle 15°). The quantitative noise levels of the MA acquisition are compared to the noise levels of corresponding voxels illustrating differences in performance and signal intensity induced effects. To better illustrate the effect of low digitization precision at high flip angles in the DNS technique, a cut-out (gray box) of the noise acquisition values corresponding to 15° and 90° signal acquisitions are displayed separately.

The results in Figure 4-23 demonstrate that while low noise values tend to be positively, and high noise values negatively biased in the difference method, noise acquisitions using the NEMA-DNS method accurately reflect the gold standard measurements. Noise quantification using the NEMA-DNS method thus not only provides adequate, but superior levels of accuracy compared to the difference method. At high flip angles, however, the accuracy of the NEMA-DNS noise quantification is reduced. This may be the result of the dynamic range of images having been set to reflect the optimum for presenting high intensity and highly homogenous signal, and thus being sub-optimal for the depiction of low intensity and highly inhomogenous noise images.

The establishment of the NEMA-DNS method as an alternative for the routine *in vivo* quantification of noise in *in vivo* single-shot EPI measurements at 7 T is thus subject to the validation of the last assumption, according to which direct noise acquisitions must reflect the noise distribution of images following reconstruction. As already pointed out, in images recorded and reconstructed under parallel imaging, the noise profile is intimately linked to the reconstructed signal. When high SENSE reduction factors are used, the reconstruction becomes ill-posed resulting in localized amplifications of noise, which are described by the g-factor.

In order for the NEMA-DNS method to be compatible with SENSE, the g-factor in the noise profiles of reconstructed noise-only images must correspond accurately with that of reconstructed signal images.

To test this, noise maps were generated from acquisitions with high SENSE factors leading to localized g-factor increases. Noise maps using the MA, difference and NEMA-DNS method were generated in a manner similar to the dataset described for the previous section. To achieve high accuracy in the reference noise maps obtained via the MA method, 100 dynamic acquisition repeats were recorded. Scans were performed at SENSE reduction factor of 5 to induce localized noise amplification effects. Data was recorded with a flip angle of 20 °, thus preventing saturation effects. Echo times of 60 ms and repetition times of 10 000 ms were used. Image resolution was fixed to 2 mm isotropic with a FOV of 192 mm. The comparison of noise maps is illustrated in Figure 4-24 below.

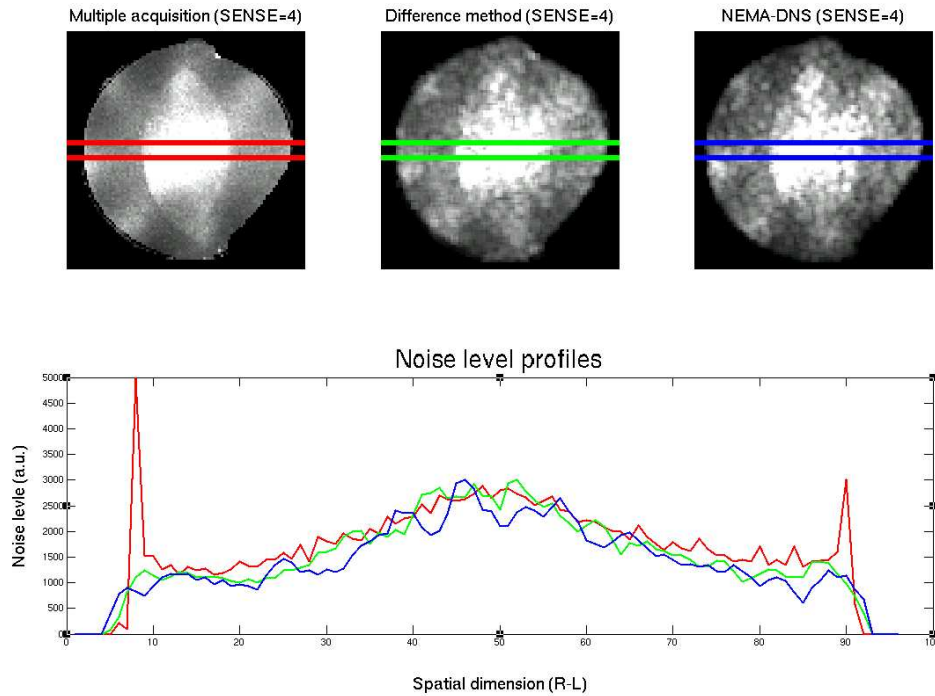


Figure 4-24: Comparison of noise profiles at high parallel Imaging reduction factor ($R = 5$). Localized noise amplifications transmitted in the NEMA-DNS method resemble those in the MA and difference method in both shape and magnitude.

The noise amplification profile of all three techniques was captured with a high level of accuracy demonstrating that the NEMA-DNS method can be used in conjunction with parallel Imaging.

In summary, shortcomings of the commonly used difference method as a measure of SNR were detected. An alternative technique which overcomes this biasing, the NEMA-DNS method, has been suggested here, and successfully implemented and validated.

4.5 Literature

1. Hayes C, Edelstein W, Schenk J, Mueller O, Eash M. An efficient, highly homogenous radio-frequency coils for the whole-body NMR imaging at 1.5T. *Magnetic Resonance* 1985;63:622-628.
2. Robitaille P, Berliner L. *Ultra High Field Magnetic Resonance Imaging*. Springer, editor. New York; 2006.
3. McRobbie D, Moore E, Graves M, Prince M. *MRI From Picture to Proton*; Second edition: Cambridge University Press; 2007.
4. Farrell J, Landman B, Jones C, Smith S, Prince J, van Zijl P, Mori S. Effects of signal-to-noise ratio on the accuracy and reproducibility of diffusion tensor imaging-derived fractional anisotropy, mean diffusivity, and principal eigenvector measurements at 1.5 T. *Journal of Magnetic Resonance Imaging* 2007;26(3):756–767.
5. Jones D, Basser P. Squashing peanuts and smashing pumpkins": how noise distorts diffusion-weighted MR data. *Magnetic Resonance in Medicine* 2004;52(5):979-993.
6. Pruessmann K, Weiger M, Scheidegger M, Boesinger P. SENSE: sensitivity encoding for fast MRI. *Magnetic Resonance in Medicine* 1999;42:952-962.
7. Hahn K, Prigarin S, Puetz B, Hasan K. DTI denoising for data with low signal to noise ratios. 2005.
8. Pizurica A, Wink A, Vansteenkiste E, Philips W, Roerdink B. A Review of Wavelet Denoising in MRI and Ultrasound Brain Imaging *Current Medical Imaging Reviews* 2006;2(2):247-260.
9. Zhang X, Ye H, Zhang H. Multi-Channel Wavelet-Based Diffusion Method for Denoising DTI Images. *International Conference on BioMedical Engineering and Informatics - Volume 02 Volume 2*. Washington DC, USA; 2008. p 178-182.
10. Redpath T. Signal-to-noise ratio in MRI. *The British Journal of Radiology* 1998;71:704-707.
11. Hoult D, Chen C-N, VJ S. Quadrature detection in the laboratory frame. *Magnetic Resonance in Medicine* 1984;1(3):39-53.
12. Hoult D, Richards R. The signal-to-noise ratio of the nuclear magnetic resonance experiment. *Journal of Magnetic Resonance* 1976;24:71-85.
13. Hall A, Barnard B, McArthur P, Gilderdale D, Young I, Bydder G. Investigation of a whole-body receiver coil operating at liquid nitrogen temperatures. *Magnetic Resonance in Medicine* 1988;7:230-235.
14. Hall A, Alford N, DButton T, Gilderdale D, Gehring K, Young I. Use of High Temperature Superconductor in a Receiver coil for Magnetic Resonance Imaging. *Magnetic Resonance in Medicine* 1991;20:340-343.
15. Morgan P. *Challenges of Diffusion Tensor Imaging at High Field*. Iceland, Reykjavik; 2008.
16. Le Bihan D, Poupon C, Amadon A, Lethimonnier F. Artifacts and Pitfalls in Diffusion MRI. *JOURNAL OF MAGNETIC RESONANCE IMAGING* 2006; 24:478-488.
17. NessAiver M. *All you really need to know about MRI Physics: Simply Physics*; 1997.

18. Jaermann T, Crelier G, Pruessmann K, Golay X, Netsch T, Van Muiswinkel A, Mori S, Van Zijl P, Valavanis A, Kollias S, Boesiger P. SENSE-DTI at 3T. *Magnetic Resonance in Medicine* 2004;51:230-236.
19. Jaermann T, Pruessmann K, Valavanis A, Kollias S, Boesiger P. Influence of SENSE on image properties in high-resolution single-shot echo-planar DTI. *Magnetic Resonance in Medicine* 2006;55(335-342).
20. Wiesinger F, Van de Moortele P, Adriany G, De Zanche N, Ugurbil K, Pruessmann K. Potential and feasibility of parallel MRI at high field. *NMR in Biomedicine* 2006;19(3):368-378.
21. Wiesinger F, Van de Moortele P, Adriany G, De Zanche N, Ugurbil K, Pruessmann K. Parallel imaging performance as a function of field-strength - An experimental investigation using electrodynamic scaling. *Magnetic Resonance in Medicine* 2004;52(5):953-964.
22. Reischauer C, Jaermann T, Staempfli P, Pruessmann K, Thompson M, Boesiger P. 16-Channel Parallel DTI at 7T: Initial Experiments. 2007; Berlin, Germany. p 3539.
23. Sammet S, Koch R, Irfanoglu O, Schmalbrock P, Machiraju R, Knopp M. SENSE Factor Optimization for Diffusion Tensor Imaging of the Human Brain at 7T. 2007; Berlin, Germany. p 1500.
24. Wiggins C, Benner T, Wiggins G, Triantafyllou C, Wald L. In-vivo, Human Diffusion Tensor Imaging at 7T: First Results. 2007; Berlin, Germany. p 1497.
25. Speck O, Zhong K. Diffusion Tensor Imaging at 7T: Expectations vs. Reality Check. 2009; Honolulu, Hawaii, USA.
26. Polders D, Hoogduin H, Donahue M, Hendrikse J, Luijten P. Comparison of SNR and Diffusion Parameters on 1.5, 3.0 and 7.0 Tesla. 2009; Honolulu, Hawaii, USA. p 1406.
27. Xu D, Han E, Hess C, Kelley D, Vigneron D, Metcalf M, Mukherjee P. 7T Diffusion Tensor Imaging and Q-Ball Imaging of the Human Brain In Vivo. 2007; Berlin, Germany. p 1466.
28. Mukherjee P, Hess C, Xu D, Han E, Kelley D, Vigneron D. Development and initial evaluation of 7-T q-ball imaging of the human brain. *Magnetic Resonance Imaging* 2008;26:171-180.
29. Jeong H-K, Anderson A. High angular resolution diffusion imaging with B₀ distortion correction at 7T. 2008; Toronto, Ontario, Canada. p 1811.
30. Bammer R, Auer M, Keeling S, Augustin M, Stables L, Prokesch R, Stollberger R, Moseley M, Fazekas F. Diffusion Tensor Imaging Using Single-Shot SENSE-EPI. *Magnetic Resonance in Medicine* 2002;51:6.
31. Luetzkendorf R, Moench T, Hollmann M, Baecke S, Tempelmann C, Stadler J, Bernarding J. In Vivo Human Brain Diffusion Tensor Imaging (DTI) at 3T and 7 T. 2008; Toronto, Ontario, Canada. p 1812.
32. Morgan P, Bowtell R, McIntyre D, Worthington B. Correction of spatial distortion in EPI due to inhomogeneous static magnetic fields using the reversed gradient method. *Journal of Magnetic Resonance Imaging* 2004;19(4):499-507.
33. Morgan P, Coxon R, Habib J, Gowland P, Bowtell R. Comparison of Sequences for Improved Diffusion Weighted Imaging at 7 T. 2008; Toronto, Ontario, Canada. p 1807.
34. Sigmund E, Gutman D, Lazar M, Jensen J, Helpert J. Optimized EPI-DTI and TSE-DTI at 3T and 7T in the Brain. 2009; Honolulu, Hawaii, USA. p 169.

35. Sigmund E, Kim D, Braga F, Xu J. Turbo Spin Echo Diffusion Tensor Imaging (TSE-DTI) in the Brain at 3T and 7T. 2008; Toronto, Ontario, Canada.
36. Smith S, Jenkinson M, Woolrich M, Beckmann C, Behrens T, Johansen-Berg H, Bannister P, De Luca M, Drobnjak I, Flitney D, Niazy R, Saunders J, Vickers J, Zhang Y, De Stefano N, Brady J, Matthews P. Advances in functional and structural MR image analysis and implementation as FSL. *NeuroImage* 2004;23:208-219.
37. National R, Association; EM. National Electrical Manufacturers Association (NEMA). Determination of signal-to-noise ratio (SNR) in diagnostic magnetic resonance imaging. NEMA Standards Publication MS 1-2001; 2001.
38. Reese T, Heid O, Weisskoff R, Weeden V. Reduction of eddy-current-induced distortion in diffusion MRI using a twice-refocused spin echo. *Magnetic Resonance in Medicine* 2003;49(1):177-182.
39. Roemer P, Edelstein W, Hayes C, Souza S, Mueller O. The NMR phased array. *Magnetic Resonance in Medicine* 1990;16:192-225.
40. Dietrich O, Raya J, Reeder S, Reiser M, Schoenberg S. Measurement of Signal-to-Noise Ratios in MR Images: Influence of Multichannel Coils, Parallel Imaging, and Reconstruction Filters. *Journal of Magnetic Resonance Imaging* 2007;26:10.
41. Muertz P, Krautmacher C, Traeber F, Gieseke J, Schild H, Willinek W. Diffusion-weighted whole-body MR imaging with background body signal suppression: a feasibility study at 3.0 Tesla. *Eur Radiology* 2007;17:3031-3037.
42. Laugenstein T. Spectral Adiabatic Inversion Recovery (SPAIR) MR Imaging of the Abdomen. 2008.
43. Nagy Z, Weiskopf N. Efficient Fat Suppression by Slice-Selection Gradient Reversal in Twice-Refocused Diffusion Encoding. *Magnetic Resonance in Medicine* 2008;60:1256-1260.
44. Wiesinger F, Boesiger P, Pruessmann K. Electrodynamics and Ultimate SNR in Parallel MR Imaging. *magnetic Resonance in Medicine* 2004;52:376-390.
45. Ledden P, Duyn J. Ultra-high frequency array performance: Predicted effects of dielectric resonance. 2002; Honolulu, Hawaii, USA. p 324.
46. Ohliger M, Grant A, Sodickson D. Ultimate intrinsic signal-to-noise ratio for parallel MRI: Electromagnetic field considerations. *Magnetic Resonance in Medicine* 2003;50(5):1018-1030.
47. Gomori J, Holland G, Grossman R, Gefter W, Lenkinski R. Fat suppression by section-select gradient reversal on spin-echo MR imaging. Work in progress. . *Radiology* 1988;168:493–495.
48. Cox E, Gowland P. Measuring T2 and T2' in the Brain at 1.5T, 3T and 7T Using a Hybrid Gradient Echo-Spin Echo Sequence and EPI. 2008; Toronto, Ontario, Canada. p 1411.
49. Cox E, Gowland P. Simultaneous Quantification of T2 and T'2 Using a Combined Gradient Echo-Spin Echo Sequence at Ultrahigh Field. *magnetic Resonance in Medicine* 2010.
50. Miller K, Bulte D, Devlin H, Robson M, Wise R. Evidence for a vascular contribution to diffusion FMRI at high b value. *PNAS* 2007;104:20967–20972.
51. P. Mansfield RJO, R Coxon. Zonally magnified EPI in real time by NMR. *J Phys E: Sci Instrum* 1988;21:275-280.
52. Schoenberg S, Dietrich O, Reiser M. Parallel Imaging in Clinical MR Applications. 2007.

53. Mc Veigh E, Henkelman R, Bronskill M. Noise and filtration in magnetic resonance imaging. *Medical Physics* 1985;12:586-591.
54. Reeder S, Wintersperger B, Dietrich O, Lanz T, Greiser A, Glazer G, Schoenberg S. Practical approaches to the evaluation of signal-to-noise ratio performance with parallel imaging: application with cardiac imaging and a 32-channel cardiac coil. 2005;54(3):748-754.
55. Habib J, Auer D, Bowtell R. Towards the accurate and precise assessment of SNR in vivo at 7T. 2010; Stockholm, Sweden. p 4676.
56. Kellman P, McVeigh E. Image reconstruction in SNR units: a general method for SNR measurement. *Magnetic Resonance in Medicine* 2005;54:9.
57. Determination of signal-to-noise ratio (SNR) in diagnostic magnetic resonance imaging. NEMA standards publication MS 1-2001: National Electrical Manufacturers Association (NEMA); 2001.
58. Ozsunar Y, Grant P, Huisman T, Schaefer P, Wu O, Sorensen A, Koroshetz W, Gonzalez R. Evolution of Water Diffusion and Anisotropy in Hyperacute Stroke: Significant Correlation between Fractional Anisotropy and T2. *American Journal of Neuroradiology* 2004;25:699-705.

Chapter 5: Conclusion

The work presented in this thesis demonstrates the use of systematic application-driven optimizations of existing acquisition protocols to provide answers to specific outstanding questions, and accessible solutions to overcome perceived limitations. Merits of this approach of maximizing the utilization of existing sequences over the development of novel techniques are particularly advantageous in translational research. These include its versatility and efficiency, as demonstrated by the range of applications presented; the retained comparability and compatibility with established sequences and infrastructure; and the obvious minimization of time-losses that come with the development and validation of new sequences. Each chapter in this thesis presents a distinct translational research project that addresses important, outstanding questions pertaining to practical Diffusion Tensor Imaging (DTI).

Chapter 2 forms part of a larger initiative towards the optimization of clinical DTI at 3 T. Specifically, it seeks to settle the hitherto unresolved question regarding the practical relevance of cardiac pulsation induced artefacts, and whether increases in scan time and/or complexity resulting from cardiac gating are merited by data quality improvements. A number of studies clearly demonstrated the susceptibility of diffusion weighted acquisitions to cardiac pulsation induced artefacts (CPAs) and the effectiveness of cardiac gating in the alleviation of these effects. Furthermore, optimized gating schemes to minimize additional scan time requirements have been proposed. Despite this, the uptake of cardiac gating in clinical practice has been sluggish. This is likely the result of adverse effects of CPAs on diffusion metrics recorded under routinely used acquisition protocols never having been quantified and/or proved to be of clinical relevance. The inevitable advent of quantitative DTI biomarkers laid additional emphasis on the need for a quantitative characterization of CPAs. Through the use of dedicated scans and Bootstrap simulations, it was shown that in group-studies, other sources of variability in fact outweigh CPAs and cardiac gating in these studies is thus not necessary. Conversely, in individual-studies, CPAs affect diffusion metrics to an extent, which may be considered

significant, depending on the application. In such studies, and when relying on DTI biomarkers for disease, the need for gating must be assessed on a case-by-case basis.

In Chapter 3, the principal feasibility of DTI of the chemically fixed whole human brain in a clinical setting was, for the first time, established. Although previous studies strongly alluded to inherent limitations in SNR as a main limiting factor and employed strategies to circumvent this, a practical assessment of SNR in this chapter proved this not to be the case. Rather, it demonstrated that the selection of appropriate averaging techniques to minimize susceptibility scanner instabilities, and the employment of appropriate Eddy-current correction strategies were essential to achieving successful DTI acquisitions of the chemically fixed whole human brain. Implementing the proposed protocol resulted in high quality DTI acquisitions within just 21 minutes. DTI of post mortem tissue using a readily available setup has considerable potential for future applications by making it accessible to non-specialized centres and improving compatibility of results with in vivo data. This opens the doors for a range of new research possibilities including high spatial and/or directional resolution DTI; histology based interpretation of changes in DTI indices; development of novel acquisition sequences etc.

Finally, in Chapter 4, the quantitative assessment and optimization of ultra high field strength (7 T) MRI for in vivo DTI applications was undertaken in two steps. First, field-strength specific advantages of using 7 T over lower field-strengths for in vivo DTI applications, independent of the influence of acquisition sequence and scanner setup were identified and characterized. Second, guidelines for the design of acquisition protocols to efficiently utilize these benefits on a specific scanner setup were formulated. The work presented in this chapter successfully demonstrated that DTI applications can indeed benefit considerably from being performed at 7 T, but that the appropriate selection of protocol parameters affecting SNR performance and receiver bandwidth is essential. The most prominent artefacts at 7 T were also investigated, and techniques towards their effective alleviation established. The developed protocols may thus be directly applied to clinical and/or biomedical research studies.